

MODELING AND CONTROL  
OF  
SURFACE ACOUSTIC WAVE MOTORS

This thesis has been completed in partial fulfillment of the requirements of the Dutch Institute of Systems and Control (DISC) for graduate study.



The research described in this thesis has been conducted at the department of Electrical Engineering at the University of Twente, Enschede and has been financially supported by the Innovative Oriented Research Program (IOP) Precision Technology from the Dutch Ministry of Economic Affairs.



Title: Modeling and Control of Surface Acoustic Wave Motors

Author: P.J. Feenstra

ISBN: 90-365-2235-8

Copyright © 2005 by P.J. Feenstra, Enschede, The Netherlands

No part of this work may be reproduced by print, photocopy or any other means without the permission in writing from the publisher.

Printed by PrintPartners Ipskamp, Enschede, Netherlands

# MODELING AND CONTROL OF SURFACE ACOUSTIC WAVE MOTORS

PROEFSCHRIFT

ter verkrijging van  
de graad van doctor aan de Universiteit Twente,  
op gezag van de rector magnificus,  
prof. dr. W.H.M. Zijm,  
volgens besluit van het College voor Promoties  
in het openbaar te verdedigen  
op donderdag 22 september 2005 om 13.15 uur

door

Philippus Jan Feenstra  
geboren op 31 maart 1975  
te Workum, Nederland

Dit proefschrift is goedgekeurd door:

prof. dr. ir. J. van Amerongen, promotor  
dr. ir. P.C. Breedveld, assistent-promotor

# Contents

<b>Contents</b>	<b>v</b>
<b>1 An introduction to SAW motors</b>	<b>1</b>
1.1 Introduction . . . . .	1
1.2 Definition and history . . . . .	2
1.3 Classification of SAW motors . . . . .	5
1.3.1 Translations . . . . .	6
1.3.2 Constrained circular motions . . . . .	6
1.3.3 Rotations . . . . .	6
1.3.4 Combinations . . . . .	7
1.4 Features and applications of a SAW motor . . . . .	8
1.5 Experimental setup . . . . .	11
1.5.1 Stator and IDT's . . . . .	11
1.5.2 Sliders . . . . .	12
1.5.3 Slider guiding . . . . .	13
1.5.4 Preload force . . . . .	14
1.5.5 Electrical circuit . . . . .	14
1.5.6 Measurement . . . . .	14
1.6 Thesis outline . . . . .	15
<b>2 Acoustic waves</b>	<b>17</b>
2.1 Wave types . . . . .	17
2.1.1 Wave equation . . . . .	17
2.1.2 Uniform plane waves . . . . .	19
2.1.3 Rayleigh waves in an isotropic half space . . . . .	21
2.1.4 Lamb waves and Rayleigh waves in a plate . . . . .	23
2.2 Rayleigh wave properties . . . . .	28
2.2.1 Power flow . . . . .	28
2.2.2 Diffraction . . . . .	30
2.2.3 Attenuation . . . . .	32
2.3 Generation of Surface Acoustic Waves . . . . .	33
2.3.1 Interdigital transducer . . . . .	34
2.3.2 Piezoelectricity . . . . .	41
2.3.3 Power distribution . . . . .	43
2.4 Conclusions . . . . .	44

<b>3</b>	<b>SAW motor modeling</b>	<b>45</b>
3.1	Introduction	45
3.2	Modeling a single point of contact	46
3.2.1	Wave motion	46
3.2.2	Normal motion	47
3.2.3	Tangential motion	53
3.2.4	Macroscopic behavior	61
3.3	Modeling multiple points of contact	65
3.3.1	Ideal situation	66
3.3.2	Actual situation	69
3.4	Model implementation	71
3.4.1	Time change	71
3.4.2	Hybrid modeling	71
3.5	Model validation	74
3.5.1	Single point of contact (with tangential compliance)	74
3.5.2	Ideal multiple points of contact	75
3.5.3	Actual multiple points of contact	77
3.5.4	Review	81
3.6	Variation of model parameters	81
3.6.1	Coefficient of friction	82
3.6.2	Young modulus stator	83
3.6.3	Preload force	83
3.7	Conclusions	84
<b>4</b>	<b>Actuation and control</b>	<b>87</b>
4.1	System	87
4.1.1	Mechanical model	87
4.1.2	System disturbances	92
4.2	Actuation methods	94
4.2.1	Single-sided actuation	95
4.2.2	Compensated single-sided actuation	96
4.2.3	Dual-sided actuation	96
4.2.4	Pulse-width modulation	97
4.2.5	Overview of actuation methods	100
4.3	Open-loop control	100
4.4	Closed-loop controller	101
4.4.1	Controller design	101
4.4.2	Experiments	103
4.4.3	Review	107
4.5	Conclusions	108
<b>5</b>	<b>Design procedures</b>	<b>111</b>
5.1	Introduction	111
5.2	Motor design	112
5.2.1	Selection rules and considerations	112
5.2.2	Design parameters	116
5.2.3	Additional design parameters	121

---

5.3	Guiding and preload mechanism design . . . . .	123
5.3.1	Slider-stator contact . . . . .	123
5.3.2	Slider/stator guiding . . . . .	124
5.3.3	Preload mechanisms . . . . .	126
5.4	Electronics of the control loop . . . . .	126
5.5	Conclusions . . . . .	128
<b>6</b>	<b>Conclusions</b>	<b>131</b>
6.1	Recommendations . . . . .	132
<b>A</b>	<b>Uniform plane wave solution</b>	<b>135</b>
<b>B</b>	<b>Rayleigh wave solution in an isotropic half-space</b>	<b>139</b>
<b>C</b>	<b>Lamb dispersion curve</b>	<b>145</b>
<b>D</b>	<b>IDT admittance matrix</b>	<b>147</b>
<b>E</b>	<b>Tangential stiffness</b>	<b>151</b>
	<b>Bibliography</b>	<b>153</b>
	<b>Nomenclature</b>	<b>159</b>
	<b>Index</b>	<b>163</b>
	<b>Summary</b>	<b>165</b>
	<b>Samenvatting</b>	<b>167</b>
	<b>Dankwoord</b>	<b>169</b>
	<b>Curriculum vitae</b>	<b>171</b>





# Chapter 1

## An introduction to SAW motors

***Overview:** This chapter describes the history and the definition of piezoelectric ultrasonic motors and, in particular, the history and the classification of SAW motors. Furthermore, features and potential applications fields of the SAW motor are enumerated. Next, an experimental SAW motor is described, which is referred to throughout this thesis. Finally, the outline of this thesis is given.*

### 1.1 Introduction

Miniaturization and more accurate control of processes and motions are two major technological trends in industry. Examples are the demand of small motors in office equipment such as printers (Uchino 1998) and optical instruments such as cameras (Zhao 2005) and motions aiming at accurately controlled manipulation like microsurgery and assembly processes. Furthermore, there is a demand for non-contaminating actuators, for instance in the field of semiconductor production equipment. Additional constraints may be the operation in vacuum and in an environment that requires absence of magnetic fields.

Electromagnetic motors also called Lorentz motors, invented in 1821 by the British physicist and chemist Michael Faraday (1791-1867), dominate the industry. However, no revolutionary improvement can be expected without the discovery of new magnetic or superconducting materials. Moreover, the energy efficiency of electromagnetic transducers decreases rapidly with smaller form factors. By contrast, the energy efficiency of piezoelectric ultrasonic motors is insensitive to size and therefore superior for mini-motors (Uchino 1998), which explains the increasing interest for this type of motor.

A particular kind of piezoelectric ultrasonic motor is the Surface Acoustic Wave (SAW) motor. In this thesis, this motor is investigated as a potential solution to the demanding problems resulting from the previously described needs. The primary goal is to determine and understand the characteristics of a SAW motor that are interesting for applications and to determine and understand the design parameters of a SAW motor.

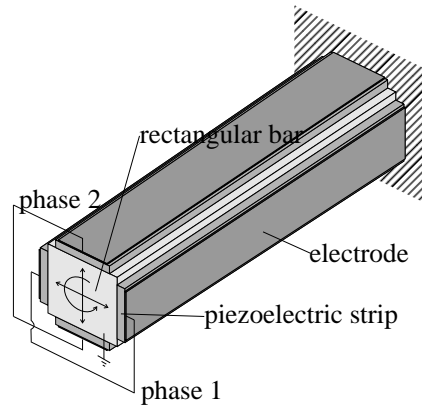


Figure 1.1: The first attempt of a piezoelectric ultrasonic motor, patented by Williams and Brown (1948). The bending modes of the rectangular bar were excited by 90 degree out-of-phase signals. Consequently, a kind of rotation motion at one end of the bar with respect to the other end was generated.

## 1.2 Definition and history

The name ‘ultrasonic motor’ commonly refers to a class of motors that uses microscopic elastic vibrations to generate macroscopic rotations or translations of a rotor or a slider respectively. The frequency of the microscopic vibrations is ultrasonic, i.e., higher than the upper limit of the human hearing range (about 20 kHz). The conversion between vibration and resulting motion is based on friction (Ueha & Tomikawa 1993). Regarding this definition, the name ‘ultrasonic motor’ is sometimes incorrectly used for motors that are driven by air-streams rather than friction (Ji & Zhao 2005) or motors that have vibration frequencies in the sonic range.

Williams & Brown (1948) patented the first attempt of a piezoelectric ultrasonic motor. It consisted of four piezoelectric rectangle elements that were bonded to the four faces of a square bar (figure 1.1). The bending modes of the rectangular bar were excited by 90 degree out-of-phase signals. Consequently, a kind of rotation motion at one end of the bar with respect to the other end was generated. The motor did not make it to a product due to the lack of proper piezoelectric materials (Koç et al. 2002). In the subsequent 34 years, only a few new types of ultrasonic motors were fabricated, e.g., Kleesattel et al. (1962) and Barth (1973). Figure 1.2 shows the ultrasonic motor by Barth. The rotor was pressed against the horns. The rotor was driven in clockwise direction by exciting horn 1 and in reverse direction by exciting horn 2 (The horns vibrated in axial direction). All these new motor types suffered from the problem of wear and tear, because the vibrating pieces were fixed almost normal to the rotor surface. In 1982 Sashida (1985, US patent) proposed a traveling-wave ultrasonic motor to solve this problem (figure 1.3). Two high-frequency 90 degrees out-of-phase signals were applied to the piezoelectric segments via electrode terminals *a* and *b*. Consequently, a traveling wave (and an associated elliptical surface motion) was generated in the elastic ring, which drove the rotor by means of friction (figure 1.4). The driving direction reversed by changing the sign of the phase. A modified version of this motor is used by Canon for automatic focusing of a camera lens. Sashida’s design initiated many proposals on how to generate an elliptical motion by using different

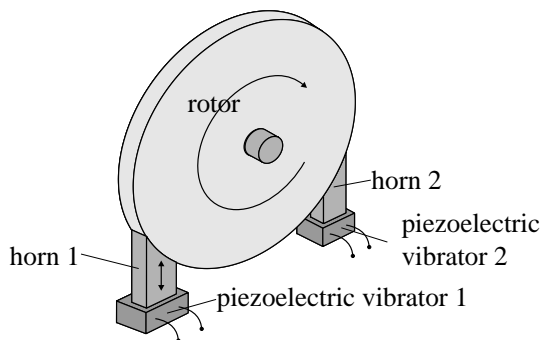


Figure 1.2: Ultrasonic motor by Barth (1973). The vibrating horns drive the rotor.

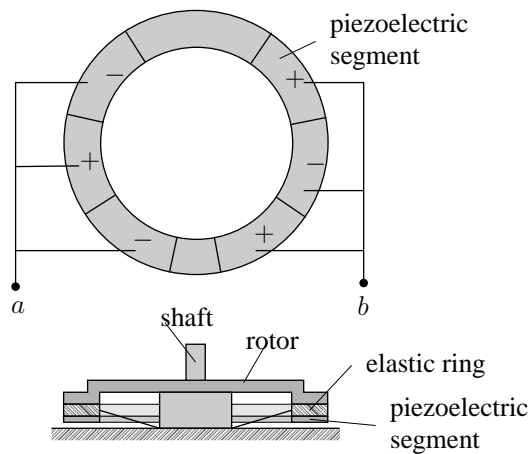


Figure 1.3: Sashida's traveling-wave ultrasonic motor. A traveling wave, generated in the elastic ring, drives the rotor.

types and combinations of vibration modes, such as longitudinal, torsional and *surface acoustic waves* (Ueha & Tomikawa 1993), (Uchino 1997), (Uchino 1998), (Zhao 2005).

A true Surface Acoustic Wave, known as a Rayleigh wave<sup>1</sup>, is a Wave that is confined to the Surface of a stator. The study of time-varying deformations or vibrations in material media is commonly addressed as Acoustics (Auld 1990). The elliptical motion of surface particles is a fundamental Raleigh-wave feature. Due to this elliptical motion, a friction force is exerted on a slider that is pressed against the stator surface, resulting in a motion of the slider (figure 1.4). The motion of the slider reverses by applying a wave in opposite direction. To obtain a proper contact between stator and slider, a slider is equipped with so-called projections (small "bumps") at its surface. The shape of these projections is for example cylindrical or semi-spherical (e.g. figures 1.13(a) and 1.13(b)). In order to motivate the use of projections consider a small gap between a vibrating element and a fixed part. If the air has enough time to flow away between the gap (in our case with respect to the SAW time-period), the air film acts a damper. Otherwise, the air film is trapped and squeezed and behaves dominantly like a spring. Due to this squeeze film, the coefficient of friction would become very low, which hampers the SAW motor operation. The time to flow away depends on the contact area and the contact pressure and reduces significantly by using projections. Hence, projections overcome a squeeze film of air between slider and stator.

Although, the potential use of surface acoustic waves (SAW) as a driving principle was already described by Sashida (1985, US patent), the first successful attempts are more recent. The seminal work in this area stems from 1992. In that year Kurosawa of the Tokyo Institute of Technology (Japan) developed some initial ideas about the SAW motor (Kurosawa et al. 2004). In the successive year, in 1993, the SAW motor project started. The challenge was to obtain a proper contact with a high contact pressure between slider

<sup>1</sup>The British mathematician and physicist Lord Rayleigh (1842 – 1919) described the Rayleigh wave in his 1885 paper 'On waves propagated along the plane surface of an elastic solid'.

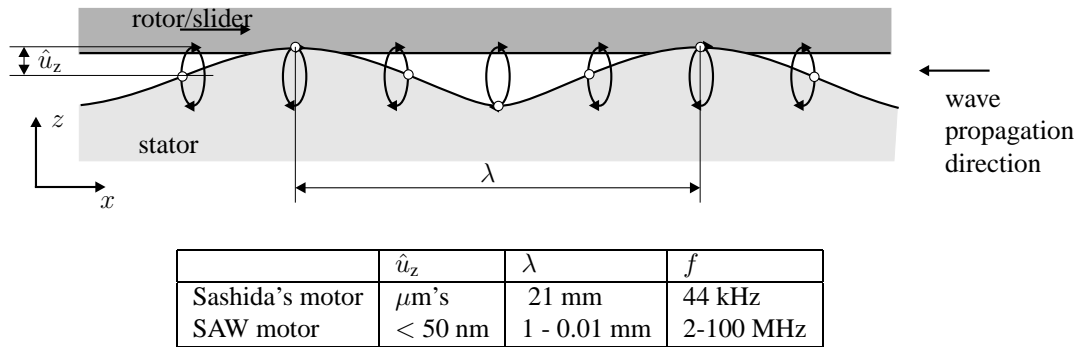


Figure 1.4: Principle of actuation of a traveling-wave motor and a SAW motor. The figure is not on scale.

and stator such that the small wave amplitude (with respect to conventional ultrasonic motors) would generate a motion. In their first successful attempt, the slider consisted of three ruby balls glued onto a washer. Due to these contact balls, the projections, a high contact pressure was obtained. Figure 1.5 shows an experimental stator of Kurosawa et al. (1994). In the subsequent years, many milestones were set, like the fabrication of silicon sliders to achieve more projections, miniaturization of the motor, application of energy recycling and the use of coatings (table 1.1).

Around 1994 Hélin et. al. started their research on the use of Lamb and Rayleigh waves for ultrasonic motors at the University of Valenciennes and Hainaut Cambrésis, France. The research resulted in a PhD. thesis (Hélin 1997).

In 1999 two students, Bergsma & de Jong (1999), of the University of Twente made a study on the possible design of a clean linear precision actuator and proposed the Surface Acoustic Wave (SAW) motor as a potential candidate. Subsequently, they analyzed the

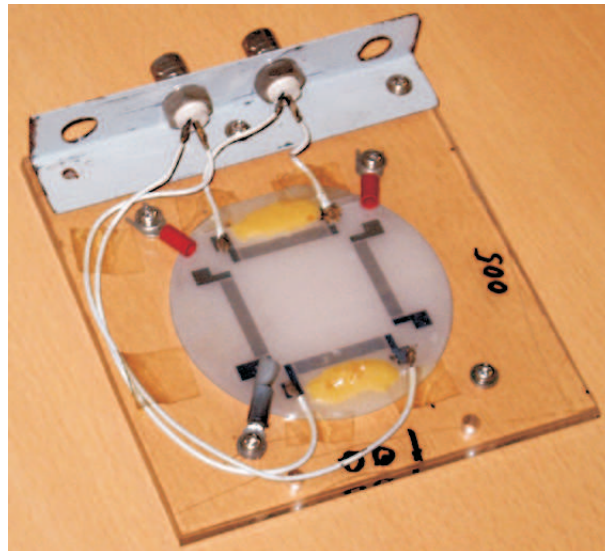


Figure 1.5: Experimental stator of Kurosawa et al. (1994).

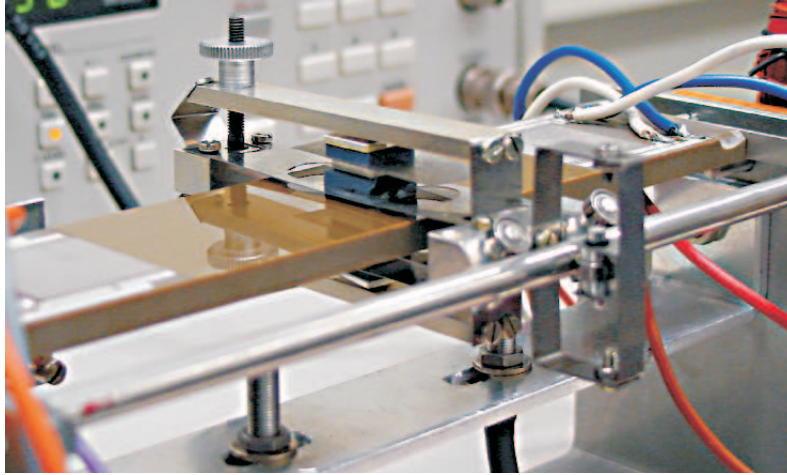


Figure 1.6: Experimental SAW motor of Dijk (2000). Use of two sliders preloaded against each other and utilizing end-of-stroke sensors.

1993	First operational SAW motor by Kurosawa et al.
1994	First (English) publication of a SAW motor ( <a href="#">Kurosawa et al. 1994</a> )
1997	A slider with 500 steel balls at the bottom ( <a href="#">Chiba et al. 1997</a> ). PhD. thesis ( <a href="#">Hélin 1997</a> ).
1998	Slider made of silicon to achieve more projections ( <a href="#">Osakabe et al. 1998</a> ) Miniaturization of a SAW motor ( <a href="#">Takasaki et al. 1998</a> )
1999	Use of energy recycling ( <a href="#">Asai et al. 1999</a> ).
2000	Use of two sliders preloaded against each other ( <a href="#">Dijk 2000</a> )
2002	Closed loop SAW planar motor ( <a href="#">Vermeulen et al. 2002</a> )
2003	The use of coatings for slider and stator ( <a href="#">Nakamura et al. 2003</a> )

Table 1.1: Some milestones in the development of SAW motors.

SAW motor in more detail. Another student of the University of Twente, [Dijk \(2000\)](#), continued their work. He designed and built a successful operational prototype of a linear SAW motor at the Philips Centre for Industrial Technology (CFT, nowadays called Philips Applied Technologies). The motor had two sliders that were preloaded against each other. Furthermore, end-of-stroke sensors were utilized to detect whether or not the motion direction of the slider should be reversed (figure 1.6 and table 1.1). In January 2001, the SAW motor was further investigated in the PhD research project described in this thesis at the University of Twente in cooperation with Philips Applied Technologies.

### 1.3 Classification of SAW motors

This section gives an overview of the possible fundamental motion patterns by utilizing Rayleigh waves.

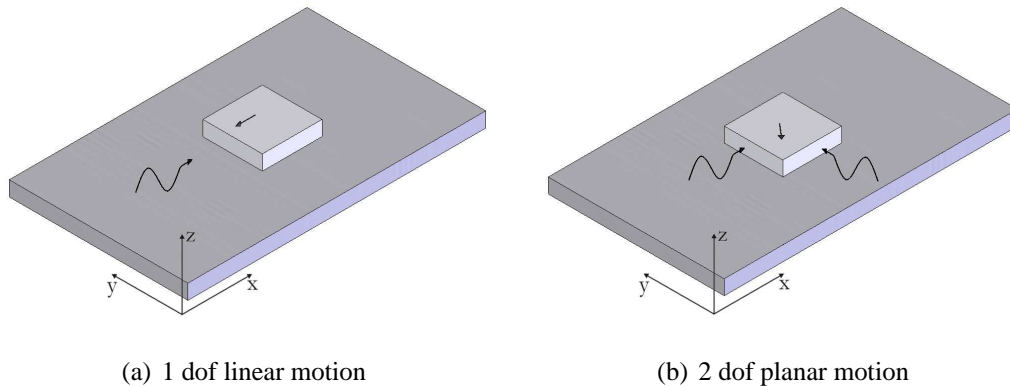


Figure 1.7: Translations

### 1.3.1 Translations

Figure 1.7(a) illustrates the basic setup of a linear 1 dof (degrees of freedom) motor. The curly arrow represents a propagating Rayleigh wave at the stator surface, which pulls the slider in  $(-x)$ -direction. For example, [Kurosawa et al. \(1994\)](#), [Hélin \(1997\)](#) and [Dijk \(2000\)](#) have demonstrated the linear translation. The linear translation extends to a planar translation - i.e. a translation in 2-dimensions- by applying a second orthogonal propagating wave front, as shown in figure 1.7(b). The rotation around  $z$  is constrained (by a slider guiding). The slider translates in a diagonal direction due to superposition of the two waves. For example, [Kurosawa et al. \(1994\)](#) and [Hélin \(1997\)](#) have described the planar translation.

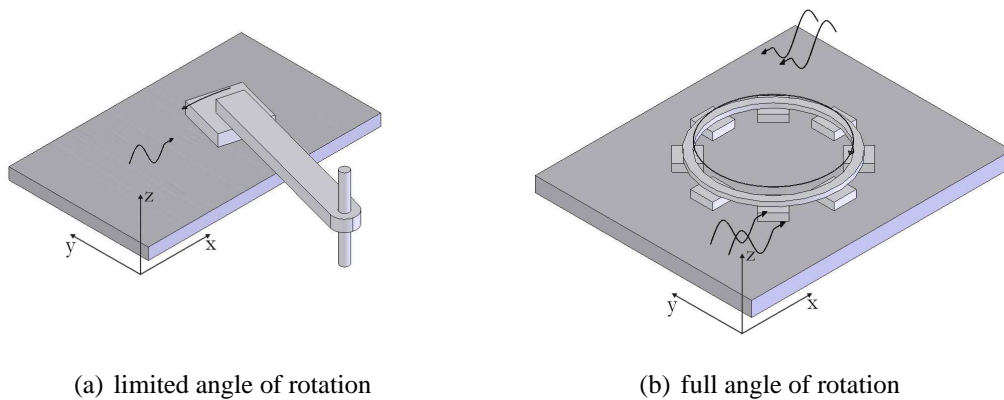
### 1.3.2 Constrained circular motions

Besides planar translations, it is possible to make planar circular motions. Figure 1.8(a) shows a basic construction of a constrained circular motion around the  $z$ -axis that is enforced by the mechanical arm. The angle of rotation is limited. Figure 1.8(b) shows a construction with eight sliders that are rigidly connected to a ring. There is no limitation in the angle of rotation. [Cheng et al. \(2002\)](#) have demonstrated this constrained circular motion.

### 1.3.3 Rotations

Figure 1.9(a) shows a construction for a one dof rotational motion around the  $y$ -axis. The surface of the rotor is equipped with rings, again to overcome a squeeze film of air. [Kamphuis \(2003\)](#) has studied this motion. In order to increase the output torque, Kamphuis recommended to increase the contact area between rotor and stator, for instance, by a trench in the stator surface (figure 1.9(a)). The one dof rotational motion extends to a two

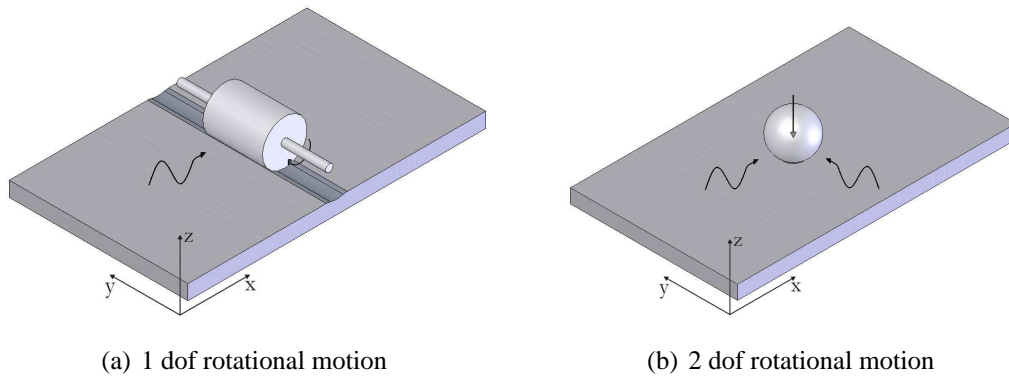




(a) limited angle of rotation

(b) full angle of rotation

Figure 1.8: Constrained circular motions



(a) 1 dof rotational motion

(b) 2 dof rotational motion

Figure 1.9: Rotations

dof rotational motion by means of a second wave front and using a sphere or hemisphere instead of a rotor, see figure 1.9(b). The direct driven, two dof, rotational motion has been proposed and tested by [Yoseph et al. \(2003\)](#).

The considered examples only utilize rectangular stators. However, the performance of the rotational motion actuators could be significantly improved by using curved stators instead. Furthermore, it is possible to exchange the role of stator and slider (rotor), i.e. such that the 'slider' is fixed and the 'stator' is moving.

### 1.3.4 Combinations

Combinations of the previously discussed motion patterns are possible too. For example, [Vermeulen, Peeters, Soemers, Feenstra & Breedveld \(2002\)](#) have demonstrated the combination of a 2 dof translational motion and a (limited) circular motion. Figure 1.10(a)

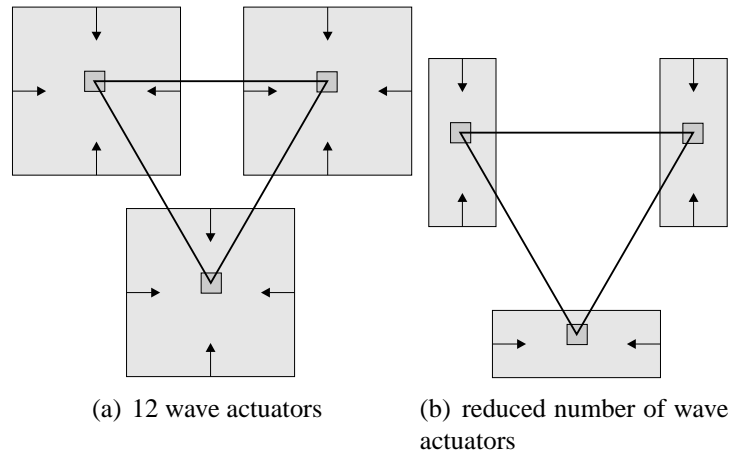


Figure 1.10: 3 dof planar motion (top view)

shows the basic structure of this setup. A preload force presses three rigidly connected sliders against three separate planar stators. The arrows represent Rayleigh wave fronts, which are generated at the edges of a stator. The number of wave actuators can be reduced while preserving the degrees of freedom as demonstrated by [Peeters & Vermeulen \(2004\)](#). Figure 1.10(b) shows the basic construction. They applied so-called Dual-Sided Actuation (section 4.2.3).

Because, the principle of actuation for all types is based on figure 1.4, it suffices to study the SAW linear motor in order to gain insight in the principle of motion actuation of all previously mentioned types of actuators.

## 1.4 Features and applications of a SAW motor

In this section we enumerate the characteristics of a SAW motor in general and with respect to a rotating traveling-wave motor (e.g. Sashida's traveling-wave motor); the principle of operation of a rotating traveling-wave motor is similar to a SAW motor. Next, we discuss some potential application fields for a SAW motor. The features and applications are partly based on results obtained during this research project.

Pros of SAW motors are:

- high force at low velocities (for example, a force of 1 N is shown in figure 3.35 and a force of 10 N is described by [Nakamura et al. \(2003\)](#)): suitable for direct drive applications;
- high acceleration (small moving mass), wide velocity range (for example, velocities of 0 - 0.047 m/s are shown in figure 3.34 and velocities of 0 - 1.5 m/s are described by [Nakamura et al. \(2003\)](#)), large blocking force and no backlash, high resolution (for example, steps of 1.7 nm are shown in figure 4.16 and steps of 0.5 nm are described by [Shigematsu & Kurosawa \(2004\)](#)), precise positioning (for example, a steady-state error of 20.3 nm is shown in figure 4.21);



- silent operation, since rotation-translation transmission and velocity-reduction gears are not required;
- relatively large stroke (for example, a stroke of 8 cm is described in section 1.5) with respect to the displacement resolution;
- no inherent lubrication requirements: suitable for vacuum applications, negligible effect of external electromagnetical fields and no inherent generation of electromagnetical fields can be expected (at the stator-slider interface);
- capable of operating in single and multiple degrees of freedom, while preserving mechanical stiffness;
- a compact and structural simple construction, lightweight, suitable for miniaturization (cm size).

Pros of a SAW motor with respect to another type of ultrasonic motor: a rotational traveling-wave motor (figure 1.3) are:

- the stator of a SAW motor can simply be attached to a frame without damping the wave, whereas the support of a stator of a traveling-wave motor requires extra attention;
- the influence of a change in motor temperature on the wave amplitude is smaller. Consequently, no additional electronics are required for shifting the excitation frequency.

Cons of a SAW motor:

- requirement of a high frequency power sources;
- necessity of wear resistant materials;
- difficult to fabricate high power (kW) motors;
- sensitive to fabrication tolerances;
- sensitive to contamination.

Cons of a SAW motor with respect to another type of ultrasonic motor: a rotating traveling-wave motor are:

- efficiency is smaller;
- driving frequency is higher – larger losses (e.g. piezoelectric losses), higher demands on electronics;
- smaller wave amplitude – influence of for instance, flatness and roughness is higher.

The features of a SAW motor differ from those of electromagnetic motors. Therefore, potential applications of a SAW motor may be in areas where the above features can be utilized or where electromagnetic motors are inadequate (due to electromagnetic fields, for example).

Potential application fields are:

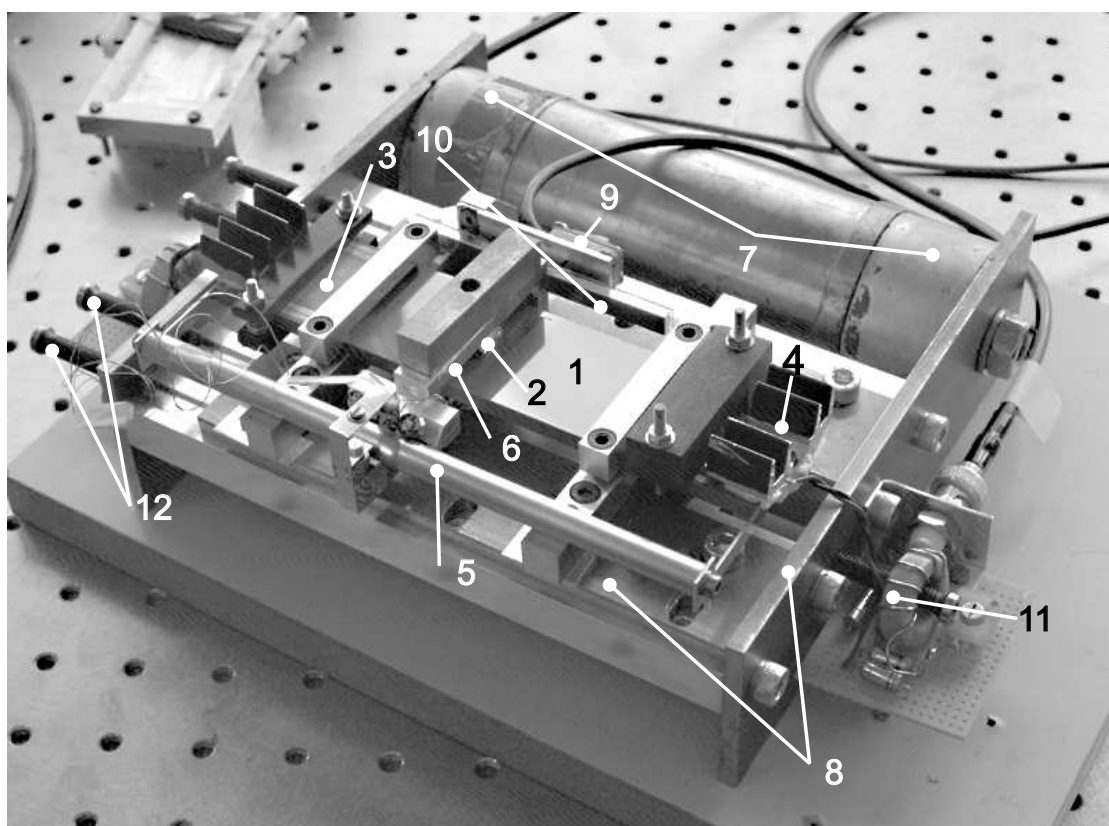
- positioning of, for example, small mirrors, lenses, lasers and sensors in optical setups;

- positioning of samples in (electron-) microscopes for visualization and for material research (e.g. magnetic resonance force microscopy);
- actuators for use in space, (no lubrication, vacuum compatible);
- actuators with extreme demands regarding (low) electromagnetic fields.

## 1.5 Experimental setup

Throughout this thesis, we will refer to the experimental setup discussed in this section. The setup is a modified version of the setup described by [Dijk \(2000\)](#) (figure 1.6). In order to better analyze the principle of operation only one instead of two sliders is used. Therefore, also the preload mechanism is different. Besides analysis of the principle of operation, the setup is employed to acquire validation data for the derived models (chapter 3) and it is used to implement and investigate actuation and control strategies (chapter 4).

Figure 1.11 shows a photo of the experimental setup. The numbers refer to part names listed at the bottom of the figure, which are used in this section. The main parts of the setup are discussed in detail.



1	stator	5	guiding axis	9	sensor
2	slider	6	slider guiding	10	encoder scale
3	IDT	7	permanent magnet	11	matching network
4	damping material	8	flux conductors	12	tunable flux shortcuts (bolts)

Figure 1.11: Experimental setup

### 1.5.1 Stator and IDT's

The stator (1) is made of a PZT piezoelectric ceramic: *PZT805*. See section 2.3.2 for a description of PZT. The stator is fabricated by Morgan Electro Ceramics, which is a former Philips-daughter. The Philips grading name was *PXE43*. The manufacturing

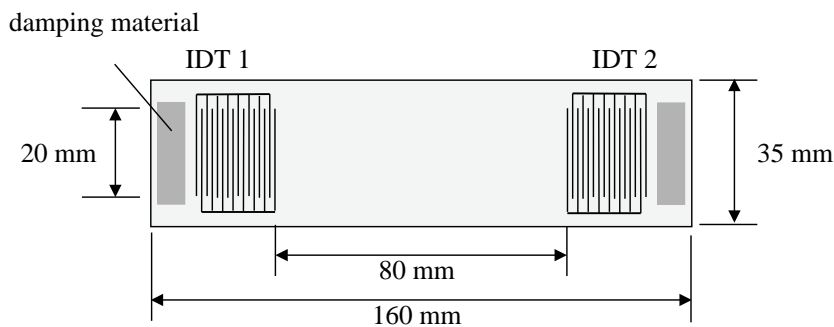
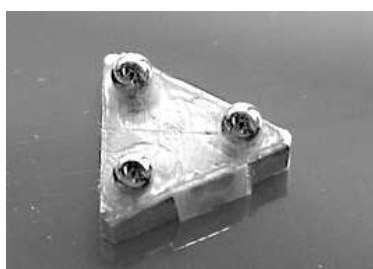


Figure 1.12: Geometry of the stator.

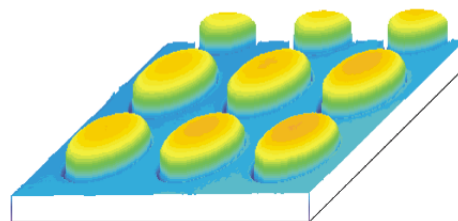
process of the stator is discussed in [Dijk \(2000\)](#). The size of the stator is  $35 \times 160 \times 5 \text{ mm}^3$ . The so-called interdigital transducers (IDT) (3) generate SAW's (detailed discussion in section 2.3.1). In the experimental setup both IDT's have 20 finger pairs and an aperture width of 20 mm (figure 1.12). The finger patterns are made of silver and have a thickness of  $6.8 \mu\text{m}$ . The stator is only poled (made piezoelectric) at the IDT's. The stator is left un-poled at the central part to prevent re-orientation of molecules, which would affect the flatness and roughness. Moreover, the un-poled ceramic may be regarded as a mass of minute crystallites, randomly oriented and hence the ceramic material will be isotropic at the central part ([Philips 1997](#)). Once a wave is generated at an IDT it will propagate to both ends of the stator. In this experimental setup, damping material (4) dissipates the remaining energy. A small heat sink is placed on top of the damping material.

## 1.5.2 Sliders

Two types of sliders are utilized. The first type of slider is an experimental slider consisting of an aluminum triangular shaped plate ( $18 \times 1.5 \text{ mm}$ ) with 3 steel balls with 1 mm radius glued at the bottom (figure 1.13(a)). The mass is  $0.6 \cdot 10^{-3} \text{ kg}$  and apart from the gravitational force, there is no additional preload applied. This slider is used without any external guiding. The second type of slider ( $1 \text{ cm}^2$ ) is made of silicon and has 40 000 ball-shaped projections (placed in a closed-packed orientation). The manufacturing process of



(a) experimental slider



(b) zoom of a silicon slider surface (obtained by an interference measurement microscope)

Figure 1.13: Two types of sliders.

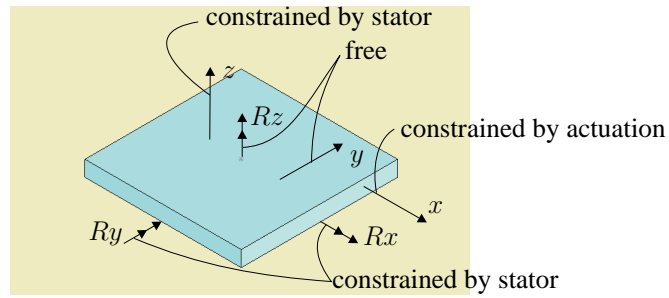


Figure 1.14: Degrees of freedom of the slider.

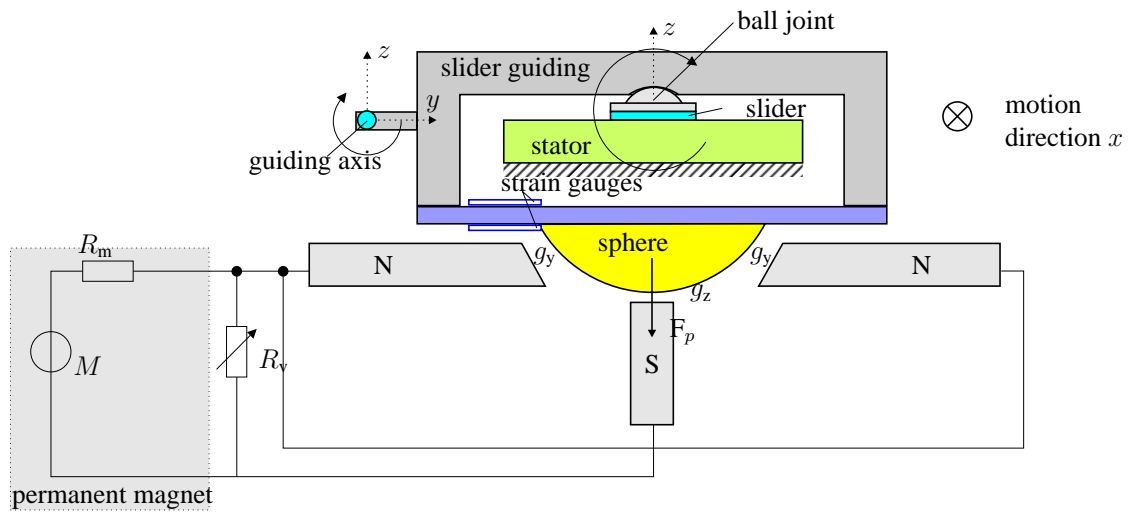


Figure 1.15: Cross section of the experimental set-up.

the silicon sliders is discussed in [Dijk \(2000\)](#) as well. [Figure 1.13\(b\)](#) shows a detail of the slider surface.

### 1.5.3 Slider guiding

Consider [figure 1.14](#). The unguided slider is constrained in 4 dof's:  $z$ ,  $R_x$ ,  $R_y$  (via the stator) and  $x$  (actuation coordinate).  $R_z$  and  $y$  are unconstrained or free. The guiding has to take care of  $R_z$  and  $y$  constraints. In the experimental setup,  $y$  is constrained by the slider guiding (6) and the guiding axis (5) ([figure 1.15](#)). However, it appeared that  $R_z$  does not have to be constrained in the practical setup; the friction of the ball-joint is sufficient to prevent rotation  $R_z$ . Refer to [section 5.3](#) for detailed information about the slider guiding. Furthermore, in the remainder of this thesis we will use the orientation of the coordinate systems of [figure 1.14](#), that is, the wave propagation along the  $x$ -axis and the  $z$ -axis normal to the stator surface.

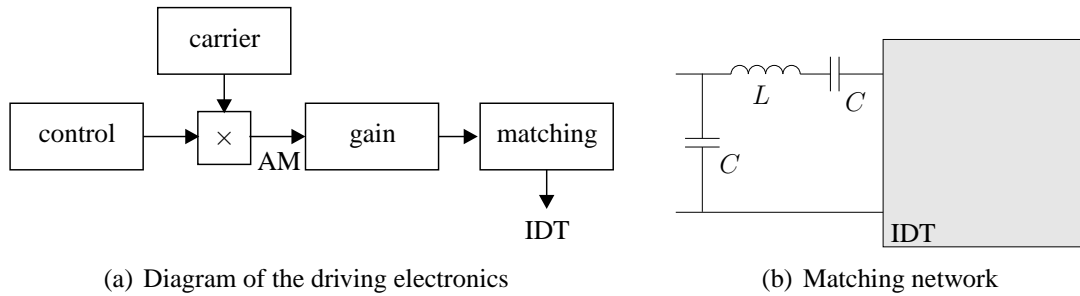


Figure 1.16: Electrical part

### 1.5.4 Preload force

The preload force for the silicon sliders is applied by means of a magnetic force achieved by permanent neodymium magnets (7). A number of flux conductors (8) guides the magnetic flux. A metal sphere that is attached to the slider guiding is pulled in the direction of the two north poles and the south pole (figure 1.15). A symmetric setup is chosen to apply a ‘stable’ force in the normal  $z$ -direction. We can vary the air gaps  $g_y$  as well as air gap  $g_z$ . The preload force  $F_p$  depends on all air gaps. The preload force can also be varied by the variable parallel flux reluctance  $R_v$ . The parallel flux reluctance consists of air gaps that can be closed by bolts (12). We did not close the bolts for the experiments discussed in this thesis.

### 1.5.5 Electrical circuit

Figure 1.16(a) shows a schematic view of the electrical part of the experimental setup. A control signal activates the system. After multiplying this signal with a high frequency signal (carrier), an amplitude-modulated signal (AM) is obtained. The frequency of the carrier signal is approximately 2.2 MHz. A power amplifier (gain) increases the voltage of the signal. Next, the signal arrives at a matching network (11) (section 2.3.1). Figure 1.16(b) shows the structure of the applied matching network. Finally, the IDT is excited.

### 1.5.6 Measurement

Table 1.2 shows an overview of the available measurement possibilities. The displacement of the silicon slider can be measured by means of a linear encoder (9) of MicroE Systems. The type is Mercury 3500, which has a resolution from  $5\mu\text{m}$  to 5 nm (depending on the chosen interpolation).

The experimental slider (figure 1.13(a)) displacement and velocity and the silicon slider (figure 1.13(b)) displacement and velocity can be measured by a so-called vibrometer fabricated by Polytec. For the velocity, a VD-01 encoder is used and for the displacement, the DD-200 encoder is used. By utilizing a vibrometer we are able to measure directly at

	preload	encoder displacement	vibrometer displacement	vibrometer velocity
silicon slider	yes	yes	yes	yes
experimental slider			yes	yes
wave amplitude			yes	

Table 1.2: Overview of the available measurement possibilities.

the slider rather than via the slider guiding. A third vibrometer encoder (VD-05) can be used to measure the high frequency wave displacement.

The preload force can be measured with two strain gauges glued to the slider guiding. See figure 1.15. The gauges measure the deformation of the guiding. The two gauges are connected to a measurement bridge such that temperature dependencies are minimized.

## 1.6 Thesis outline

There exist a strong relationship between the experimental setup and the thesis outline as demonstrated by figure 1.17.

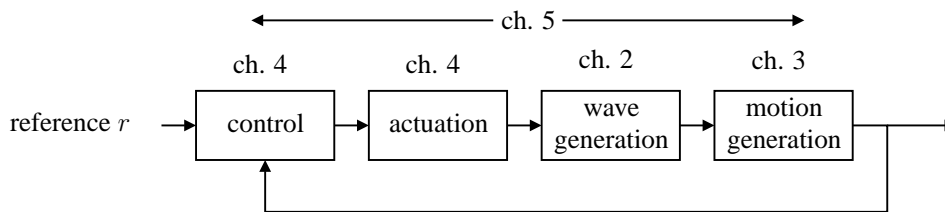


Figure 1.17: Outline of the thesis.

In the first part of chapter 2 (Acoustic waves) we introduce Rayleigh waves and the propagation of Rayleigh waves in different stator configurations. Furthermore, Raleigh waves properties that are important for modeling and design of a SAW motor are discussed, like a relation for the minimal stator thickness, the required wave power and a relation for the stator length. In the second part, the generation of Rayleigh waves by so-called interdigital transducers is discussed. Furthermore, we examine applicable materials and losses associated with wave generation and wave propagation.

In chapter 3 (SAW motor modeling), the principle of operation of a SAW motor and the inherent properties are analyzed. To this end, three contact models are derived that describe the microscopic and macroscopic behavior simultaneously. The different contact models are:

- a contact model that describes the microscopic behavior between a single projection and the wave motion. This model is used to explain the principle of operation in detail;

- a contact model that describes the microscopic behavior for a small number of projections. The model is used to describe the influence of multiple projections in the ideal case.
- the microscopic behavior for a large number of projections. The purpose is to fit the SAW motor behavior and discuss the implication of a large number of projections.

Next, the models are validated. Finally, the influence of the model parameters on the SAW behavior is studied in order to find the requirements for an optimal contact between slider and stator.

Chapter 4 (Actuation and control) investigates the actuation and closed-loop control of a SAW motor. First, a linear time invariant system model of the SAW motor is derived. Next, the disturbance sources of the SAW motor are discussed. Hereafter, different strategies to actuate the motor are examined. For one actuation strategy a controller is designed. Finally, the SAW behavior under closed-loop control is demonstrated for some example trajectories.

In chapter 5 (Design procedures), we consider the design of a SAW motor to obtain an indication for the applied materials, the geometry, the construction, the actuation and the practical limitations. First, the inherent SAW motor is discussed, where a design trajectory is proposed to obtain design parameters. Next, the guiding design and the preload mechanism are examined. Finally, the electronics of the control loop are discussed.

Chapter 6 (Conclusions) lists the conclusions and gives recommendations for future SAW motor research.



# Chapter 2

## Acoustic waves

***Overview:** This chapter starts with a brief description of acoustic plane waves and, in particular, Rayleigh waves. Next, properties related to Rayleigh waves are discussed. An interdigital transducer can generate Rayleigh waves. The last part of this chapter will focus on features, loss and design of an interdigital transducer.*

### 2.1 Wave types

A SAW motor utilizes surface acoustic waves (SAW) or more specifically Rayleigh waves to generate a motion. Knowledge of Rayleigh waves and its properties is therefore a prerequisite to design a SAW motor (chapter 5), explain SAW behavior and predict SAW behavior (chapter 3 and chapter 4).

Figure 2.1 shows an outline of this section. In order to point out which physical principles are required to describe acoustic waves, a brief derivation of a wave equation is given in subsection 2.1.1. In order to introduce wave terminology, subsection 2.1.2 discusses acoustic plane wave solutions. The existence of Rayleigh waves in an elastic half space is discussed in subsection 2.1.3. Finally, Rayleigh waves in a more realistic elastic plate are considered in subsection 2.1.4.

#### 2.1.1 Wave equation

In this section, we derive a wave equation of a linear, homogeneous solid. The goal is to show which physical principles pertain to acoustic waves and to introduce wave related variables. For a rigorous derivation see for example Auld (1990) or Oliner et al. (1978). Consider an infinitesimal control volume of a solid in an Euclidian 3-space with Cartesian coordinates  $\mathbf{x} = (x_1, x_2, x_3)^T$ . The displacement of this infinitesimal control volume (particle) is represented by the vector  $\mathbf{u} = (u_1, u_2, u_3)^T$ . (In order to compactly describe tensor relations, we use a slightly different notation in this chapter, e.g.,  $(x_1, x_2, x_3)$  instead of  $(x, y, z)$ ). The body forces exerted by the neighboring volumes on the infinitesimal vol-

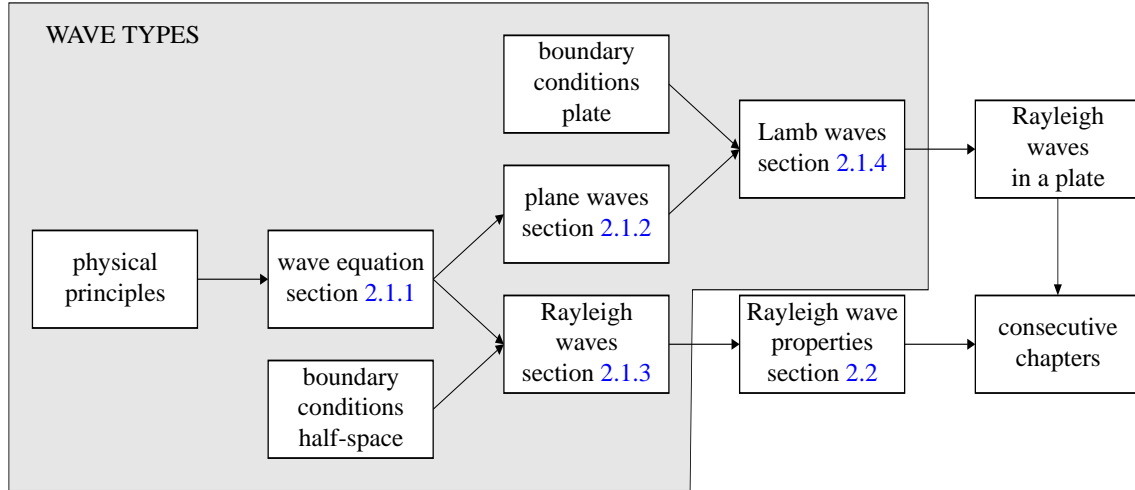


Figure 2.1: Outline of the wave-types section.

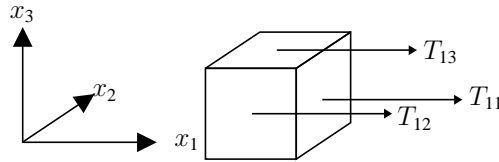


Figure 2.2: Three stress tensor components.

ume are described by a stress tensor<sup>1</sup> with components  $T_{ij}$  where  $i$  is the direction of the force and  $j$  is the surface normal to  $x_j$  ( $i, j \in \{1, 2, 3\}$ ). Figure 2.2 shows an example of stress components acting in the  $x_1$ -direction. The stress component  $T_{11}$  is a tensile stress and the components  $T_{13}$  and  $T_{12}$  are shear stresses. The resulting ‘force’ acting on the infinitesimal volume is determined by the stress differential between two faces times the corresponding face-area. For example, the resulting ‘force’ in  $x_1$ -direction is

$$\begin{aligned} dF_1 &= \frac{\partial T_{11}}{\partial x_1} dx_1 (dx_2 dx_3) + \frac{\partial T_{12}}{\partial x_2} dx_2 (dx_1 dx_3) + \frac{\partial T_{13}}{\partial x_3} dx_3 (dx_1 dx_2) \\ &= \left( \frac{\partial T_{11}}{\partial x_1} + \frac{\partial T_{12}}{\partial x_2} + \frac{\partial T_{13}}{\partial x_3} \right) dx_1 dx_2 dx_3 \end{aligned} \quad (2.1)$$

The forces in the remaining two directions are found in a similar way. By using Einstein’s summation convention (the convention that repeated indices are implicitly summed over), we can compactly write the force in all three directions.

$$dF_i = \frac{\partial T_{ij}}{\partial x_j} dx_1 dx_2 dx_3 \quad (2.2)$$

<sup>1</sup>While the distinction between covariant and contravariant indices must be made for general tensors, the two are equivalent for tensors in the Euclidean 3-space (Dubrovin et al. 1984) and therefore omitted.

By using Newton's second law, the equation of motion per unit of volume (for no external forces and no dissipation) becomes

$$\rho \frac{\partial^2 u_i}{\partial t^2} = \frac{\partial T_{ij}}{\partial x_j} \quad (2.3)$$

where  $\rho$  denotes the mass density of the solid. Equation 2.3 gives a relation between the particle displacement and the stress. Next, we consider the elasticity of the solid. To this end, we define the strain-displacement relation for small deformations.

$$S_{kl} = \frac{1}{2} \left( \frac{\partial u_k}{\partial x_l} + \frac{\partial u_l}{\partial x_k} \right) \quad (2.4)$$

The elastic constitutive relation between stress  $T_{ij}$  and strain  $S_{kl}$  is described by Hooke's law.

$$T_{ij} = c_{ijkl} S_{kl} \quad (2.5)$$

where  $c_{ijkl}$  are the components of the stiffness tensor ( $i, j, k, l \in \{1, 2, 3\}$ ). By substitution of equation 2.4 in equation 2.5 and this again in equation 2.3 and by using the symmetry  $S_{kl} = S_{lk}$  we obtain the wave equation in tensor notation.

$$\rho \frac{\partial^2 u_i}{\partial t^2} - c_{ijkl} \frac{\partial^2 u_k}{\partial x_j \partial x_l} = 0 \quad (2.6)$$

Summarizing, we have used Newton's second law of motion (equation 2.3) and Hooke's law (equation 2.5) to derive a wave equation for a linear, homogenous (non-piezoelectric) solid. This wave equation is used to find plane waves (section 2.1.2) and Rayleigh waves (section 2.1.3).

## 2.1.2 Uniform plane waves

This subsection discusses uniform plane waves – sometimes called bulk waves – in a linear, homogeneous solid. For details, refer to [Auld \(1990\)](#). A uniform plane wave, the simplest example of an acoustic wave solution, propagates along a particular direction and has a field that is uniform in a plane perpendicular to the propagation direction. We discuss plane waves to introduce wave terminology and because plane waves are used to explain so-called Lamb waves and Rayleigh waves in a plate (section 2.1.4).

Basically, a uniform plane wave solution is found in three steps. First, a solution is proposed. Second, this solution is substituted in the wave equation. Finally, the wave equation is solved (appendix A).

Consider a general plane wave solution that propagates along the  $\mathbf{l} = (l_1, l_2, l_3)^T$  direction, where  $|\mathbf{l}| = 1$  (figure 2.3). The general solution of such a plane wave solution is

$$\mathbf{u} = \hat{\mathbf{u}} \cos(\omega t - k \mathbf{l} \cdot \mathbf{x}) \quad (2.7)$$

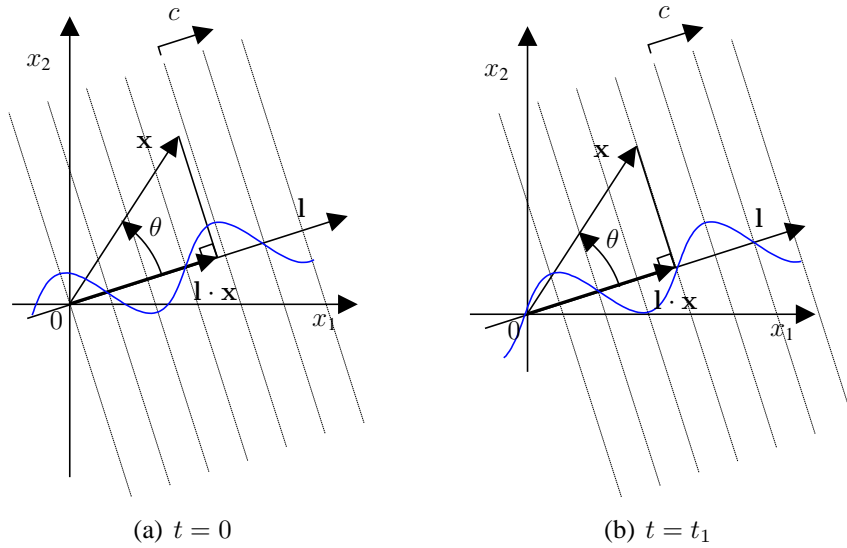


Figure 2.3: Illustration of a propagating uniform wave along  $\mathbf{l}$ .

The argument of the  $\cos$  is a function of time  $t$  and position  $\mathbf{x}$ . First suppose  $\mathbf{x} = \mathbf{0}$ , such that the argument of the  $\cos$  is  $\omega t$ , where  $\omega$  is the vibration frequency of material particles. Secondly, suppose  $\mathbf{x} \neq \mathbf{0}$ . Consider figure 2.3. The additional phase at a position  $\mathbf{x}$  with respect to  $\mathbf{x} = \mathbf{0}$  is

$$-\frac{2\pi}{\lambda} |\mathbf{x}| |\mathbf{l}| \cos(\theta) = -\frac{2\pi}{\lambda} \mathbf{x} \cdot \mathbf{l} = -k \mathbf{x} \cdot \mathbf{l} \quad (2.8)$$

where dot product  $\mathbf{x} \cdot \mathbf{l}$  determines the length of the projection of  $\mathbf{x}$  onto the propagation vector  $\mathbf{l}$ . The wave vector  $k$  ('spatial frequency') relates to the wavelength  $\lambda$  and the phase velocity  $c$  of the wave by

$$k = \frac{2\pi}{\lambda} = \frac{\omega}{c} \quad (2.9)$$

The phase velocity  $c$  of a plane wave is defined as the propagation velocity of an equiphase wavefront (figure 2.3). The amplitude vector  $\hat{\mathbf{u}}$  in equation 2.7 determines the type of the plane wave solution. For a linear, homogenous, non-piezoelectric solid, there are in general three uniform plane wave solutions and three associated phase velocities. Figure 2.4 shows an example of three uniform plane wave solutions, which propagate along  $\mathbf{l} = (1, 0, 0)^T$  (refer to appendix A for the calculation). The corresponding amplitude vectors (eigenvectors) are:

$$\hat{\mathbf{u}}_l = \begin{bmatrix} 1 \\ 0 \\ 0 \end{bmatrix}, \quad \hat{\mathbf{u}}_{sv} = \begin{bmatrix} 0 \\ 0 \\ 1 \end{bmatrix}, \quad \hat{\mathbf{u}}_{sh} = \begin{bmatrix} 0 \\ 1 \\ 0 \end{bmatrix}$$

where the subscript 'l' denotes a longitudinal wave, 'sv' a vertically polarized shear wave and 'sh' a horizontally polarized shear wave. For an isotropic material the two shear waves degenerate, i.e., the shear wave phase velocities are equal  $c_{sh} = c_{sv}$ .

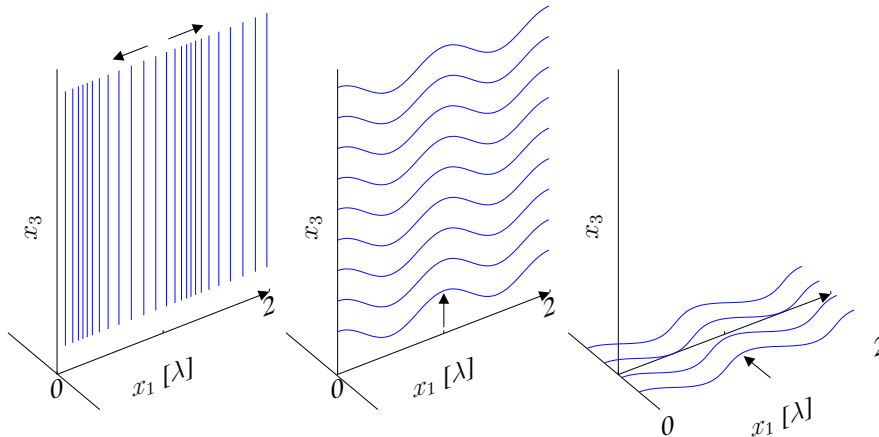


Figure 2.4: Uniform plane wave field displacement distribution. From left to right, longitudinal wave (l), vertically polarized shear wave (sv) and a horizontally polarized shear wave (sh).

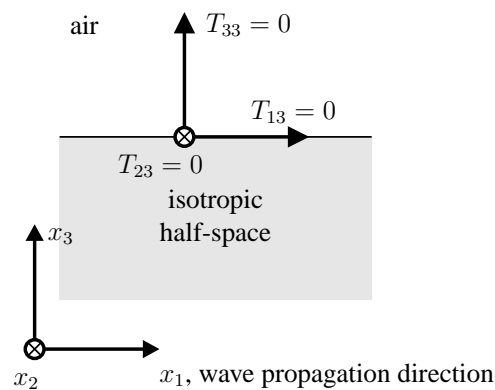


Figure 2.5: Isotropic half-space that is stress free at the surface.

### 2.1.3 Rayleigh waves in an isotropic half space

A SAW motor utilizes Rayleigh waves. In this subsection, we examine Rayleigh wave features that are used in the next chapters, e.g., the elliptical surface motion. Related Rayleigh wave properties are discussed in section 2.2.

An isotropic half-space is one of the simplest waveguide structures in which a Rayleigh wave can exist (figure 2.5). In this structure we only consider two dimensions ( $x_1, x_3$ ), i.e., the particle displacement in  $x_2$  direction is assumed uniform. The Rayleigh wave solution is derived in appendix B by using the potential theory (Auld 1990), (Kino 1987). The resulting Rayleigh wave solution satisfies both, the wave equation (equation 2.6) and the stress-free boundary conditions (figure 2.5).

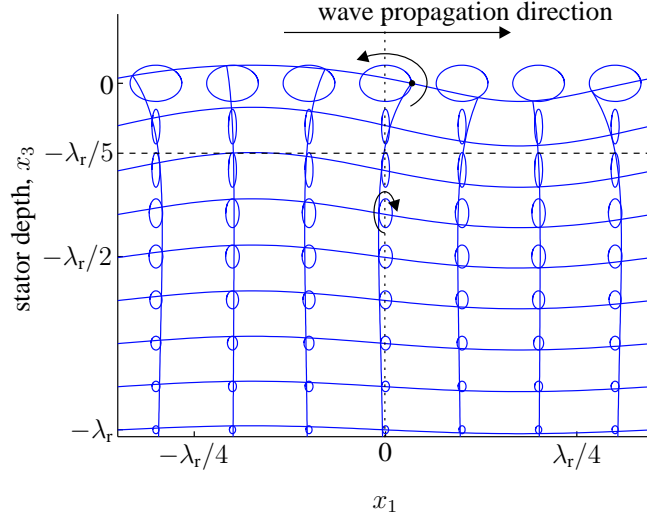


Figure 2.6: Displacement field distribution as a function of the depth for an isotropic material (un-poled PXE43, material grade of the experimental slider).

The found displacement components in  $x_1$  and  $x_3$  direction are

$$\begin{aligned}
 u_1 &= \frac{C_e}{q} \underbrace{(2sqe^{x_3s} - (k_r^2 + s^2)e^{x_3q})}_{\hat{u}_1(x_3)} \cos(\omega t - k_r x_1) \\
 u_3 &= \frac{C_e}{k_r} \underbrace{(2k_r^2 e^{x_3s} - (k_r^2 + s^2)e^{x_3q})}_{\hat{u}_3(x_3)} \sin(\omega t - k_r x_1)
 \end{aligned} \tag{2.10}$$

where  $C_e$  depends on the excitation and  $s$  and  $q$  are constants.

$$s = \sqrt{k_r^2 - k_s^2} \quad q = \sqrt{k_r^2 - k_l^2} \tag{2.11}$$

The wave vectors  $k_l$ ,  $k_s$  and  $k_r$  correspond to a longitudinal wave, a shear wave and a Rayleigh wave respectively. The Rayleigh wave vector  $k_r$  is a solution of an implicit 6th order polynomial the so-called Raleigh equation (equation B.29). An approximate solution of this equation, which is better than 0.5%, is (Auld 1990):

$$\frac{k_s}{k_r} = \frac{c_r}{c_s} = \frac{0.87 + 1.12\sigma}{1 + \sigma} \tag{2.12}$$

where  $\sigma$  is Poisson's ratio and  $c_s$  the shear wave phase velocity.

Equation 2.10 and figure 2.6 demonstrate the elliptical motion of material particles. Note that the rotation direction of the surface particles is anticlockwise, whereas the propagation direction is positive. The amplitude of the particle motions only depend on the depth  $x_3$ . Figure 2.7 shows the relation between the amplitudes  $\hat{u}_1(x_3)$  and  $\hat{u}_3(x_3)$ . The amplitudes decay inside the material as a function of the wavelength, i.e., the decay is reciprocal with the frequency. Furthermore, the rotation reverses at approximately one

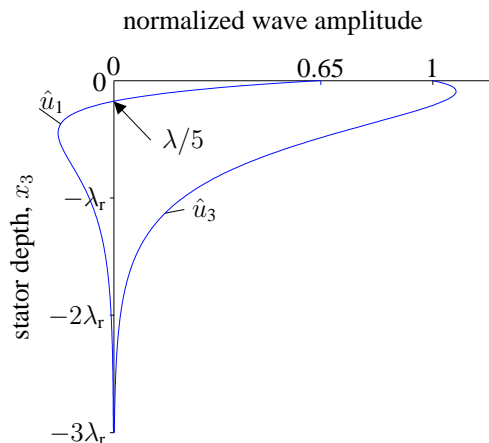


Figure 2.7: Displacement amplitude as a function of the depth for an isotropic material. (un-poled PXE43, material grade of the experimental stator ).

fifth of the depth. (figure 2.6 and figure 2.7). An interesting SAW motor parameter is the ratio between the tangential and the normal displacement at the surface. This parameter is used in the SAW motor model, which is derived in the next chapter. In this example the material dependent ratio is 0.65 (figure 2.7).

Table 2.1 lists the Rayleigh wave and the plane-wave phase velocities of the experimental setup (section 1.5). The longitudinal wave and the shear wave phase-velocity are calculated directly by the material parameters (equation A.7). The Rayleigh-wave phase-velocity is obtained by equation 2.12. Observe that  $c_l > c_s > c_r$ .

longitudinal wave, $c_l$ m/s	shear wave, $c_s$ m/s	Rayleigh wave, $c_r$ m/s
4050	2117	1963

Table 2.1: The phase velocities of the experimental setup (section 1.5).

### Rayleigh waves at a thin layer on a half space

Consider a substrate covered with a thin solid layer of thickness  $h$ , for example a coating to improve tribological behavior. According to Oliner et al. (1978), the distribution of the particle displacements as a function of depth and the relative values of the components do not change much with respect to a free surface as long as the layer is thin compared to the wavelength ( $h \ll \lambda_r$ ).

#### 2.1.4 Lamb waves and Rayleigh waves in a plate

In the previous subsection, we considered the existence of a Rayleigh wave in an infinitely thick half-space. However, a practical stator substrate has a finite thickness, which can influence the wave propagation negatively. Therefore, we will derive a relation that de-

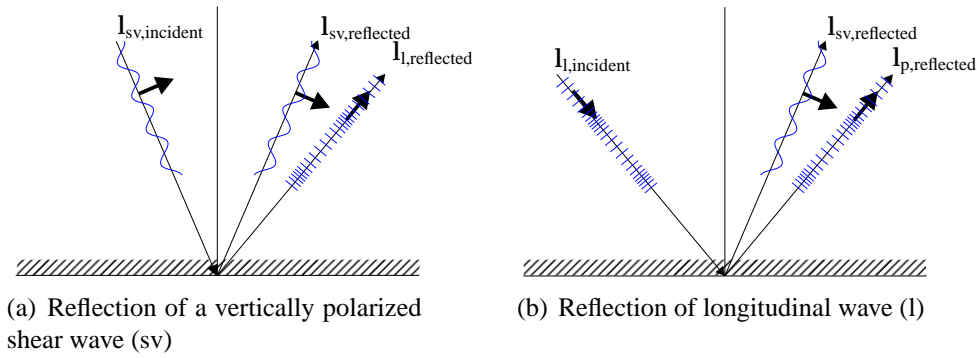


Figure 2.8: Reflection of uniform plane waves at a stress free boundary of an isotropic solid.

scribes the influence of plate thickness and wave frequency on the wave propagation. This relation yields a design parameter for the stator thickness (chapter 5).

We start with a brief introduction of Lamb waves, because a Rayleigh-wave like in a plate can be considered as the superposition of two Lamb wave modes. For detailed information, see Auld (1990). Subsequently, a Lamb wave can be considered as a superposition of successive reflected uniform plane waves (section 2.1.2) against the lower and upper faces of a plate. First, consider the reflection at one face. Figure 2.8 shows the scattering of incident plane waves at a stress free boundary of an isotropic solid. According to Auld (1990), a vertically polarized shear wave (sv) and a longitudinal wave (l) reflect partly into the other type. Figure 2.8(a) shows that that a shear wave (sv) reflects into a shear wave and a longitudinal wave. Figure 2.8(b) shows the same for a longitudinal wave.

Figure 2.9 shows a reflection pattern of waves within a plate. Depending on the thickness of the plate and the frequency of the waves different modes can occur. These modes are symmetric or anti-symmetric with respect to the  $x_1 - x_2$  plane. A so-called dispersion curve visualizes the different modes. Figure 2.10 shows the dispersion curve that was calculated (appendix C) for the isotropic stator material that is used in the experimental setup (section 1.5). Figure 2.10 shows that for a small frequency-thickness product ( $\omega b$ ) only two modes can exist; an asymmetric wave mode  $F_1$  and a symmetric wave mode  $L_1$ . The number of possible modes increases with increasing frequency and plate thickness. Moreover, for a high frequency and a large thickness, the velocity of the lowest two Lamb modes ( $L_1, F_1$ ) approach the Rayleigh wave phase velocity  $c_r$ ; indeed a Rayleigh wave is a superposition of the lowest two Lamb wave modes. Figure 2.11 illustrates this.

## Beating

There is a continuous coupling between surface waves at the upper and lower faces when the plate thickness is finite. Therefore, surface waves at the top and at the bottom of the plate cannot be treated independently but should be treated as a fundamental symmetric and an asymmetric Lamb wave. The phase velocity of the fundamental modes is different for a finite plate thickness. Hence, due to an associated phase shift a Rayleigh-wave like



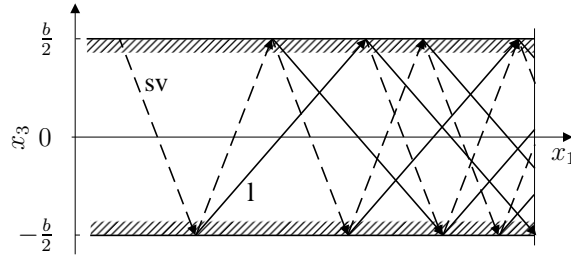


Figure 2.9: Reflection pattern of longitudinal (solid) and sv shear (dashed) waves within a plate.

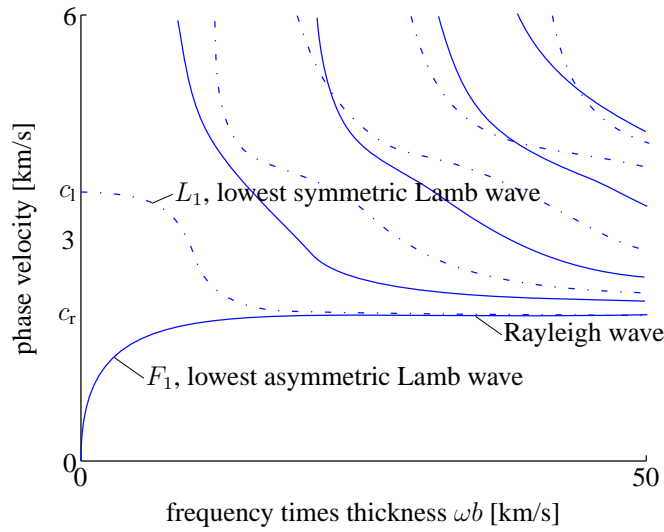


Figure 2.10: Lamb wave dispersion curve for an isotropic material (un-poled PXE, material of experimental stator). The solid lines are asymmetric waves and the dashed lines are symmetric waves.

excited at the upper boundary will propagate to the lower boundary of the plate and back again (figure 2.12). This is called beating.

We like to prevent beating at the stator of a SAW motor, i.e., we prefer a uniform wave amplitude. Therefore, anticipating a discussion in chapter 5 on SAW-motor design, we like to find the minimal thickness to keep the Rayleigh wave predominately at one side of a stator. The length of the stator is  $x_{\text{length}}$  and the thickness of the stator is  $b$ . Consider the superposition of a fundamental symmetric  $L_1$  and an asymmetric  $F_1$  Lamb wave with equal amplitude. The normalized normal-vibration amplitude of these Lamb waves and the sum of these Lamb waves, at the surface, is

$$\begin{aligned}
 u_{3,L_1} &= \cos\left(\omega t - \frac{1}{c_{L1}}\omega x_1\right) \\
 u_{3,F_1} &= \cos\left(\omega t - \frac{1}{c_{F1}}\omega x_1\right) \\
 u_{3,L_1} + u_{3,F_1} &= \underbrace{2 \cos\left(-\omega t + \frac{1}{2}\left(\frac{1}{c_{F1}} + \frac{1}{c_{L1}}\right)\omega x_1\right)}_{\text{carrier}} \underbrace{\cos\left(\frac{1}{2}\left(\frac{1}{c_{F1}} - \frac{1}{c_{L1}}\right)\omega x_1\right)}_{\text{envelope}}
 \end{aligned} \tag{2.13}$$

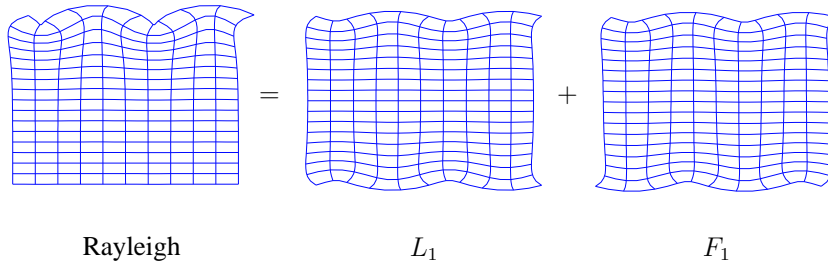


Figure 2.11: A Rayleigh wave equals the sum of the two lowest Lamb wave modes, for  $\lim \omega b \rightarrow \infty$ .

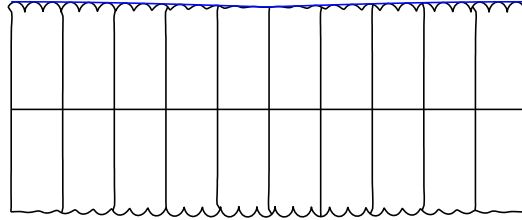


Figure 2.12: Beating in a plate due to a velocity difference between the  $L_1$  and the  $F_1$  Lamb wave mode.

where  $c_{L1}$  and  $c_{F1}$  are the phase velocities of the two Lamb wave modes (figure 2.10). The superposition is written as the product of a carrier signal and an envelope. The tangential vibration amplitude  $u_{1,L1} + u_{1,F1}$  yields a similar expression

$$\begin{aligned}
 u_{1,L1} &= \sin\left(\omega t - \frac{1}{c_{L1}}\omega x_1\right) \\
 u_{1,F1} &= \sin\left(\omega t - \frac{1}{c_{F1}}\omega x_1\right) \\
 u_{1,L1} + u_{1,F1} &= \underbrace{2 \sin\left(-\omega t + \frac{1}{2}\left(\frac{1}{c_{F1}} + \frac{1}{c_{L1}}\right)\omega x_1\right)}_{\text{carrier}} \underbrace{\cos\left(\frac{1}{2}\left(\frac{1}{c_{F1}} - \frac{1}{c_{L1}}\right)\omega x_1\right)}_{\text{envelope}}
 \end{aligned} \tag{2.14}$$

Hence, the resulting surface amplitude of a Rayleigh-wave like in a finite plate is

$$\hat{u} = \hat{u}_0 \left| \cos\left(\frac{1}{2}\left(\frac{1}{c_{L1}} - \frac{1}{c_{F1}}\right)\omega x_1\right) \right| \tag{2.15}$$

By using

$$\omega = \frac{2\pi c_r}{\lambda_r} \quad x_1 = n_{\text{length}} \lambda_r \tag{2.16}$$

where the subscript  $r$  refers to a Rayleigh wave, we find

$$\hat{u} = \hat{u}_0 \left| \cos\left(\left(\frac{c_s}{c_{L1}} - \frac{c_s}{c_{F1}}\right) \pi n_{\text{length}} \frac{c_r}{c_s}\right) \right| \tag{2.17}$$

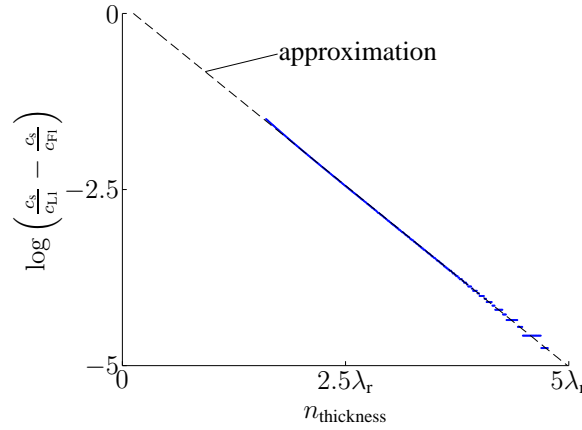


Figure 2.13: Polynomial curve fitting of the velocity ratio. The deviation for  $n > 4$  is due to numerical inaccuracy.

where  $c_s$  is the shear wave phase velocity. For an isotropic material, the argument  $\left(\frac{c_s}{c_{L1}} - \frac{c_s}{c_{F1}}\right)$  depends only on Poisson's ratio  $\sigma$  and  $n_{\text{thickness}} = b/\lambda_r$  where  $b$  is the stator thickness. An analytical approximation of the derived numerical relation can be obtained by means of polynomial least-square curve-fitting (figure 2.13). The approximation for  $\sigma = 0.3$  in the interval  $n_{\text{thickness}} = [1.5 \dots 5]$  is

$$\frac{c_s}{c_{L1}} - \frac{c_s}{c_{F1}} \approx 1.33 \cdot 10^{-1.03n_{\text{thickness}}} \quad (2.18)$$

Furthermore, for  $\sigma = 0.3$  the ratio  $c_r/c_s = 0.93$  (equation 2.12). Hence, we can approximate the amplitude by

$$\hat{u} \approx \hat{u}_0 \left| \cos \left( 3.87n_{\text{length}} 10^{-1.03n_{\text{thickness}}} \right) \right| \quad (2.19)$$

Figure 2.14 shows the amplitude decrease due to beating of a Rayleigh-wave like for three different thickness values. The minimal stator thickness for a specified maximal amplitude decrease  $\frac{\hat{u}}{\hat{u}_0}$  is

$$b = \lambda_r \log \left( \frac{3.87n_{\text{length}}}{\arccos \left( \frac{\hat{u}}{\hat{u}_0} \right)} \right) \frac{1}{1.03} = \lambda_r \log \left( \frac{3.87x_1}{\arccos \left( \frac{\hat{u}}{\hat{u}_0} \right) \lambda_r} \right) \frac{1}{1.03} \quad (2.20)$$

Concluding, the minimal stator thickness reduces by decreasing the wavelength  $\lambda_r$  (or increasing frequency), when the condition  $3.87n_{\text{length}} > \arccos(\hat{u}/\hat{u}_0)$  is satisfied. In chapter 5 we will use this stator thickness relation.

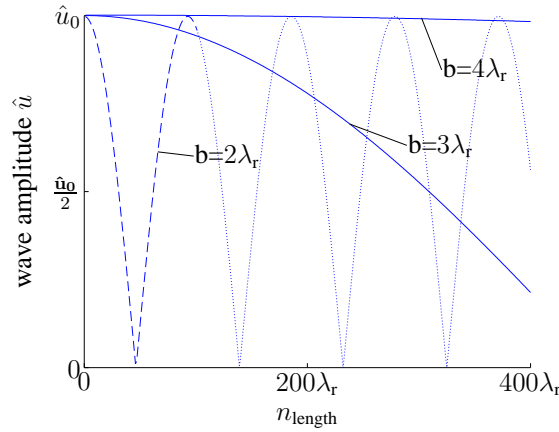


Figure 2.14: The decrease in wave amplitude due to beating for an isotropic material with a Poisson's ratio  $\sigma = 0.3$ . The stator thickness  $b$  is 2, 3 and 4 wavelengths.

## 2.2 Rayleigh wave properties

The properties derived in this section are under the assumption that the plate thickness is sufficiently large such that the Rayleigh wave is not affected by beating (section 2.1.4).

### 2.2.1 Power flow

We derive a relation between the power flow –the power transported by a Rayleigh wave– the frequency and the particle velocity/displacement amplitude at the surface. This relation is an important criterium for finding design parameters (chapter 5). Furthermore, it is convenient to know the power flow as a function of the particle velocity/displacement amplitude, because these variables can be measured directly as the power flow cannot.

According to [Auld \(1990\)](#), the time-average power flow across a unit area normal to the  $x_i$  direction is

$$\mathcal{P}_{s,i} = -\frac{1}{2}\text{Re} \left\{ j\omega T_{ij} u_j^* \right\} \quad \left[ \frac{W}{m^2} \right] \quad (2.21)$$

where  $*$  denotes the complex conjugated and  $j$  is the imaginary unit. The power flow  $\mathcal{P}_s$  is the acoustic equivalent of the electromagnetic time-average Poynting vector ([Cheng 1989](#)). [Oliner et al. \(1978\)](#) note that in piezoelectric material applicable for ultrasonics the acoustic term is dominating. Therefore, equation 2.21 is also valid for piezoelectric material. Furthermore, assume that the wave propagates in a pure mode direction, i.e., there is only a power flow in the direction of the wave propagation vector ( $\mathbf{l}$ ). This assumption is valid for isotropic materials and for anisotropic materials where the wave transducer (section 2.3) is set along a pure mode direction. A Rayleigh wave is a non-leaky SAW such that the power flow in  $x_3$  direction is zero. With these assumptions the Rayleigh wave power per unit width carried along the propagation direction ( $x_1$ ) is

$$\mathcal{P}_1 = -\frac{1}{2}\text{Re} \left\{ \int_{-\infty}^0 j\omega T_{1j} u_j^* dx_3 \right\} \quad \left[ \frac{W}{m} \right] \quad (2.22)$$

Substitution of Hooke's law (eq. 2.5), the strain-displacement relation (eq. 2.4) and the Rayleigh wave particle distribution (eq. 2.10) in equation 2.22 leads to

$$\begin{aligned}\frac{\hat{u}_3|_{x_3=0}}{\sqrt{\mathcal{P}_1}} &= c_3\sqrt{\omega} \\ \frac{\hat{u}_1|_{x_3=0}}{\sqrt{\mathcal{P}_1}} &= c_1\sqrt{\omega}\end{aligned}\quad (2.23)$$

where  $c_3$  and  $c_1$  are constants that depend on the stator material. Table 2.2 shows some power flow constants.

material	$\frac{\hat{u}_3 _{x_3=0}}{\sqrt{\mathcal{P}_1}}$ [ $10^{-6} \frac{\text{m/s}}{(\text{W/m})^{1/2}}$ ]	$\frac{\hat{u}_1 _{x_3=0}}{\sqrt{\mathcal{P}_1}}$ [ $10^{-6} \frac{\text{m/s}}{(\text{W/m})^{1/2}}$ ]	reference
unpoled-PXE 43	$4.3\sqrt{\omega}$	$2.8\sqrt{\omega}$	calculated
unpoled-PXE 5	$4.3\sqrt{\omega}$	$2.6\sqrt{\omega}$	calculated
Quartz Y cut – X	$4.3\sqrt{\omega}$	$2.9\sqrt{\omega}$	Auld (1990)
128°Y-X Lithium Niobate	$\approx 3.25\sqrt{\omega}$	$\approx 2.27\sqrt{\omega}$	calculated

Table 2.2: Some power constants

The next relations can be derived from equation 2.23.

$$\begin{aligned}\hat{u}_1, \hat{u}_3 &\propto \frac{1}{\sqrt{f}} \text{ for } \mathcal{P}_1 = \text{constant} \\ \hat{u}_1, \hat{u}_3 &\propto \sqrt{f} \text{ for } \mathcal{P}_1 = \text{constant} \\ \mathcal{P}_1 &\propto f \text{ for } \hat{u}_3 = \text{constant} \\ \hat{u}_1 &\propto \hat{u}_3 \text{ for } f = \text{constant}\end{aligned}$$

where  $\propto$  means 'proportional to'. The relations are visualized in figure 2.15.

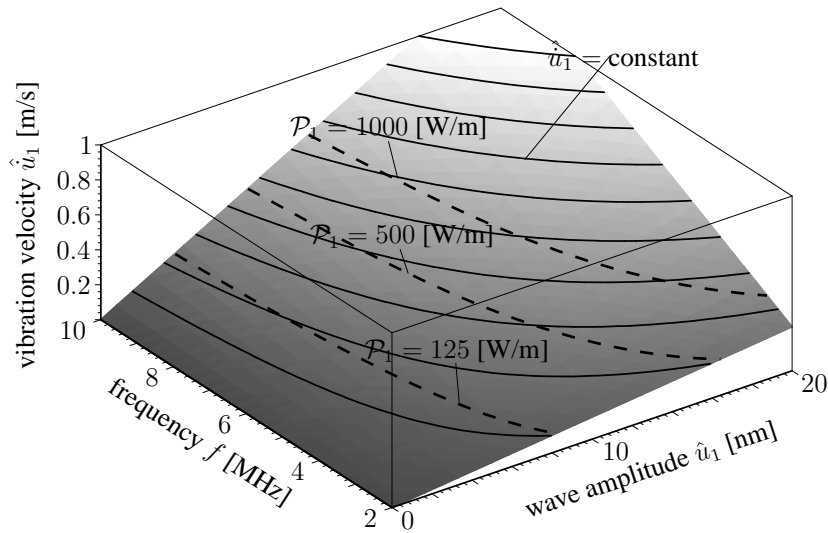


Figure 2.15: A graphical representation of the relations between wave amplitude, power flow, vibration velocity and the frequency. (For PXE43, the material grade of the experimental setup.)

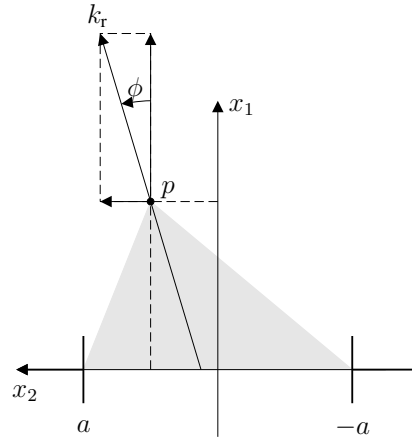


Figure 2.16: Geometry of a SAW wavefront with a limited width  $2a$ .

### 2.2.2 Diffraction

In the previous sections, we only considered wave propagation in the two dimensional  $x_1x_3$  plane. The assumption is that the wave motion in  $x_2$  direction is uniform. However, in practice this will be not true, for example due to the limited width of the SAW wave transducer; the so-called aperture width (section 2.3). The generated Rayleigh wavefront will locally be equal to the aperture width. But along the propagation path, this width and also the wave amplitude and phase will change, i.e., the wave diffracts. The diffraction of waves limits the useful stator length and thereby the stroke of a SAW motor (chapter 5). In this subsection, we discuss the cause of diffraction. Furthermore, we describe the relation between the aperture width, the frequency and the useful stator length. In chapter 5 we will use these relation to find design parameters.

Figure 2.16 shows the geometry of the considered problem. We like to find the wave amplitude at a point  $p$ . The width of the aperture is  $2a$ , i.e., the amplitude on the  $x_2$ -axis is zero for  $|x_2| > a$  and (supposed) constant for and uniform  $|x_2| \leq a$ . The desired wave propagation direction is  $x_1$  and  $k_r$  is the wave vector. The so-called wave directionality at a point at the  $x_2$ -axis ( $|x_2| < a$ ) explains the cause of diffraction. Figure 2.17 demonstrates the directionality as a function of  $\phi$  for different aperture width - wavelength ratios (refer to Oliner et al. (1978)). It demonstrates that the directionality increases by increasing the aperture width and by the increasing frequency ( $\frac{1}{\lambda_r} = \frac{f}{c_r}$ ). There is only radiation in the  $x_1$ -direction for  $\lim a \rightarrow \infty$ . The wave amplitude at a point  $p$  is the superposition of the waves radiating from every angle  $\phi$ . Figure 2.18 shows the resulting wave amplitude at different distances. Due to phase shift, there are points where the amplitude increases and points where the amplitude decreases.

Similar to optics, it is convenient to denote the distance from the aperture by a dimensionless parameter

$$\mathcal{X} = \frac{\lambda_r}{a^2} x_1 \quad (2.24)$$

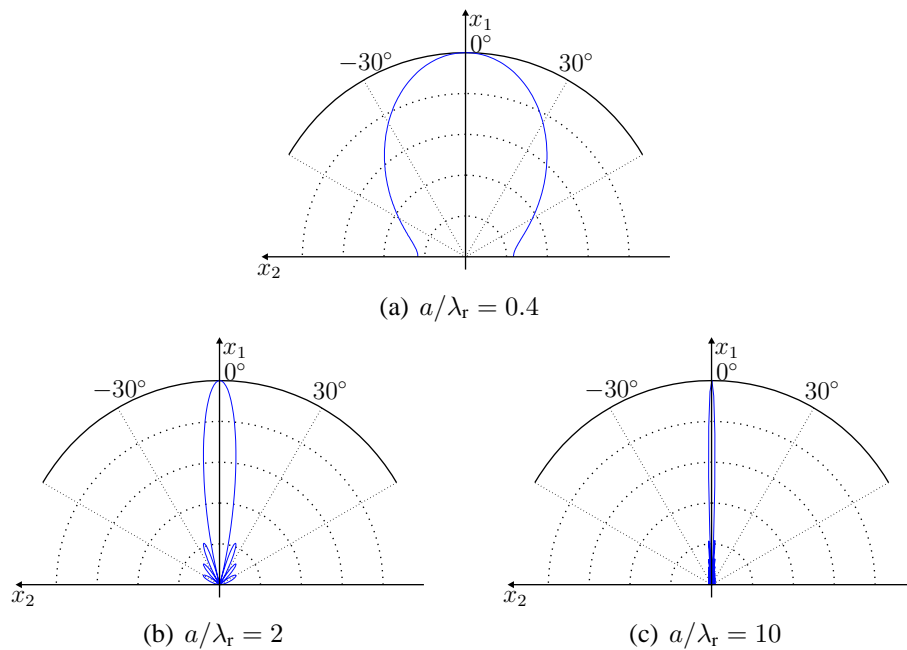


Figure 2.17: Polar plots of the directionality for different aperture width/wavelength ratio.

where  $\mathcal{X}$  is the so-called Fresnel parameter. For details, refer to [Kino \(1987\)](#). Most energy stays within the aperture width if  $\mathcal{X} < 1$ , i.e.,

$$x_1 < \frac{a^2}{\lambda_r} \quad \text{e.g.} \quad x_1 < \frac{a^2 f_r}{c_r} = \frac{0.01^2 \cdot 2.2 \cdot 10^6}{2000} = 0.11 \text{ [m]} \quad (2.25)$$

This region is called the Fresnel or near-field region. From an efficiency point of view, it is beneficial to stay within this region. The wave energy diverges if  $\mathcal{X} > 1$ . This region is the Fraunhofer or far-field region.

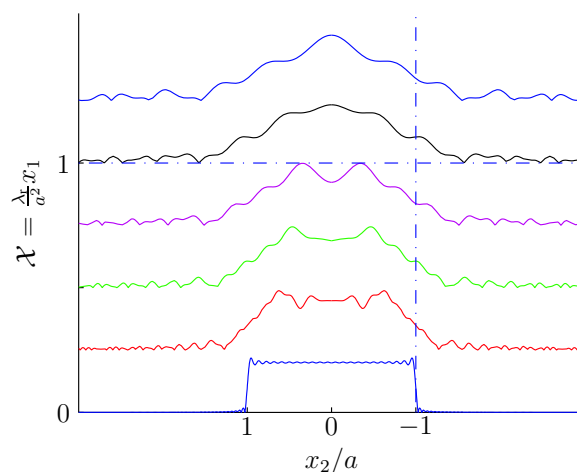


Figure 2.18: Wave amplitude at different values of the normalized distance from the aperture.

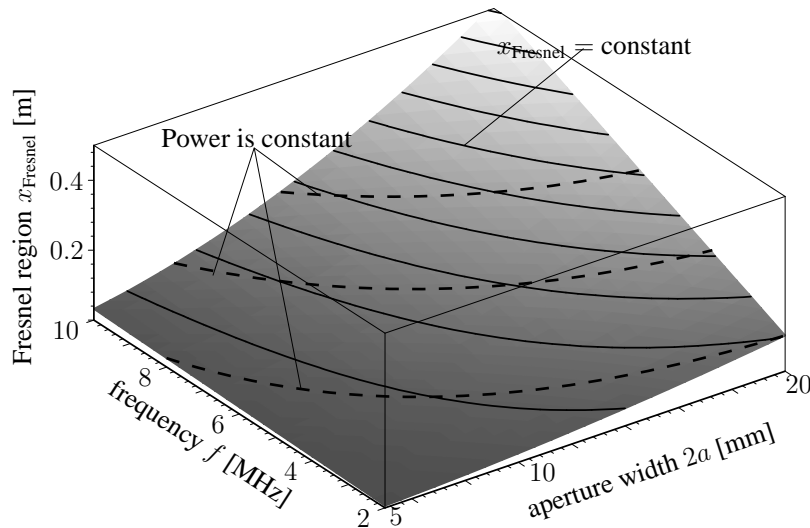


Figure 2.19: A graphical representation of the relations between Fresnel region, frequency and aperture width. (For PXE43, the material grade of the experimental set-up)

Hence, the stator length should be within the Fresnel region. Furthermore, a larger Fresnel region is achieved by increasing  $a^2 f_r$ . Figure 2.19 demonstrates that in order to achieve a larger Fresnel region at a constant power it is better to increase the aperture width rather than the frequency.

### 2.2.3 Attenuation

This subsection describes different causes of attenuation in the context of a SAW motor. On the one hand, to see where energy is dissipated and how this can be prevented and on the other hand, to describe how waves can be deliberately attenuated. Different causes of attenuation are:

1. Intrinsic loss in the solid. The intrinsic loss (of piezoelectric material) will be discussed in section 2.3.2.
2. Loss due to scattering and conversion to bulk waves by a change in material properties (elastic discontinuities, *mass loading* at the surface etc.). This can be caused by a slider that is pressed against the stator.
3. Conversion of energy from fundamental to harmonic frequencies in a non-linear medium, e.g., for large amplitudes.
4. Loss associated with a *leaky surface acoustic wave*.
5. Loss due to *viscous contamination* of various kinds, including deliberate damping on the surface.

The dominating mechanisms depend on the setup and the ambient conditions. Some of the causes are discussed in more detail.



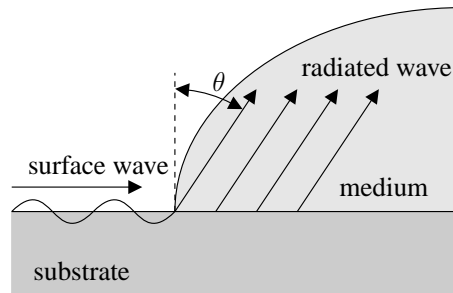


Figure 2.20: Leaky surface acoustic waves are radiated into a medium.

### Wave scattering

An example of mass loading is a slider pressed with a large preload force against the stator surface. Besides loss to surface waves, incident energy is lost in bulk waves (Munasinghe & Farnell 1972). De Benedictis (2003) has measured the reflected surface acoustic waves. He observed an increase in reflection with increasing preload force.

### Viscous contamination and leaky waves

Consider the effect on a Rayleigh wave when an isotropic substrate at which a wave is propagating is loaded by a medium such as water (Auld 1990), (Kino 1987). Assume that the wave in this medium can propagate with a longitudinal phase velocity  $c_1$  that is lower than the Rayleigh velocity  $c_r$  of the substrate. If the Rayleigh wave vector is  $k_r$ , then it is expected that a quasi-plane wave with a wave vector  $k_1$  is excited in the liquid with an angle  $\theta$  to the normal. See figure 2.20

$$\begin{aligned} k_1 \sin(\theta) &= k_r \\ c_r \sin(\theta) &= c_1 \end{aligned} \tag{2.26}$$

Hence, the Rayleigh wave attenuates due to the radiation of wave energy into the medium, i.e., mode conversion. This mechanism is positively used in the experimental setup (section 1.5), that is, absorption material is placed at both ends of the stator to overcome reflection. Such a loading medium is finite in size. Hence, the wave scatters within the absorber and will finally be converted to heat. The attenuation due to radiation is for example large for polymers, plastics, and rubbers, which are therefore suitable absorber materials.

## 2.3 Generation of Surface Acoustic Waves

The goal of a SAW motor wave transducer is to generate Rayleigh waves with a large amplitude. Criteria for the choice of a particular transducer and the design of this transducer are:

- complexity of the transducer;
- efficiency/power consumption;
- compactness;
- absence of magnetic fields;
- suitable for control;
- vacuum compatibility;
- fabrication complexity/cost.

In the literature, e.g., [White \(1970\)](#) and [Auld \(1990\)](#), various transducers are described. The conversion of these transducers is based on Lorentz forces, thermoelastic effects or piezoelectric effects. A magnetic-based (Lorentz force) transducer is not recommended. Because, this would void a key feature of the SAW motor namely the *absence of magnetic fields*. Furthermore, thermoelastic transducers are among other things not *ideal from a control point of view*.

Table 2.3 shows some piezoelectric transducers. A wedge transducer utilizes a longitudinal bulk wave transducer to generate a unidirectional Rayleigh wave. The incident longitudinal wave is directed towards the substrate at an angle  $\theta$  such that the tangential longitudinal wave vector  $\sin(\theta)k_1$  equals the Rayleigh wave vector  $k_r$  (similar to the situation shown in figure 2.20). The wedge transducer is widely used in non-destructive evaluation to detect flaws in non-piezoelectric material.

An edge transducer is a localized sv-shear wave transducer with a width comparable with the penetration depth of the Rayleigh wave. This transducer is used in non-destructive evaluation and for delay lines which are employed in for example color TV sets.

An interdigital transducer (IDT) consists of a metallic finger structure on a piezoelectric substrate or on a non-piezoelectric substrate with a piezoelectric layer. A voltage applied to the finger structure causes a spatial periodic electric ‘fringing’ field at the substrate. Accordingly, due to piezoelectric coupling, a strain field is generated. The accompanying elastic stress will propagate to the left and right side, as a superposition of all kind of waveguide modes. However, the surface waves are favored because the electrical and mechanical fields confine to the electrode surface. Furthermore, due to spatially periodicity of the transducer fingers, another selection mechanism is provided; waves add constructively and reach its maximum if the distance between two adjacent fingers is half a wavelength. Interdigital transducers are for example used in different kind of SAW filters and they are in general utilized for surface acoustic wave motors. The next subsection discusses the IDT in more detail and motivates why IDT’s are favored.

### 2.3.1 Interdigital transducer

An IDT has some advantageous features with respect to other piezoelectric-based SAW transducers. An IDT is *simple* in the sense that no transition from one material to another is required. A transition from one material to another is affected by scattering and hence additional power loss. Furthermore, well-established lithographical processes can be used to apply a finger pattern. Moreover, no mode conversion is necessary, which overcomes a possible source of power loss. The wave generation of an IDT is distributed, which

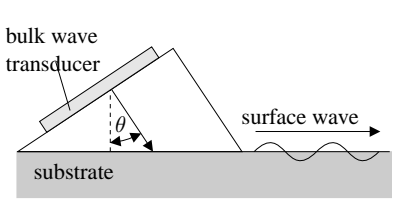
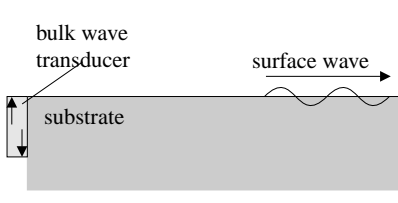
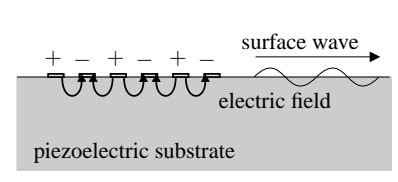
	features	application
 <p>wedge transducer</p>	<ul style="list-style-type: none"> <li>- mode conversion</li> <li>- longitudinal bulk wave</li> <li>- non piezoelectric substrate</li> <li>- unidirectional</li> <li>- broad frequency band</li> </ul>	Non Destructive Evaluation
 <p>edge transducer</p>	<ul style="list-style-type: none"> <li>- SV shear wave</li> <li>- non piezoelectric substrate</li> <li>- unidirectional</li> <li>- broad frequency band</li> </ul>	delay line, Non Destructive Evaluation
 <p>interdigital transducer</p>	<ul style="list-style-type: none"> <li>- distributed transducer</li> <li>- piezoelectric substrate</li> <li>- bidirectional</li> <li>- small frequency band</li> </ul>	SAW filter, SAW motor

Table 2.3: Some examples of piezoelectric transducers

increases the *efficiency* (White 1970). A drawback is the increase of transducer length (*compactness*) when lowering the center frequency, in particular when the number of fingers is large for example in the case of a unidirectional transducer. Furthermore, when a piezoelectric substrate is used for wave generation and for driving a slider, the choice in design is limited. However, this can be overcome by using a piezoelectric layer on a non-piezoelectric substrate or by applying a coating on a piezoelectric substrate.

Figure 2.21 shows the top view of a bidirectional IDT. A bidirectional IDT generates a wave in both directions. The number of finger pairs  $N = 5$  and the overlap of the fingers is equal to the aperture width  $2a$ . When the overlap differs, it is called an apodized or weighted IDT. The metallization ratio, the ratio between the electrode width and the gap, is chosen 0.5 in this case. The distance between two adjacent fingers of the same polarity is the center wavelength  $\lambda_0$ .

### IDT model

A model is used to obtain the electrical input admittance and the transfer function between the electrical input voltage and the wave vibration velocity (e.g.  $\hat{u}_3$ ). A relation of the input admittance is useful for the design of an IDT, e.g., to obtain an IDT that can be easily matched. (Matching is discussed in the next subsection). The transfer function between the electrical input voltage and the wave vibration velocity is important in determining the SAW motor displacement resolution (section 4.3).

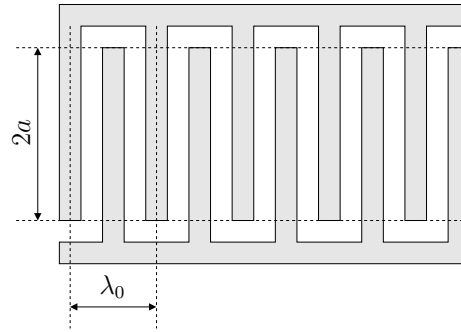


Figure 2.21: Top view of an unapodized IDT finger pattern. The number of finger pairs  $N = 5$  and the metallization ratio is 0.5.

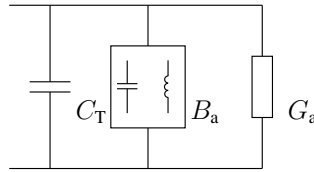


Figure 2.22: Model of the unperturbed IDT input admittance.

**IDT admittance** In the literature, e.g., (Campbell 1998), different models and analytical techniques to model an interdigital transducer have been presented, e.g. impulse response, coupling of modes, perturbation technique etc. Among those, the equivalent circuit model (also known as the Smith circuit model) has been widely used because of its simplicity and good insight (Inagawa & Koshiya 1994). In appendix D such an equivalent circuit model is utilized to find the electrical input admittance:

$$Y_{el} = \underbrace{8N^2G_0 \frac{\sin^2(x)}{x^2}}_{G_a} + j \underbrace{8N^2G_0 \frac{\sin(2x) - 2x}{2x^2}}_{B_a} + j\omega C_T \quad (2.27)$$

where  $N$  is the number of finger pairs,  $G_0 = K^2 C_s f_0$  the equivalent acoustic admittance,  $x = N\pi(f - f_0)/f_0$ ,  $C_T = NC_s$  the total IDT capacitance,  $f_0$  denotes the IDT center frequency,  $C_s$  is the static capacitance of one periodic section and  $K^2$  is the Raleigh wave electromechanical coupling factor. The admittance consists of three parts;  $G_a$  the radiation conductance,  $B_a$  the susceptance and  $j\omega C_T$  the part due to the electrical capacitance. Figure 2.22 shows a representation of the input admittance and figure 2.23 shows an example. In general  $B_a$  behaves as a capacitance for  $f < f_0$ , as an inductance for  $f > f_0$  and is zero at the center frequency  $f = f_0$ . Hence, we do not have to consider  $B_a$  in the region of this center frequency.

**IDT response** For slowly varying input signals we may use a static function to describe the relation between the input voltage and the wave vibration velocity. However, for short bursts signals we need to consider the IDT response. A so-called delta-function model describes the qualitative relation between the input voltage and the wave velocity in the

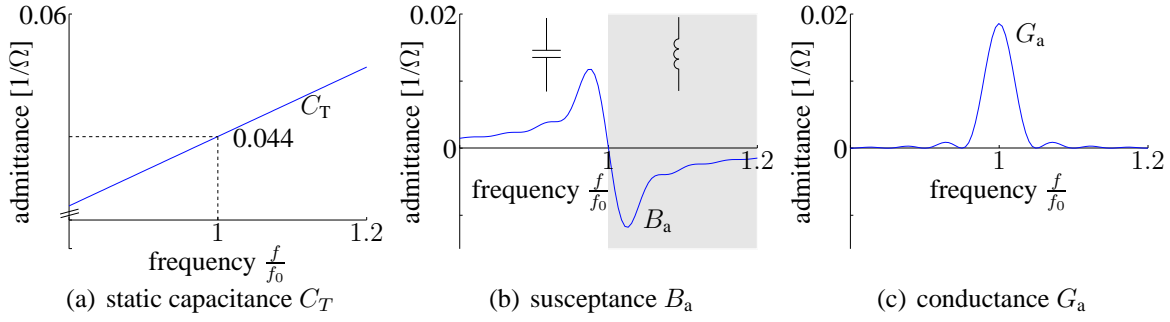


Figure 2.23: The static capacitance  $C_T$ , the susceptance  $B_a$  and the radiation conductance  $G_a$  for PXE43. ( $N = 20$ ,  $a = 1$  cm,  $f_0 = 2.2$  MHz,  $K^2 = 1.65$  %,  $C_T = 3.17$  nF).

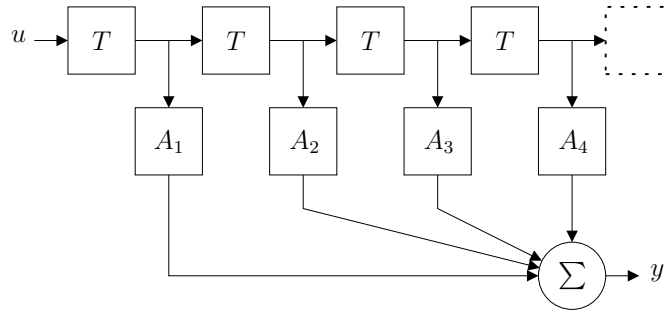


Figure 2.24: An delta function model of an IDT.

time domain (figure 2.24). The output  $y$  (wave vibration velocity) is the superposition of the weighted and the delayed excitation signal  $u$  (voltage). The weighting factors  $A_n$  correspond to the finger overlap and  $T$  is the time it takes for a wave to propagate from one finger pair to the adjacent one. The output for  $N$  finger pairs is

$$y(t) = \sum_{n=1}^N A_n u(t - n T) \quad (2.28)$$

This can be written as a convolution between the IDT impulse response  $h$  and the input  $u$ .

$$y(t) = (h * u)(t) = \int_{-\infty}^{\infty} h(\tau) u(t - \tau) d\tau \quad (2.29)$$

where

$$h(t) = \sum_{n=1}^N A_n \delta(t - n T) \quad (2.30)$$

where  $\delta$  is the delta function.

Figure 2.25 demonstrates the convolution (with some additional delay). The four step responses are measured at the unapodized bidirectional IDT of the experimental setup

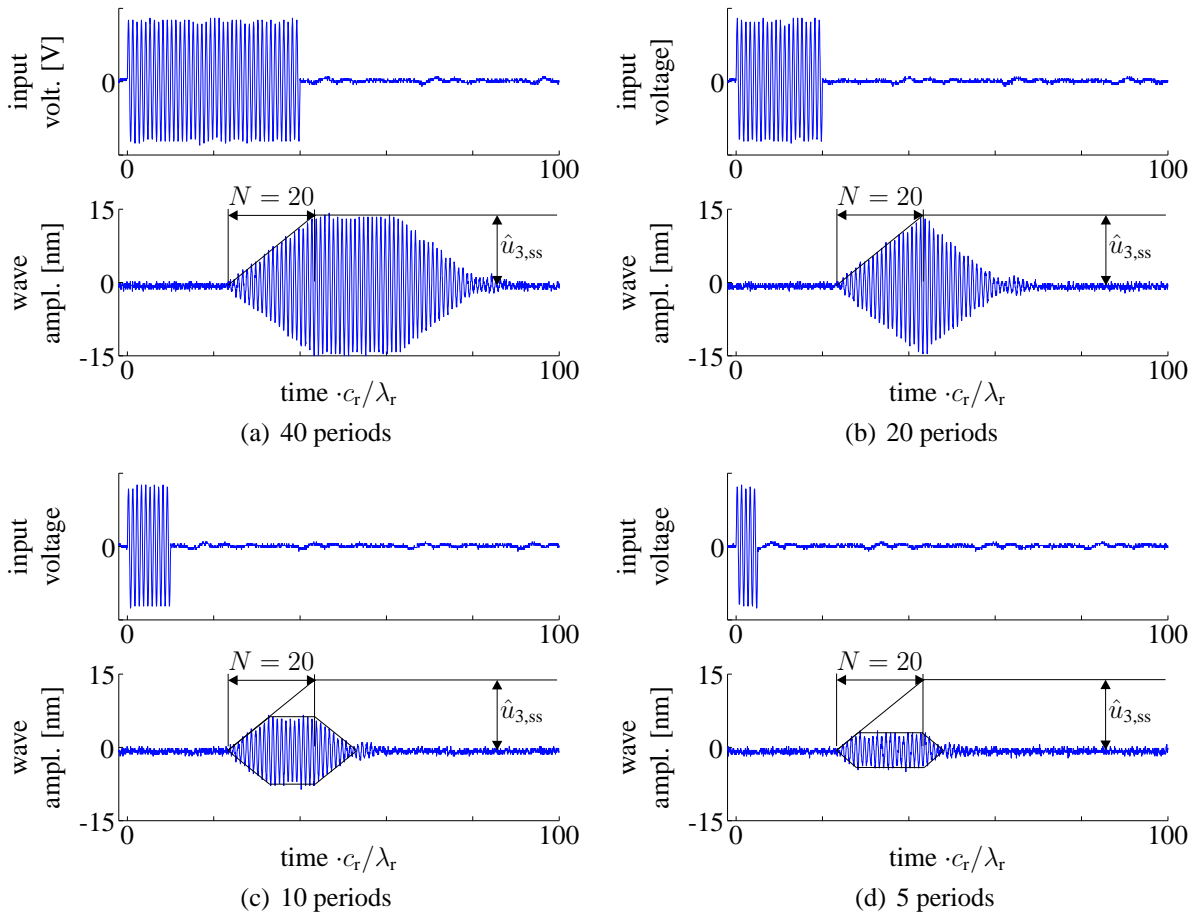


Figure 2.25: Measurement of the input voltage and the normal wave amplitude  $\hat{u}_3$ . The burst length of the input voltage is varied.

(section 1.5). The number of finger pairs  $N = 20$  and the delay  $T$  between two finger pairs is  $\lambda_r/c_r$ . In figure 2.25(a), the input voltage is a burst of 40 sinusoids. The wave amplitude increases due to the superposition of waves (figure 2.24). Therefore, a steady-state value  $u_{3,ss}$  is reached after 20 wave periods, i.e., when the number of periods corresponds to the number of finger pairs. The wave amplitude starts decreasing after 40 periods, because the excitation of waves stops. The wave response after excitation is due to the ‘outflow’ of the IDT. The response of figure 2.25(b) reaches the steady-state value  $u_{3,ss}$  after 20 wave periods as well. However, after 20 periods the generation of waves stops, hence, the wave amplitude decrease. Figure 2.25(c) shows the wave response for a burst of 10 periods. The wave amplitude does not reach the ‘static value’  $u_{3,ss}$ , because the number of periods is smaller than the number of finger pairs. A constant wave amplitude is reached after 10 periods. The remaining part of the response is due to the ‘outflow’ of the IDT, i.e., the constant value is due a superposition of 10 waves and after 20 periods the number of added waves is decreased one by one. A similar result can be seen for 5 periods (figure 2.25(d)). An IDT is linear; hence by doubling the input voltage, the wave amplitude response doubles as well.

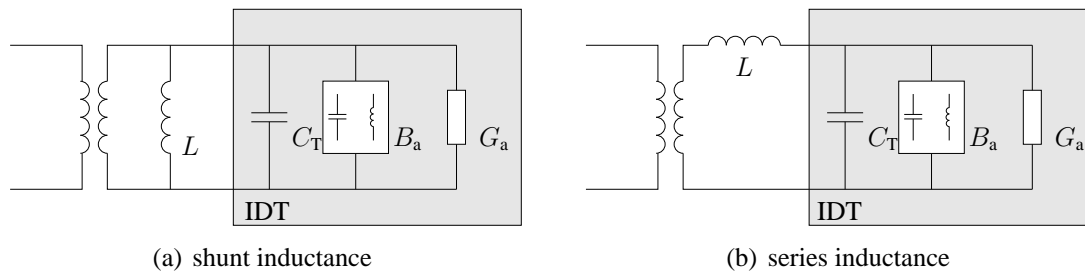


Figure 2.26: A matching network with an inductance and a transformer.

### Matching network

Consider a load  $Z_L$  that is driven via a transmission line with a characteristic impedance  $Z_C$ . To achieve a maximum power transfer between the line and the load, the load impedance  $Z_L$  should match the characteristic impedance  $Z_C$  (Cheng 1989). Moreover, matching prevents reflection of electrical energy and thereby protecting the driving circuit from being damaged. The transmission line has a real-valued line impedance ( $Z_C$  is usually  $50 \Omega$ ) and the load (the IDT) has a complex impedance. By using a matching circuit the total impedance of load and matching circuit can be made equal to the line impedance.

Equation 2.27 shows that at the center frequency the radiation susceptance  $B_a$  is zero. Hence, the load admittance is the sum of the radiation conduction and the IDT capacitance admittance. (Note that we disregard the small wire resistance and the parasitic capacitances and inductances).

There are many matching circuits possible. However, not all are equally realistic from a component-value point of view, e.g., inductances in the nanohenry range are difficult to obtain. In Davis (1993) 5 types of high-frequency  $\Pi$  and T matching networks are described that consists out of 3 or 4 components (only inductances and capacitances). Given the load impedance (IDT impedance) and an extra variable, a quality factor of the matching network, some networks are labeled as preferred based on the practical realizability of the component values. Campbell (1998) and Oliner et al. (1978) describe another kind of network with a series or shunt inductance in cascade with a transformer. See figure 2.26. The inductance in figure 2.26(a) should compensate  $C_T$  and the transformer should transform the remaining real impedance to the characteristic one. Similar, the series inductance of figure 2.26(b), should compensate the imaginary part of the electrical impedance.

Some practical considerations for matching networks are:

- frequency dependency of capacitances – suitable types are polystyrene (PS) capacitances and mica and glass capacitances of ceramic class I;
- type of cores– ferrite rings (e.g., Philips type 4C65) is suitable for frequency in the order of MHz;
- generated flux – a ferrite ring has a saturating magnetic flux density;
- loss in the ferrite ring;
- wire diameter – depends on current.

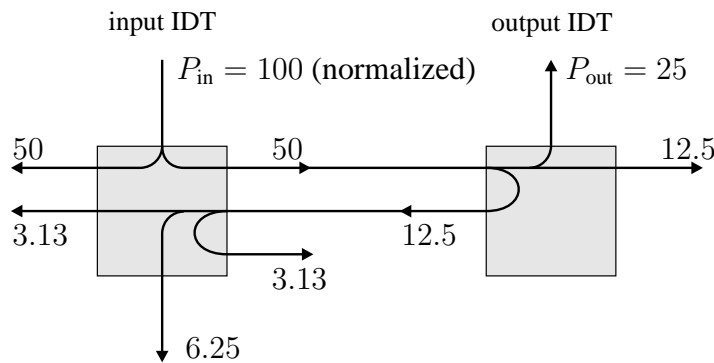


Figure 2.27: Normalized power flow of bidirectional IDT's that are perfectly matched.

Concluding, the type of matching network needs to be chosen on the basis of the IDT impedance, the electrical power and the frequency.

### Second order effects

There are some effects that degrade an interdigital transducer's performance.

- We already mentioned that a bidirectional IDT generates waves in two directions. The inherent insertion loss is 3dB. The same relation holds for an output IDT in which acoustic energy is converted back into electrical energy (Auld 1990). An output IDT can be used for example for energy reuse (Asai et al. 1999). Due to the so-called reciprocity relation waves will reflect or regenerate at the transducers due to the induced voltage. This phenomenon causes *triple transit interference*. Figure 2.27 illustrates this phenomenon for perfectly matched transducers (without a slider). Only 50 % of the normalized input power transforms into acoustic power. Next, at the output IDT, 25 % of the power transforms into electrical power and the remaining power is equally re-emitted as acoustic energy in two directions (12.5 %) and so on. Less energy is re-emitted (and transformed to electrical energy) if the transducers are deliberately mismatched or mismatched due to the use of not back drivable amplifiers.
- Besides the generation of Rayleigh waves, *bulk waves* are generated. The bulk waves propagate inside the stator substrate and reflect at the stator faces. The generation of bulk waves increases the insertion loss. It is found that for YZ Lithium Niobate the amount of power radiated in bulk waves drastically increases when the number of finger pairs is reduced below  $N = 5$ . For  $N = 5$ , 10% of input energy is converted to bulk waves. For 128 degrees rotated YX Lithium Niobate, experimental experience indicates that the same situation holds (Campbell 1998). For an increasing number of finger pairs the efficiency increases as well.
- An input and an output IDT may be considered as the plates of a parasitic capacitor. A signal applied to the input IDT will couple directly to the output IDT at the velocity of light, known as *electromagnetic feedthrough* or as crosstalk (Campbell



1998). This property falsifies the feature that a SAW motor does not generate EM fields. However, it is expected that the IDT's can be shielded such that the slider is (almost) EM-field free. Research is recommended.

- The thin metal fingers deposited on a piezoelectric substrate introduce impedance and mass loading discontinuities and accordingly reflections (Campbell 1998). Those reflections can lead to *internal resonances and associated losses*. Furthermore, the input impedance spectrum will change. However, when the film-thickness ratio  $h/\lambda_0$  is smaller than 1% the reflection is small. The finger thickness  $h$  is usually within the range of 500 – 2000 Å (1Å=  $10^{-10}$  m). For smaller thickness ( $< 500$  Å) the conductivity will be poor.
- According to Uchino & Hirose (2001) the admittance frequency spectrum could become distorted for high vibration amplitudes at the resonance frequency due to the non-linear behavior of the elastic compliance. An associated problem is the heat generation of piezoelectric material, which could cause a *degeneration of the transducer characteristic*. The inherent losses of piezoelectric material will be discussed in the next subsection.

### 2.3.2 Piezoelectricity

#### Suitable types of piezoelectric material

Different types of piezoelectric material are used for SAW devices. The most popular are *single-crystal* materials such as quartz, Lithium Niobate ( $\text{LiNbO}_3$ ) and Lithium Tantalate ( $\text{LiTaO}_3$ ). These crystals are available in different cuts, which give them particular specifications. For example,  $128^\circ$ Y-cut X-propagating Lithium Niobate has a high electromechanical Rayleigh wave coupling factor (in X direction). Apart from single-crystals, zinc oxide (ZnO) *thin films* deposits on a fused quartz, glass or sapphire substrate are commercially used for SAW devices. A third type is the piezoelectric *ceramics*, which are only used at low frequencies  $\ll 100$  MHz (Ikeda 1990). An example of a piezoelectric ceramic is the group of solid solution of lead titanate and lead zirconate modified additives, known as PZT (Philips 1997). PZT is a polycrystalline ferroelectric material that can be fashioned into components of almost any shape and size. Hence, stators with a relative large thickness (section 2.1.4) can be fabricated. An additional advantage of PZT is the complete rotational symmetry with respect to the poling axis, i.e., PZT is isotropic in a plane normal to the poling axis.

#### Coupling factor

In the previous subsection we introduced the electromechanical coupling factor  $K^2$ . This constant is a measure of the ability to convert electrical energy to mechanical energy and vice versa or as stated by Ikeda (1990) a measure of ‘the smallness of the ineffective fraction of energy’. The coupling  $K^2$  can be derived from the constitutive relations when the vibration mode of a transducer is taken along one of its axes. However, for an IDT  $K^2$  is difficult to determine because the fields are no longer uniform. Hence, the coupling

	material	$K^2$ [%]	reference	$Q_m^E$	reference
single crystal	Quartz ST-X	0.16	<a href="#">Uchino (2000)</a>	$> 10^5$	<a href="#">Uchino (2000)</a>
	LiNbO <sub>3</sub> 128°Y-X	5.5	<a href="#">Uchino (2000)</a>	$10^4 - 2 \cdot 10^4$	<a href="#">Nakamura &amp; Adachi (1998)</a>
ceramic	PXE 5 soft PZT			75	<a href="#">Philips (1997)</a>
	PXE 43 hard PZT	$\approx 1.6$	calculated	1000	<a href="#">Philips (1997)</a>
thin film	ZnO/glass	0.64	<a href="#">Uchino (2000)</a>		
	ZnO/sapphire	1.0	<a href="#">Uchino (2000)</a>		

Table 2.4: Piezoelectric materials.

constant is usually determined experimentally. For a SAW motor, a piezoelectric material with a large coupling factor is preferred.

### Mechanical and dielectric loss

The loss of piezoelectric ceramics is large compared to single-crystal piezoelectric materials. For instance, the mechanical quality factor of PZT is more than a factor 100 smaller than that of quartz. [Härdtl \(1982\)](#) wrote in a review article that below the Curie temperature the domain wall motion is the main cause of this large loss. This domain wall motion causes both extrinsic dielectric loss  $\tan \delta$  and extrinsic mechanical loss  $Q_m^E$  ([Uchino & Hirose 2001](#)). Extrinsic refers respectively to a stress-free condition and a short-circuit condition. At resonance the mechanical loss is dominant and at off-resonance the dielectric loss.

An additional effect in PZT is the decrease of the mechanical quality factor when the vibration velocity is increased ([Uchino & Hirose 2001](#)). This causes a significant rise in temperature when a certain velocity is exceeded. This critical velocity is defined as the velocity where the temperature is 20 degrees Celsius above the room temperature and lies within 0.3 and 0.6 m/s. According to [Nakamura & Adachi \(1998\)](#) this quality factor degradation effect is small for single-crystal Lithium Niobate.

For SAW motor applications, it is recommended to use piezoelectric material with a high mechanical quality factor to suppress heat generation ([Uchino & Hirose 2001](#)).

### Material choice

In the previous subsections, we concluded that for a SAW-motor application a high electromechanical coupling factor and a high mechanical quality factor is preferred. Table 2.4 lists some materials. The single crystal 128°Y– X Lithium Niobate appears to be the best material for SAW motor applications. If for some reason a ceramic material is preferred, a hard ceramic material with high quality factor is recommended.

The stator of the experimental setup (section 1.5) is made of a hard PZT material. The historical reasons for this choice were the availability of PZT material and the available knowledge of PZT at Philips. However, since 128°Y– X Lithium Niobate is superior, we can expect better results when using Lithium Niobate.

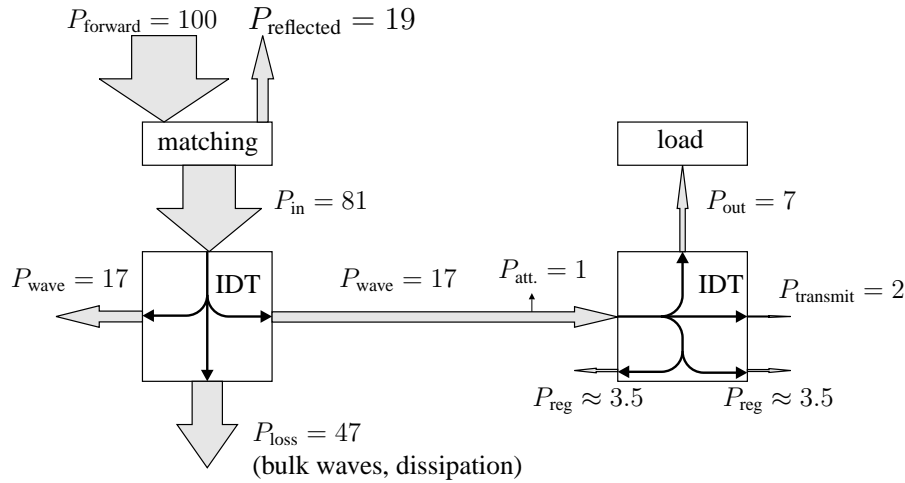


Figure 2.28: Power distribution of the stator (without slider) of section 1.5.

### 2.3.3 Power distribution

In this subsection, we give an estimate of the power loss mechanisms of the stator used in the next chapters. The stator consists of two IDT's applied on a piezoelectric ceramic substrate (PXE43), where  $h/\lambda_0 = 0.74\%$  and  $f_0 = 2.2$  MHz ( $h$  is the finger thickness). See section 1.5 for details. The goal is to obtain an indication of the power distribution of the stator (without slider) and to identify points for efficiency improvement.

Figure 2.28 shows the estimate of the power loss mechanisms. The electrical input power  $P_{\text{forward}}$  and the reflected power  $P_{\text{reflected}}$  are measured with a standing wave ratio (SWR) / power meter. The reflection is due to the not perfect matching networks. The acoustic power flow  $P_{\text{wave}}$  is calculated from the measured wave amplitude (section 2.2.1). The power loss of the input IDT is simply the difference ( $P_{\text{in}} - 2P_{\text{wave}}$ ) and is among other things due to the loss of the piezoelectric material and the generation of bulk waves. The wave attenuation  $P_{\text{att.}}$  is estimated by using the coefficient of attenuation given in White (1970) and compensating for the assumed squared frequency dependency (Campbell 1998). The output power is determined by measuring the output voltage at the known load. By means of the IDT reciprocity, the regenerated acoustic power  $P_{\text{reg}}$  is determined from  $P_{\text{out}}$ . The transmitted power  $P_{\text{transmit}}$  is due to mismatching of the output IDT. The insertion loss  $10 \log \left( \frac{P_{\text{forward}}}{P_{\text{wave}}} \right) = 7.8$  dB.

Possible points of improvement are:

- use of material with a higher quality factor – piezoelectric loss and wave attenuation reduces;
- decreasing the film-thickness ratio  $h/\lambda_0$  – decreases reflection and associated loss;
- use of unidirectional transducers instead of bidirectional transducers White (1970), Oliner et al. (1978) and Campbell (1998) describe different kinds of unidirectional transducers.

## 2.4 Conclusions

In this chapter background information has been discussed, which will be used in the consecutive chapters. These corresponding chapters are denoted between brackets.

- Acoustic waves and in particular Rayleigh waves have been discussed. A Rayleigh wave is a surface acoustic wave that propagates along the surface of a half-space and rapidly decays inside the material. As a result, material particles at the surface of a stator perform an *elliptical motion*. [chapters 3 and 4]
- The IDT *relation* between input *voltage* and wave *vibration velocity* may in general be considered as *static*. However, we have to account for the IDT dynamics if the envelope of the input voltages abruptly changes or if the duration of the input voltages is short with respect to the IDT length (open-loop stepping, for example). [chapter 4]

The remaining conclusions are used in chapter 5.

- A practical stator has a finite size. Therefore, the Rayleigh-wave *frequency times* the stator *thickness* should be chosen sufficiently *high* to overcome so-called *beating*. A relation for the minimum stator thickness has been derived.
- A *relation* between the *power* flow and the wave *amplitude* has been derived. This relation is used as a criterium for finding design parameters.
- A Rayleigh wave diffracts due to the limited transducer aperture width. However, most power stays within the aperture width if the *length of the propagation path* is *within the Fresnel region*.
- Absorption material placed at the stator ends is required to damp Rayleigh waves. The damping is due to wave conversion to longitudinal waves.
- An *interdigital transducer* (IDT) has been *recommended* for Rayleigh wave generation.
- An IDT generates *electromagnetic fields*.
- Low insertion loss is achieved if the transducer impedance *matches* the line impedance, a piezoelectric material with a *high quality factor* and a *large coupling factor* is chosen and if the *number of finger pairs* is *large*.

# Chapter 3

## SAW motor modeling

*Overview: In this chapter, we develop contact models of a SAW motor. These models are utilized to describe the principle of operation and to explain some inherent SAW motor properties and features. Moreover, they will be applied to investigate the influence of material variations on the motor behavior. The models are validated by using data obtained from an experimental setup.*

### 3.1 Introduction

Models for stator-slider behavior are often called contact models even if they include a description of the behavior of stator and slider beyond the intrinsic contact. In the next sections such contact models of a SAW motor are developed. The goal of the models is twofold: to analyze and explain the motor behavior and to get an impression of the design parameters. A model has the advantage that parameters can be varied easily. Furthermore, non-measurable behavior can be examined, e.g., the stick-slip behavior that underlies the actuation and impractical parameters values can be investigated to find tendencies or for explanatory reasons. To simplify the analysis, the stator-slider behavior is approximated by a discrete-parameter or lumped model. The models we will examine describe respectively:

1a) A *single* point of contact between a spherical slider (ball) and a Rayleigh wave. The tangential contact is *rigid*. This model is examined to explain the basic principle only. It does not model the key features of an SAW motor. In the literature, e.g., [Hélin \(1997\)](#) and [Morita et al. \(1999\)](#), similar models are described.

1b) A *single* point of contact between a spherical slider (ball) and a Rayleigh wave. The tangential contact is *compliant*. This model predicts the key features of a SAW motor and is used to analyze and explain the motor behavior and to find design parameters. The model is based on [Feenstra & Breedveld \(2003\)](#). The tangential compliance has been also included by [Asai et al. \(2000\)](#) for *pillar-shaped* projections. Furthermore, [Asai & Kurosawa \(2004\)](#) have described a similar model with similar results for a spher-

ical slider as well, which supports our model; the differences are related to the model implementation.

2a) Contact between *multiple* spherical projections and a Rayleigh wave. Each projection is treated as a single projection. This model is valid for a small number of projections. The model is used to describe the qualitative tendency of multiple projections.

2b) Contact between *multiple* spherical projections and a Rayleigh wave. Empirical parameters are used to model a large number of projections. The purpose is to fit the SAW motor behavior to the experimental data and discuss the implication of a large number of projections.

In section 3.2, the single point of contact models are derived. In section 3.3, the multiple points of contact models are examined. Next, the models are validated. Finally, in section 3.6 the influence of parameter variations on the motor behavior is investigated.

## 3.2 Modeling a single point of contact

As mentioned above, we will derive a model of a spherical slider (ball) in contact with a Rayleigh wave. The wave motion is considered first. Second, the behavior in normal direction is considered. In order to explain the basic principle, the tangential contact is first assumed rigid. Next, we consider a compliant tangential contact to explain the SAW motor key features. Finally, the macroscopic behavior is analyzed.

### 3.2.1 Wave motion

In this section, a simplified relation for the wave motion is derived. Consider the situation drawn in figure 1.4. The wave propagates to the left ( $-x$ ) and the surface particles make a clockwise elliptical motion. The normal and tangential displacement surface components are respectively

$$\begin{aligned} u_z &= \hat{u}_z \cos(\omega t + k_r x) \\ u_x &= \hat{u}_x \sin(\omega t + k_r x) \end{aligned} \quad (3.1)$$

where  $\omega$  is the angular frequency,  $k_r$  is the Rayleigh wave vector and  $x$  is a position. To simplify this wave displacement relation, we rewrite the argument of the sin and cos terms as

$$\omega t + k_r x = k_r(c_r t + x) \quad (3.2)$$

where  $c_r = \omega/k_r$  is the Rayleigh phase velocity (wave propagation velocity). Suppose that the initial slider position  $x(0) = 0$  and that slider velocity  $\dot{x} \leq \dot{x}_{\max}$ . The maximal slider velocity  $\dot{x}_{\max}$  is in general  $\ll c_r$ . Hence,  $x \leq \dot{x}_{\max} t \ll c_r t$  such that

$$\begin{aligned} k_r(c_r t + x) &\approx k_r c_r t \\ &= \omega t \end{aligned} \quad (3.3)$$

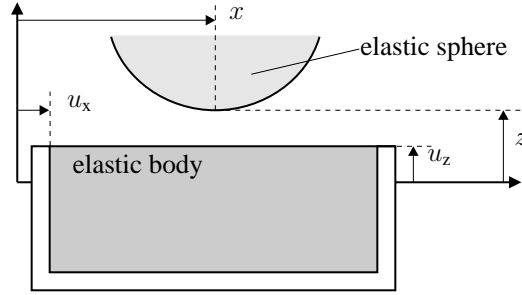


Figure 3.1: Illustration of the impact.

Therefore, the wave displacement is simplified as

$$\begin{aligned} u_z &\approx \hat{u}_z \cos(\omega t) \\ u_x &\approx \hat{u}_x \sin(\omega t) \end{aligned} \quad (3.4)$$

Figure 2.7 shows the particle displacement vs. the stator depth. For small depths ( $\ll \lambda_r$ ), the particle displacements amplitudes are approximately constant. Accordingly, the wave motion can be interpreted as a solid elastic body that performs an elliptical motion, see figure 3.1. If a slider loads the stator, the wave amplitude decreases due the reflections against the slider (section 2.2.3). We assume that the decrease in amplitude due to one projection is small and may therefore be disregarded.

### 3.2.2 Normal motion

The first question that arises is whether the normal motion may be considered independent of the tangential traction. Johnson (1994) points out that the tangential tractions do not effect the normal motion if the materials of the two bodies are elastically similar. Moreover, it is shown that, even for dissimilar materials, the effect is small and may be reasonably neglected. Accordingly, the problem simplifies to a normal impact between two bodies: an elastic sphere and an elastic body.

During impact, energy is stored at the contact region of slider and stator, which can be described by a stiffness element. We assume that the impact is frictionless, quasi static and elastic. (These assumptions are validated at the end of this subsection). Hence, we can use the static contact theory of Hertz (e.g. Johnson (1994)). The normal force  $F_n$  for a sphere-plane contact is (the radius of the wave is large relative to the radius of the slider)

$$F_n = \underbrace{\frac{4}{3}\sqrt{RE}}_{k_n} \delta_z^{3/2} \quad (3.5)$$

where  $\delta_z$  is the sum of the indentation of slider and stator, which equals  $u_z - z$  for  $u_z - z > 0$  and 0 otherwise. See figure 3.1. The radius of the slider is  $R$  and the composite Young

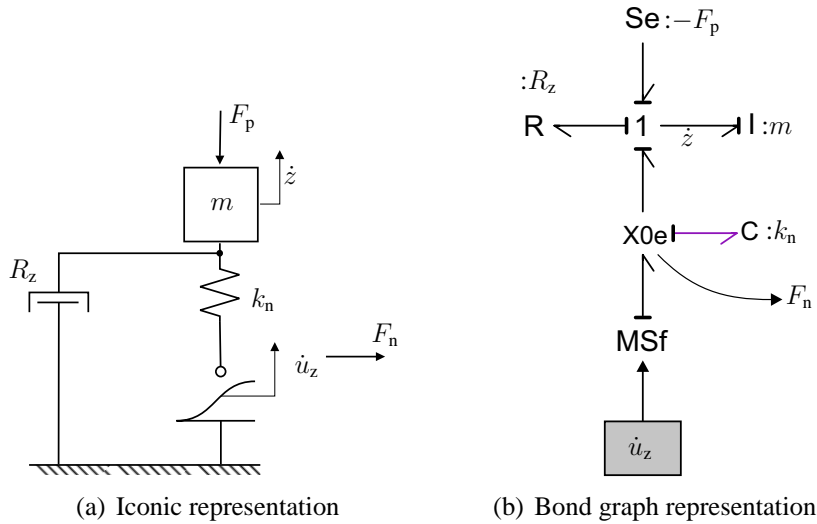


Figure 3.2: Normal impact model.

modulus is

$$E = \left( \frac{1 - \sigma_1^2}{E_1} + \frac{1 - \sigma_2^2}{E_2} \right)^{-1} \left[ \frac{N}{m^2} \right] \quad (3.6)$$

The material parameters  $E_1$ ,  $\sigma_1$  and  $E_2$ ,  $\sigma_2$  are the Young modules and the Poisson ratio of respectively the slider and the stator. Dissipation could be included by defining a complex composite Young modulus  $E_c = E(1 + i \tan \phi)$ , where  $\tan \phi$  is a loss factor that depends on both materials.

$$\begin{aligned} F_n &= \frac{4}{3} \sqrt{R} E_c \delta_z^{3/2} \\ &= \frac{4}{3} \sqrt{R} E \left( \delta_z^{3/2} + \frac{3 \tan \phi}{2 \omega} \delta_z^{1/2} \dot{\delta}_z \right) \\ &= \underbrace{k_n \delta_z^{3/2}}_{\text{stiffness}} + \underbrace{R_n \delta_z^{1/2} \dot{\delta}_z}_{\text{damping}} \end{aligned} \quad (3.7)$$

However, it appears from material data that the damping force is negligibly small. Therefore, the material dissipation  $R_n$  is disregarded in the remainder of this thesis.

Equation 3.8 shows the non-linear differential equations, which describe the normal behavior. The slider mass is denoted by  $m$  and  $R_z$  represents air damping, which is assumed to be linear. (In subsection 3.2.3, we will see that the structure and the value of the air damping is not critical for the total contact behavior). The slider is pressed against the stator with a preload force  $F_p$ , which is the sum of the gravitational force ( $m.g$ ) and an additional applied external force.



description	parameter	value	unit
Normal wave amplitude	$\hat{u}_z$	10	nm
Wave frequency	$f$	2.2	MHz
Young modulus slide	$E_1$	213	GPa
Young modulus stator	$E_2$	77	GPa
Poisson ratio sphere	$\sigma_1$	0.3	-
Poisson ratio stator	$\sigma_2$	0.3	-
Radius sphere	$R$	1	mm
Mass of sphere	$m$	0.2	g
Preload force	$F_p$	2	mN
Air damping	$R_z$	2	Ns/m

Table 3.1: Simulation parameters of the normal model.

$$\begin{aligned}
\text{contact: } u_z - z > 0 & \quad \begin{cases} \dot{z} = \frac{1}{m} \int (k_n \delta_z^{3/2} - R_z \dot{z} - F_p) dt \\ \delta_z = \hat{u}_z \cos(\omega t) - z \end{cases} \\
\text{no-contact: } u_z - z \leq 0 & \quad \begin{cases} \dot{z} = \frac{1}{m} \int (-R_z \dot{z} - F_p) dt \\ \delta_z = 0 \end{cases}
\end{aligned} \tag{3.8}$$

Figure 3.2(a) shows an iconic representation of the normal model. The open circle indicates a contact point that detects the moment of contact and accordingly switches between ‘contact’ and ‘no-contact’. The normal force  $F_n$  is an input variable for the tangential models. This model and next models are implemented as bond-graph models and simulated in the modeling and simulation package *20-sim* (2003). See for example [Breedveld \(1984\)](#), [Karnopp et al. \(2000\)](#) and [Van Amerongen & Breedveld \(2003\)](#) for detailed information about bond graphs. Figure 3.2(b) shows an bond-graph representation of the normal model. Sub-model *X0e* is a so-called switched junction, which detects the moment of contact and accordingly switches between ‘contact’ and ‘no-contact’. The remaining sub-model are standard sub-model in the bond-graph paradigm.

### Contact behavior

Consider a setup consisting of a steel sphere with a diameter of 1 mm and a stator made of PZT. Table 3.1 lists the parameters. The damping value  $R_z$  is estimated from experimental data. The remaining parameters are taken from literature.

Figure 3.3 shows the contact behavior in normal direction during one period of contact. In figure 3.3(a) the normal displacement  $z$  is not at steady state and in figure 3.3(b)  $z$  is at steady state. The top plots show the normal wave displacement  $u_z$  and normal slider displacement  $z$ . There is ‘contact’ between wave and slider when  $-\theta < \omega t < \theta$ . The figures demonstrate that the slider displacement does not follow the wave motion, which is due to the high frequency of the wave motion with respect to the mass of the slider and the compliance of the normal contact. The inset shows the small variation of the slider displacement within one wave period. The bottom subplots shows the normal force  $F_n$ ,

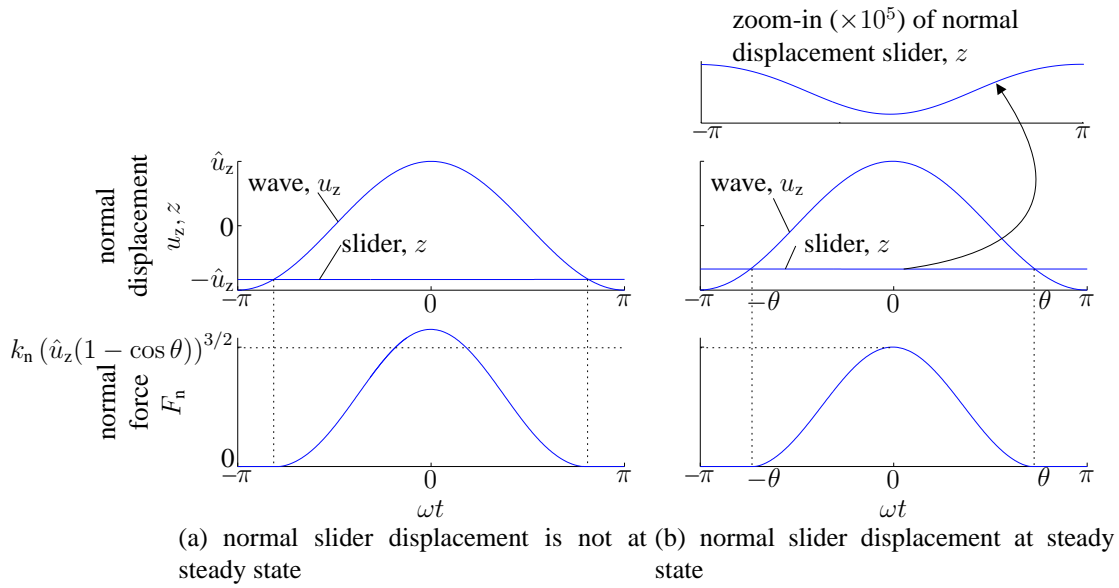


Figure 3.3: Normal contact behavior of a sphere.

which increases when slider and wave start contacting (second subplot). The difference between the wave and the slider displacements determines the normal force  $F_n$ .

### Step response

The results of figure 3.3 take place within one period of contact ( $0.45\mu\text{s}$ ). The time span of next result is significantly larger (1 ms). Figure 3.4 shows the response of the normal slider displacement  $z$ , when driven by a burst of waves. Two features are discussed:

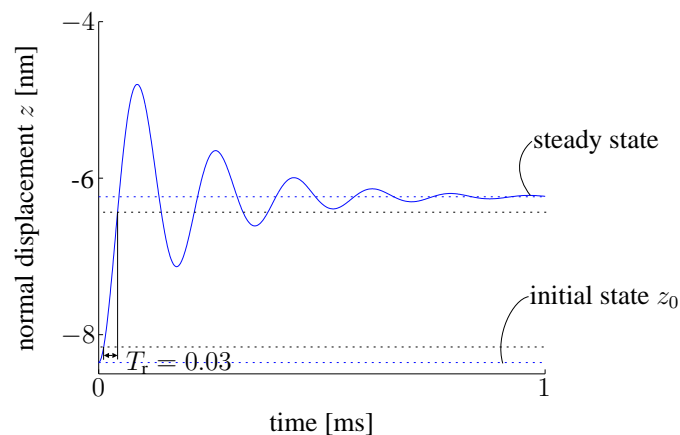


Figure 3.4: Normal slider behavior between sphere and wave motion.

**1. Rise time** There are various definitions for the rise time  $T_r$ . The definition we use is the time required going directly from 10 % to 90 % of the final value. It will be demonstrated in next section that the rise time in normal direction ( $T_r \approx 0.03$  ms) is significantly smaller than the rise time in tangential direction. Therefore, the normal behavior is not observable in the tangential behavior.

**2. Steady state** The slider displacement approaches a steady-state value, due to dissipation by  $R_z$ . We will derive a relation for this steady state condition. We disregard the air-damping  $R_z$  and the slider inertia term  $m\ddot{z}$ , since  $\dot{z} \approx 0$  and  $\ddot{z} \approx 0$  (the slider cannot follow the wave motion). Consequently, only a balance between preload force  $F_p$  and average normal force  $\bar{F}_n$  remains (equation 3.8 and equation 3.5). The ‘bar’ at  $\bar{F}_n$  indicates that we consider the average force per period of time.

$$\begin{aligned} F_p &= \bar{F}_n \\ &= \frac{1}{2\pi} \int_{-\pi}^{\pi} F_n \, d\omega t \\ &= k_n \frac{1}{\pi} \int_0^{\theta} (\hat{u}_z \cos(\omega t) - z)^{3/2} \, d\omega t \end{aligned} \quad (3.9)$$

where  $\theta$  is the angle where slider and stator make contact (see figure 3.3). Because equation 3.9 is an elliptic integral, it does not have a general analytical solution. Therefore, the steady state slider velocity needs to be found numerically (e.g. by simulation) or by approximation. However, there are two particular cases where an analytical solution exist. The slider displacement for zero wave amplitude  $z = z_0$  is a trivial case,

$$z_0 = - \left( \frac{F_p}{k_n} \right)^{2/3} \quad (3.10)$$

For the second case, consider the transition point between continuous contact and intermittent contact of wave and slider; for a small wave amplitude there is always contact ( $\theta = \pi$  in figure 3.3) and if the wave amplitude is increased the contact becomes intermittent ( $\theta < \pi$  in figure 3.3). We call the wave amplitude at the transition point the ‘release’ amplitude  $\hat{u}_{z,r}$ . The slider displacement at this transition point is  $z = -\hat{u}_{z,r}$ . Therefore,

$$\begin{aligned} F_p &= k_n \frac{1}{\pi} \int_0^{\pi} (\hat{u}_{z,r} \cos(\omega t) + \hat{u}_{z,r})^{3/2} \, d\omega t \Rightarrow \\ \hat{u}_{z,r} &= \left( \frac{3}{16} \frac{\pi F_p \sqrt{2}}{k_n} \right)^{2/3} \end{aligned} \quad (3.11)$$

Figure 3.5 shows the (simulated) steady state slider displacement versus the wave amplitude. Indeed, for small amplitudes, there is always contact between slider and stator. If the wave exceeds the ‘release’ amplitude, the contact is intermittent. In section 3.6 –variation of model parameters– and chapter 5 –design parameters– we utilize the release amplitude.

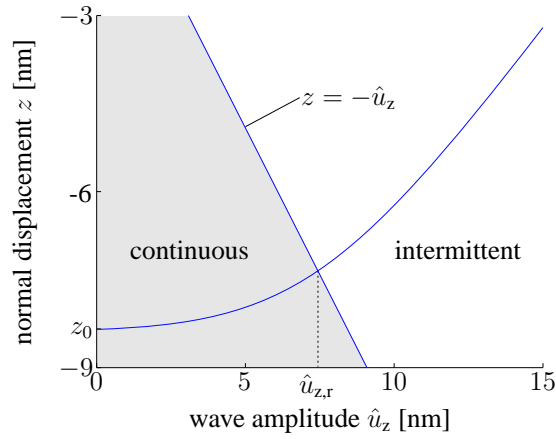


Figure 3.5: Normal displacement versus wave amplitude.

### Validation of the assumptions

In this subsection, we discuss the validity of the assumptions made in subsection 3.2.2. We assumed a frictionless impact. According to [Faik & Witteman \(2000\)](#), the dissipation due to friction is small compared to material damping, if the coefficient of friction is smaller than unity. This condition holds (the material damping is negligibly small and the in this thesis considered coefficients of friction are smaller than unity), therefore we may assume a frictionless impact. Second, we validate the assumption that the contact is quasi-static. Often the criterion of Love is used ([Johnson 1994](#)); the influence of generated waves due to impact may be neglected if the acoustic waves travel back and forth several times before the impacts ends. However, this criterion is too restrictive for three-dimensional bodies and in particular for the considered sphere-plane impact. An alternative criterion by Hunter ([Johnson 1994](#)) is based on the impact velocity; the response is dominated by the compliant contact if the relaxation time is short compared with the period of the pulse. Based on this criterion, [Johnson \(1994\)](#) states that in most cases a more severe restriction is placed on the limit of elastic behavior.

The limit of elastic behavior of an elastic-plastic sphere-plane contact is at a point beneath the surface of impact. The corresponding maximal contact pressure  $p_Y$ , at the surface of impact, is related to the so-called yield stress  $Y$  of the softer body. The yield stress is a material dependent constant. The maximal contact pressure of a sphere-plane contact is  $p_Y = 1.6Y$  where, according to Hertz's theory

$$p_Y = \frac{3}{2\pi} \frac{k_n \sqrt{\delta_{z,Y}}}{R} \quad (3.12)$$

Hence, the corresponding maximal indentation in the range of elastic indentation is

$$\delta_{z,Y} = \frac{4}{9} \left( \frac{1.6YR\pi}{k_n} \right)^2 \quad (3.13)$$

The maximal elastic indentation, using the parameters of table 3.1 and  $Y_1 > Y_2 = 600$  MPa ([Philips 1997](#)), is 590 nm. The simulated maximal indentation is significant smaller. Therefore, all assumptions are valid.

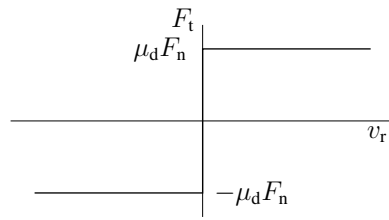
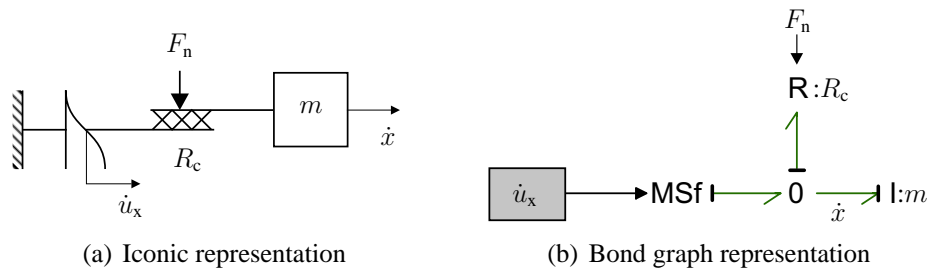
Figure 3.6: Dry friction model,  $R_c$ .

Figure 3.7: Tangential model of a rigid slider and a rigid stator.

### 3.2.3 Tangential motion

#### Rigid behavior

Consider again figure 3.1. We assume that the slider and stator are rigid in tangential direction and that the interaction between wave and slider resembles dry (Coulomb) friction. Figure 3.6 shows the dry friction behavior. The frictional force  $F_t$  depends on the sign of the sliding velocity  $v_r$ , the coefficient of friction  $\mu_d$  and the normal force  $F_n$ . The sliding velocity is zero if  $|F_t| < \mu_d F_n$ .

Equation 3.14 shows the relations for the tangential motion. The sliding velocity  $v_r$  is  $\dot{u}_x - \dot{x}$ , where  $\dot{u}_x$  is the tangential wave vibration velocity and  $\dot{x}$  the slider velocity. The slider mass is  $m$ . Figure 3.7(a) and figure 3.7(b) show an iconic representation and a bond graph representation respectively. The friction sub-model  $R_c$  is implemented as  $F_t = F_n \mu_d \tanh(\text{slope } v_r)$  where the parameter *slope* determines the steepness of the dry friction and the variable  $F_n$  modulates the friction force.

$$\begin{aligned}
 \dot{x} &= \frac{1}{m} \int F_t dt \\
 F_t &= \mu_d F_n \text{sign}(\dot{u}_x - \dot{x}) \\
 \dot{u}_x &= \hat{u}_x \omega \cos(\omega t)
 \end{aligned} \tag{3.14}$$

**Contact behavior** With the aid of the derived normal and tangential model we are able to explain the basic principle of operation of a SAW motor. Consider again the setup of a steel sphere and a PZT stator. Table 3.2 lists the simulation parameters.

description	parameter	value	unit
Normal wave amplitude	$\hat{u}_z$	10	nm
Tangential/Normal amplitude	ratio	0.65	-
Wave frequency	$f$	2.2	MHz
Young modulus slider	$E_1$	213	GPa
Young modulus stator	$E_2$	77	GPa
Poisson ratio slider	$\sigma_1$	0.3	-
Poisson ratio stator	$\sigma_2$	0.3	-
Radius slider	$R$	1	mm
Mass of slider	$m$	0.2	g
Preload force	$F_p$	2	mN
Air damping	$R_z$	2	Ns/m
Coulomb coefficient of friction	$\mu_d$	0.18	-
Steepness of friction implementation	$slope$	5000	-

Table 3.2: Simulation parameters for the rigid and the compliant tangential models.

Figure 3.8 shows the simulated contact behavior. Figure 3.8(a) shows the behavior during acceleration and figure 3.8(b) shows the behavior at a steady state slider velocity. The first two subplots of both figures show the normal behavior. The slider displacement  $z$  in figure 3.8(a) already reached steady state. The normal behavior is similar to figure 3.3. The third subplots show the slider velocity  $\dot{x}$ , the tangential vibration velocity of the wave  $\dot{u}_x$  and the sliding velocity  $v_r = \dot{u}_x - \dot{x}$ . These subplots demonstrate that the slider velocity  $\dot{x}$  does not follow the wave vibration velocity  $\dot{u}_x$ . This is due to the small variation of the tangential force relative to the stored momentum of the slider mass. The slider mass behaves like a ‘flywheel’. The wave vibration velocity is larger than the slider velocity at  $-\psi < \omega t < \psi$ . The bottom plots show the tangential force as imposed by figure 3.6; the tangential force is positive if  $v_r$  is greater than zero and negative otherwise. In figure 3.8(a) the average tangential force per period  $\bar{F}_t$  is greater than zero (the average of the light-gray area); the slider will accelerate. In figure 3.8(b), the steady state velocity is reached; the average tangential force is zero.

**Step response** Figure 3.9 shows a typical response of a SAW motor. A burst of waves drives the slider and accelerates it from zero velocity to a steady state velocity. If the wave amplitude becomes zero again, the slider starts decelerating, until the velocity is zero. The rise time  $T_r$  in figure 3.9 is 66 ms. The rise time of the normal impact was 0.03 ms (figure 3.4). In general, the rise time of the normal impact is significantly smaller. Consequently, the dynamics of the normal motion are not observable in the tangential direction.

As mentioned, the slider starts braking when the wave amplitude becomes zero. This happens in figure 3.9 for  $t = 0.2$  s. The model simplifies during braking (figure 3.10). The normal force  $F_n$  at sliding equals the preload  $F_p$  force almost instantaneously. Accordingly, the slider slips with a constant deceleration, i.e.,  $\ddot{x} = -\frac{1}{m}F_p\mu_d$ .

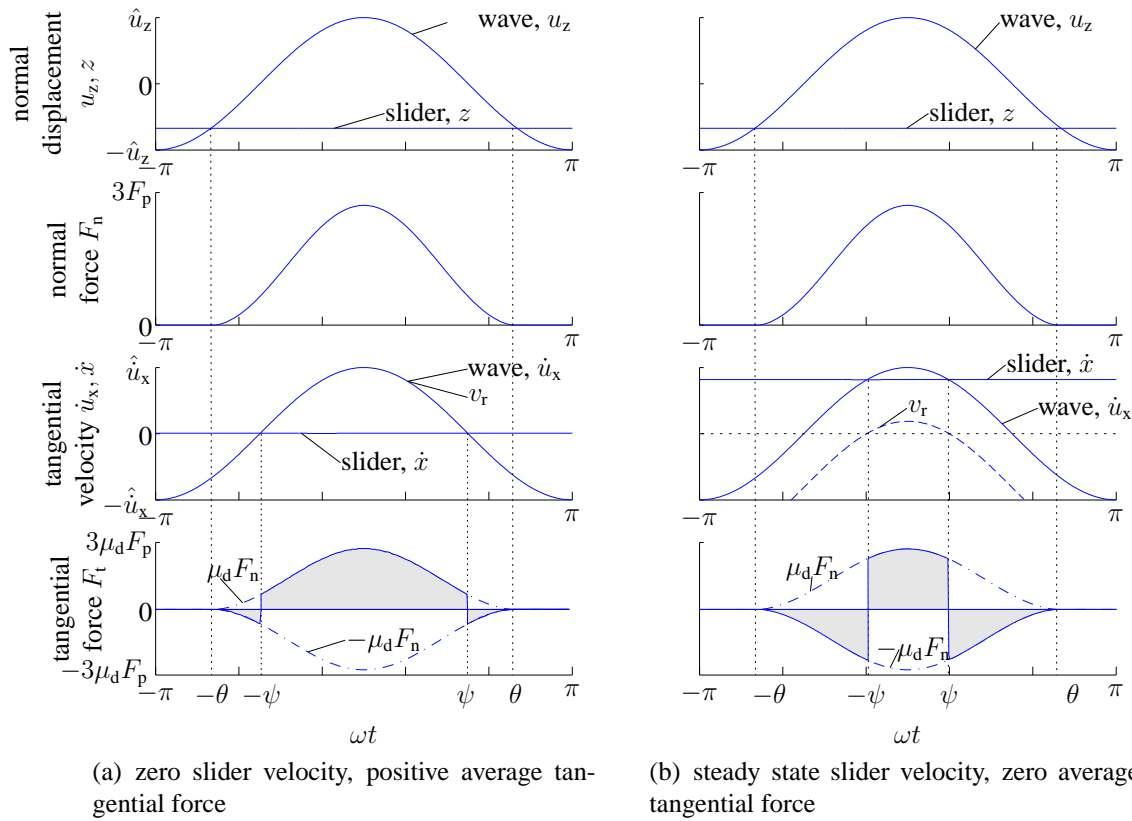


Figure 3.8: Contact behavior. The slider and stator are rigid in tangential direction.

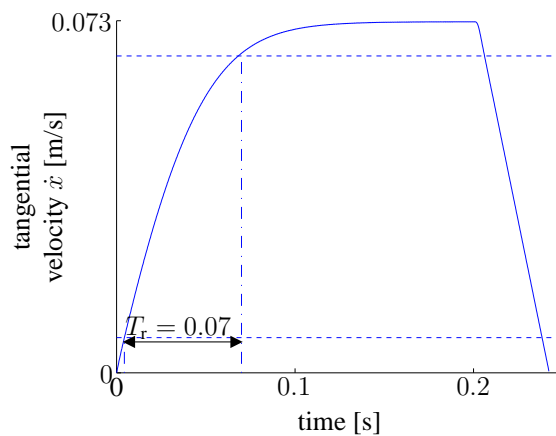


Figure 3.9: Tangential slider velocity when driven by a burst of waves.

### Compliant behavior

In the previous section we have discussed the contact behavior for a rigid tangential contact. Although it explains the basic behavior, later results will show that it does not predict the SAW motor behavior accurately. Therefore, compliant tangential behavior is included.

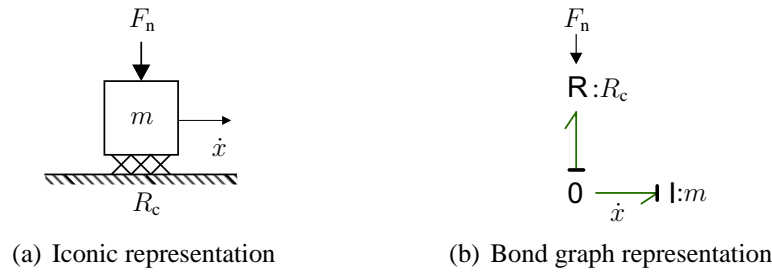


Figure 3.10: Tangential model of a rigid slider and a rigid stator when braking.

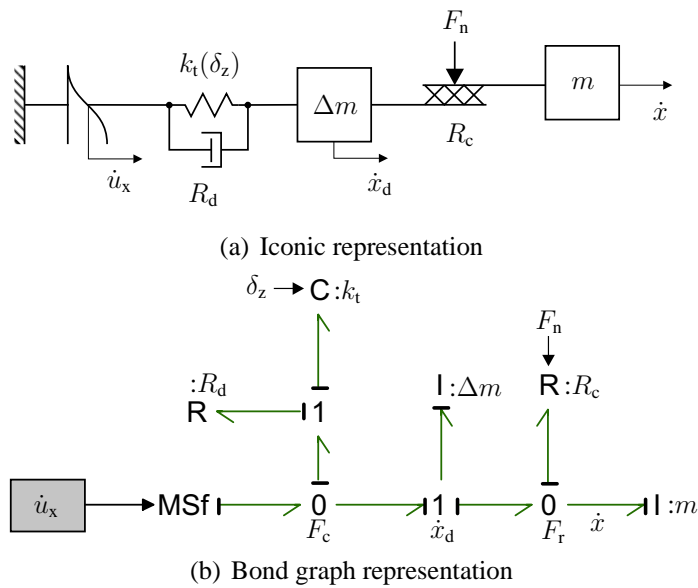


Figure 3.11: A compliant tangential model.

We propose the model shown in figure 3.11. A stiffness sub-model  $k_t$  accounts for both the sphere and the stator tangential deformation. The small mass  $\Delta m$  represents the mass of deformed stator and slider material, however, it has no dominant influence on the behavior, but it accounts for a preferred model causality<sup>1</sup>. Compliant damping  $R_d$  represents material damping and is added for numerical stability. The compliant damping has no influence on the behavior as well. The remaining sub-models were discussed previously. Equation 3.15 shows the relations, where  $F_r$  and  $F_c$  are the forces applied by the friction and the stiffness sub-models respectively.

<sup>1</sup>To simulate a model, the input and output variables of the sub-models have to be determined, i.e., the causality has to be assigned (Karnopp et al. 2000). The preferred causality (integral causality) for a stiffness sub-model is force out (and velocity in) rather than force in (and velocity out). The fixed causality for a friction sub-model is force out as well. By using a small mass in between the friction and stiffness sub-models the preferred causality can be satisfied (equation 3.15).



$$\begin{aligned}
\dot{x} &= \frac{1}{m} \int F_r dt \\
\dot{x}_d &= \frac{1}{\Delta m} \int (F_c - F_r) dt \\
F_r &= \mu_d F_n \tanh((\dot{x}_d - \dot{x}) \text{ slope}) \\
F_c &= k_t \int (\dot{u}_x - \dot{x}_d) dt
\end{aligned} \tag{3.15}$$

Consider the tangential stiffness  $k_t$ . When a tangential force is applied to two bodies pressed into contact, which is less than the limiting force, no sliding motion will occur. Nevertheless, there will be a relative motion referred to as presliding displacement  $\delta_x$ . According to [Johnson \(1994\)](#), [Cattaneo \(1938\)](#) proposed a solution to the problem of tangential loading for a constant normal force  $F_n$  (appendix E). However, when the normal force is changing, the behavior may be quite complex, because normal force, normal stiffness and tangential stiffness are non-linear, interacting functions of the normal displacement. In general, the state of contact between two bodies subjected to variations in normal and tangential load depends on the history. As a first approximation it is actually the breakaway displacement  $\delta_{x,\max}$  that is constant ([Armstrong-Hélouvy et al. 1994](#)). The stiffness function is than

$$\begin{aligned}
F_t &= \frac{F_b}{\delta_{x,\max}} \delta_x \\
&= \frac{16G\sqrt{\delta_z R}}{3} \delta_x \\
&= k_t(\delta_z) \delta_x
\end{aligned} \tag{3.16}$$

where  $F_b = \mu_d F_n$  is the breakaway force,  $\delta_z$  the normal indentation,  $R$  the radius of the spherical slider and,

$$G = \left( \frac{2 - \sigma_1}{G_1} + \frac{2 - \sigma_2}{G_2} \right)^{-1} \left[ \frac{N}{m^2} \right] \tag{3.17}$$

where  $G_1$  and  $G_2$  are respectively the shear modulus of slider and stator. For an isotropic material  $G_i = \frac{E_i}{2+2\sigma_i}$ . Some remarks should be made:

- The dissipation due to micro-slip is neglected.
- The tangential stiffness function  $k_t$  is modulated by the normal indentation  $\delta_z$ , i.e.,  $F_t = F_t(\delta_z, \delta_x)$ . Due to the assumption that the normal impact is not influenced by the tangential motion, the normal stiffness function is only a function of  $\delta_z$ , i.e.,  $F_n = F_n(\delta_z)$ . Consequently, the storage of elastic energy is not conservative. However, the deviation is small, i.e., the power ‘transported’ from the tangential power-port ( $F_t, \dot{\delta}_x$ ) to the normal power-port ( $F_n, \dot{\delta}_z$ ) is negligibly small compared to the intrinsically stored elastic energy of the normal stiffness  $\int F_n d\delta_z$ . Therefore, the total contact stiffness can be modeled as a modulated tangential stiffness and a separate independent normal stiffness.

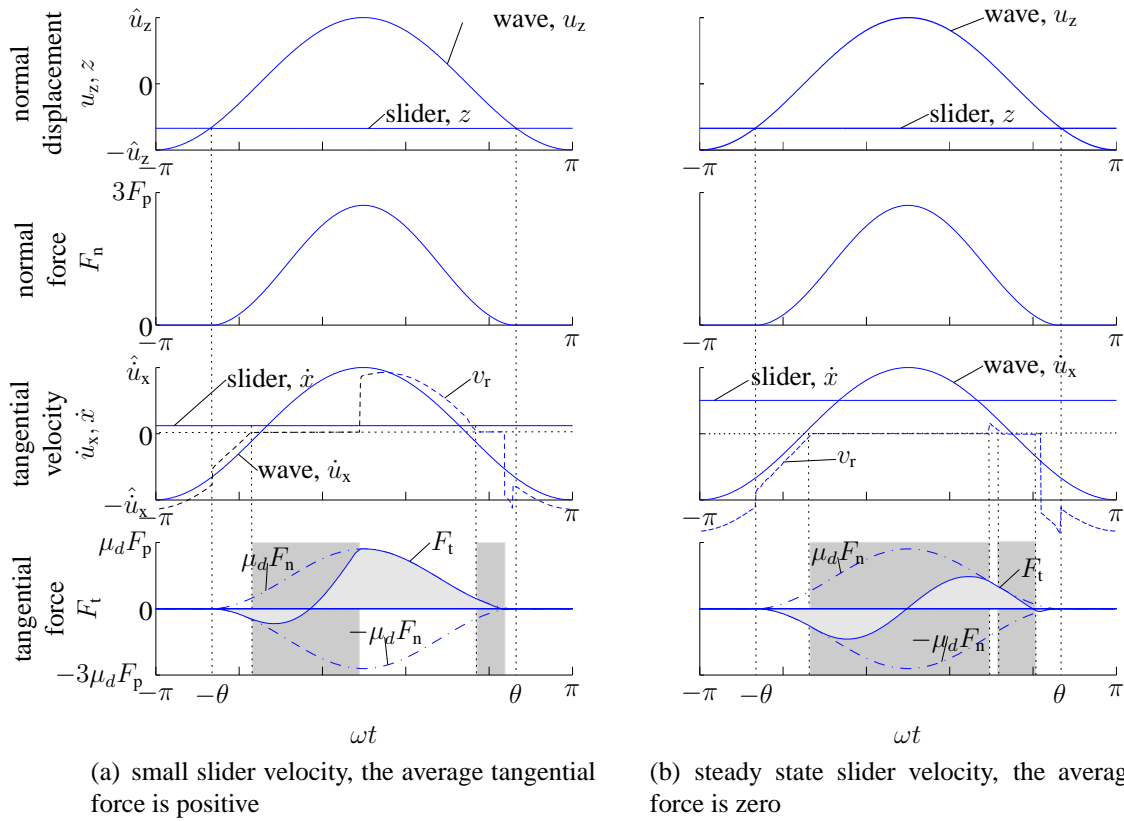
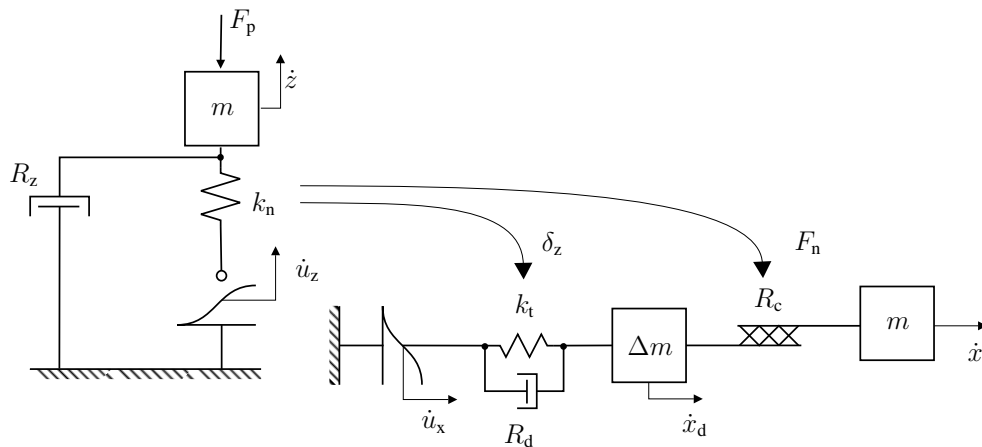


Figure 3.12: Contact behavior between slider and stator that are compliant in tangential direction. The dark grey areas indicate regions where slider and stator stick.

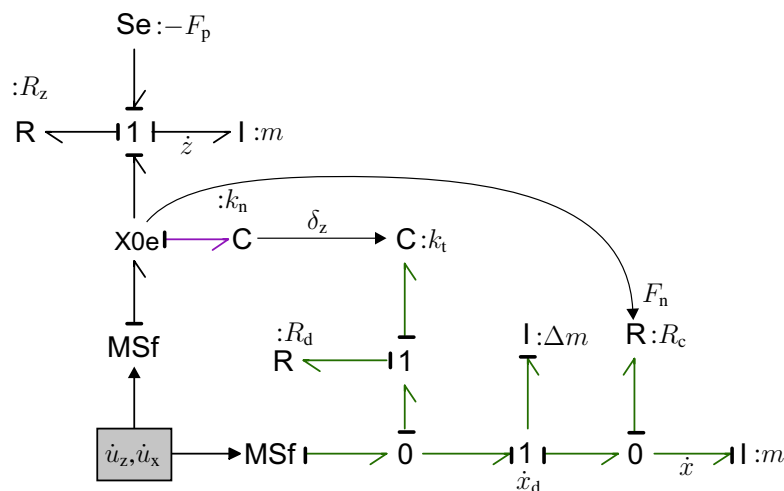
**Contact behavior** Figure 3.12 shows the contact behavior of a steel sphere and a PZT stator with compliant tangential contact. Figure 3.12(a) shows the behavior during acceleration. Figure 3.12(b) shows the behavior for a steady state slider velocity. The only additional simulation parameters, with respect to the rigid tangential model (table 3.14), are the mass of deformed material  $\Delta m$  and the compliant damping  $R_d$ . (The parameters for the tangential stiffness are the same as for the normal stiffness). The mass and the damping should be chosen sufficiently small such that they do not affect the overall behavior:  $\Delta m = 10^{-15}$  kg and  $R_d = 10^{-6}$  Ns/m.

The first two subplots of figure 3.12(a) and figure 3.12(b) show behavior which is identical to figure 3.2; the top subplots show the wave and slider displacements and the second subplots show the normal force  $F_n$ . The third subplots shows the tangential velocities  $\dot{u}_z$ ,  $\dot{x}$  and  $v_r$ . The sliding velocity  $v_r = \dot{x}_d - \dot{x}$ , the velocity across  $R_c$ , is zero in case slider and stator stick. These stick regions are indicated in the bottom subplots by the dark-grey areas. Furthermore, the tangential force is shown in the bottom subplots. The average tangential force (average of the light-gray areas) of figure 3.12(a) is positive, hence the slider accelerates (as mentioned before). The average tangential force of figure 3.12(b) is zero hence the slider velocity is at steady state.

For completeness the total contact model is shown in figure 3.13. It demonstrates the unidirectional coupling between normal and tangential motion, i.e., the tangential motion



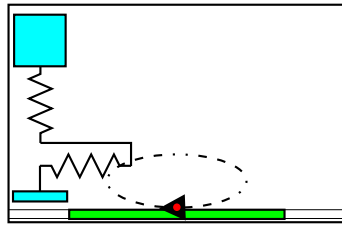
(a) Iconic representation



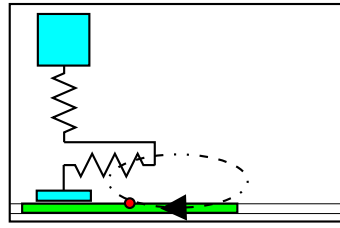
(b) Bond graph representation

Figure 3.13: Total contact model.

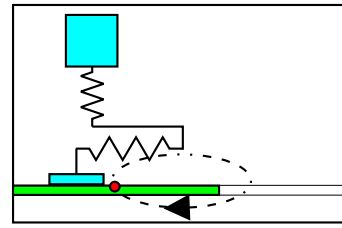
has no influence on the normal motion. Figure 3.14 clarifies the principle of operation in more detail. The normal and tangential sphere and stator deformation are represented by the springs ( $k_n$  and  $k_t$  in figure 3.13). The tangential wave motion is exaggerated for explanatory reasons. Every picture has a number that refers to the event numbers which are shown at the bottom plot of figure 3.14.



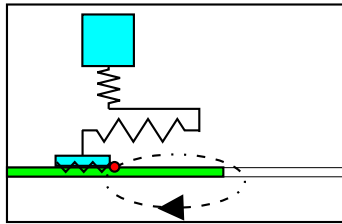
1. There is no contact between wave and slider.



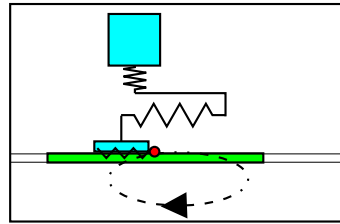
2. There is no contact between wave and slider.



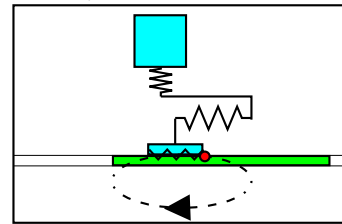
3. The wave touches the slider and the contact is sliding. The wave velocity is smaller than the slider velocity. The tangential spring is stretched. A negative force  $F_t$  acts on the slider.



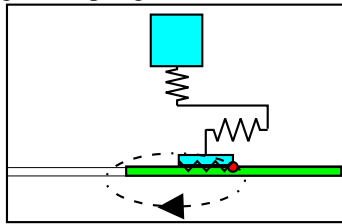
4. The sliding velocity  $v_t = 0$ , i.e., the contact 'sticks' as indicated by the wavy line at the contact interface. The tangential force is negative because the tangential spring is stretched.



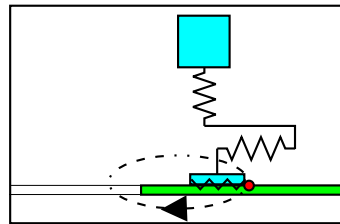
5. The behavior is similar to event 4.



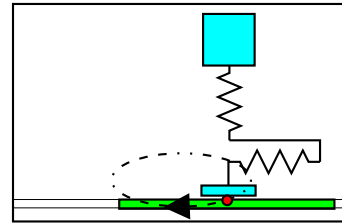
6. The contact still sticks but now the spring is compressed. Hence the tangential force is positive.



7. The behavior is similar to event 6.



8. The second 'stick' region. The tangential spring is a bit compressed.



9. There is no-contact between wave and slider. The sequence of stick and sliding starts all over again.

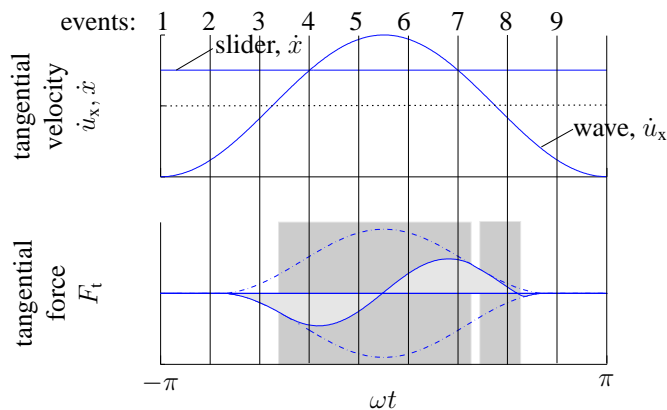


Figure 3.14: Principle of operation

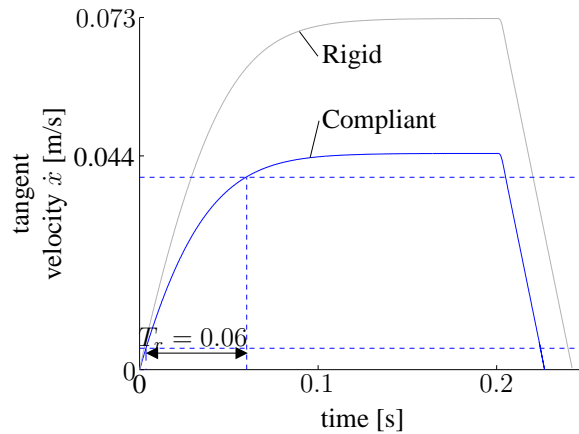


Figure 3.15: The step response for the contact model with and without tangential compliance.

**Step response** Figure 3.15 shows the slider velocity when driven by a burst of waves. The figure demonstrates the decrease of the steady state slider velocity  $\dot{x}_s$  due to the tangential compliance ( $0.073 \rightarrow 0.044$  m/s). The change in rise time  $T_r$  is less ( $66 \rightarrow 56$  ms). In section 3.5 we will see that this model predicts the slider behavior rather accurately.

### 3.2.4 Macroscopic behavior

In this subsection, we will examine the macroscopic behavior of a SAW motor by utilizing the previous derived contact model. The goal is to explain the macroscopic behavior from a microscopic point of view. This insight is used to improve the SAW motor specifications and to eliminate some less favorable features of a SAW motor (chapter 4). Furthermore, we use the interpretation of the macroscopic behavior in the next chapter (chapter 4) to describe a model for controller design. First, we discuss the motor characteristic. Next, this motor characteristic is analyzed by splitting it up into two parts.

#### Motor characteristic

The considered macroscopic variables are the average tangential force  $\bar{F}_t$  and the slider velocity  $\dot{x}$ , which are the variables that ‘interact’ with a load like the slider mass.

$$\bar{F}_t = \frac{1}{2\pi} \int_{-\pi}^{\pi} F_t d\omega t \quad (3.18)$$

The relation between these two variables is static and can be visualized by a so-called *motor characteristic*. Figure 3.16(a) shows a motor characteristic, which is obtained by the model of figure 3.12 and the parameters of table 3.2. The tangential average force is ‘measured’ while applying a known slider velocity  $\dot{x}$ . Consider the first quadrant of the motor characteristic. It shows a large tangential force for a small slider velocity. The force

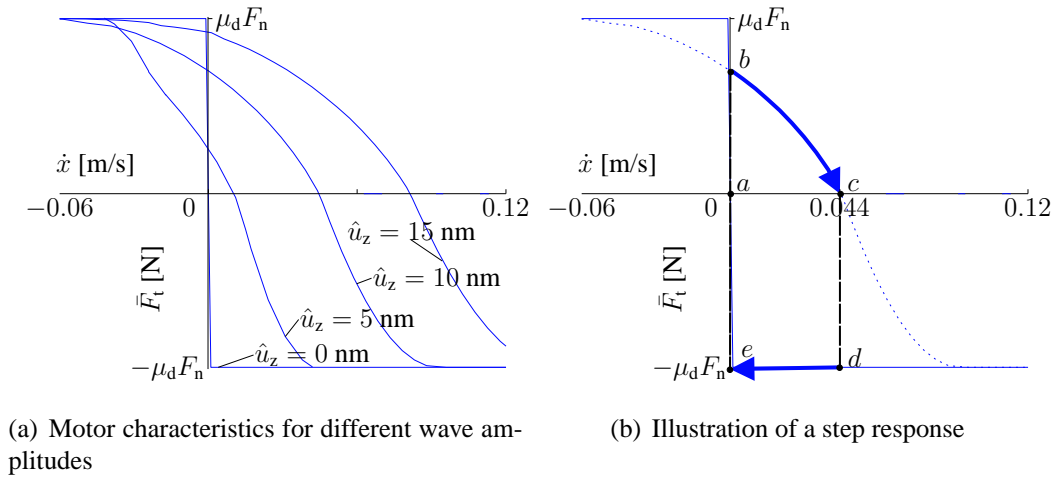


Figure 3.16: Motor characteristic

decreases for an increasing wave velocity. Besides that it shows that the driving force is limited by the maximum friction force  $\mu_d F_n$ .

Figure 3.16(b) illustrates a path that is followed when a slider mass is actuated by a burst of waves (the step response of figure 3.15). The slider is initially at rest, which corresponds to point *a*. Due to the burst, the slider accelerates from point *b* to the steady-state velocity *c*. After a while, the wave amplitude becomes zero again. Consequently, the slider brakes due to the negative friction force  $d \rightarrow e$ . At zero velocity, the braking force changes to zero  $e \rightarrow a$ .

Observe that a motor characteristic can be split-up into two relations:

1. a relation between the wave amplitude  $\hat{u}_z$  and the no-force slider velocity  $\dot{x}_s$ . The  $\dot{x}$ -axis of figure 3.16(a). (The steady-state velocity of the previous subsections equals the no-force velocity);
2. a non-ideal non-linear force source that may be interpreted (by using Norton-Thvenin equivalence relation) as a series connection of
  - an ideal velocity source  $\dot{x}_s$ ;
  - a non-linear damper, which depends on both the velocity difference  $\dot{x}_s - \dot{x}$  and the wave amplitude  $\hat{u}_z$ .

First, we analyze the relation between the wave amplitude and the no-force velocity. Next, we examine the non-ideal non-linear velocity source.

### No-force (steady-state) velocity

Figure 3.17 shows the no-load slider velocity  $\dot{x}_s$  versus the normal wave amplitude  $\hat{u}_z$ . Three regions can be distinguished, which are separated by the ‘threshold’ and ‘release’ amplitude.

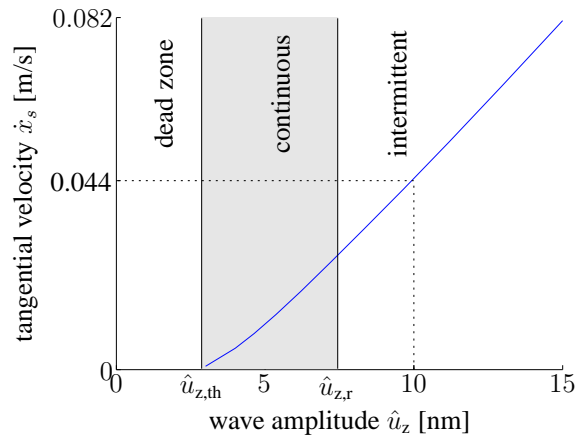


Figure 3.17: Tangential slider velocity versus wave amplitude.

**Dead-zone** There is no slider motion if the wave amplitude is smaller than the threshold amplitude  $\hat{u}_{z,th}$ . The contact behavior explains this phenomenon; the slider and the stator continuously stick within the dead-zone region. The tangential spring stretches and compresses, but the slider will remain at rest. The average tangential force  $\bar{F}_t$  is zero.

**Continuous** The slider starts to move if the wave amplitude exceeds the ‘threshold’ amplitude. There is always contact between wave and slider if the wave amplitude does not exceed the ‘release’ amplitude (see page 52). In this region, the contact between wave and slider slides and sticks.

**Intermittent** In region 3, the wave amplitude is greater than the ‘release’ amplitude. Therefore, the contact between slider and wave is intermittent. See for example figure 3.14. The ‘modes’ during operation are stick, sliding and no-contact.

### Non-ideal non-linear force source

The characteristics (the curves) in figure 3.16(a) can be described by a non-ideal non-linear force source, which is a function of both the velocity difference  $\dot{x}_s - \dot{x}$  and the wave amplitude  $\hat{u}_z$ .

$$\bar{F}_t = \bar{F}_t(\dot{x}_s - \dot{x}, \hat{u}_z) \quad (3.19)$$

Figure 3.18(a) shows the force source  $\bar{F}_t$  as a function of the velocity difference. It demonstrates that  $\bar{F}_t$  resembles dry friction for zero wave amplitude. Furthermore, it shows that the ‘friction force’ decreases by an increase of  $\dot{x}_s - \dot{x}$  and an increase of  $\hat{u}_z$ . Subsequently, the non-ideal non-linear force source can be interpreted as a series connection of an ideal velocity source  $\dot{x}_s$  and an equivalent non-linear damper  $R_t$ . We emphasize that this damper is not physical present; the damper relation changes by applying a different

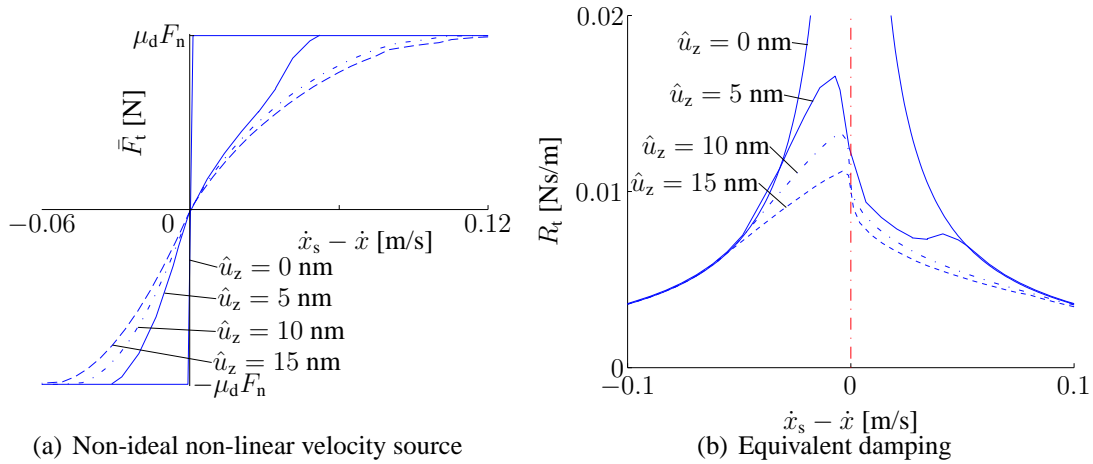


Figure 3.18: The equivalent damping/friction.

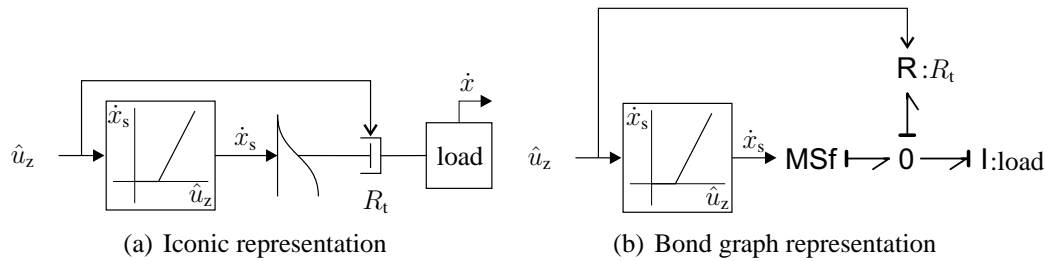


Figure 3.19: Total interpretation of the macroscopic behavior.

SAW frequency or a different so-called actuation method (section 4.2).

$$\bar{F}_t = \underbrace{R_t(\dot{x}_s - \dot{x}, \hat{u}_z)}_{\substack{\text{equivalent} \\ \text{non-linear damper}}} \times \underbrace{(\dot{x}_s - \dot{x})}_{\substack{\text{velocity} \\ \text{difference}}} \quad (3.20)$$

Figure 3.18(b) shows the equivalent damper values versus  $\dot{x}_s - \dot{x}$  for different wave amplitudes. The equivalent damper values are determined using the model in figure 3.12. We ‘measured’ the tangential average force for a fixed slider velocity  $\dot{x}$ . The damping values decrease for increasing wave amplitude. Figure 3.19 shows the total interpretation of the macroscopic behavior. Note that we have not derived a relation for both  $\dot{x}_s(\hat{u}_z)$  and  $R_t(\dot{x}_s - \dot{x}, \hat{u}_z)$ , i.e., we still need a contact model to compute the macroscopic behavior.

### Input power and efficiency

Figure 3.20 shows the first quadrant of the motor characteristic in which the output power (mechanical power) as a function of the slider velocity is drawn. The output power reaches its maximum value a little right of the ‘50 % no-force velocity’ - point.



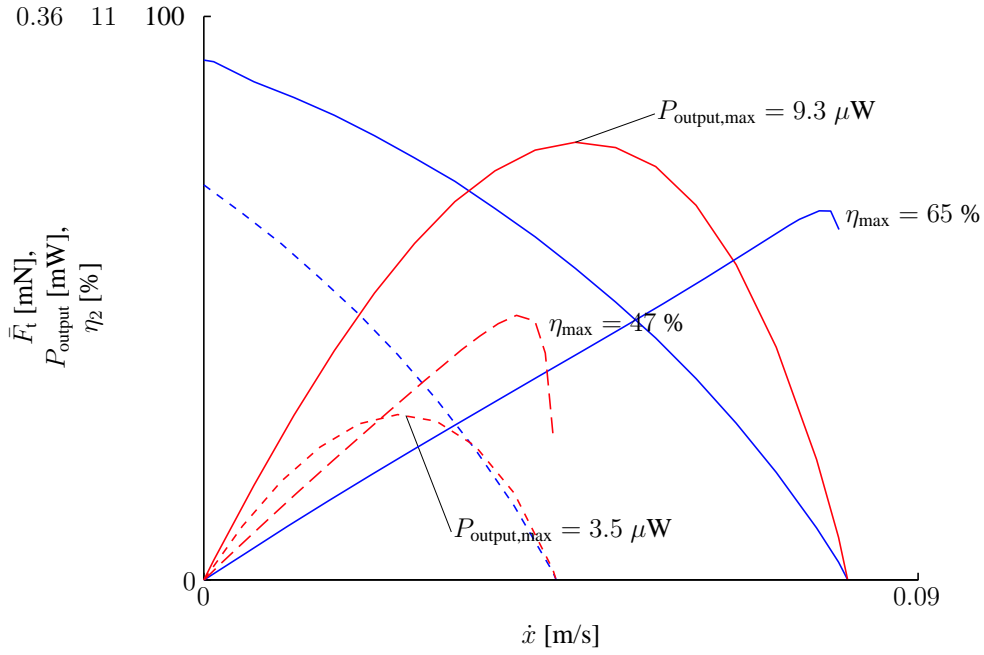


Figure 3.20: Output power  $P_{\text{output}}$  and efficiency  $\eta_2$ .

We will consider two definitions of the efficiency. It is reasonable to designate the power flow of the wave (section 2.2.1) as the input power. Accordingly, the input power is independent of the slider velocity such that the efficiency has the same shape as the output power.

$$\eta_1 = \frac{P_{\text{output}}}{P_{\text{wave}}} = \gamma P_{\text{output}} \quad (3.21)$$

where  $\gamma$  is a constant. An alternative –theoretical– way to determine the efficiency, is by utilizing a contact model. In the model we can probe the input power and the output power.

$$\eta_2 = \frac{P_{\text{output}}}{P_{\text{output}} + P_{\text{dissipated}}} \quad (3.22)$$

The corresponding efficiency  $\eta_2$  is shown in figure 3.20.

### 3.3 Modeling multiple points of contact

In the previous section, the behavior of an s-poc (single point of contact) was examined. This section discusses the behavioral consequences for m-poc (multiple points of contact). First, the ideal (theoretical) situation is discussed. The goal is to show the tendency of multiple projections on the motor behavior. Furthermore, the model is used to demonstrate that an m-poc model can be simplified to an s-poc like model. This model is valid

for a small number of projections only. Second, the anomalies of the actual situation are determined and discussed. Finally, additional parameters are introduced to account for the anomalies.

### 3.3.1 Ideal situation

In this section, it is demonstrated that the ideal (theoretical) m-poc behavior can be modeled by an s-poc model. The assumptions for the considered ideal situation are:

1. wave motion is not influenced by slider;
2. preload force is uniformly distributed over contacts;
3. stator surface is flat;
4. slider projections are identical;
5. projections are rigidly connected;
6. deformation of one point of contact is not influenced by the neighboring contact points;
7. only translation in normal and tangential direction is possible.

#### Example

With these assumptions, we first build an m-poc model and show the contact behavior. The model is illustrated for a slider with 3 spherical projection, i.e., 3 spherical projections. The slider is connected to a frictionless linear guiding to allow only motion in  $x$  direction (assumption 7). Figure 3.21 shows the normal impact model, which is actually a parallel connection of three s-poc models. It consists of a single slider mass  $m$  with air damping  $R_z$  driven by the normal vibration velocities via three compliant contacts  $k_n$ . The phase lag between the wave motions is  $2\pi/3$ . The tangential model is shown in figure 3.22. The mass  $m$  is driven in tangential direction by three sources. The interaction is via a compliant contact  $k_t$ , a small mass  $\Delta m$  and a friction sub-model  $R_c$ .

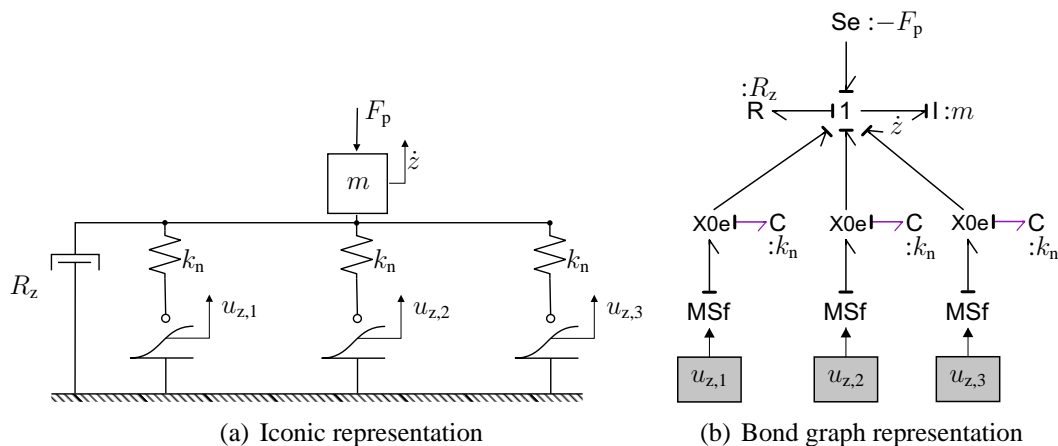


Figure 3.21: Normal impact model for three points of contact.

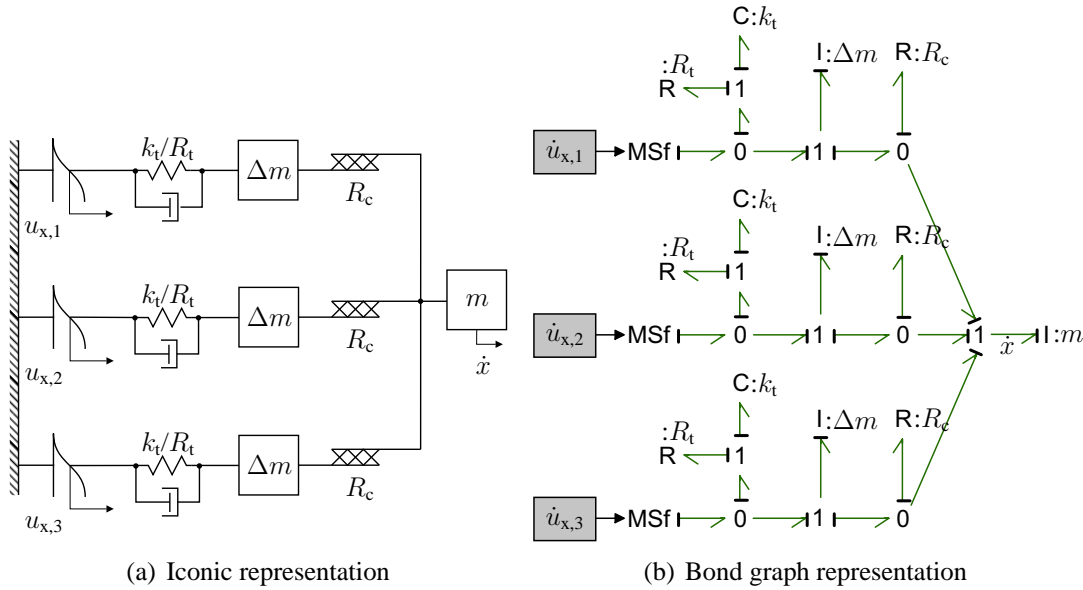


Figure 3.22: Tangential model for three points of contact.

Figure 3.23 shows the contact behavior of the m-poc model. Figure 3.23(a) shows the behavior during acceleration and figure 3.23(b) shows the behavior at steady state slider velocity. The simulation parameters are listed in table 3.3. The top plots show the normal slider displacement  $z$  and the three normal wave displacements. The second subplots show the normal force  $F_n$  of each projection and the sum of the three forces  $F_{n,sum}$ . The third subplots show the tangential wave velocities and the tangential slider velocity  $\dot{x}$ . The bottom plots show the tangential force  $F_t$  of each projection and the sum of these forces  $F_{t,sum}$ . The average normal force  $\bar{F}_{n,i}$  of each projection  $i \in \{1, 2, 3\}$  is the same. Therefore the total average force is  $\bar{F}_{n,sum} = 3\bar{F}_{n,i}$ . Furthermore, the average tangential force  $\bar{F}_{t,i}$  of each projection is the same as well. Therefore, the total tangential average force  $\bar{F}_{t,sum}$  is  $3\bar{F}_{t,i}$ . In figure 3.23(b)  $\bar{F}_{t,i} = 0$  because the slider velocity is at steady state.

The same results are obtained for an arbitrary number of projections  $p$ . We conclude that for the considered ideal situation with  $p$  projections and an unchanged preload force per projection

- the steady state velocity does not change;
- the average tangential slider force is  $p$  times greater.

### Model simplification

In this subsection, we demonstrate that an s-poc model can replace an m-poc model. The macroscopic behavior predicted by an equivalent s-poc suffices when we are not interested in the behavior of each individual projection. A simpler analysis and a reduction of computational load motivates the simplification. First, we will discuss the tangential motion and second the normal motion.

description	parameter	value	unit
Normal wave amplitude	$\hat{u}_z$	10	nm
Tangential/Normal amplitude ratio		0.65	-
Wave frequency	$f$	2.2	MHz
Young modulus slider	$E_1$	213	GPa
Young modulus stator	$E_2$	77	GPa
Poisson ratio slider	$\sigma_1$	0.3	-
Poisson ratio stator	$\sigma_2$	0.3	-
Radius sphere	$R$	1	mm
Mass of slider	$m$	0.6	g
Preload force	$F_p$	6	mN
Air damping	$R_z$	2	Ns/m
Coulomb coefficient of friction	$\mu_d$	0.18	-
Number of projections	$p$	3	-
Steepness of friction implementation	$slope$	5000	-
Mass of deformation	$\Delta m$	$10^{-15}$	kg
Compliant damping	$R_d$	$10^{-6}$	Ns/m

Table 3.3: Simulation parameters for an ideal multiple contact point slider.

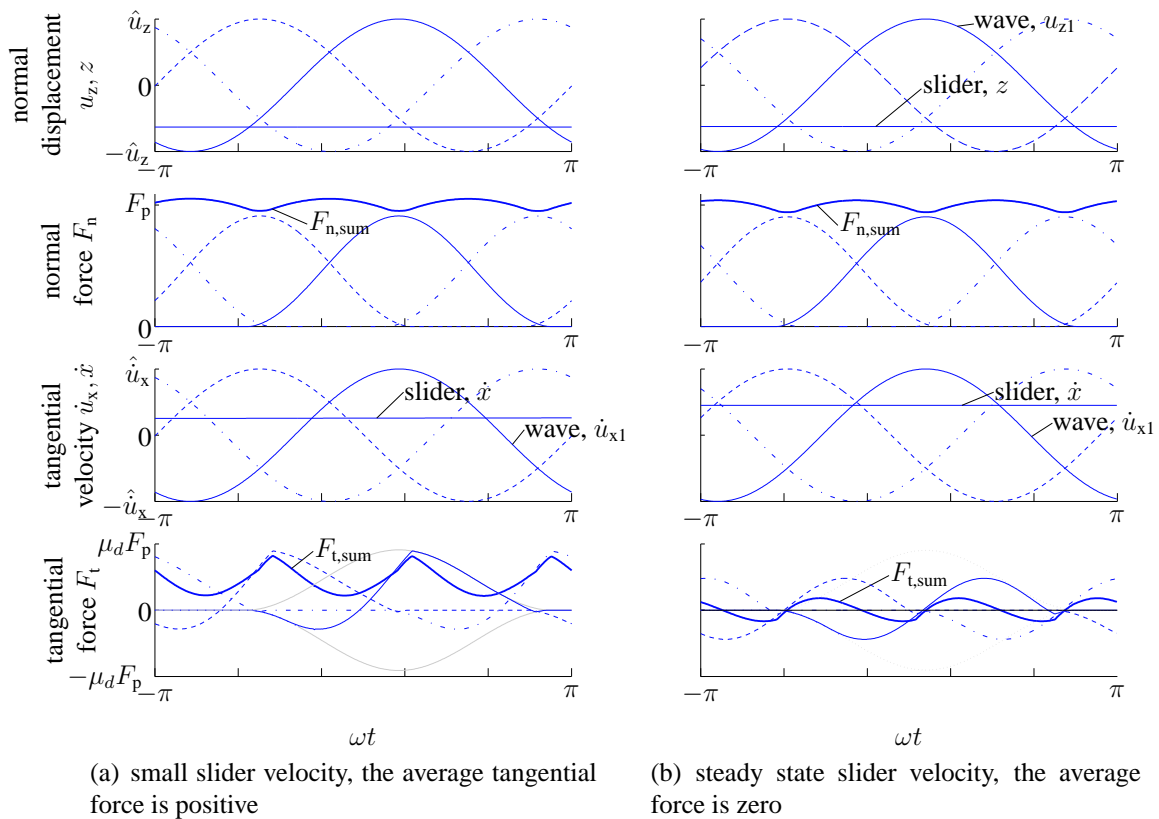


Figure 3.23: Contact behavior for 3 points of contact.

**Tangential motion** The tangential force, which acts on the slider mass (and any additional load) is

$$F_{t,\text{sum}} = \sum_{i=1}^p F_{t,i}$$

where  $p$  is the number of projections and  $F_{t,i}$  the tangential force of projection  $i$ . The wave period is very small relative to the tangential rise time, i.e., the contributed momentum of one projection per period of time is very small with respect to the total slider momentum. Hence, we may use the average force  $\bar{F}_{t,\text{sum}} = p\bar{F}_t$ . This implies that we may also use an equivalent force  $pF_t$ , where  $F_t$  is the tangential force of only one projection.

**Normal motion** Because the wave period is small compared to the normal rise time we may also use the average normal force

$$\begin{aligned} m\ddot{z} &= \bar{F}_{n,\text{sum}} - F_p - R_z\dot{z} \\ &= p\bar{F}_n - F_p - R_z\dot{z} \end{aligned}$$

This implies that an equivalent normal force  $pF_n$  may be used as well.

Therefore, we can compute the macroscopic behavior by using an s-poc model. We will refer to this simplified model as the ideal m-poc model.

### 3.3.2 Actual situation

A practical number of projections lies within the range 1000-40000. For such a large number of contact points the previously mentioned assumptions are not valid anymore. Accordingly, a discrepancy will exist between measurement and simulation. First, the anomalies are discussed. Next, two additional parameters are added to the model to account for the non-idealness.

#### Anomalies

**Wave motion** The wave amplitude varies along the slider length due to reflections against the slider projections. Figure 3.24 illustrates the decrease. The reflectivity is due to mass loading and due the elastic discontinuity (subsection 2.2.3). De Benedictis (2003) observed an increase in reflection with increasing preload force. Furthermore, measurements showed that a rather uniform wave amplitude pattern at the leading edge of the slider is changed to a rather chaotic and attenuated pattern at the trailing edge of the slider.

**Normal distribution** The preload force at each projection is not the same due to a number of reasons:

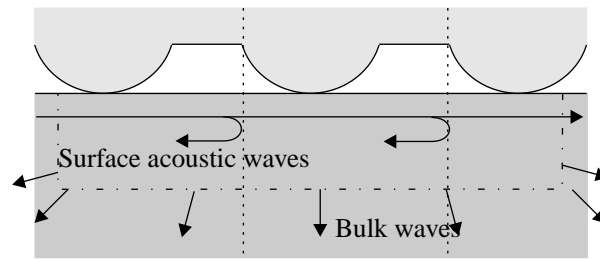


Figure 3.24: Reflection of Rayleigh wave against the slider.

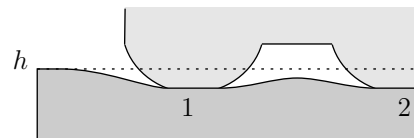


Figure 3.25: The indentation is influenced by a neighboring projection.

1. A slider is not uniformly loaded by the applied preload force, which produces stress and displacement in the slider. Consequently, the pressure at each projection is not uniform. See for example (Johnson 1994);
2. Not all the slider projections are identical. The difference in shape may arise from production tolerances and due to wear;
3. The stator surface is not perfectly flat due to production tolerances and due to wear.

**Mutual interference** Figure 3.25 shows an illustration of mutual interference of slider projections that are placed close to each other. The value  $h$  is the stator height without any loading. The stator material between projection 1 and 2 does not come back to the original height. Hence, in this situation the theory of Hertz is not valid anymore. (Further research is recommended to explore this phenomenon).

**Additional parameters** In the foregoing subsections we have discussed the differences between an ideal m-poc model and an actual motor. This discussion suggests the definition of at least two new parameters.

1. effective wave amplitude;
2. effective number of projections.

Anticipating section 3.5, figure 3.26 demonstrates (by simulation) that these two parameters form a kind of ‘basis’, e.g., an increase of the number of projections  $p$  and an increase of the wave amplitude results in two responses with the same steady state velocity but with a different slope. Therefore, by using these parameters together, we can change both the slope and the steady-state velocity. We assume that the ratio between the normal and tangential wave displacement remains the same. The new parameters have to be found experimentally.

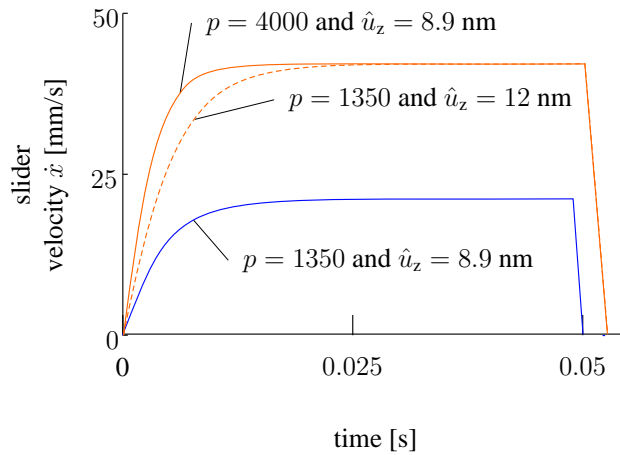


Figure 3.26: The number of projections  $\tilde{p}$  and the wave amplitude  $\hat{u}_z$  form a kind of ‘basis’.

## 3.4 Model implementation

### 3.4.1 Time change

The proposed model predicts the contact behavior of one wave period. As a consequence a large number of simulation steps are necessary to simulate the macroscopic response behavior. Therefore, the total computation time can be relatively large, particularly when the model complexity is high. We will demonstrate that the computation time can be decreased by using model knowledge.

The variation of the average forces ( $\bar{F}_n$  and  $\bar{F}_t$ ) within  $n$  periods is small. Therefore, it suffices to calculate the normal force and the tangential forces only once in  $n$  periods. To account for the remaining  $n - 1$  periods we need to multiply the tangential force with  $n$ , such that the tangential momentum (the integral of the tangential force) remains the same. Figure 3.27 illustrates this. The top plot shows the tangential force and the second plot shows the equivalent tangential force for  $n = 4$  periods. The second subplot indicates that we already know the momentum after 1 period of time. Therefore, the successive ‘active’ contact period can already be calculated. The bottom plot illustrates this. We may interpret this ‘trick’ as a ‘time/frequency change, which decreases the computation time significantly. The maximum allowed speed-up factor  $n$  for a certain accuracy has to be found by trial and error.

### 3.4.2 Hybrid modeling

In the previous subsection, we discussed a method to decrease the computation time. In this subsection we discuss the use of a hybrid model in order to further reduce the computation time. In fact, the proposed model is already hybrid because of the switching between contact and no-contact mode.

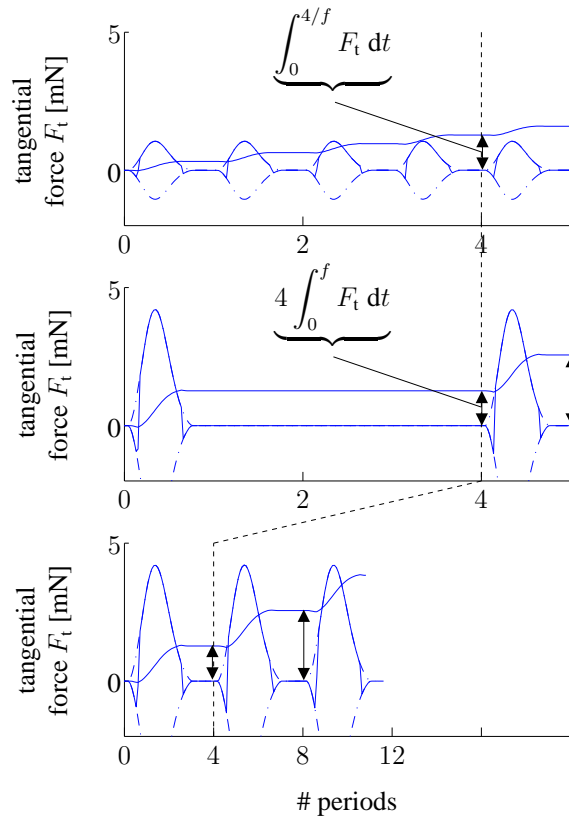


Figure 3.27: Illustration to speedup the simulation by a factor  $n = 4$ .

For the friction implementation we used a tanh-function to model the friction in a very simple and straightforward manner. This non-linear smooth function is utilized to build up the force to the breakaway level. However, due to the high differential resistance around the origin a stiff set of differential equations remains. A variable-step integration method deals rather efficiently with these kinds of models (Breedveld 2000). However, for a large number of crossings around this origin the total simulation time will increase by this implementation.

Hybrid modeling is a way to overcome a stiff set of differential equations; instead of a smooth transition we switch between discrete ‘modes’. Each mode has a behavior in the sense of Polderman & Willems (1998), which represent the continuous dynamics of the system. In our particular case, we distinguish three discrete modes. Figure 3.28 shows the hybrid automaton (Van der Schaft & Schumacher 2000).

The four discrete modes are:

- Init** The hybrid automaton starts at the initial discrete mode ‘Init’, where the wave amplitude and the slider velocity are zero. From the initial mode the automaton evolves to ‘stick’.
- Stick** The tangential stiffness determines the tangential force  $F_t$ . The sliding velocity  $v_t$  is set to zero. Hence, we omit the time-consuming friction submodel. A transition to ‘sliding’ takes place if  $|F_t| \geq |\mu_d F_n|$ .



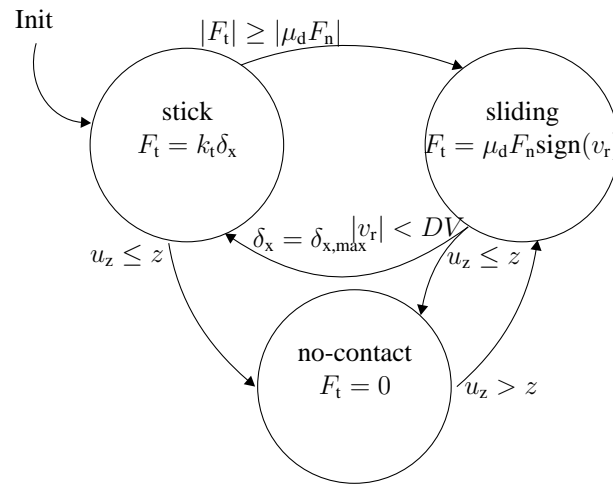


Figure 3.28: Hybrid automaton of the tangential model.

**Sliding** The tangential force is determined by the friction, where the sliding velocity  $v_r$  is  $\dot{u}_x - \dot{\delta}_{x,\max} - \dot{x}$ . Figure 3.29 illustrates the relation between the velocities. The presliding velocity  $\dot{\delta}_{x,\max}$  is due to a change in normal displacement. The contact evolves again to ‘sliding’ if  $|v_r| < DV$ , where  $DV$  represents an infinitesimal neighborhood around  $v_r = 0$  (Karnopp 1985). The reset  $\delta_x = \delta_{x,\max}$  explicitly resets the presliding displacement.

**No-contact** A transition from ‘stick’ or ‘sliding’ to the ‘no-contact’ mode takes place if  $u_z \leq z$ . The tangential force is zero. The transition from ‘no-contact’ is always to ‘slip’ and is enabled if  $u_z > z$ .

This hybrid model contains additional code for detection, switching and resetting of integrators, which requires extra time to implement. However, there is a net gain in computation time.

The total model, hybrid and with the ‘time change’, is implemented and simulated in 20-sim. For simulation we use the suitable ‘Vode Adams’ integration method. This is the explicit variable-step stiff integration algorithm of Cohen and Hindmarsh. This method is specially suited for explicit models that combine high and low frequency vibrations with little damping (20-sim 2003).

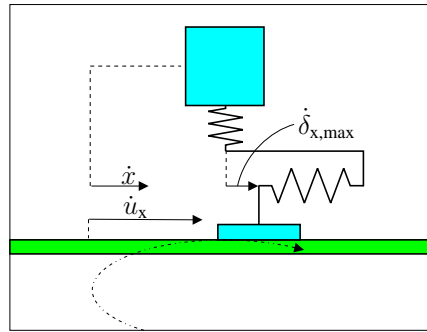


Figure 3.29: Velocities in tangential direction.

## 3.5 Model validation

In this section, we check the validity of the developed models by experiments performed with a 1 projection, a 3 projections and a multiple projections slider. The models that are validated are respectively the s-poc model, the ideal m-poc model and the actual (not-ideal) m-poc model.

### 3.5.1 Single point of contact (with tangential compliance)

In this subsection, the s-poc model of section 3.2 will be validated. Since we do not have the ability to perform an experiment with only one point of contact, an experiment from literature (Kurosawa et al. 1996) is taken. In this experiment a stator made of  $127.8^\circ$   $y$ -rotated  $x$ -propagating  $\text{LiNbO}_3$  (Lithium Niobate) is used, which is equipped with two IDT's with a driving frequency of 9.6 MHz, see figure 3.30. The slider consists of only one small steel ball, which is preloaded by means of a permanent Neodymium magnet placed at the back of the stator. The preload is changed by varying the spacer thickness between magnet and stator. Kurosawa et al. state that, due to the effect of the magnetization of the steel ball, the slider moved without rotation. Furthermore, the uniformity of the magnetic force was confirmed within the operational area of the motor.

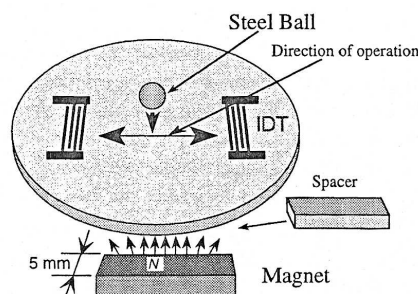


Figure 3.30: Experimental setup of Kurosawa et al.

Table 3.4 lists the model parameters. The wave amplitude is measured by means of a laser dopler vibrometer. The Young modulus of the steel ball and the stator and the Poisson ratio of the steel ball are taken directly from literature. Since  $\text{LiNbO}_3$  is anisotropic, an average value of the Poisson ratio was derived by [Asai & Kurosawa \(2004\)](#). The friction coefficient is measured by a tribo-meter and the slider mass is calculated from the ball radius and the mass density.

description	parameter	value	unit
Normal wave amplitude	$\hat{u}_z$	18.8	nm
Tangential/normal amplitude ratio	ratio	0.89	-
Wave frequency	$f$	9.6	MHz
Young modulus slider	$E_1$	210	GPa
Young modulus stator	$E_2$	172	GPa
Poisson ratio slider	$\sigma_1$	0.3	-
Poisson ratio stator	$\sigma_2$	0.27	-
Radius slider	$R$	0.5	mm
Mass of slider	$m$	4.13	mg
Preload force	$F_p$	{7.3, 3.7, 0.9}	mN
Air damping	$R_z$	2	Ns/m
Coulomb coefficient of friction	$\mu_d$	0.15	-
Transition stick-slip velocity	$DV$	0.005	m/s
Speed-up	n	200	

Table 3.4: Simulation parameters for figure 3.31.

Figure 3.31 shows the measured data (crosses) together with the simulated data (solid-lines). The slider is driven by a burst of waves and the velocity is measured by means of a high-speed camera. The variable  $F_p$  is the preload force. The increase in the acceleration/tangential force with increasing preload force is clearly visible in both experiment and simulation. Furthermore, the slopes during acceleration correspond well, in particular at the bottom plot. However, the simulated steady state velocity is larger than the experiment. For comparison, we also show the simulated responses for a wave amplitude of a factor 1.1 smaller (dashed-lines). The resemblance with the steady state velocity is better. The cause of the small differences between model and experiment is not clear. The wave motion could be influenced by the slider contact, which causes a smaller amplitude at the contact. The parameters are uncertain. Alternatively, the model structure inaccuracy could be the cause of the difference.

### 3.5.2 Ideal multiple points of contact

In this section, we compare the ideal m-poc model with the experimental -3 ball- slider. The experimental setup is described in section 1.5. In section 3.3.1, we have demonstrated that an s-poc model can approximate an ideal m-poc. If we study the assumptions, we recognize that the first assumption cannot a-priori be assumed: The wave motion is not influenced by slider contact. Indeed, we will see that a better result is obtained if the wave amplitude for simulation is chosen smaller than the measured wave amplitude (without slider). Furthermore, assumption 7 does not hold -only translation in tangential and normal direction is possible-, because the experimental -3 ball- slider can rotate as

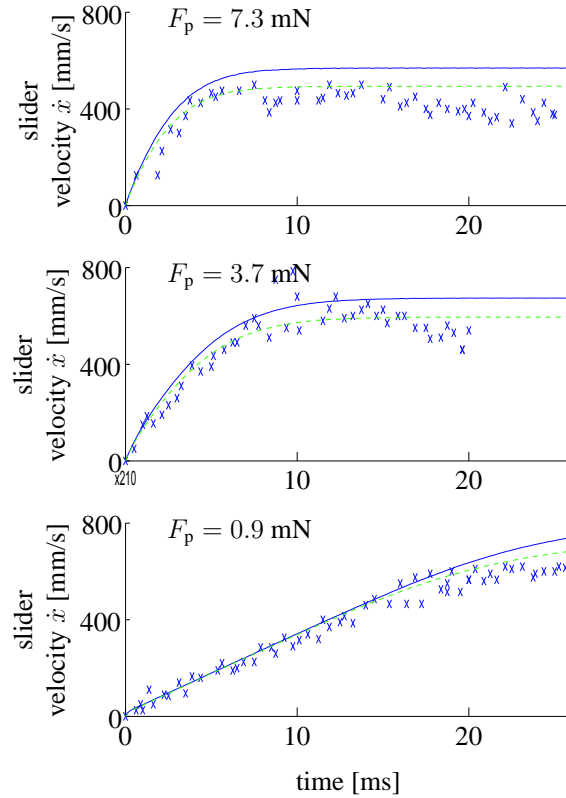


Figure 3.31: Experimental data taken from Kurosawa et. al. and simulation data obtained with the s-poc model. The wave amplitudes are  $\hat{u}_{z,\text{exp}} = 18.8$  nm (crosses),  $\hat{u}_{z,\text{sim}} = 18.8$  nm (solid-line) and  $\hat{u}_{z,\text{sim}} = 17.1$  nm (dashed line).

well. However, we minimized the change of rotation by setting the initial slider position symmetrical with respect to the wavefront (figure 3.32).

In the previous experiment, the stator was made of  $\text{LiNbO}_3$ , where in the next experiments the stator material is PZT. The simulation parameters listed in table 3.5 are found from literature and separate measurements. (The Young modulus of the stator corresponds to the value of poled PZT, because the value of unpoled PZT was not supplied). The vibrometer measures the slider velocity. Figure 3.33 shows the step responses for different wave amplitudes. We adapted the wave amplitude of the first plot in such a way that it coincides with the first part of the response. Approximately the same factor 1.1 is used to adapt the wave amplitude of the second and third plot. We see that the slopes and the

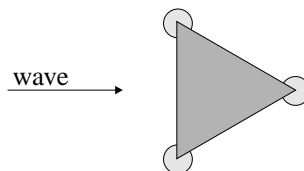


Figure 3.32: Initial position of experimental slider.

description	parameter	value	unit
Tangential/Normal amplitude	ratio	0.65	-
Wave frequency	$f$	2.2	MHz
Young modulus slider	$E_1$	210	GPa
Young modulus stator	$E_2$	77	GPa
Poisson ratio slider	$\sigma_1$	0.3	-
Poisson ratio stator	$\sigma_2$	0.3	-
Radius spheres	$R$	1	mm
Mass of slider	$m$	0.6	g
Preload force	$F_p$	6	mN
Air damping	$R_z$	2	Ns/m
Coulomb coefficient of friction	$\mu_d$	0.18	-
# projections	$p$	3	-
Transition stick-slip velocity	$DV$	0.005	m/s
Speed-up		200	

Table 3.5: Simulation parameters for figure 3.33.

steady state velocities fit reasonably well. The velocity variation of the slider is partly due to the rotation of the slider.

### 3.5.3 Actual multiple points of contact

In this experiment, the silicon slider is utilized in the experimental setup of section 1.5. The behavior of such an m-poc slider is not ideal and therefore the two proposed additional parameters;

- effective wave amplitude;
- effective number of contact points.

are used (section 3.3.2).

#### Step response

Table 3.6 lists the parameters. The coefficient of friction is found by a tribo-meter, the total preload force is measured, the contact point radius is found by curve fitting and the Young moduli and Poisson ratios are taken from literature. The two new parameters are found by curve fitting (by using the gradient search algorithm in 20-sim (2003)).

Consider figure 3.34. The slider velocity is measured directly at the slider by means of the vibrometer. The second plot is used to find the two additional parameters. For the remaining three plots only one parameter - the effective wave amplitude- is found. The ratio between the experimental and simulated wave amplitudes is for the first three plots 1.0 and for the last plot 1.1. The effective number of contact points  $\tilde{p}$  is 1350, which is much smaller than the real number of contact points (40000). The figure demonstrates that the ‘actual m-poc’ model behavior can be fit on the measured behavior by adapting both the wave amplitude and the number of projections.

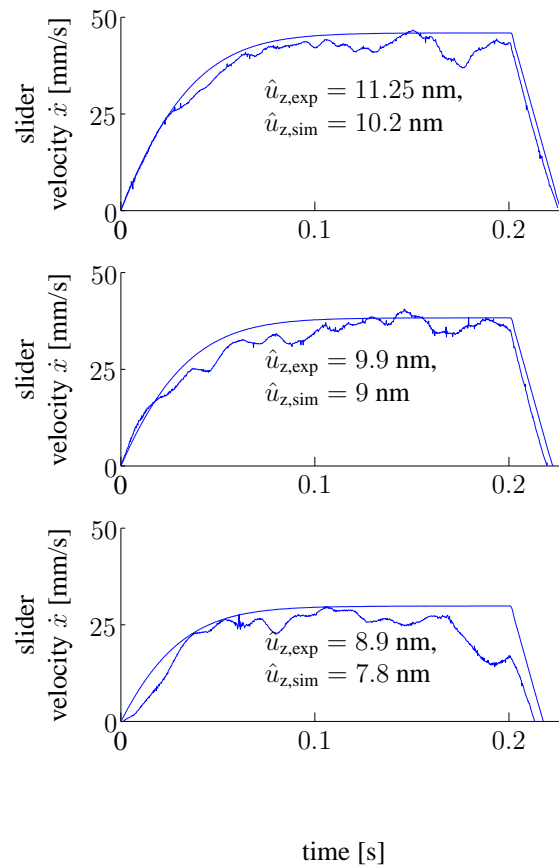


Figure 3.33: Validation of the ideal m-poc model by means of the experimental - 3 ball-slider.

Figure 3.34 also shows the slider velocity in case the wave amplitude becomes zero. Since the mass and preload force are known, the coefficient of friction can be calculated. The calculated coefficients equal the coefficients found by the tribo-meter. This implies that once the coefficient of friction is known we can determine the preload force by the braking velocity.

### Motor characteristic

In this experimental setup, the SAW motor was placed on a platform that could be tilted such that the load -the gravitational force- changes. (The slider is attached in a slightly different way with respect to previous experiment). The velocity is calculated from the encoder position measurement. Table 3.7 lists the simulation parameters. Figure 3.35 shows the motor characteristic of the experimental setup, in which the open circles are obtained by measurements. The effective number of contact points and the amplitude are found by curve fitting.

The ratios between the simulated and experimental wave amplitude for line b, c and d are respectively  $\{2.0, 1.8, 1.5\}$ . These ratios are large compared to the previous experiment. Also the number of effective contact points is larger  $1350 \rightarrow 6000$ . The differences

description	parameter	value	unit
Tangential/Normal amplitude	ratio	0.65	-
Wave frequency	$f$	2.2	MHz
Young modulus slider	$E_1$	107	GPa
Young modulus stator	$E_2$	77	GPa
Poisson ratio slider	$\sigma_1$	0.3	-
Poisson ratio stator	$\sigma_2$	0.3	-
Radius slider	$R$	5	mm
Mass of slider	$m$	106	g
Preload force	$F_p$	14	N
Air damping	$R_z$	2	Ns/m
Coulomb coefficient of friction	$\mu_d$	0.13	-
# projections	$p$	40000	-
Transition stick-slip velocity	$DV$	0.005	m/s
Speed-up	$n$	200	-
effective # projections	$\tilde{p}$	1350	-

Table 3.6: Simulation parameters for figure 3.34.

description	parameter	value	unit
Normal wave amplitude sim.	$\hat{u}_{z,sim}$	{7.5, 6.1, 4.6}	nm
Normal wave amplitude exp.	$\hat{u}_{z,exp}$	{11.4, 10.8, 9}	nm
Tangential/Normal amplitude	ratio	0.65	-
Wave frequency	$f$	2.2	MHz
Young modulus slider	$E_1$	107	GPa
Young modulus stator	$E_2$	77	GPa
Poisson ratio slider	$\sigma_1$	0.3	-
Poisson ratio stator	$\sigma_2$	0.3	-
Radius sphere	$R$	5	mm
Mass of slider	$m$	106	g
Preload force	$F_p$	10.7	N
Air damping	$R_z$	2	Ns/m
Coulomb coefficient of friction	$\mu_d$	0.13	-
# projections	$p$	40000	-
Transition stick-slip velocity	$DV$	0.005	m/s
effective # projections	$\tilde{p}$	6000	-

Table 3.7: Simulation parameters for figure 3.35.

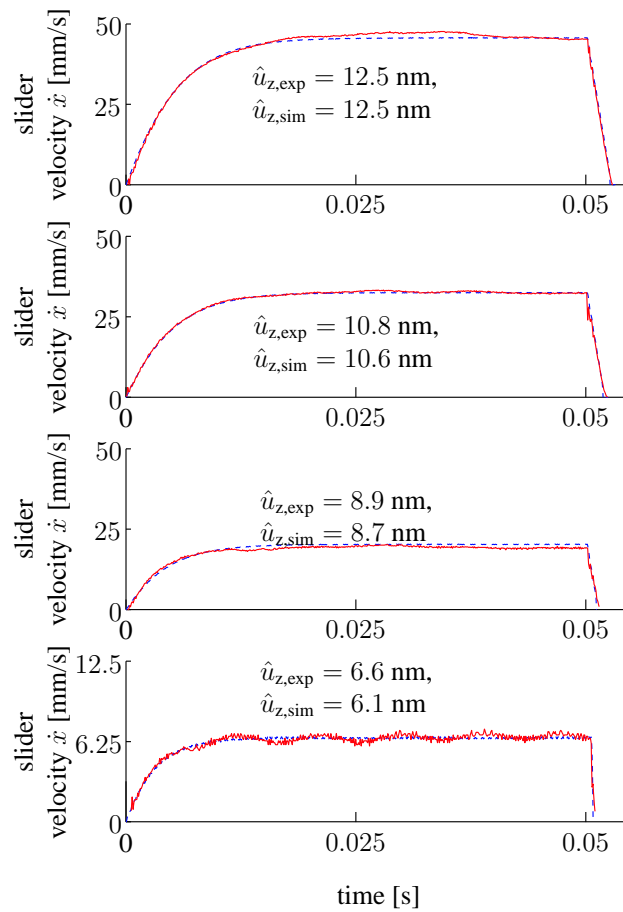


Figure 3.34: Experimental (solid-line) and simulation data (dashed-line) of a SAW motor with a silicon slider. Note that the scalin of the bottom subplot is different.

are explained by the slightly different slider attachment. Concluding we can say that the macroscopic behavior of the actual m-poc model can be fitted onto the measured macroscopic behavior by utilizing the two additional parameters.



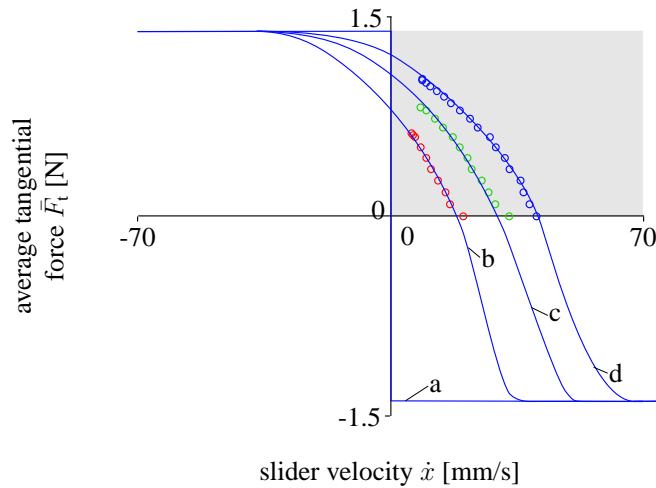


Figure 3.35: Motor characteristic of the experimental setup. The circles are found by measurements and the solid lines are found by simulation. The simulation wave amplitude for respectively line a, b, c and d are 0 4.6, 6.1 and 7.5 nm

### 3.5.4 Review

Table 3.8 shows an overview of the discussed validation experiments. The s-poc and the ideal m-poc models predicted the experiments quite well. The fit was better when the wave amplitude decreased approximately a factor 1.1. The actual m-poc model fitted the measured behavior well by the aid of two additional parameters. The ratio between the simulation and the experimental wave amplitude lies between the value 1 and 2. The ratio between the effective and the real number projections lies between the value 3 % and 15 %. A better fit of the m-poc model is probably possible by elaborating the mutual interference of the neighboring projections.

model	# projections	stator material	slider	adaptation
s-poc	1	LiNbO <sub>3</sub>	steel ball	wave amplitude
ideal m-poc	3	PZT	steel balls	wave amplitude
actual m-poc	multiple	PZT	Si slider	{ wave amplitude effective number of projections

Table 3.8: Overview of the validation experiments.

## 3.6 Variation of model parameters

This section is based on [Feenstra & Breedveld \(2004\)](#). In order to design a SAW motor with prescribed specifications (e.g., force-velocity relation) it is helpful to use design parameters. To get a first impression of the design parameters, the influence of parameter variations on the motor behavior is investigated by means of the s-poc model with tangential compliance. The material parameters that are varied, are the friction coefficient and the Young modulus of the stator. Besides material parameters, the influence of the

preload force is examined. In the past, some work has been performed to obtain ‘better’ specifications. For example, Hélin (1997) did an experiment with sliders with a variety of friction coefficients, Nakamura et al. (2003) investigated the hardness and Kurosawa et al. (1996) studied the influence of the contact point radius and the number of contact points. (The contact points in Kurosawa’s study had a cylindrical shape and the definition of radius is therefore different). However, in practice there is always interdependency between parameters, whereas the use of a model has the advantage that parameters can be varied independently. Furthermore, non-measurable behavior can be examined and unrealistic parameter values can be used to find tendencies or to improve understanding.

### 3.6.1 Coefficient of friction

The nominal parameters are listed in table 3.2. First, we study the influence of the coefficient of friction on the no-force velocity. Figure 3.36(a) shows the relation for three different wave amplitudes. Two limiting situations are considered. If the coefficient of friction approaches zero, the influence of the tangential stiffness becomes negligibly small. Accordingly, the velocity increases to a value that corresponds with the rigid tangential model of figure 3.7 (where the coefficient of friction does not influence the no-force slider velocity). If the coefficient of friction approaches infinity, the tangential stiffness will dominate. For a *continuous contact amplitude*,  $\hat{u}_z = 4$  nm, (see page 61) the slider velocity becomes zero because the slider sticks to the stator. For an *intermittent contact amplitude*,  $\hat{u}_z = 8$  nm and 12.5 nm, the velocity approaches a constant value. The contact sticks during contact.

Figure 3.36(b) shows the tangential average force. Clearly, if  $\mu_d$  approaches zero, the force becomes zero. If the coefficient of friction approaches infinity, the average force for *continuous contact amplitude* becomes zero and for *intermittent contact amplitude* it approaches a constant value. Hence, a high coefficient of friction is beneficial to obtain a large force at an *intermittent contact amplitude*.

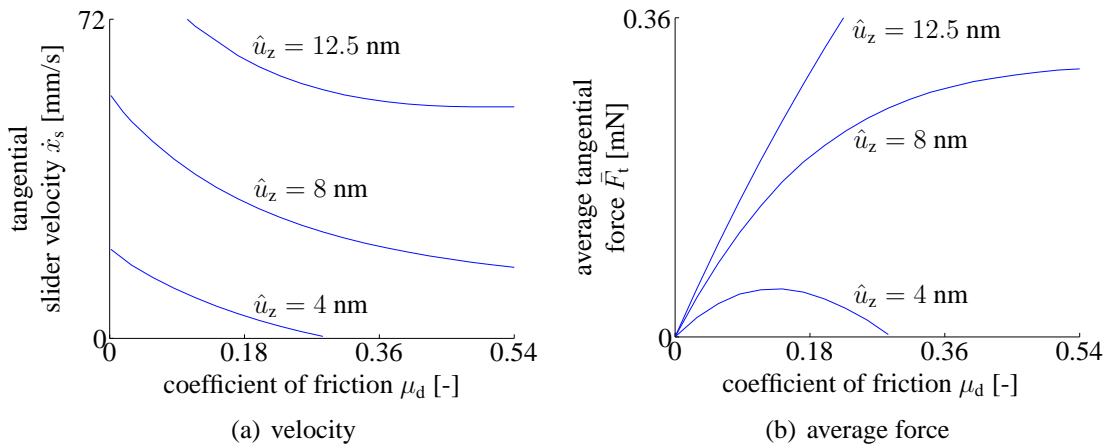


Figure 3.36: Velocity and average force as function of the coefficient of friction.

### 3.6.2 Young modulus stator

Figure 3.37 shows the influence of the stator its Young modulus  $E_2$  on the motor behavior. Again we consider two limiting situations. Parameter  $E_2$  becomes dominant with respect to the slider Young modulus  $E_1$  if it approaches zero. Consequently, the normal and tangential contact stiffness decrease. The contact becomes *continuous* for all wave amplitudes because the normal slider displacement  $z$  decreases. Furthermore, the contact sticks such that the tangential slider velocity and the average tangential force become zero. If  $E_2$  approaches infinity, the influence of the modulus becomes negligibly small. The elastic behavior is determined by  $E_1$ . Hence, the velocity and force approach a constant value.

Therefore, a stator *and* a slider with a high stiffness (Young modulus) is advantageous to obtain a high velocity, a large force and thereby a larger motor efficiency. Apart from increasing the stiffness by the Young modulus, the projection geometry can be adapted or the number of projections can be increased. The increase in velocity and force by increasing the number of projections is demonstrated by Kurosawa et al. (2001).

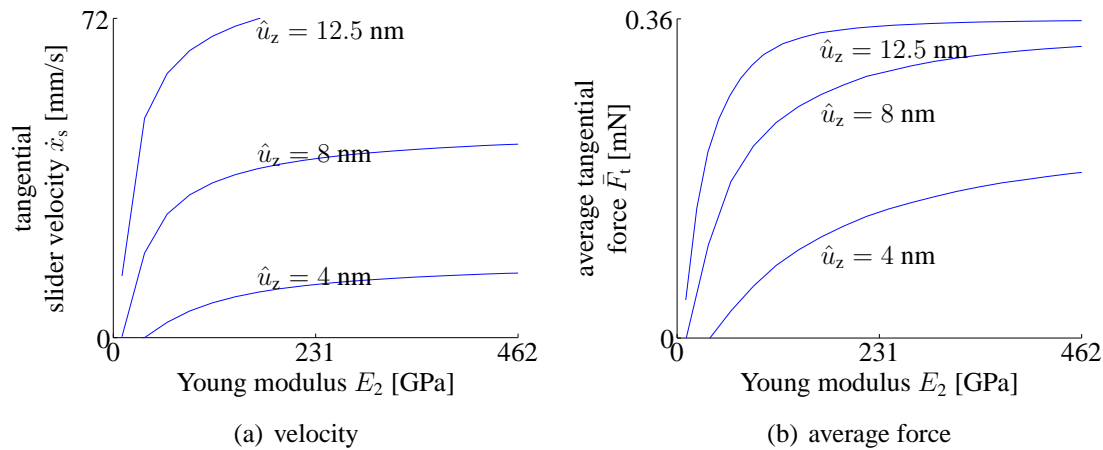


Figure 3.37: Velocity and average force as a function of the Young modulus of the stator.

### 3.6.3 Preload force

Figure 3.38(a) shows the slider velocity as a function of the preload force  $F_p$ . The preload force is the sum of the gravitational force and an additional applied external force. Consider a preload force that approaches zero. Consequently, the normal slider displacement approaches the wave amplitude, i.e.,  $\lim_{F_p \rightarrow 0} z = \hat{u}_z$ . The contact becomes intermittent for all wave amplitudes and the slider velocity approaches the tangential wave velocity amplitude  $\hat{u}_x$ . If the preload force increases, the opposite happens. The normal slider displacement  $z$  decreases and the contact becomes continuous and sticks. Hence the velocity approaches zero.

Figure 3.38(b) shows the tangential average force  $\bar{F}_t$  versus the preload force  $F_p$ . Clearly, the force  $\bar{F}_t$  approaches zero for a decreasing preload force. For an increasing preload

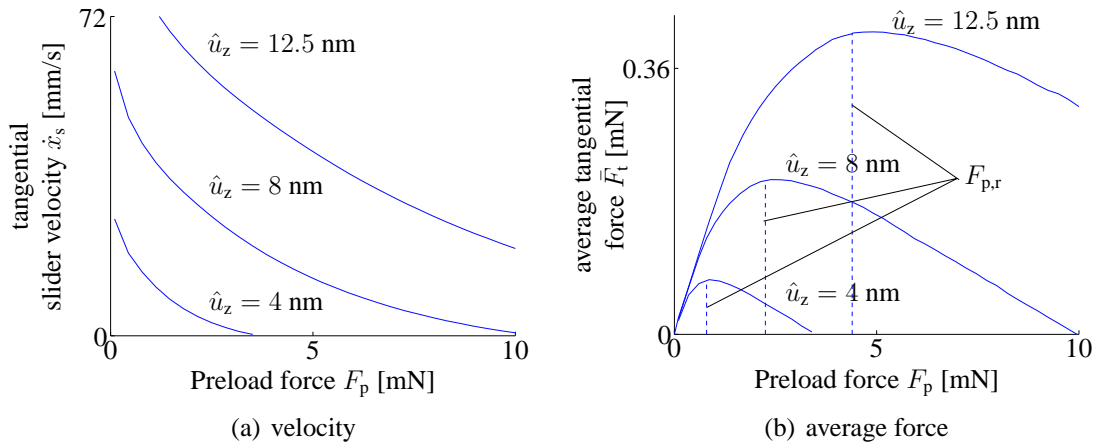


Figure 3.38: Velocity and average force as function of the preload force.

force, a similar explanation holds as for the slider velocity. The contact is or becomes continuous and sticks. In between those limits, there exists a point of maximum tangential force. (Kurosawa et al. (2001) have measured the same qualitative behavior for cylindrical contact points). It is not possible to find an analytical solution for the ‘optimal preload force’, however we can find an approximation. Equation 3.11 defines the release amplitude  $\hat{u}_{z,r}$ ; the amplitude at the transition point from continuous to intermittent contact. By rewriting we find the ‘release preload force’

$$\hat{u}_{z,r} = \left( \frac{3 \pi F_p \sqrt{2}}{16 k_n} \right)^{2/3} \Rightarrow F_{p,r} = \hat{u}_z^{3/2} \frac{16 k_n}{3 \pi \sqrt{2}} \quad (3.23)$$

where  $k_n$  is the normal stiffness. Figure 3.38(b) demonstrates that this ‘release-preload force’ approximates the preload force for a maximum tangential force. In chapter 5 we use this approximation.

### 3.7 Conclusions

The main purpose of this chapter was to analyze the principle of motion of a surface acoustic wave motor. To this end, contact models of a SAW motor have been built in order to describe the principle of operation, explain inherent SAW motor features and for finding design parameters. It has been shown that

1. the wave motion may be interpreted as an elastic body that is driven by two displacement sources;
2. the variation in the normal slider displacement and the tangential slider velocity per wave period is very small;

3. the rise time of the normal displacement is significantly smaller than the rise time of the tangential velocity, therefore the response of the normal motion is not observable in the tangential motion;
4. the driving wave amplitude can be categorized in one of three regions.
  - In the dead-zone region the wave amplitude is small. The slider does not move because the slider and the stator continuously stick.
  - In the continuous region, the wave amplitude is larger than the dead-zone amplitude and therefore the contact will slide and stick. The slider moves.
  - If the wave amplitude is larger than the threshold amplitude the contact will become intermittent. The ‘modes’ are stick, slide and no-contact.
5. the SAW motor its macroscopic behavior can be interpreted as a velocity source in series connection with a equivalent damper;
6. the macroscopic behavior of an ideal multiple point of contact (m-poc) model is exactly predicted by a single point of contact (s-poc) model;
7. for an *ideal* slider with  $p$  projections and a preload force of  $F_{p,slider} = p \times F_{p,projection}$ , the steady state slider velocity does not depend on the number of projections and the average tangential slider force will be linearly proportional to the number of projections;
8. an actual motor has some anomalies relative to an ideal m-poc model. Among other things,
  - the wave motion decreases along the slider length;
  - the normal force is not uniformly distributed over the contact surface;
  - the deformation at one point of contact is influenced by neighboring points.

However, by introducing two additional parameters the experimental responses can be fitted.

Data from literature and data acquired with the described experimental setup has been utilized to validate the different models.

1. The s-poc model predicted reasonably accurately the step response behavior of a steel ball on a  $\text{LiNbO}_3$  stator. The result became better if a smaller wave amplitude (of the simulation) was chosen.
2. In a second experiment the experimental 3-ball slider has been considered. The stator is made of PZT, which is less stiff than  $\text{LiNbO}_3$ . The ideal m-poc model predicted the measured step behavior rather well. The resemblance improved by decreasing again the wave amplitude of the simulation.
3. In the third experiment a silicon slider was used. The ‘actual m-poc’ model could be fit on the measured behavior by adapting both the wave amplitude and the number of projections.

To get a first impression of the design parameters, the influence of parameter variations on the motor behavior has been investigated. The results are

1. A high coefficient of friction is beneficial to obtain a large force at an *intermittent contact amplitude*.
2. A high stiffness (Young modulus) of both stator and slider is advantageous to obtain a high velocity, a large force and thereby a higher motor efficiency. Apart from increasing the stiffness by the Young modulus, the projection geometry can be adapted or the number of projections can be increased.
3. There is an optimum preload force for the average tangential force, which is approximated by the so-called release preload force.

# Chapter 4

## Actuation and control

*Overview: This chapter investigates the actuation and closed-loop control of a SAW motor. First, a linear time invariant mechanical model is derived. Next, the disturbance sources of the SAW motor are discussed. Hereafter, different strategies to actuate the motor are examined. For one actuation strategy a controller is designed and tested for different trajectories on the experimental setup.*

### 4.1 System

In the previous chapter, we have modeled the intrinsic SAW-motor behavior. Direct measurements of the slider velocity –by means of a vibrometer– were used to validate the dynamic behavior of these models. For closed-loop control of the experimental SAW-motor we utilize a displacement encoder (section 1.5). The encoder ruler is connected via the guiding to the slider. The introduced additional dynamics have a negative influence on the closed-loop behavior. Therefore, we analyze the guiding dynamics for reason of controller design and to discuss improvements of the guiding. Finally, disturbances of the SAW motor are examined in order to gain insight and discuss approaches to prevent or eliminate these disturbances.

#### 4.1.1 Mechanical model

In this subsection, we derive a mechanical model in which we include the first vibration mode of the slider guiding. This first vibration mode is the  $Rz$  mode (figure 4.1(a)). Figure 4.1(b) shows an ideal physical model of the considered problem. The center of rotation is in the center of gravity (cog). The  $Rz$  mode is excited since the point of actuation of the slider  $x_m$  does not correspond to this cog. The encoder ruler is attached to one side of the slider guiding. The other side of the slider guiding is connected via bearings to the slider axis. The connection to the slider axis is compliant and enables the guiding to rotate. The angle of rotation is small, which allows simplification of the model.

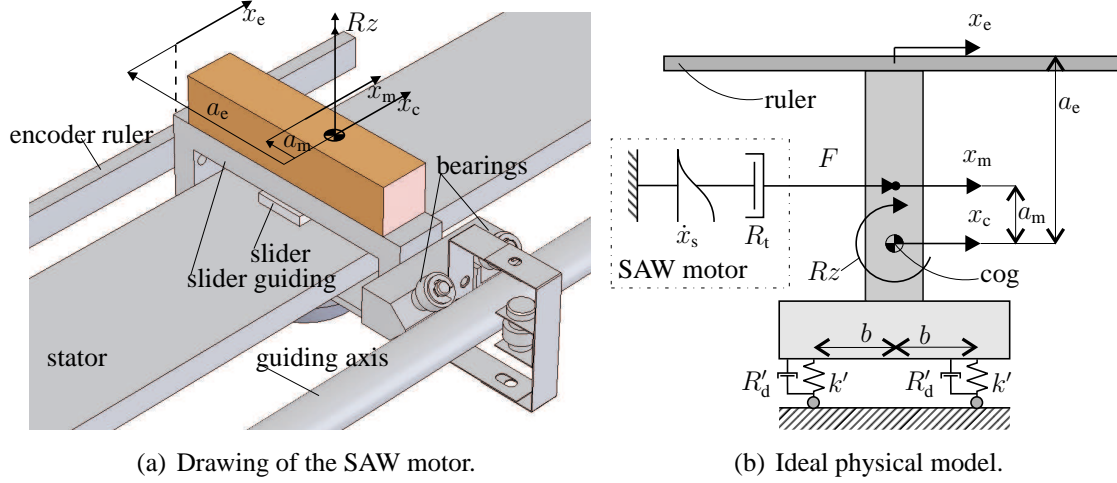


Figure 4.1: Slider guiding.

We have shown that the intrinsic SAW motor model may be interpreted as a series connection of a velocity source  $\dot{x}_s$  and a non-linear equivalent damper  $R_t$  (section 3.2.4). Furthermore, a linear-time-invariant (LTI) mechanical model is required to allow simple controller design in the frequency-domain and the complex-plane. Therefore, we assume that this equivalent damper  $R_t$  is linear. Due to this rough approximation we may expect differences between model behavior and actual behavior. Furthermore, we assume a linear compliant-damping  $R_d = 2b^2R'_d$  and a linear stiffness  $k = 2b^2k'$ . Figure 4.2 shows an iconic and a bond graph representation of the model. The encoder displacement is  $x_e = \int(\dot{x}_c + a_e\dot{R}z)dt$ . The transfer functions from  $\dot{x}_s$  to  $\dot{x}_c$  and from  $\dot{x}_s$  to  $\dot{R}z$  are respectively

$$\begin{aligned} H_{\dot{x}_s \rightarrow \dot{x}_c}(s) &= \frac{R_t(s^2J + sR_d + k)}{s^3mJ + s^2(mR_d + a_m^2mR_t + JR_t) + s(mk + R_tR_d) + kR_t} \\ H_{\dot{x}_s \rightarrow \dot{R}z}(s) &= \frac{a_m m R_t}{s^3mJ + s^2(mR_d + a_m^2mR_t + JR_t) + s(mk + R_tR_d) + kR_t} \end{aligned} \quad (4.1)$$

and the fourth order transfer function from the velocity source  $\dot{x}_s$  to the encoder displacement  $x_e$  is

$$\begin{aligned} H_{\dot{x}_s \rightarrow x_e}(s) &= \frac{1}{s}H_{\dot{x}_s \rightarrow \dot{x}_c}(s) + a_e \frac{1}{s}H_{\dot{x}_s \rightarrow \dot{R}z}(s) \\ &= \frac{R_t(s^2J + s(R_d + a_e a_m m) + k)}{s(s^3mJ + s^2(mR_d + a_m^2mR_t + JR_t) + s(mk + R_tR_d) + kR_t)} \end{aligned} \quad (4.2)$$

### Parameter estimation

In this subsection we estimate the parameters of the transfer function given by equation 4.2. The mass  $m = 0.1$  kg and the length  $a_e = 33$  mm are measured. The inertia



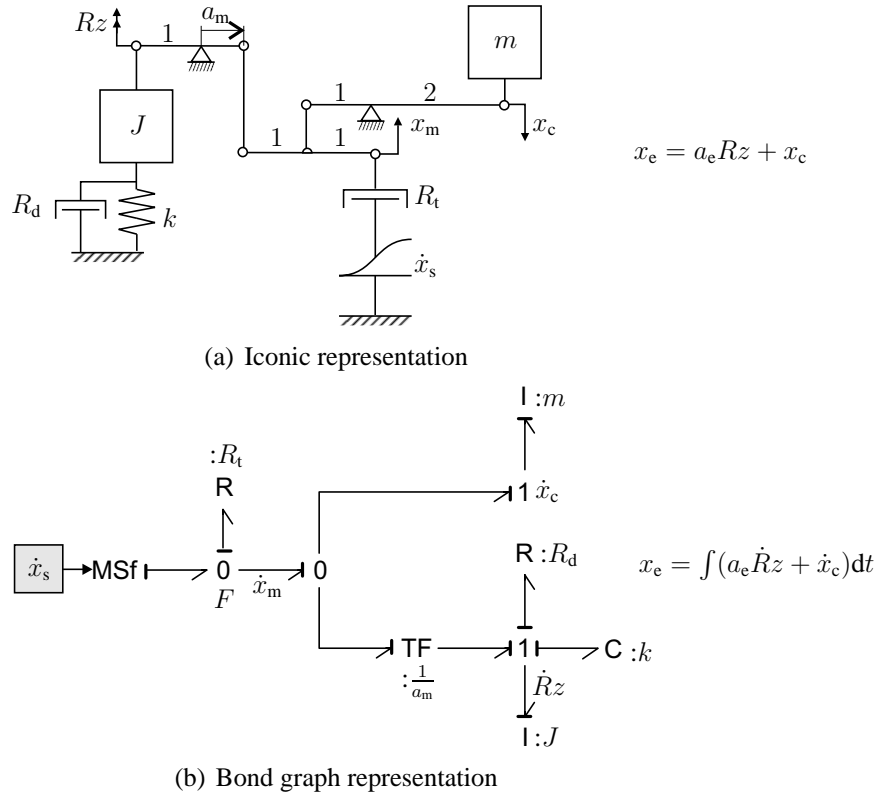


Figure 4.2: Mechanical model.

$J = 2.7 \cdot 10^{-5} \text{ kg m}^2$  and the length  $a_m = 0.7 \text{ mm}$  are calculated with the help of Solidworks (Solidworks corporation 2004). We estimate the remaining parameters by step response identification. Figure 4.3 shows the velocity  $\dot{x}_e$ , which is derived from the measured displacement and filtered by a 4th order low pass butterworth filter with a cutoff frequency of 2000 Hz. The noise superimposed on the signal is caused by the stator roughness to be elaborated in subsection 4.1.2. The equivalent damper  $R_t$  is found by the dominant step response behavior, which is described by equation 4.2 if the guiding stiffness  $k$  approaches infinity.

$$\begin{aligned}
 \tilde{H}_{\dot{x}_s \rightarrow \dot{x}_e} &= \lim_{k \rightarrow \infty} sH_{\dot{x}_s \rightarrow \dot{x}_e} \\
 &= \frac{R_t}{sm + R_t} \Rightarrow \\
 \ddot{x}_e \frac{m}{R_t} + \dot{x}_e &= \dot{x}_s \Rightarrow \\
 \dot{x}_e &= \dot{x}_s \left(1 - e^{-\frac{R_t}{m}t}\right)
 \end{aligned} \tag{4.3}$$

The resulting behavior corresponds with the linearized intrinsic SAW motor behavior, i.e., a series connection of a velocity source  $\dot{x}_s$ , a damper  $R_t$  and a mass  $m$ . The damper value  $R_t = 19$  is found by fitting the solution equation 4.3 to the rising slopes of figure 4.3. The  $Rz$  vibration mode is visible for time  $t > 0.08 \text{ s}$ . An inset of figure 4.3 shows a detail of the vibration. The frequency is 130 Hz. We estimate stiffness  $k = 18$  by using this

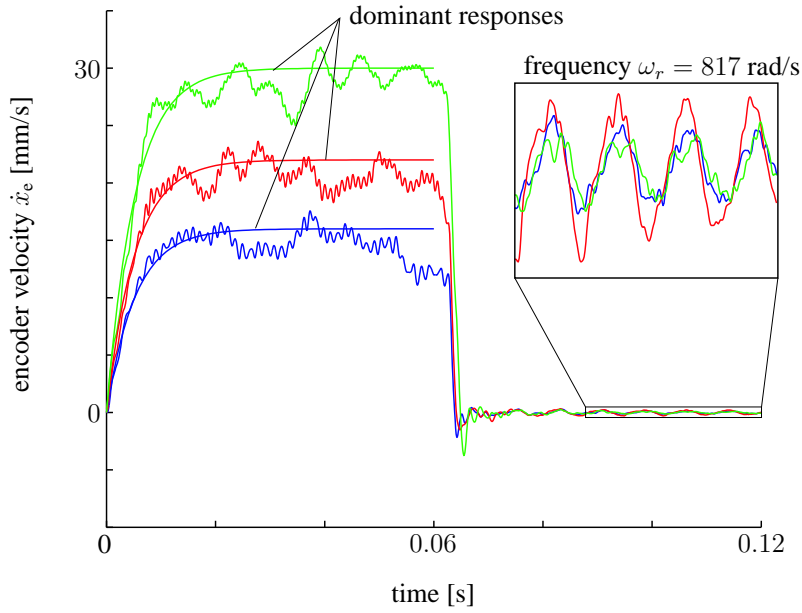


Figure 4.3: Parameter identification.

name	parameter	value	unit
equivalent motor damping	$R_t$	19	Ns/m
motor mass	$m$	0.1	kg
motor inertia	$J$	$2.7 \cdot 10^{-5}$	kg m <sup>2</sup>
stiffness	$k$	18	Nm
damping	$R_d$	0.001	N m s
length	$a_f$	0.7	mm
length	$a_e$	33	mm

Table 4.1: Parameters of the LTI mechanical model.

resonance frequency and the relation for the resonance frequency

$$\omega_r \approx \sqrt{\frac{k}{J}} \quad (4.4)$$

Finally, the damping  $R_d = 0.001$  is estimated from the attenuation of the resonance (figure 4.3). Table 4.1 lists all the parameters.

Figure 4.4 shows different representations of the mechanical model. The bode plot of figure 4.4(a) shows the transfer function from the velocity source  $\dot{x}_s$  to the encoder displacement  $x_e$ . The transfer from  $\dot{x}_s$  to  $x_e$  is fourth order. The slope of the modulus is  $-20$  dB per decade for frequencies lower than  $\omega = \frac{R_t}{m}$  and  $-40$  dB otherwise. The resonance frequency of the  $Rz$ -mode is denoted by  $\omega_r$ . Figure 4.4(b) shows the pole zero mapping of the system. There are 4 poles and two zeros. The step response of the encoder velocity is shown in figure 4.5. As expected, there is a considerable deviation during braking due the assumption that  $R_t$  is linear. We utilize this mechanical model in section 4.4.

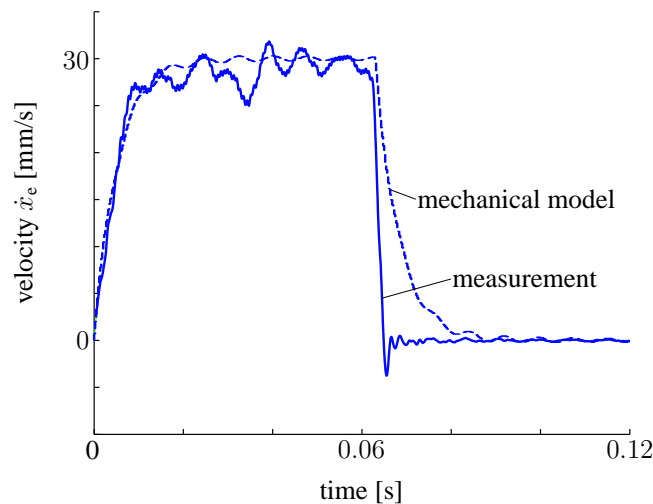


Figure 4.5: Step response: from input velocity to encoder velocity  $\dot{x}_s \rightarrow \dot{x}_e$ .

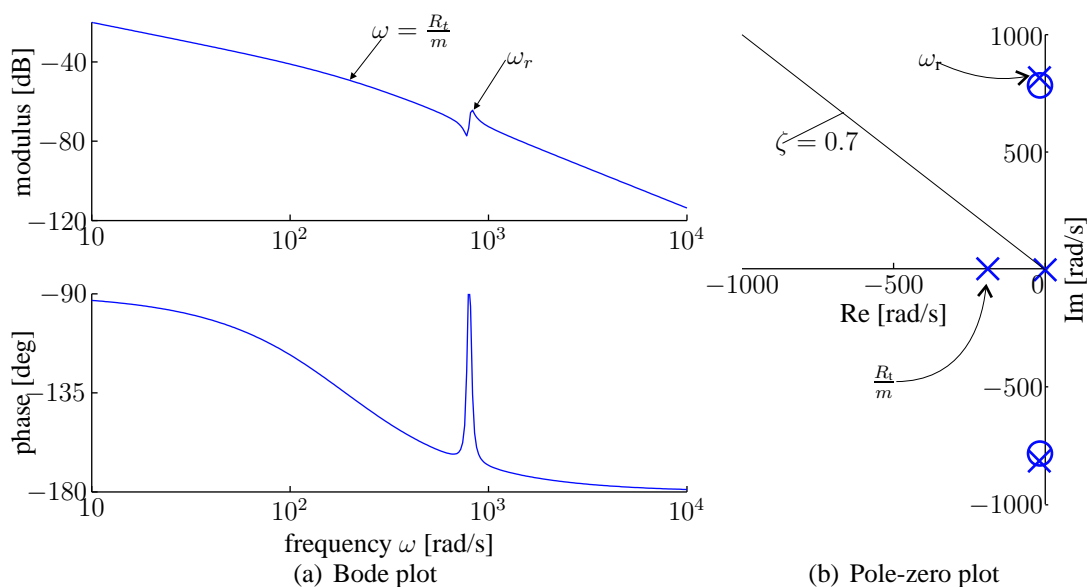


Figure 4.4: Different representations of the system: from input velocity to encoder displacement  $\dot{x}_s \rightarrow x_e$ .

**Improvements** The vibration modes of a system often limit the closed-loop bandwidth. Shifting of the resonance frequencies to a higher value can therefore be beneficial. The resonance frequencies introduced by the slider guiding can be increased by

- reducing the mass and inertia of the moving part, for example  $J$  in equation 4.4;
- increasing the stiffness of the guiding, for example  $k$  in equation 4.4;
- coincide the cog of the moving part with the point of actuation (interface between slider and stator);

- measuring at the center of mass, for example  $a_e = 0$  in equation 4.4.

We will continue this discussion in chapter 5.

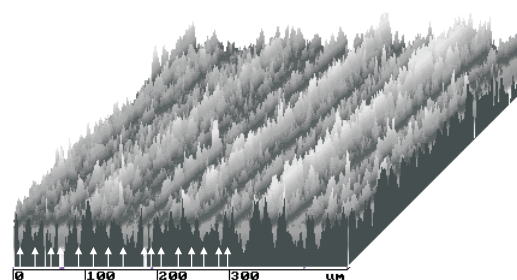
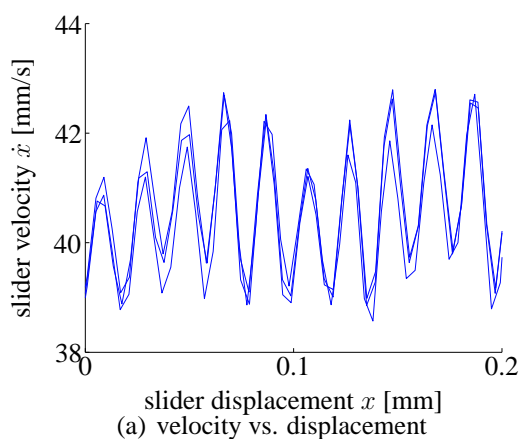
### 4.1.2 System disturbances

The motor behavior is affected by different sources of disturbance. We examine these sources for controller and actuation design and to discuss improvements in the motor design. In chapter 2 we have shown that the wave amplitude at the stator surface is not uniform due to

1. attenuation (section 2.2.3);
2. diffraction (section 2.2.2);
3. reflection (section 2.2.3);
4. beating (section 2.1.4).

Another source of disturbance is the friction force of the slider guiding. Furthermore, the contact interface between slider and stator plays an important role in the SAW motor behavior. We elaborate the sources that disturb the contact interface.

**Stator roughness** In figure 4.3 the stator roughness is clearly visible as a high frequency disturbance superimposed on the dominant response. This disturbance is position dependent as shown in figure 4.6(a). This figure shows the slider velocity as a function of the slider displacement for three repetitions. The dominating spatial frequency is  $20 \mu m$ . Figure 4.6(b) shows the stator relief. The direction of the slider motion is perpendicular to the grooves. The arrows indicate the grooves and the average distance between the arrows is indeed  $\Delta x \approx 300/15 = 20 \mu m$ .



(b) Stator surface, where the arrows indicate the grooves. The motion direction is perpendicular to these grooves.

Figure 4.6: The periodicity of the stator surface.

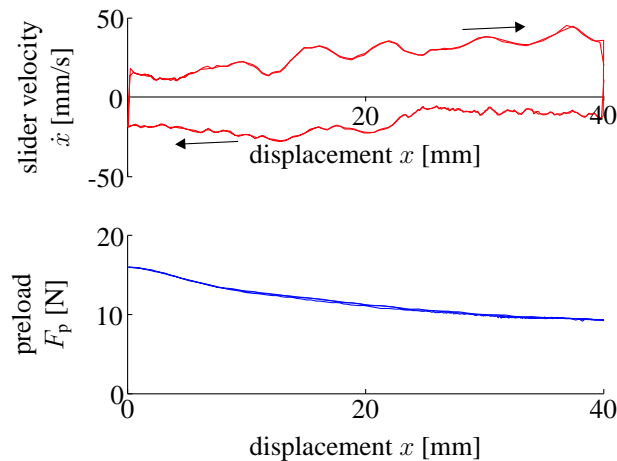


Figure 4.7: The slider velocity and the preload force as a function of the slider displacement.

**Variation of the preload force** Figure 4.7 shows the slider velocity as a function of the slider displacement for 2 experiments. Note that the displacement range is larger than the range of figure 4.6(a). The overlaying responses demonstrate that the variations in velocity are indeed position dependent. The bottom plot shows the preload force, which becomes smaller when moving in  $x$ -direction. In section 3.6 we have demonstrated that the slider velocity increases when the preload decreases. Hence, when moving in  $x$ -direction, the preload force, the attenuation and the diffraction contribute all to an increase of the slider velocity. In the opposite direction the effects do not add up, i.e., the preload force decreases, which reduces the slider velocity and the decrease of attenuation and diffraction increases the wave velocity.

**Variation of the coefficient of friction** The SAW motor is driven by friction. The motor behavior is therefore disturbed by variation of the coefficient of friction due to:

1. slider and stator conditions (contamination, scratches, wear);
2. ambient conditions (humidity, temperature, etc.);
3. Rayleigh wave (amplitude, shape of the wave envelope, frequency of the wave envelope etc.).

The first two items are rather obvious. The third item is predominantly due to the increase of the coefficient of static friction  $\mu_{st}$  with time (Armstrong-Hélouvy et al. 1994), i.e., the value  $\mu_{st}$  depends on the history.

We assume that the deviations in the wave amplitude, guiding friction and stator roughness can be modeled as input disturbances. The variation of the preload force is disregarded, because we mainly consider small displacements ranges. The variation of the coefficient of friction is reduced by cleaning the SAW motor on a regular basis, by working in an environment with a low humidity and by applying so-called PWM actuation (section 4.2.4).

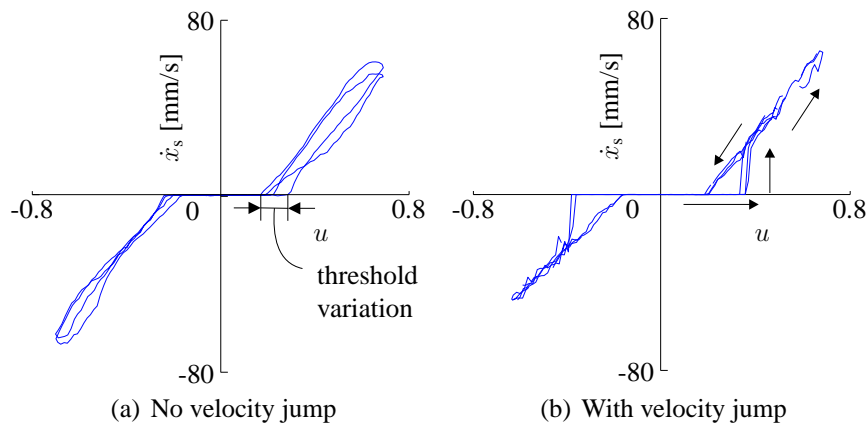


Figure 4.8: The steady state slider velocity  $\dot{x}_s$  as function of the input  $u$ . (Single-Sided Actuation). The experiments (a) and (b) are performed at different moments.

**Improvements** We refer to chapter 2 for suppression of the wave amplitude variation along the stator length. Disturbances of the contact interface can be decreased by:

- applying a stator with a smaller roughness, e.g., by polishing;
- using a different preload mechanism (chapter 5 design procedures);
- putting the SAW motor in a clean and controlled environment.

### Threshold amplitude

A slider starts to move when the wave amplitude exceeds a certain threshold amplitude. In practice the threshold amplitude varies due to the previous described disturbance sources (see figure 4.8(a)). Moreover, compare figure 4.8(a) and figure 4.8(b), which are acquired at the same setup at a different day. It shows the relation between an input signal  $u$  (linear proportional to the wave amplitude) and the slider velocity. The input of figure 4.8(b) increases steadily starting from zero. At a certain value the slider velocity jumps discontinuously to a steady state value. When the input decreases from a positive value, the velocity decreases continuously to zero. On the other hand, figure 4.8(a) does not show the discontinuous jumps. The difference in the behavior is explained by the variation in the frictional behavior.

A dead zone with a time-variant and position-dependent threshold amplitude is not beneficial from a control point of view. Therefore, four actuation methods are compared in order to examine their ability to deal with this problem.

## 4.2 Actuation methods

This section is based on (Feenstra et al. 2005).

A so-called Interdigital Transducer (IDT) can generate Rayleigh waves. Two IDT's are required to obtain a one degree of freedom motion, i.e., one IDT to generate a wave in

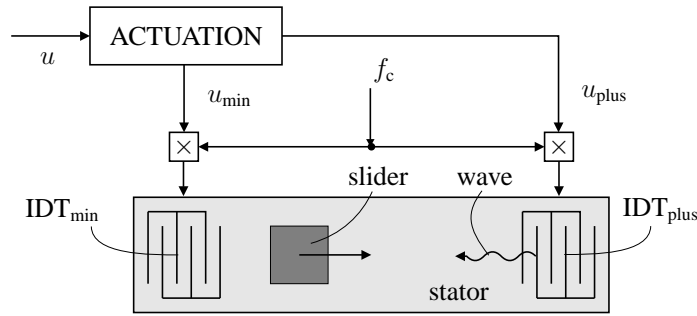


Figure 4.9: Actuation of a SAW motor.

positive direction and one IDT to generate a wave in the opposite direction (figure 4.9). The actuation block calculates both actuation signals ( $u_{\min}$  and  $u_{\text{plus}}$ ) as a function of the control input  $u$ . Subsequently, a high frequency  $f_c$  (MHz) carrier signal multiplies the signals to obtain an amplitude modulated (AM) signal. The AM signals drive the IDT's of the SAW motor. The four strategies that are discussed are qualified by their relative efficiency and their ability to eliminate the dead zone.

### 4.2.1 Single-sided actuation

The simplest way to achieve two actuation signals is by using the sign of  $u$  for switching. Signal  $u_{\text{plus}}$  is  $u$  if the sign of  $u > 0$  and signal  $u_{\min}$  is  $u$  if the sign of  $u < 0$ . Figure 4.8 already showed two experiments performed with this so-called Single-Sided Actuation (SSA). It demonstrates that both the dead zone and the variation remain. In order to define the relative efficiency, we approximate the relation between the no-force velocity  $\dot{x}_s$  and the control input  $u$  where  $0 \leq u \leq 1$  (figure 4.8) by:

$$\dot{x}_s = \begin{cases} \frac{\dot{x}_{s,\max}}{1-u_{\text{th}}} (u - u_{\text{th}}) & \text{for } u > u_{\text{th}} \\ 0 & \text{for } 0 \leq u \leq u_{\text{th}} \end{cases} \quad (4.5)$$

where  $u_{\text{th}}$  is the threshold control input and  $\dot{x}_{s,\max}$  is the slider velocity for  $u = 1$ . By rewriting equation 4.5 we can find  $u = u(\dot{x}_r)$  for  $0 \leq \dot{x}_r \leq 1$ , where  $\dot{x}_r = \dot{x}_s / \dot{x}_{s,\max}$  is the normalized slider velocity.

$$u(\dot{x}_r) = (1 - u_{\text{th}})\dot{x}_r + u_{\text{th}} \quad \text{for } 0 \leq \dot{x}_r \leq 1 \quad (4.6)$$

Accordingly, the wave power can be written as a function of  $\dot{x}_r$ .

$$\begin{aligned} P_{\text{ssa}} &= P_{\text{ssa,max}} (u_{\text{plus}}^2 + u_{\text{min}}^2) \\ &= P_{\text{ssa,max}} (\dot{x}_r - \dot{x}_r u_{\text{th}} + u_{\text{th}})^2 \quad \text{for } 0 \leq \dot{x}_r \leq 1 \end{aligned} \quad (4.7)$$

where  $P_{\text{ssa,max}}$  is the wave power for  $|u| = 1$ . Now, we can define the relative efficiency as the wave power of other actuation methods  $\alpha$  (to be discussed next) with respect to SSA:

$$\eta_{\text{rel}} = \frac{P_{\text{ssa}}}{P_{\alpha}} \quad (4.8)$$

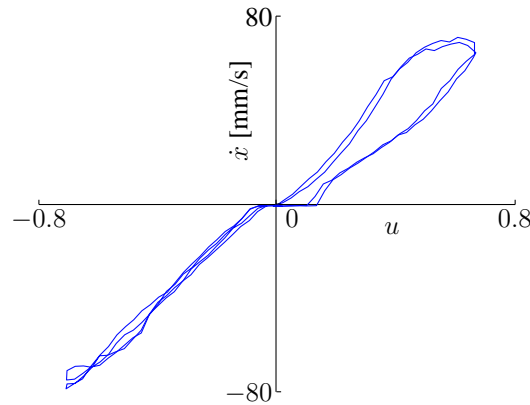


Figure 4.10: Relation between input signal and actuation signals for single-sided actuation with compensation.

### 4.2.2 Compensated single-sided actuation

It is possible to eliminate the dead zone if the threshold amplitude  $u_{th}$  is known; a value corresponding to the (smallest) threshold amplitude is added to the steering signal  $u$ . Note that overcompensation occurs when the compensation is larger than the actual dead zone. Velocities near zero are not reachable in case of overcompensation. Figure 4.10 shows results of an open-loop experiment performed with compensated single-sided actuation (CSSA). It demonstrates the intended decrease of the dead zone. However, the dead zone is not completely eliminated, as could be expected. The relative efficiency  $\eta_{rel}$  is 100 %, because the relation between  $\dot{x}_s$  and  $u_{plus}$  or  $u_{min}$  is identical to SSA.

### 4.2.3 Dual-sided actuation

A third strategy is proposed by Vermeulen, Peeters, Soemers, Feenstra & Breedveld (2002). They assumed that the stator roughness causes the dead zone, rather than the stick behavior. Nevertheless, this method implicitly tackles the stick phenomena and consequently eliminates the dead zone. Since both IDT's are actuated simultaneously, this method is called Dual-Sided Actuation (DSA). For example, if DSA for  $u = 1$  corresponds to SSA (only one wave) the actuation signals are

$$u_{plus} = \frac{1+u}{2} \quad u_{min} = \frac{1-u}{2} \quad (4.9)$$

The principle of slider motion is explained by the surface particle displacement shown in figure 4.11. For equal wave amplitudes ( $u = 0$ ), the motions are symmetric (a standing wave). Consequently, the slider does not move. For unequal wave amplitudes, the surface particle motion is elliptical and may generate slider motion. The dead zone disappears when the normal wave amplitude is such that constant stick behavior between slider and stator is overcome. For a smaller wave amplitude, the threshold amplitude only reduces. Overcompensation is not possible. Figure 4.12 shows the results of an experiment per-



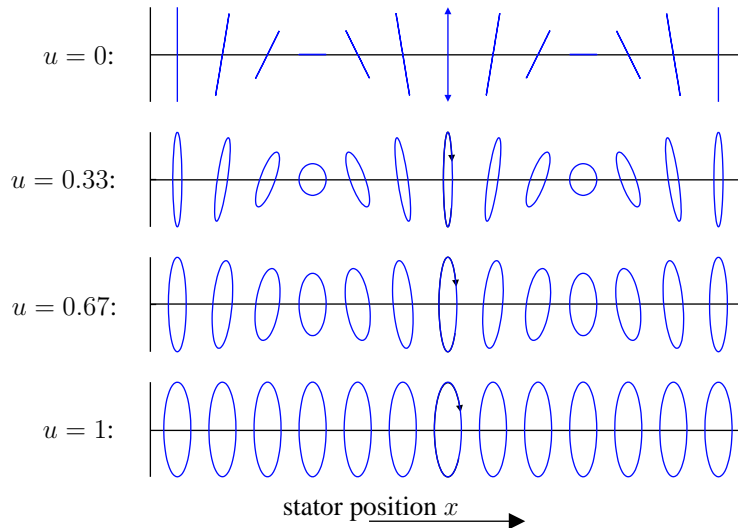


Figure 4.11: The particle motions due to DSA at the surface of a stator.

formed with this strategy, which shows that this actuation method almost eliminates the dead zone.

However, figure 4.11 shows that the particle displacement amplitudes depend on the position  $x$ . This dependency causes an additional position dependent disturbance. Apart from the position dependent disturbance, this method has another drawback: the relative efficiency is decreased. Consider equation 4.9 and suppose  $u = \dot{x}_r$ . Then, the input power for DSA is

$$P_{\text{dsa}} = P_{\text{ssa,max}} (u_{\text{plus}}^2 + u_{\text{min}}^2) = P_{\text{ssa,max}} \frac{1 + \dot{x}_r^2}{2} \quad \text{for } -1 \leq \dot{x}_r \leq 1 \quad (4.10)$$

Hence, 50 % of the maximal power is dissipated for a zero slider velocity. Figure 4.13 shows  $\eta_{\text{rel}}$  for  $u_{\text{th}} = 0.2$ . The relative efficiency of DSA is 100 % for  $\dot{x}_r = 1$  and only 8 % for  $\dot{x}_r = 0$ .

#### 4.2.4 Pulse-width modulation

The fourth actuation method consists of the application of a pulse train of constant amplitude but variable pulse-width, therefore, this method is called pulse-width modulation (PWM). We emphasize that the PWM signals are multiplied by a carrier signal before the motor is driven, rather than driving the motor directly which is sometimes the case for ultrasonic motors (Ueha & Tomikawa 1993). The dead zone disappears if the applied amplitude exceeds the threshold amplitude. Figure 4.14 illustrates the principle of operation. In order to visualize the behavior, the PWM frequency is chosen rather small. The top plot shows the PWM signal for a duty cycle ( $dc$ ) of 0.5 (dashed) and 0.25 (solid). The second subplot shows a step response and two PWM signals with  $dc = 0.5$  (dashed) and  $dc = 0.25$  (solid). The bottom plot shows the slider displacement, which contains a small

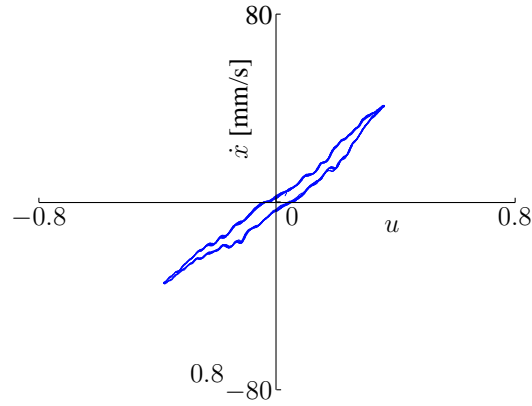


Figure 4.12: Experiment performed with dual side actuation. Experiment is taken from Vermeulen et al. (2002).

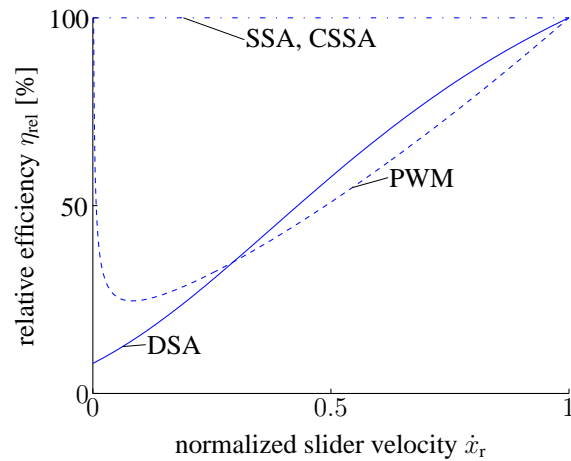


Figure 4.13: The relative efficiency of the four actuation methods.

ripple. This ripple decreases with an increasing PWM frequency. Depending on the sign of  $u$  the signals  $u_{\min}$  and  $u_{\text{plus}}$  are zero or equal to the generated PWM signal.

**PWM frequency** The allowable ripple on the displacement and the allowable acoustic noise limits the lower bound of the PWM frequency. Acoustic noise is an undesired audible disturbance in the audio frequency range. Acoustic noise is circumvented when the frequency is chosen above 20 kHz. At this frequency, the ripple is negligibly small because the frequency is considerably larger than the bandwidth of a practical SAW motor. On the contrary, the pulse train length ( $dc/f_{PWM}$ ) should be sufficient large to reach the constant wave amplitude; the IDT response becomes dominant for small pulse train lengths (section 2.3.1). Therefore, a proper choice is a frequency of 20 kHz. We emphasize that  $f_{PWM} \ll f_{r=\text{Rayleigh}}$ .

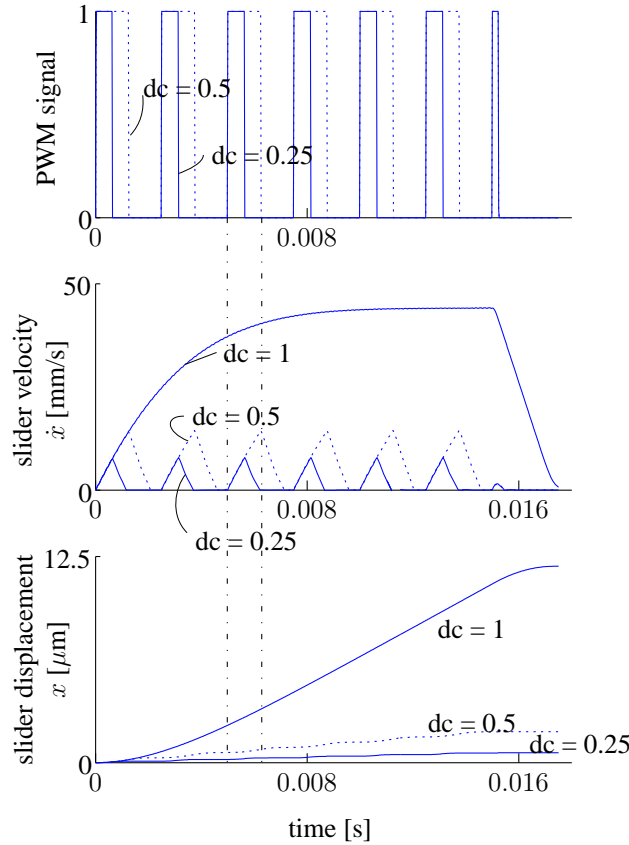


Figure 4.14: Slider behavior with pulse-width modulation (simulation).

**Equivalent damper** In section 3.2.4, we have discussed the motor characteristic of a SAW motor. We have demonstrated that a SAW motor characteristic can be interpreted as series connection of an ideal velocity source and an equivalent damper. However, as expected, the relation of the equivalent damper  $R_t$  changes by applying PWM actuation. Experiments showed that the equivalent damper value increases with a decreasing duty cycle. A sound relation between the equivalent damper and the duty cycle requires further research.

**Experiment** Figure 4.15 shows the result of an experiment with a PWM frequency of 20 kHz that demonstrates the elimination of the dead zone. The ratio between input signal  $u$  and slider velocity  $\dot{x}_s$  is rather constant and is defined as the velocity constant  $K_v$ . The velocity constant is 0.1. This linear relation is obtained by assigning the duty cycle value as  $dc = \sqrt{|u|}$ . Accordingly, the PWM wave power for a constant amplitude ( $\hat{u} = 1$ ) and variable width is

$$P_{\text{pwm}} = P_{\text{ssa,max}} \hat{u}^2 dc = P_{\text{ssa,max}} \sqrt{\dot{x}_r} \quad \text{for } 0 \leq \dot{x}_r \leq 1 \quad (4.11)$$

Hence, the input power is zero for a zero slider velocity. Figure 4.13 shows  $\eta_{\text{rel}}$  for PWM actuation. The relative efficiency is 100 % for  $dc = 1$  and  $dc = 0$ . The minimum efficiency is 25 %. A drawback of this method is the requirement of extra hardware.

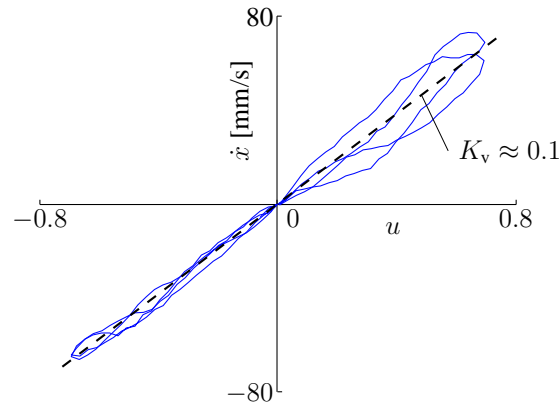


Figure 4.15: Experiment performed with pulse-width modulation.

### 4.2.5 Overview of actuation methods

Table 4.2 contains an overview of the four discussed actuation methods. By comparing the discussed methods it follows that the best results are obtained for PWM actuation: it eliminates the dead zone and its efficiency can be qualified as good. Therefore, actuation by means of PWM is to be preferred and is used in the remainder of this chapter.

method	eliminates dead zone	relative efficiency
SSA	no	best
SSA + compensation	partly	best
DSA	yes	low
PWM	yes	good

Table 4.2: Actuation methods.

## 4.3 Open-loop control

It is informative to analyze the smallest (open-loop) slider displacement possible, e.g., to determine the specifications of a SAW motor or to select a measurement system. The slider displacement depends on the duration of actuation  $T$  (length of a burst) and on the wave amplitude. We assumed in the previous chapters that the ratio between the input amplitude and the wave amplitude is constant (static). This assumption is valid if the input is smooth or if length of a burst is large, i.e.,  $T \gg 2N/f_c$ , where  $N$  is the number of finger pairs and  $f_c$  the center frequency. However, for small bursts the transient response of the active IDT needs to be taken into account (section 2.3.1).

It turns out that the step size can be made very small by choosing a fixed (small) number of periods and simply decreasing the wave amplitude. The slider displacement of the experimental setup is measured for a number of bursts with different durations. A laser vibrometer with a resolution of 2 nm measures the displacement. Figure 4.16 shows the result. The displacement is averaged 10 times for the bursts consisting of 11 periods and 5 times for the other experiments. The minimal step size in this experiment is 1.7

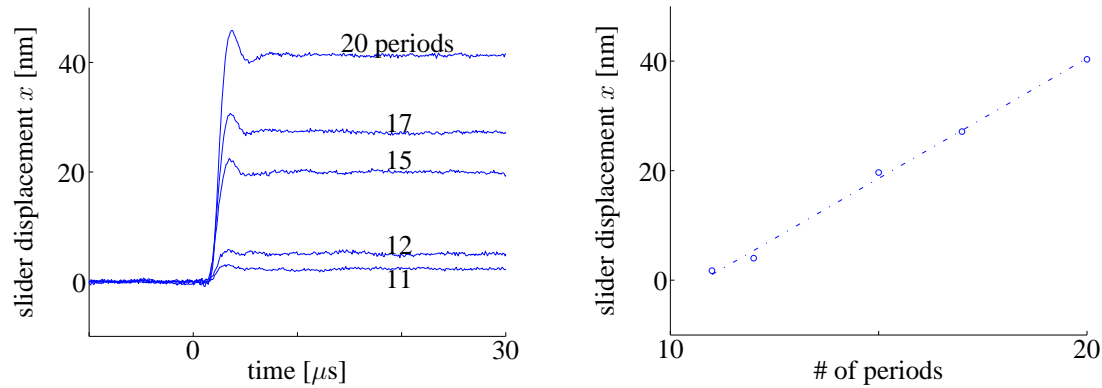


Figure 4.16: Measurement of the slider displacement. The burst length is varied.

nm for 11 periods, which is already below the vibrometer resolution. In literature, e.g. [Shigematsu et al. \(2003\)](#) and [Shigematsu & Kurosawa \(2004\)](#), steps are mentioned of 2 and 0.5 nm. Therefore, it seems that the step size can be made infinitesimally small.

Open-loop control by using stepping motion is possible. However, attention should be paid to the reproducibility of the step size, because the variation in the step size increases with a smaller number of excitation periods.

## 4.4 Closed-loop controller

In this section, we propose a controller for a SAW motor with PWM actuation. The controller parameters are found by utilizing an LTI model. Finally, the controller is implemented and tested.

### 4.4.1 Controller design

We choose to control the plant  $P$  – the SAW motor by PWM actuation – by a PID controller. Figure 4.17 shows the basic structure. Signal  $r$  is a reference signal,  $K_P$  is the proportional gain and  $(1 + \frac{K_I}{s} = \frac{s+K_I}{s})$  represents a pure integrator with an extra zero in  $s = -K_I$ . The integrator deals with the quasi constant disturbances  $d$  (e.g. guiding friction) at the input of the plant. The derivative action  $K_D$  is applied for extra damping and the low-pass filter  $LP$  is used to suppress high-frequency noise in the velocity measurement. The displacement  $x_e$  is measured by the encoder and the slider velocity  $\dot{x}_m$  is measured by the vibrometer (figure 4.1(a)).

The controller parameters will be found by a model of the plant. So far we have found an LTI mechanical model which describes the relation between the no-force velocity  $\dot{x}_s$  and the encoder displacement  $x_e$  and the slider velocity  $\dot{x}_m$  (section 4.1). Furthermore, we have shown that the dead zone between the actuation signals,  $u_{\min}$  and  $u_{\text{plus}}$ , and the no-force slider velocity  $\dot{x}_s$  can be eliminated by utilizing PWM actuation (section 4.2.4), such that a linear relation  $K_v$  remains. The combined model – the mechanical model

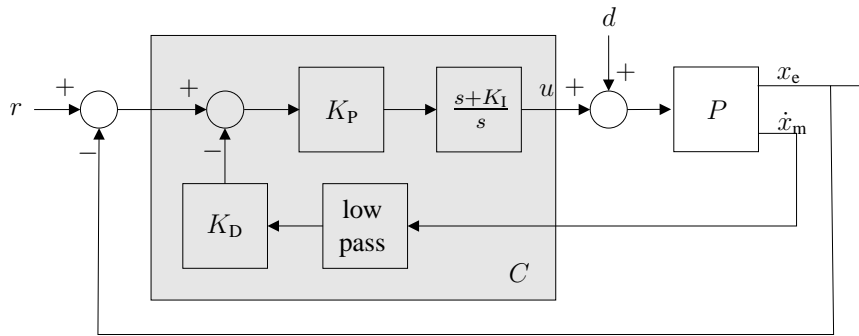


Figure 4.17: Control scheme of the system.

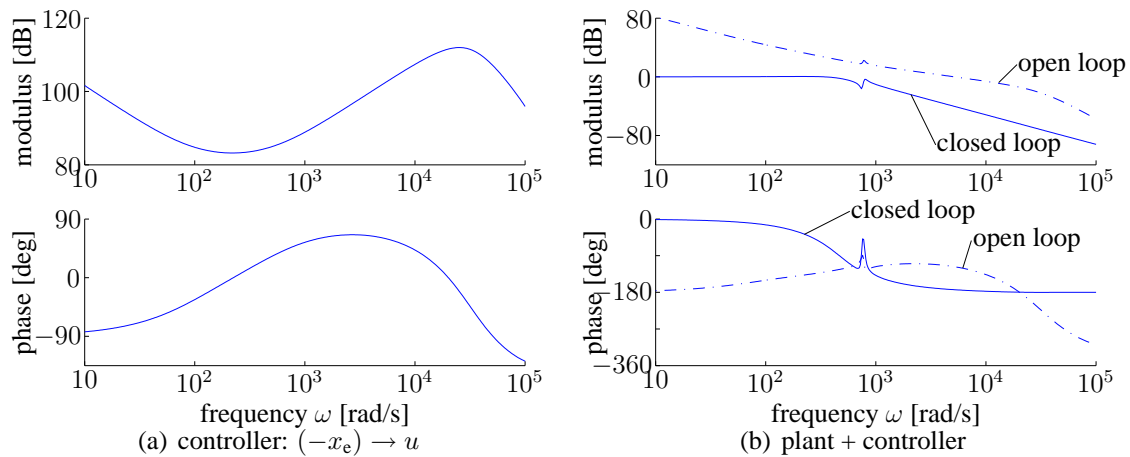


Figure 4.18: Bode plot of controller and plant + controller.

plus the linear relation – will serve as plant model. We use the parameters of table 4.1. Therefore, the value of the equivalent damper  $R_t$  corresponds with a duty cycle with a value of 1. Damper  $R_t$  will increase for smaller values of the duty cycle (section 4.2.4). Therefore, the controller parameters derived from the model may be changed at the real setup in order to improve the closed-loop behavior.

The controller parameters are found by pole placement. First, the proportional gain  $K_P$  is determined. Suppose a specified  $-3$  dB bandwidth of  $460$  rad/s. Accordingly, the gain  $K_P$  is chosen  $12 \cdot 10^3$  such that the smallest conjugated closed-loop poles are a factor 1.7 below the resonance frequency  $\omega_r = 800$  rad/s. Next, the damping gain  $K_D$  is chosen  $2.2 \cdot 10^{-3}$  such that the smallest complex conjugated poles have a relative damping of approximately 0.7. The integrator gain  $K_I$  is chosen 100 such that it is large and that it does not influence the relative damping a lot. The low pass filter, a third order Bessel filter with a cut of frequency of 5 kHz, is part of the vibrometer controller.

Figure 4.18(a) shows the resulting bode-plot of the controller ( $-x_e \rightarrow u$ ), where we assumed that  $\dot{x}_m = \dot{x}_e$ . Figure 4.18(b) shows the bode plot of the open and the closed-loop system (plant + controller). The bandwidth is about 800 rad/s. The pole-zero configuration of the closed-loop and open-loop system and the root loci of the open-loop system is

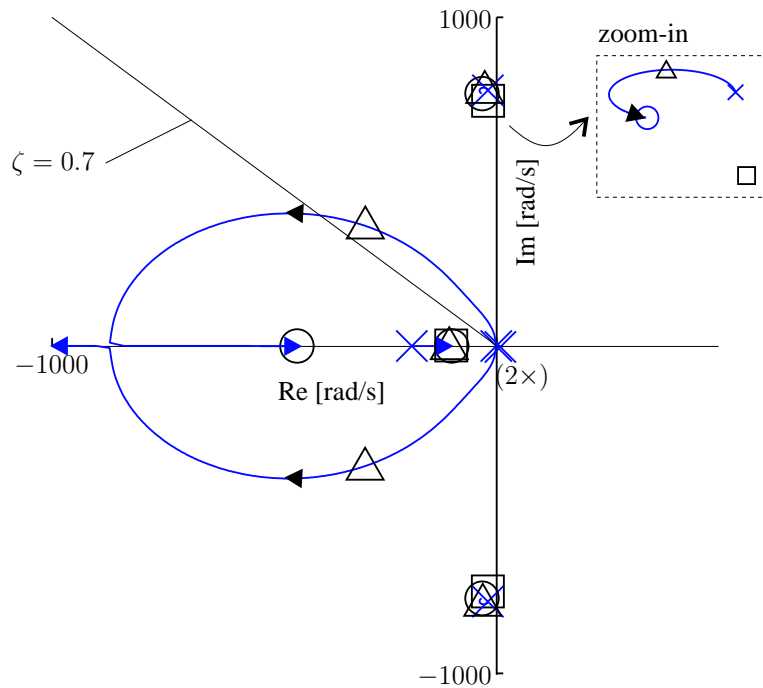


Figure 4.19: Pole-zero configuration of open-loop and closed-loop system and root loci of open-loop system. ( $\Delta$  is a closed-loop pole,  $\square$  a closed-loop zero,  $\times$  an open-loop pole and  $\circ$  is an open-loop zero).

shown in figure 4.19. The root loci demonstrate that the two open-loop poles in the origin move to approximately  $s = -300 \pm 370i$ . Figure 4.4.1 shows the step response of the closed-loop system. The overshoot is 13 % and the resonance behavior due to the poles is  $\omega = 786$  rad/s.

#### 4.4.2 Experiments

The controller is implemented in Simulink (Mathworks, Inc. 2003). The code for the acquisition hardware (dSPACE 2001) -DS1103- is directly generated by Simulink. By using the graphical user interface ControlDesk (dSPACE 2001) that runs on the acquisition hardware, we can set parameters and observe signals. The sample frequency is 10 kHz. Three experiments are discussed with successively a cycloid step, a constant velocity and a continuous cycloid reference profile.

##### Tracking of a cycloid step

In this experiment we are interested in the steady state error rather than the maximal tracking error. The duration of the step is 0.13 seconds and the stroke is 1.5 mm. The controller of figure 4.17 is used with controller parameters  $K_P = 12 \cdot 10^3$ ,  $K_D = 10^{-4}$  and  $K_I = 100$ . The motor velocity is filtered with a low pass filter with a cut-off frequency

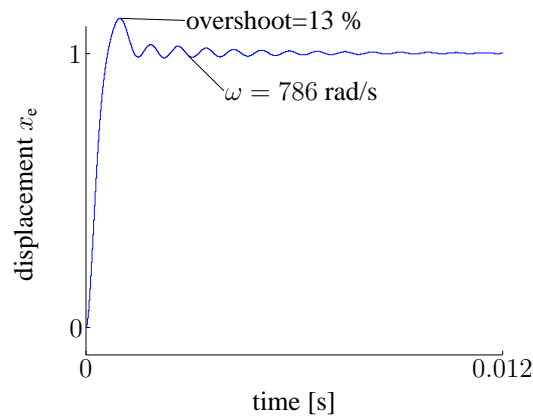


Figure 4.20: Step response of the closed-loop system.

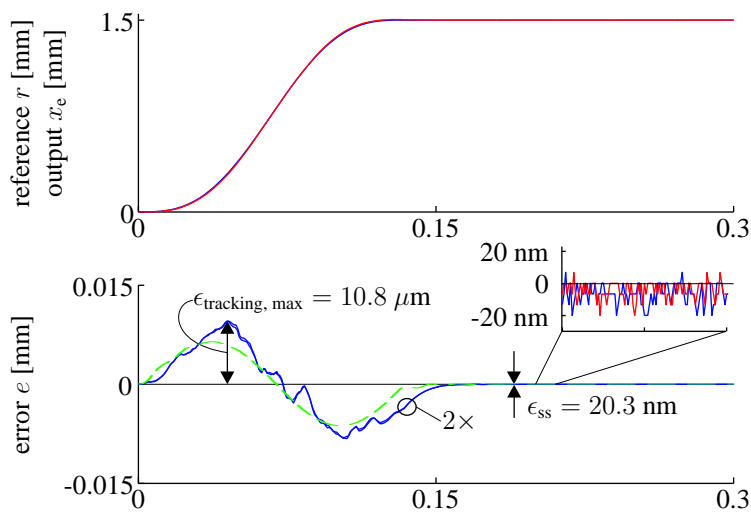


Figure 4.21: Cycloid step. The error is plotted for two experiments. The dashed line is the simulated error.

of 5 kHz and the measurement resolution of  $x_e$  is 6.67 nm. To obtain better results, the D-action is chosen a factor 22 smaller than determined in subsection 4.4.1. This is not a surprise, since the system model is considerably simplified for the purpose of controller design. The decrease of  $K_D$  is explained by an increase of the equivalent damper  $R_t$  due to PWM actuation. An increase of  $R_t$  causes more mechanical damping hence less D-action ( $K_D$ ) is required. Although the D-action appears to be small, it still has its influence on the closed-loop behavior. Figure 4.21 shows the measured (solid) and the simulated (dashed) result. For the simulation we used the LTI model of figure 4.17 and the model parameters of table 4.1 and the controller parameters applied for the real setup. The results are remarkably close, despite the considerable model simplification. The non-smooth reproducing error while moving is due to the surface roughness as will be shown in the next experiment.

To obtain an indication for the reproducibility, the experiment is repeated 15 times. The maximal tracking error  $\epsilon_{\text{tracking, max}}$  and the maximal steady state error  $\epsilon_{\text{ss}}$  are determined



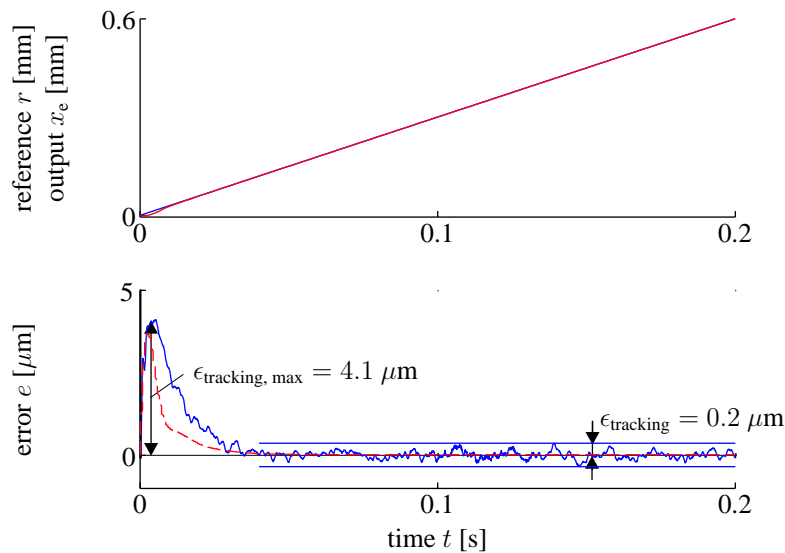


Figure 4.22: Tracking of a constant motion experiment. The dashed line is a simulation result.

for each experiment. Next, the mean value  $\mu$  and the standard deviation  $\sigma$  are calculated. For the maximal tracking error we found  $\mu = 10.8 \mu\text{m}$  and  $\sigma = 0.81 \mu\text{m}$  and for the steady state error  $\mu = 20.3 \text{ nm}$  and  $\sigma = 1.7 \text{ nm}$ . See the inset of figure 4.21. Because the standard deviation is small with respect to the mean value, we conclude that the experiment is reproducible. The steady state error has a mean value of three encoder increments. Therefore, the steady state error is mainly limited by the measuring resolution.

### Tracking of constant motion

In this experiment, we are interested in the error during a constant motion rather than a transient. The reference signal is a ramp with a constant velocity of 3 mm/s. The controller parameters are  $K_P = 10 \cdot 10^3$ ,  $K_D = 10^{-3}$  and  $K_I = 100$ . The motor velocity is again filtered with a low pass filter with a cut-off frequency of 5 kHz and the measurement resolution is 13 nm. In this experiment, the errors are not limited by the measurement resolution<sup>1</sup>. Figure 4.22 shows the measured (solid) and simulated (dashed) result, which match again well. The maximal measured tracking error  $\epsilon_{\text{tracking, max}}$  during the transient is  $4.1 \mu\text{m}$  and the tracking error  $\epsilon_{\text{tracking}}$  during motion is  $0.2 \mu\text{m}$ . Figure 4.23(a) shows the error as a function of the displacement for three repetitions. It shows that the tracking error is position dependent. Figure 4.23(b) shows the absolute value of the fast fourier transform (FFT) of the error vs. the displacement. The dominating spatial period is  $20 \mu\text{m}$ , which corresponds with the stator roughness. The associated (time) frequency is  $3\text{mms}^{-1}/20\mu\text{m} = 150\text{Hz}$ .

<sup>1</sup>The encoder input of the acquisition hardware has a maximum counting frequency, which should not be exceeded to preserve stability of the closed-loop plant. The number of pulses generated by the encoder measurement system is proportional to the velocity times the measurement interpolation. Hence, the maximum velocity increases by lowering the measuring interpolation and thereby the resolution or the measurement accuracy increases for lower velocities.

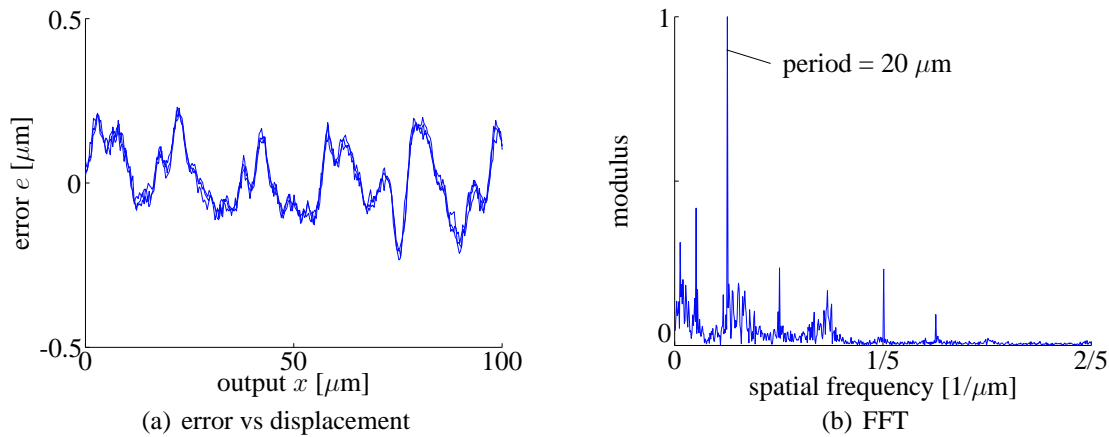


Figure 4.23: Position dependent error

In this particular experiment the frequency of the error is constant due to the constant velocity. Therefore, the controller could be designed such that this frequency is suppressed. Because the error is position dependent, it would also be possible to compensate the error by means of (learning) feed forward control (Velthuis 2000), (De Kruif 2004). The error could be decreased by design as well. One possibility is to decrease the stator roughness. For example, the RMS roughness of a Lithium Niobate stator could be as small as 1.3 nm, while the RMS roughness of the applied stator is 9.5 nm. Another possibility is to increase the proportional gain, which increases the error suppression and the bandwidth. However, the practical maximum bandwidth is often limited by the ‘parasitic’ vibration modes of the system.

### Tracking of a continuous cycloid reference

In this final closed-loop experiment, the reference is a continuous cycloid signal with an amplitude of 10 mm and a period time of 13.3 s. We use the controller of the previous experiment with an additional I-action. The motivation for the extra I-action is discussed next.

The number of pure integrators in the forward path (plant plus controller) determines the type-number of the system. This is 1 for the ‘plant’ and 1 for the I-action of the controller of the previous section, which makes the type-number 2. The highest power of the poles in the denominator of the Laplace transform of a profile determines the order of the profile. Hence, for a ramp profile ( $1/s^2$ ) the order is 2 and for a cycloid profile ( $1/s^2(s^2 + 1)$ ) the order is 4. The type-number of the system should be no more than one integer value lower to achieve a bounded steady state error (Van Amerongen 1992). Therefore, for the slowly varying cycloid path we use an additional I-action, which makes the type-number 3. See figure 4.24. The controller parameters are:  $K_P = 12 \cdot 10^3$ ,  $K_D = 0.2 \cdot 10^{-3}$  and  $K_I = 100$ . The motor velocity is filtered with a low pass filter with a cut-off frequency of 5 kHz and the measurement resolution is again 13 nm. The reason for the smaller  $K_D$  value is discussed in the first closed-loop experiment.

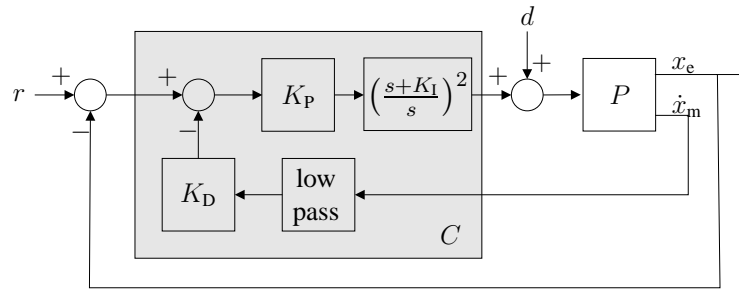


Figure 4.24: Control scheme for the continuous cycloid reference.

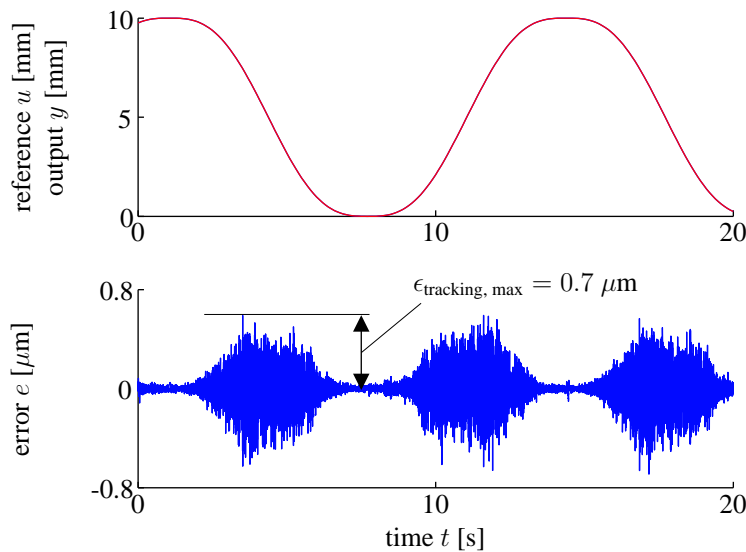


Figure 4.25: Continuous cycloid experiment.

Figure 4.25 shows the experimental result. The maximal tracking error is  $0.7 \mu\text{m}$ . The error  $\epsilon_{\text{tracking, max}}$  is again dominantly caused by the roughness of the stator. In order to suppress this disturbance, the sensitivity function  $x_e/d = 1/(1 + PC)$  should be chosen small in the disturbing frequency band, rather than at one frequency only. Alternative solutions were discussed in the previous experiment.

### 4.4.3 Review

In the previous subsection different experiments were discussed. Table 4.3 list the results.

experiment	$\hat{x}$ [mm]	$T_{\text{motion}}$ [s]	$\dot{u}_{\text{max}}$ [mm/s]	$F_{t,\text{max}}$ [N]	$\epsilon_{\text{track, max}}$ [ $\mu\text{m}$ ]	$\epsilon_{\text{ss}}$ [ $\mu\text{m}$ ]
cycloid step	1.5	0.13	22.5	0.06	10.8	$20.3 \cdot 10^{-3}$
constant motion	-	-	3	-	4.1	0.2
continuous cycloid	10	13.3	3	$0.15 \cdot 10^{-3}$	0.7	

Table 4.3: Summary of the experiments.

## 4.5 Conclusions

In this chapter we have examined the actuation and closed-loop control of a SAW motor. To this end, a linear dynamic model of the SAW motor was derived, which took the first vibration mode of the guiding into account. Next, the disturbances sources of the motor were discussed, which are:

- variation of wave amplitude along stator length;
- friction of slider guiding;
- stator roughness;
- variation of preload force;
- variation of frictional behavior between stator and slider.

We have shown that the inherent SAW motor threshold amplitude varies due to these disturbances. A dead zone with a time-variant and position depending threshold amplitude is not beneficial from a control point of view. Therefore, four actuation methods have been compared:

- single-sided actuation (SSA);
- compensated single-sided actuation (CSSA);
- dual-sided actuation (DSA);
- pulse width modulation (PWM).

By adding a constant value with a proper sign the dead zone only partly disappears (CSSA). Furthermore, CSSA allows overcompensation. The use of two opposite propagating waves (DSA) eliminates the dead zone without the risk of overcompensation. However, the input power for a zero slider velocity is large. Finally, this examination has shown that pulse width modulation (PWM) also eliminates the dead zone, also without the risk of overcompensation, but with considerably smaller input power compared to DSA in case of small slider velocities. Therefore, this method is recommended for SAW motor control, in particular closed-loop control.

An experiment was performed to determine the stepping resolution of the SAW motor. The smallest open-loop steps measured were 1.7 nm. Smaller steps could not be measured due to the limited measurement resolution. However, it seems that the step size can be made infinitesimally small.

A PID and a PI<sup>2</sup>D controller was used for closed-loop control of the SAW motor. The controller parameters were determined by pole-placing utilizing the derived linear dynamical model. The controller was implemented and experiments were performed. Some conclusions regarding the closed-loop experiments were:

- The maximal tracking error depends on the velocity and is predominantly caused by the stator roughness.
- The steady state errors are small and are limited by the resolution of the measurement system.

Hence, a SAW motor with PWM actuation performs well for positioning applications, especially regarding the relative large stroke. Since the SAW motor tracking is predominately hampered by the stator roughness, we expect improved results by applying a stator with a *smaller roughness*. Alternatively, the error could be decreased by *improving* the *sensitivity function* for the associated roughness frequency band. Finally, since the error due to roughness is position dependent, it could be possible to compensate it by means of *feed forward control*.



# Chapter 5

## Design procedures

*Overview: In this chapter, we consider the design of a SAW motor to obtain an indication for the applied materials, the geometry, the construction and the actuation. First, the inherent SAW motor is discussed, where a design trajectory is proposed to obtain design parameters. Next, the guiding design and the preload mechanism are examined. Finally, the electronics of the control loop are discussed.*

### 5.1 Introduction

Suppose we need to design a system which has to perform a certain task, for example the displacement of a sample with a particular motion profile and with a maximum allowable tracking error. By considering a mechatronic design trajectory, we could distinguish different phases and iterations of such a system until the final design is ready (Coelingh 2000) (Van Amerongen & Breedveld 2003). This final design contains the specification for the construction (configuration, stiffness, mass), the controller structure and parameters, the sensor placement and requirements and the specifications for the actuator(s) or in particular the specifications for a SAW motor. Based on these specifications a SAW motor has to be designed.

The goal of this chapter is to give an indication of the applied materials, the geometry, the construction and the actuation, such that the specified motor specifications are satisfied. Furthermore, the parameter limits and the effect of a parameter change on the motor behavior are discussed. To this end, we have subdivided the SAW motor design into three parts: the inherent SAW motor design (section 5.2), guiding and preload mechanism design (section 5.3) and the design of the electronics for the control-loop (section 5.4).

In the SAW motor design section a design trajectory is proposed. The guiding and preload mechanism design section gives suggestions to achieve a well-conditioned slider-stator contact interface. Furthermore, the guiding itself and the preload mechanism are considered. Finally, in the electronics for the control-loop section we briefly discuss the electronics and related aspects of the SAW motor control-loop.

## 5.2 Motor design

In this section, we discuss a possible design trajectory for a SAW motor (without guiding). The goal of the design trajectory is to generate a set of design parameters –the required choice of, for example, material and geometry in order to satisfy the given specifications– and to show the relation between specifications and design parameters. Figure 5.1 shows the flow chart of the design trajectory. We distinguish two kinds of input parameters. The first kind is the group of predefined *specifications* of a SAW motor, e.g., the stroke and the velocity. These specifications are underlined in figure 5.1. The second kind of input parameters is the group of *selections*, which are related to the projection geometry, the properties of the applied materials and quality related parameters, e.g., the attainable attenuation due to beating (section 2.1.4) and the wave amplitude. In subsection 5.2.1, we discuss rules and considerations to utilize a proper selection. The interrelations between the design parameters, the selections and specifications are examined in subsection 5.2.2. Additional design parameters are explored in subsection 5.2.3.

### 5.2.1 Selection rules and considerations

#### Stator-IDT material and composition

The stator-IDT composition of a SAW motor has two functions; one function is to generate waves and the other function is to use these waves to generate a slider motion. For the generation of waves, a piezoelectric material is required with preferably

- a high piezoelectric coupling factor;
- and a large quality factor.

(section 2.3.2). For the generation of a slider motion we prefer a stator with

- a high stiffness (Young modulus, Poisson ratio);
- a high coefficient of friction with respect to the slider material;
- high wear resistance.

The first two properties have been elaborated in section 3.6. The property of wear is important in the context of lifespan and vacuum applications. We will not explore the wear resistance in this thesis. Additional issues are the stator roughness, which should be small to minimize the associated disturbance and the stator flatness, which should be high to achieve a conditioned contact with the slider projections (section 5.3).

We discuss three possibilities to obtain a stator-IDT composition with the summarized properties. One possibility is to apply *one material* that meets (in some degree) all summarized properties. Materials that have proven to work are 128°Y-X Lithium Niobate (LiNbO<sub>3</sub>) and PZT (PXE43). Lithium Niobate is recommended because the stiffness, the piezoelectric coupling factor and the quality factor are larger than those of the PZT type. A second possibility is to generate waves by using a *piezoelectric thin film on a non-piezoelectric substrate* (section 2.3.2). The application of thin films increases the design freedom since the substrate does not have to be piezoelectric. A SAW motor based on



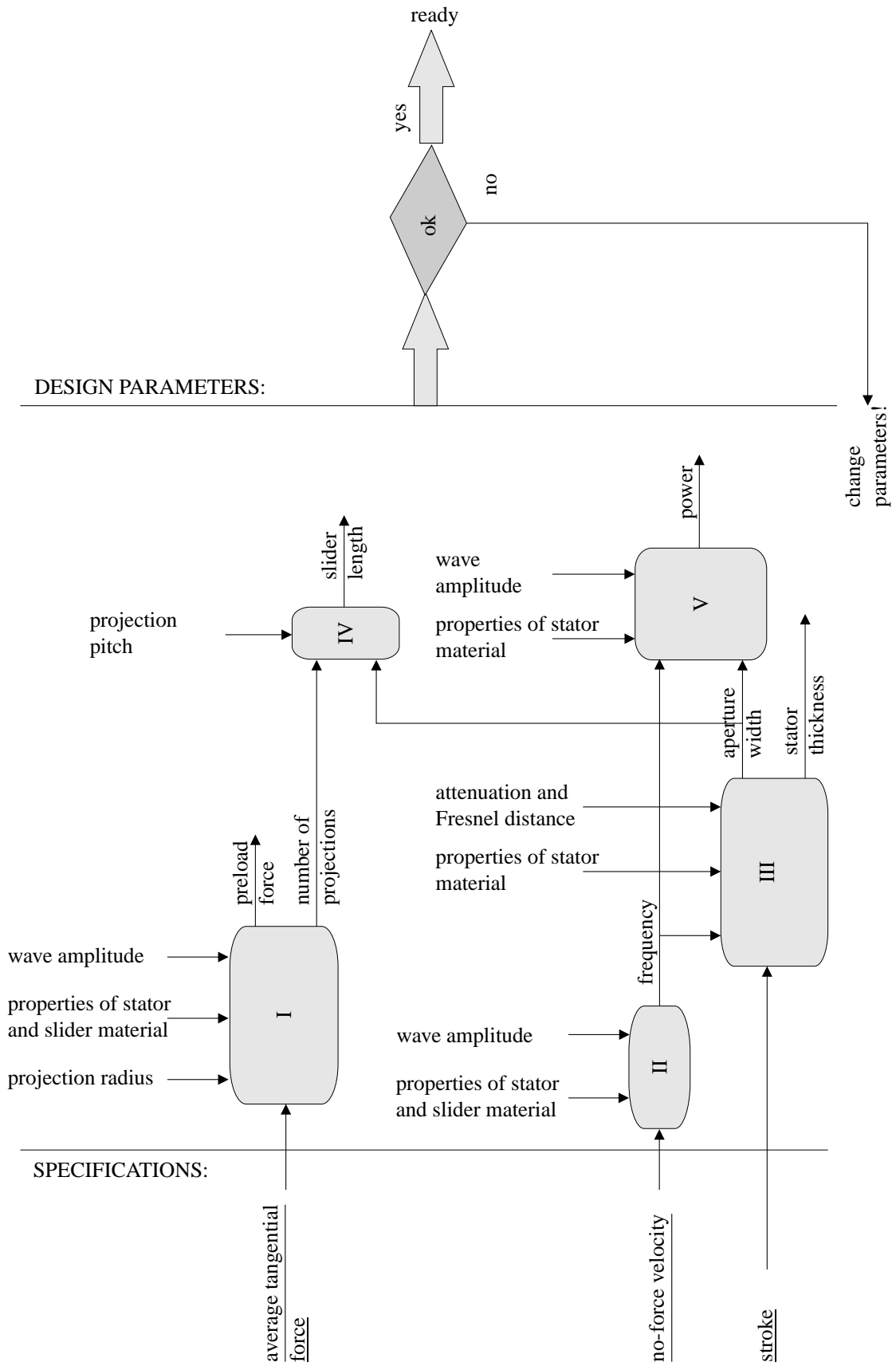


Figure 5.1: SAW motor design trajectory

piezoelectric thin films has not yet been fabricated. A third option, is the application of *a coating on a piezoelectric substrate* (section 2.1.3), e.g., to improve the contact stiffness or decrease wear. Nakamura et al. (2003) have demonstrated that the application of coatings can increase the motor force and velocity. A material with a high stiffness, good wear properties and that can be applied as coating is Alumina (Aluminum Oxide,  $\text{Al}_2\text{O}_3$ ). This material is applied as stator material in the commercially available ultrasonic motors of the company Nanomotion Ltd. Table 5.1 summarizes the possibilities.

substrate	thin film for wave generation	coating for slider motion	SAW motor reference
PZT (PXE43)	-	-	Dijk (2000)
$128^\circ$ LiNbO <sub>3</sub>	-	-	Kurosawa et al. (1994)
Sapphire; $\text{Al}_2\text{O}_3$ in the purest form	ZnO	-	-
LiNbO <sub>3</sub>	-	$\text{Al}_2\text{O}_3$	Nakamura et al. (2003)

Table 5.1: Examples of stator composition.

The input parameters (selections) for the design trajectory of figure 5.1 are the stator material properties, which include the Young moduli  $E$  and the Poisson ratios  $\sigma$  of the stator coating and the stator substrate<sup>1</sup>.

### Slider material and projection geometry

We prefer, similar to the stator, a slider with

- a high contact stiffness (Young modulus, projections, number of projections), (section 3.6);
- a high coefficient of friction with respect to the stator material (section 3.6);
- high wear resistance.

The projections are commonly fabricated by lithographic techniques. Therefore, silicon (Si) is a useful slider material as the fabrication of semiconductors has given rise to the collection of a large volume of knowledge (Madou 2002) (Senturia 2001). For reference: the Young modulus of silicon lies in between the Young modulus of lithium niobate and PZT (PXE43). Furthermore, similar to the stator, the tribological properties can be improved by a coating.

The slider projections in the experimental setup were ball-shaped. Although, cylindrically shaped projections have been used as well, for example by Shigematsu et al. (2003), we only elaborate ball-shaped projections. Ball-shaped projections can be fabricated by so-called thermal reflow processes and reactive ion etching (RIE) processes (Dijk 2000), where the errors between the desired radius and the fabricated radius can be less than  $\pm 8\%$  (Yang et al. 2004). The optimal geometry of the ball-shaped projections, which

<sup>1</sup>The Raleigh wave velocity for a stator with a small coating thickness ( $h \ll \lambda_r$ ) is determined by the stator substrate properties (Oliner et al. 1978).

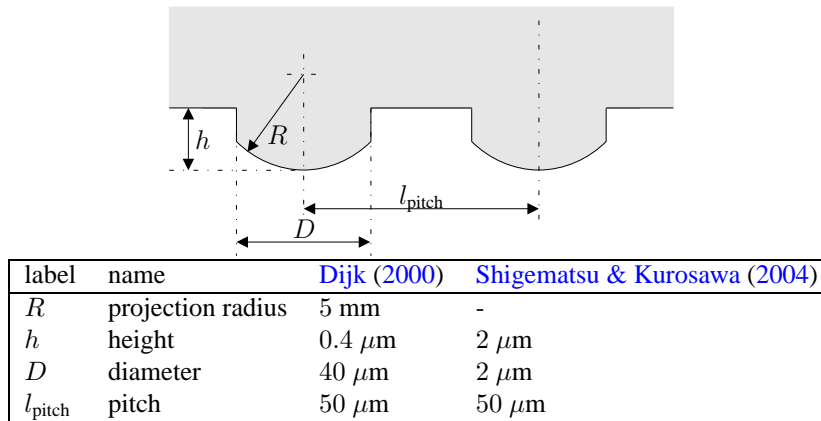


Figure 5.2: Ball-shaped projection values

is determined by the balance between the contact stiffness and the prevention of an air-film, is not explored. Instead, figure 5.2 shows typical dimensions, which can be used as starting point.

The length and width of the slider follows from the design trajectory (subsection 5.2.2) and the thickness of the slider is discussed in subsection 5.3.1. For reference; the slider size of fabricated SAW-motors varied between  $10 \cdot 10 \cdot 1 \text{ mm}^3$  (Dijk 2000) and  $2 \cdot 2 \cdot 0.5 \text{ mm}^3$  (Shigematsu & Kurosawa 2004).

Additional input parameters (selections) for the design trajectory of figure 5.1 are the properties of the slider coating or substrate material and the geometry (radius and pitch) of the projections.

### Nominal wave amplitude

An increase of the wave amplitude increases the motor force and the motor velocity but also the power consumption. Furthermore, the wave amplitude at a constant power decreases with the frequency. These relations demonstrate that it is difficult to choose a wave amplitude at forehand. Nevertheless, we recommend to start with an amplitude in the range of 5 – 15 nm and approach a suitable nominal amplitude value by iteration using the design trajectory of figure 5.1.

The maximal amplitude of PZT material is limited by quality factor degradation, which results in considerable heat generation if a certain vibration velocity is exceeded:  $\hat{u}_{z, \text{max}} = 0.3 - 0.6 \text{ m/s}$  (section 2.3.2). Therefore,

$$\hat{u}_{z, \text{max}} = \frac{1}{2\pi f_r} \hat{u}_{z, \text{max}} \quad (5.1)$$

The effect of degeneration is small for single-crystal material.

Peeters & Vermeulen (2004) mention that the wave amplitude should exceed the stator roughness, which implies the existence of a minimal wave amplitude. However, the stator roughness of the experimental setup of section 1.5 is  $R_a = 13 \text{ nm}$  (measured over a distance of  $50 \mu\text{m}$ ) and we have utilized wave amplitudes below 7 nm to generate a slider

motion (figure 3.34). Our experiment falsifies this hypothesis. Consequently, research is required to lay down a rule for a minimum wave amplitude.

### Interdigital transducer

In this thesis we have only considered bidirectional IDT's. The length of a bidirectional IDT is determined by the number of finger pairs times the wavelength. There exist no general rule for the number of finger pairs (section 2.3.1). Often the number is chosen between 10 and 20. Alternatively, the number can be chosen such that the electrical admittance is easily matched (section 2.3.1). Bulk wave generation reduces for an increasing number of finger pairs.

The length of bidirectional IDT's is small compared to the length of unidirectional transducers, which is an advantage of bidirectional IDT's. Especially at low frequencies, the absolute length of unidirectional IDT's can be large (for example 50 mm for 50 finger pairs at 2.2 MHz on a PZT stator). On the other hand, the efficiency of a unidirectional transducer is approximately 3 dB better. Refer to [White \(1970\)](#), [Oliner et al. \(1978\)](#) and [Campbell \(1998\)](#) for some possible configurations.

In order to overcome reflections between the fingers, the thickness of the fingers should be much smaller than the wavelength ( $h/\lambda < 1\%$ ). However, the thickness should be larger than 50 nm in order to obtain a good conductivity ([Campbell 1998](#)). A common used material for an IDT finger pattern is aluminum. The fingers of our experimental stator are made of silver, since this material attached well to the stator and since it had a high conductivity. For the manufacturing process we refer to [Senturia \(2001\)](#), [Madou \(2002\)](#) and [Dijk \(2000\)](#).

## 5.2.2 Design parameters

In this subsection, we estimate the interrelations between the design parameters, the selections and the specifications. These interrelations are denoted in figure 5.1 by the gray blocks.

### Average tangential force

We will derive a relation between the input and output parameters that are shown in table 5.2 and indicated by block I in figure 5.1. The goal is to find the optimal preload force and the minimal number of projections. A global analytical relation between the parameters cannot be found. However, for one specific case we can find a solution.

Figure 3.38(b) demonstrates that for each wave amplitude a preload force exists for which the tangential force is maximal. From simulation it appears that the so-called release preload force (equation 3.23) approximates this optimal preload force.

$$F_{p,\text{opt}} = \hat{u}_z^{3/2} \frac{16}{3} \frac{k_n}{\pi\sqrt{2}} \quad (5.2)$$

selection (input):	stator Young modulus $E_2$ stator Poisson ratio $\sigma_2$ slider Young modulus $E_1$ slider Poisson ratio $\sigma_1$ radius of ball-shaped projection $R$ coefficient of friction $\mu_d$ force ratio $r_F$ normal wave amplitude $\hat{u}_z$
specification (input):	average tangential force $\bar{F}_t$
design parameters (output):	preload force $F_p$ number of contact points $p$

Table 5.2: Overview of input and output parameters used in the subsection ‘Average tangential force’.

R [mm]	$\hat{u}_z$ [nm]		
	4	8	12.5
1	0.5802	0.5799	0.5811
5	0.5798	0.5791	0.5804
10	0.5797	0.5798	0.5802

Table 5.3: Force ratios  $r_F = \bar{F}_t / (\mu_d F_p)$  for different radii and wave amplitudes found by simulation. The preload is set to the optimal value. The slider is made of silicon and the stator is made of PZT (PXE43).

where  $k_n$  is the normal stiffness of one projection (equation 3.5), which is a function of the selection parameters (table 5.2). In the remainder, we denote the approximated preload force by  $F_{p,\text{opt}}$ . Furthermore, the ratio  $r_F$  between the average tangential force  $\bar{F}_t$  and the maximum tangential force  $\mu_d F_p$  is approximately constant if the preload force equals  $F_{p,\text{opt}}$ .

$$r_F = \frac{\bar{F}_t}{\mu_d F_p} \quad (5.3)$$

Moreover, this ratio is almost independent of the projection radius and the wave amplitude. The simulation values in table 5.3 demonstrate this relation for a silicon slider and a PZT stator. The simulation is performed with the model of section 3.2 and the simulations parameters of table 5.4. The force-ratio  $r_F$  is approximately 0.58 for all simulated configurations. Table 5.4 lists also the force-ratio  $r_F$  for a slider made of silicon and a stator made of lithium niobate. Now it is possible to calculate the preload force and the *ideal* number of projections. With *ideal* we assume that every projection behaves like a single projection (section 3.3.1). The actual number of projections can be estimated on the basis of performed experiments. We illustrate the calculation with an example.

**Example 5.1.** We like to move a load with a certain motion profile. This requires a maximal no-velocity force of  $\bar{F}_t = 0.8$  N. The stator and slider materials are respectively  $128^\circ$  Y-X  $\text{LiNbO}_3$  and silicon. The radius of one slider projection is 6 mm and the wave amplitude is 10 nm.

slider (1)	stator (2)	$E_1$ [Gpa]	$E_2$ [Gpa]	$\sigma_1$	$\sigma_2$	$\mu_d$	$r_F$
Silicon	PXE43	107	77	0.3	0.3	0.13	0.58
Silicon	LiNbO <sub>3</sub> 128 ° Y-X	107	172	0.3	0.27	0.18	0.52

Table 5.4: Force-ratios  $r_F$  found by simulation.

**Solution:** The normal contact stiffness of one projection (equation 3.5) is

$$k_n = \frac{4}{3} \sqrt{RE} = 7.4 \text{ [GPa m}^{1/2}] \quad (5.4)$$

The optimal preload force of one projection is accordingly

$$F_{p,\text{opt}} = \hat{u}_z^{3/2} \frac{16}{3} \frac{k_n}{\pi \sqrt{2}} = 8.9 \text{ [mN]} \quad (5.5)$$

and the tangential force of one projection is found by

$$\bar{F}_{t,\text{single}} = \mu_d F_{p,\text{opt}} r_F = 0.84 \text{ [mN]} \quad (5.6)$$

The *ideal* number of projections and the total preload force are therefore respectively

$$\begin{aligned} p_{\text{ideal}} &= \frac{\bar{F}_t}{\bar{F}_{t,\text{single}}} = \frac{0.8}{0.84 \cdot 10^{-3}} \approx 1000 \\ F_{p,\text{total}} &= p_{\text{ideal}} F_{p,\text{opt}} = 1000 \cdot 8.9 \approx 9 \text{ [N]} \end{aligned} \quad (5.7)$$

In section 3.5 it is shown that the actual number of projections is approximately a factor 30 larger than the ideal number of projections. Hence, an indication for the actual number of projections is  $p = 30000$ .  $\square$

We showed that the motor force can be increased by the choice of material, the projection radius/shape and the number of projections. The effect of improvement (with respect to already a proper material choice) is the highest for the number of projections, medium for the projection radius and low for the material choice. Moreover, the number of applicable materials is limited. The projection shape is constrained by an emerging air-film that degrades the motor behavior. The number of projections is limited by the slider size, which complicates the uniform preload distribution (section 5.3) and an increasing slider length increases the wave attenuation at the contact interface, such that the trailing edge of the slider can block. Note that the number of projections can be increased by applying multiple sliders.

### Slider velocity

We will derive a relation between the input and output parameters that are shown in table 5.5 and indicated by block II in figure 5.1. The goal is to find the minimal SAW frequency, given the no-force slider velocity  $\dot{x}_s$ .

$R$ [mm]	$\hat{u}_z$ [nm] $f_r = 2.2$ [MHz]			$\hat{u}_z$ [nm] $f_r = 5$ [MHz]		$\hat{u}_z$ [nm] $f_r = 10$ [MHz]
	4	8	12.5	4	12.5	8
1	0.4682	0.4731	0.4746	0.4713	0.4730	0.4689
5	0.4693	0.4755	0.4775			
10	0.4709	0.4772	0.4803			

Table 5.6: Velocity ratios  $r_v$  for different radii, wave amplitudes and frequencies found by simulation. The preload is set to the optimal value. The slider is made of silicon and the stator is made of PZT (PXE43).

slider (1)	stator (2)	$E_1$ [Gpa]	$E_2$ [Gpa]	$\sigma_1$	$\sigma_2$	$\mu_d$	$r_{xz}$	$r_v$
Silicon	PXE43	107	77	0.3	0.3	0.13	0.64	$\approx 0.47$
Silicon	LiNbO <sub>3</sub> 128 ° Y-X	107	172	0.3	0.27	0.18	0.89	$\approx 0.45$

Table 5.7: Velocity-ratios  $r_v$  found by simulation.

selection (input):	stator wave amplitude ratio $r_{xz}$ velocity ratio $r_v$ normal wave amplitude $\hat{u}_z$
specification (input):	no-force slider velocity $\dot{x}_s$
design parameters (output):	frequency $f$

Table 5.5: Overview of input and output parameters used in the subsection ‘No-force slider velocity’.

In theory,  $\dot{x}_s$  does not depend on the number of projections  $p$  if the preload force per projection remains the same. Therefore, we only consider one projection for determining the frequency. Furthermore, we can also determine a ratio  $r_v$  between the no-force slider velocity  $\dot{x}_s$  and the tangential wave velocity amplitude  $\hat{u}_x$ , where the preload force equals the optimal preload force (optimal with respect to the tangential force). Note that a higher velocity is obtained with a smaller preload force).

$$r_v = \frac{\dot{x}_s}{\hat{u}_x} = \frac{\dot{x}_s}{\hat{u}_z \omega r_{xz}} \quad (5.8)$$

where  $r_{xz} = \frac{\hat{u}_x}{\hat{u}_z}$ , (section 2.1.3). Table 5.6 tabulates  $r_v$  for different radii, frequencies and amplitudes. The values are found using the simulation model of section 3.2 and the simulations parameters of table 5.7. The velocity-ratio  $r_v$  is approximately 0.47 for all configurations. The resulting velocity-ratios  $r_v$  are listed in table 5.7. We demonstrate the obtained design parameter by an example.

**Example 5.2.** The parameters and variables of example 5.1 are used. We like to find the frequency required to achieve a no-force velocity of 0.3 m/s.

**Solution:** The SAW frequency  $f_r$  follows directly from the data given in table 5.7

$$f_r = \frac{\dot{x}_s}{2\pi \hat{u}_z r_{xz} r_v} = 12 \quad [\text{MHz}] \quad (5.9)$$

□

Indeed, the velocity can be increased by increasing the frequency or by the choice of material. A velocity increase by applying a different material is marginal with respect to frequency sensitivity. The frequency is hardly limited for a SAW motor; frequencies larger than 1 GHz are possible. The theoretical maximal slider velocity  $\dot{x}_s = \omega \hat{u}_z r_{xy}$  is achieved when the normal force approaches zero.

### Stroke

Table 5.8 shows the input and output parameters for block III of figure 5.1. The frequency was found by the relation derived in the previous subsection. The goal is to find the minimal stator thickness and the IDT aperture width.

selection (input):	frequency $f_r$ stator (substrate) Rayleigh phase velocity $c_r$ beating attenuation $\frac{\hat{u}}{\hat{u}_0}$ Fresnel distance $\mathcal{X}$
specification (input):	stroke $x_{\text{stroke}}$
design parameters (output):	thickness stator $b$ IDT aperture width $2a$

Table 5.8: Overview of input and output parameters used in the subsection ‘Stroke’.

In section 2.1.4 we have found a relation between the stator thickness and the decrease of the wave amplitudes  $\frac{\hat{u}}{\hat{u}_0}$  due to beating (equation 2.19). The relation is valid for an isotropic plate that is free at both surfaces and has a Poisson ratio of  $\sigma = 0.3$ . The expression for the stator thickness was found to be:

$$n_{\text{thickness}} = -\log \left( \frac{\arccos \left( \frac{\hat{u}}{\hat{u}_0} \right)}{3.87 n_{\text{length}}} \right) \frac{1}{1.03} \quad (5.10)$$

where  $n_{\text{thickness}} = \frac{b}{\lambda_r}$  is the stator thickness in wavelengths and  $n_{\text{length}} = \frac{x}{\lambda_r}$  is the distance to the wave generating IDT in wavelengths. The wavelength of the SAW is found by  $\lambda_r = c_r/f_r$  where  $c_r$  is the Rayleigh wave phase velocity of the stator. In order to find a value for the thickness, we need to specify the wave amplitude decrease  $\frac{\hat{u}}{\hat{u}_0}$  at  $x = x_{\text{stroke}}$ .

We continue with the IDT aperture width. In section 2.2.2 we have mentioned that the diffraction of power is small if a point  $x$  lies within the Fresnel region, i.e., if the dimensionless Fresnel parameter  $\mathcal{X} < 1$ . By rewriting equation 2.24, we find an expression for the IDT aperture width  $2a$  ( $x = x_{\text{stroke}}$ ).

$$x_{\text{stroke}} = \mathcal{X} \frac{a^2}{\lambda_r} = \mathcal{X} \frac{a^2 f_r}{c_r} \Rightarrow 2a = 2 \sqrt{\frac{x_{\text{stroke}} c_r}{f_r \mathcal{X}}} \quad (5.11)$$

In order to find an aperture width, we need to specify  $\mathcal{X}$ . Furthermore, for an optimal use of the wave, the IDT aperture width should equal the slider width  $b_{\text{slider}}$ .

$$b_{\text{slider}} = 2a \quad (5.12)$$



The two design parameters are demonstrated by an example.

**Example 5.3.** The parameters of example 5.2 are used. We calculate the minimal stator thickness and the minimal slider aperture width. This minimal stator thickness is only a rough estimate because lithium niobate is anisotropic (and the relation is only valid for an isotropic material). The SAW frequency and the SAW phase velocity are 12 MHz and  $c_r = 3980$  m/s respectively. The stroke (plus the slider length) is  $x_{\text{stroke}} = 4$  cm, the maximal attenuation  $\frac{\hat{u}}{\hat{u}_0}$  at  $x = x_{\text{stroke}}$  is 0.95 and the Fresnel parameter is  $\mathcal{X} = 0.85$ .

**Solution:** First, the minimal thickness  $b$  of the stator is determined. The wavelength is:

$$\lambda_r = \frac{c_r}{f_r} = 0.33 \text{ [mm]} \quad (5.13)$$

Hence, the stroke in wavelengths is

$$n_{\text{length}} = \frac{x_{\text{stroke}}}{\lambda_r} = 114 \quad (5.14)$$

The minimal stator thickness is found by using equation 5.10

$$b = -\lambda_r \log \left( \frac{\arccos \left( \frac{\hat{u}}{\hat{u}_0} \right)}{3.87 n_{\text{length}}} \right) \frac{1}{1.03} = 1 \text{ [mm]} \quad (5.15)$$

Because this thickness is rather small we recommended to support the stator (section 5.3.2). Next, the aperture width  $2a$  is found by equation 5.11

$$2a = 2 \sqrt{\frac{x_{\text{stroke}} c_r}{f_r \mathcal{X}}} = 8 \text{ [mm]} \quad (5.16)$$

Hence, the slider width should also be 8 mm. □

Concluding, the stroke may be increased by increasing the IDT aperture width and the frequency by satisfying the stator thickness relation (equation 5.10). The effect of the aperture width with respect to the stroke is quadratic and with respect to the frequency linear. Since both parameters equally contribute to the power consumption (for  $u_z$  constant), it is preferred to increase the aperture width rather than the frequency.

### 5.2.3 Additional design parameters

Additional design parameters can be calculated by using the previously discussed design parameters.

### Slider length

The slider length is calculated in block IV of figure 5.1. We have found relations for estimating the number of projections  $p$  and the slider width  $b_{\text{slider}} = 2a$ . By specifying the pitch  $l_{\text{pitch}}$  between the projection, we can calculate the minimal slider length  $l_{\text{slider}}$ .

$$p = \left( \frac{b_{\text{slider}}}{l_{\text{pitch}}} + 1 \right) \left( \frac{l_{\text{slider}}}{l_{\text{pitch}}} + 1 \right) \Rightarrow$$

$$l_{\text{slider}} = \frac{pl_{\text{pitch}}^2}{b_{\text{slider}} + l_{\text{pitch}}} - l_{\text{pitch}} \approx \frac{pl_{\text{pitch}}^2}{b_{\text{slider}}} \quad (5.17)$$

**Example 5.4.** We continue with example 5.3. The projection pitch is  $l_{\text{pitch}} = 50 \mu\text{m}$ , the found number of projections was 30000 and  $b_{\text{slider}} = 2a = 8 \text{ mm}$ .

Accordingly the minimal slider length is  $l_{\text{slider}} = 10 \text{ mm}$ .  $\square$

The maximum slider length depends on the wave attenuation, i.e., the wave amplitude at the trailing edge of the slider should be sufficiently large to drive rather than block the slider.

### Power flow

The power flow is calculated in block V of figure 5.1. The total power flow  $P$  transported by the propagating SAW is (section 2.2.1)

$$P = 2a \frac{\hat{u}_z^2 \omega}{c_3^2} \quad (5.18)$$

where  $c_3$  is a material constant. Table 2.2 lists some power constant for different materials. Moreover, the power delivered by the power amplifiers, in the case of bidirectional IDT's, should at least be 2 times as large (section 2.3.1). If the power is too large we recommend to decrease the amplitude by a factor  $\kappa$ . This results in a proportional frequency increase and satisfies a decrease of the aperture width with the square root. Because the power is proportional to the frequency, quadratic to the amplitude and again proportional to the aperture width, the total power is decreased by a factor  $\kappa\sqrt{\kappa}$ . Unfortunately, an amplitude decrease reduces the tangential force.

**Example 5.5.** We continue with example 5.4. The IDT aperture width is  $2a = 8 \text{ mm}$ , the frequency is  $f_r = 12 \text{ MHz}$ , the wave amplitude is  $\hat{u}_z = 10 \text{ nm}$  and the power constant is approximately  $3.25 \cdot 10^{-6} \left[ \frac{m\sqrt{m}}{\sqrt{Ws}} \right]$ .

Accordingly, the total power flow is 5.6 W and the power delivered by the amplifiers is 11.2 W  $\square$ .

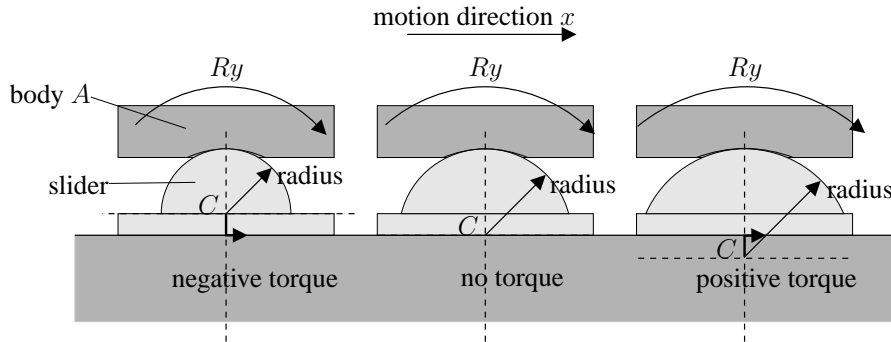


Figure 5.3: Ball-joint: variation of the rotation point  $C$ .

## 5.3 Guiding and preload mechanism design

In the previous section, we examined the inherent SAW motor design for which we supposed the presence of a preload force and a guiding of the slider motion. Design rules and design considerations of those two items are examined in this section.

### 5.3.1 Slider-stator contact

A well conditioned interface between the slider surface, or rather the projections of the slider and the stator surface is crucial for a proper SAW motor performance. One aspect is that slider and stator should be enabled to make contact over the whole slider area, i.e., the proper degrees of freedom between slider and stator need to be free. A second aspect is that the surfaces should be sufficiently flat. In the experimental setup we use a ball joint to set  $R_x$  and  $R_y$  of the slider free (figure 5.3) (Also  $R_z$  is free). The center  $C$  of the ball determines the point of rotation of the slider with respect to body  $A$ . Hence, due to the generated force of a SAW a negative torque will act on the slider if point  $C$  is above the stator surface and *vice versa*. As a consequence the pressure distribution at the slider stator interface is not uniform and moreover it depends on the tangential force. The pressure distribution is uniform if the  $C$  lies in the contact, which is the preferred situation. A ball joint is a simple but frictional configuration. In the literature, for example [Koster \(2000\)](#), alternative constructions are given.

A second aspect is the preload distribution at the slider-stator interface, which ideally should be uniform, again, for a proper SAW motor performance. However, when a slider is not uniformly preloaded (for example point loading), the slider deforms due to the limited stiffness. Consequently, the preload distribution at the slider-stator surface is not uniform. The distribution improves by

- increasing the rigidity/stiffness of the slider arrangement, e.g., by increasing the thickness (figure 5.4) or decreasing length and width of the contact interface;
- including a rubber ‘force distributor’ block in between a joint and a relatively compliant slider (figure 5.4).

By using multiple sliders, the length and width of a *single* slider can be decreased, while preserving the projection pitch and the number of projections. Some examples are pre-

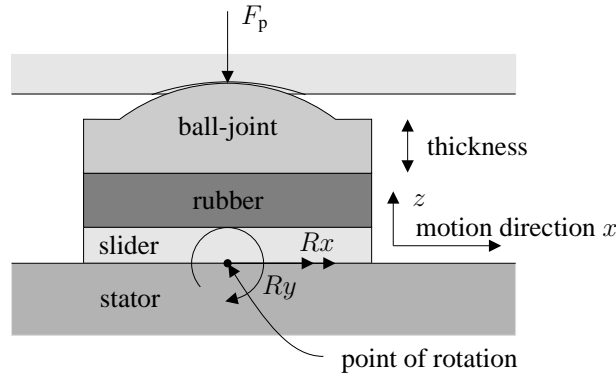


Figure 5.4: Improvement of the preload distribution.

sented in subsection 5.3.3. Rubbery materials, easily change shape but not volume (similar to water). The incompressibility is described by Poisson's ratio. For rubber, the Poisson ratio is close to the theoretical upper limit of 0.5. A rubber block has the advantages that it can accommodate also some degree of misalignment. Furthermore, production tolerances of the slider flatness are partly eliminated by applying a sufficiently small slider thickness in combination with a rubber block. In the experimental setup, we use dual-sided tape as a force distributor (section 1.5).

### 5.3.2 Slider/stator guiding

We start with a brief motivation. A slider that is pressed against a stator will block in  $x$ - and  $y$ -direction in absence of waves. The corresponding (dry) friction forces  $F_x$  and  $F_y$  are determined by the direction of the slider motion;

$$\begin{aligned} \begin{bmatrix} F_x \\ F_y \end{bmatrix} &= -\mu_d F_n \frac{1}{|\mathbf{v}|} \mathbf{v} \\ &= -\mu_d F_n \frac{1}{\sqrt{\dot{x}^2 + \dot{y}^2}} \begin{bmatrix} \dot{x} \\ \dot{y} \end{bmatrix} \quad \text{for } \sqrt{\dot{x}^2 + \dot{y}^2} > 0 \end{aligned} \quad (5.19)$$

where  $\dot{x}$  and  $\dot{y}$  are the slider velocity components,  $\mu_d$  the coefficient of friction and  $F_n$  the normal force. The friction forces change when a SAW propagates in  $x$ -direction. For explanation reasons we consider a rigid tangential contact. Thus, the tangential friction forces acting on the slider are

$$\begin{bmatrix} F_x \\ F_y \end{bmatrix} = -\mu_d F_n \frac{1}{|\mathbf{v}|} \begin{bmatrix} \dot{x} - \hat{u}_x \cos(\omega t) \\ \dot{y} \end{bmatrix} \quad \text{for } |\mathbf{v}| > 0 \quad (5.20)$$

where  $F_n = F_n(t)$  is the time dependent normal force,  $\hat{u}_x \cos(\omega t)$  the tangential wave velocity and

$$|\mathbf{v}| = \sqrt{(\dot{x} - \hat{u}_x \cos(\omega t))^2 + \dot{y}^2} \quad (5.21)$$

is the modulus of the sliding velocity. These relations demonstrate a considerably friction force decrease in  $y$ -direction if the ratio between the velocity difference in  $x$ -direction and  $\dot{y}$  is large. Therefore, also the average (macroscopic) friction force in  $y$ -direction decreases (Storck 2004), i.e., the  $y$ -motion is not constrained by a large friction force. Concluding, a slider guiding is necessary to conduct the slider in  $x$  direction and prevent a translation in  $y$ -direction (and a rotation around the  $z$ -axis).

There are numerous ways to achieve a (linear) guiding. We mention only two types.

- Linear ball bearings guiding, which consists of a rail/axis and a slide;
- Flexible beams (flexures) applied in different configurations. The material can for example be steel (Koster 2000) or silicon, which is usually applied in MEMS devices.

The stroke of a linear ball bearing is basically unlimited as the stroke of a flexure guiding is not. Furthermore, flexures have the drawback of generating counter forces. Nevertheless, they are suitable for application in micro structures (miniaturization) and in vacuum since they do not require additional precautions as ball bearings do. Furthermore, flexures are not affected by backlash and have (almost) no friction.

The specified closed loop motor performance, for example the tracking accuracy of a displacement reference profile, determines the guiding specifications. These specifications include the guiding configuration, stiffness and mass. Some basic design rules to increase the frequency of the slider-guiding vibration-modes are (section 4.1.1)

- a decrease of the moving mass;
- an increase of the stiffness of the guiding construction.

The mass is decreased by using truss or sheet constructions, light materials and by integrating the preload mechanism in the guiding construction. The stiffness is increased by reducing the distance between the point of actuation and the guiding. Furthermore, the guiding behavior is improved if the center of the moving mass lies in the center of actuation and if the guiding is symmetric with respect to the plane of actuation.

The recommendation are applied in the design of the preload mechanisms.

### Stator support

In subsection 5.2.1, we mentioned that a high stator flatness is preferred. To preserve the flatness of a (compliant) stator it is important to overcome stator deformation when attaching the stator to a motor frame or guiding (when the stator moves). This is achieved by statically determining the connection between stator and frame. The approach depends on the preload mechanism and the stator thickness. For a thin stator it may useful to first support the stator by a base plate, preferably with a similar relative expansion, before attaching it to the frame/guiding. Examples of statically determined construction are given in Koster (2000).

### 5.3.3 Preload mechanisms

In order to generate a friction force, it is necessary to preload the slider against the stator. The numerous preload mechanisms can be classified as one of the following types:

1. mechanical (springs);
2. magnetic (permanent magnets);
3. gravitational force;
4. electrostatic;
5. electromagnetic;
6. vacuum;
7. piezoelectric;
8. thermoelastic.

Types 4 until 8 require a power source and are therefore less suitable. However, electrostatic preloading can become interesting if the size of a SAW motor is downscaled, since the electrostatic force gains over inertial forces as the size of a system is decreased (Madou 2002). Types 1 until 3 are all tested on a SAW motor. Gravitational force is less useful for a practical SAW motor application, since it restricts the orientation of a SAW motor. Permanent magnets generate magnetic fields, which are unwanted in certain applications. Furthermore, the design of a ‘stable’ and relatively high preload-force-generating magnetic circuit is not trivial, which is seen as a drawback. The use of springs enables a light design that can generate large preload forces, which is therefore recommended.

The choice of a preload mechanism is determined by

- the required number of sliders;
- whether the stator or slider moves.

Figure 5.5 shows the basics of some mechanical preload mechanisms. The preload is adjustable and the guiding is placed symmetrically with respect to the plane(s) of actuation. Flexures, if required, may replace the ball bearing guiding.

## 5.4 Electronics of the control loop

In this section, we briefly enumerate the design considerations for the electronics of the control loop. See figure 5.6. First, we consider the displacement/velocity *measurement(s)* of a SAW motor. Basically, there are two limiting actuation – measurement configurations possible, which generate respectively.

1. non-observable behavior: the sensor is placed in the cog while the moving mass is *not* actuated in the cog;
2. non-controllable behavior: the moving mass is actuated in the cog while the sensor is *not* placed in the cog.

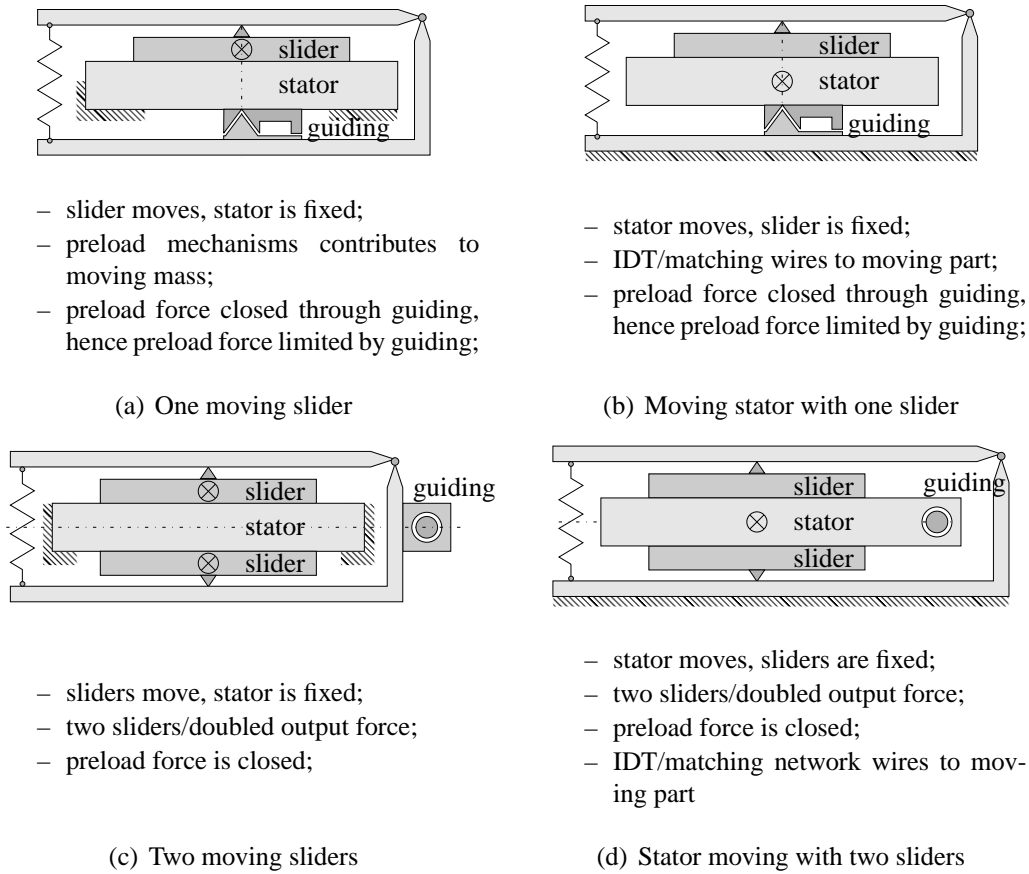


Figure 5.5: Basic configurations for mechanical preload.

The optimal location is determined by the system requirements.

The *controller* can be implemented in various ways, for instance on a computer with dedicated acquisition hardware, on a stand-alone digital signal processor (DSP) or with analog electronics. The controller discussed in section 4.4 does contain specific features (besides a homing algorithm).

Next, the control output is converted. In section 4.2, we have investigated different *actuation* schemes and recommended PWM actuation. The PWM signals can be generated by the controller hardware or by separate electronics. Subsequently, the PWM signals are *amplitude modulated* (AM). The amplitude modulation electronics can be combined with the PWM electronics. The resulting signals are high frequency signals. Hence, the energy is electromagnetic of nature. Therefore, coaxial cables (wave-guides) are utilized

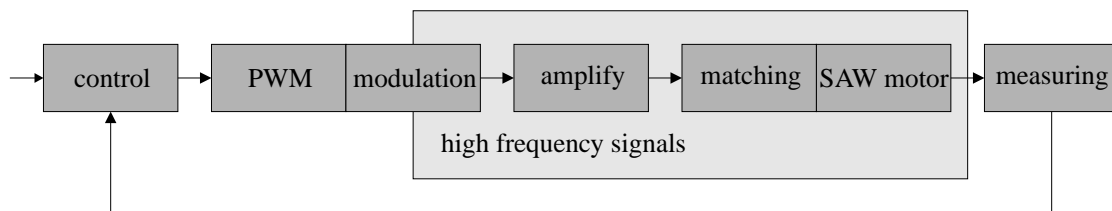


Figure 5.6: Overview of SAW motor control-loop hardware.

to confine the energy. Furthermore, the amplifiers and the IDT's should be matched to the characteristic impedance of the coaxial cables to overcome reflection and dispersion of the signals.

Next, the high frequency signals are *amplified*. Since, SAW motors operate in the high frequency (HF) band (3MHz to 30MHz), commercially power amplifier (broadcasting) are available. A *matching* network adapts the HF power before it reaches the IDT's. The components of the matching network should be rated to handle the power and the applied frequency. The generated waves drive the slider, which closes the loop.

## 5.5 Conclusions

In this chapter, we have discussed the design of a SAW motor to obtain an indication for the applied materials, the geometry, the construction and the electronics. First, the inherent SAW motor design was discussed and a design trajectory was proposed. The trajectory input parameters are the specifications of

- force;
- velocity;
- stroke;

and the properties of the selected

- stator and slider materials;
- geometry of slider;
- wave amplitude.

The resulting design parameters were derived at the preload force that maximizes the tangential force (optimal preload force). The resulting design parameters were the

- preload force;
- number of projections;
- frequency;
- aperture width;
- stator thickness;
- slider length;
- required power.

We have derived new relations to obtain these parameters. The *optimal preload* force is given by equation 5.2. The *force ratio*, the ratio between tangential slider force and preload force is given by equation 5.3, the *velocity ratio*, the ratio between tangential slider velocity and wave amplitude is given by equation 5.8 and a relation for the *minimal slider thickness* is given by equation 5.10.

Secondly, the guiding and the preload mechanism design were examined. We concluded



- that the contact between stator and slider is improved by using a ball-joint, a force distributor and restricting the maximal slider size;
- the necessity of a guiding;
- that guiding dynamics are improved by reducing mass and increasing stiffness, actuate in the center of mass and positioning the guiding symmetrical with the plane of actuation;
- the stator attachment should be statically determined to preserve stator flatness;
- mechanical preloading by springs enables a light design that can generate large preload forces.

Finally, we have briefly discussed the electronics of the closed loop. We concluded that

- coaxial cables should be utilized after the control signal is amplitude modulated;
- the transmitting and receiving high frequency parts should be matched to the characteristic impedance of the coaxial cables;
- the components of the matching networks should be rated to handle the power and the frequency.



# Chapter 6

## Conclusions

In this thesis, we have determined and analyzed the characteristics of a SAW motor which are interesting for potential applications and we have determined and explained the design parameters of a SAW motor. The insight was obtained by developing a SAW motor contact model, which describes the contact point behavior and the macroscopic motor behavior simultaneously.

The main results are:

- Both the maximum motor force and maximum motor velocity increase for rising contact stiffness. The contact stiffness increases by applying materials or coatings with a high Young modulus, by optimizing the projection shape and by increasing the number of projections. Furthermore, the motor force increases for a larger coefficient of friction.
- There exists an optimal preload force to achieve a maximum motor force for a given wave amplitude. At this optimum preload force, the contact behavior transits from continuous contact to intermittent contact. Moreover, at this preload force the ratio between the wave vibration velocity and the slider velocity is (almost) independent of projection radius and wave amplitude. Similarly, the ratio between the braking force and the motor force is (almost) independent of projection radius and wave amplitude.
- By means of a design trajectory, we can estimate design parameters of a SAW motor as a function of requirements like motor velocity, motor force and stroke. The resulting design parameters are the preload force, number of projections, frequency, aperture width, stator thickness, slider length and the required power.
- The wave amplitude has to exceed a dead zone before the motor starts to operate. This phenomenon is explained at contact point level, i.e., below the threshold amplitude (of the dead zone) the contact between slider and wave remains in stick-mode and accordingly no effective motion of the slider occurs. The threshold amplitude reduces by increasing the contact stiffness, decreasing the coefficient of friction and decreasing the preload force.
- In practice, the dead zone of the motor varies. By using PWM actuation (PWM of the high frequency carrier envelope), it is possible to eliminate this dead zone,

without the risk of overcompensation and without a large increase of wave power at small motor velocities.

- By simple closed-loop control, we have achieved a repetitive positioning accuracy of 20 nm (which corresponds to 3 encoder counts). This accuracy is high with respect to the stroke of the motor, which is 8 cm.
- The observed tracking error in closed-loop control is related to the roughness periodicity of the stator surface.
- The features of a SAW motor differ from those of electromagnetical motors. Therefore, potential applications of a SAW motor may be in areas where those features can be utilized or where electromagnetical motors are inadequate, especially applications that have low duty cycles, require a high accuracy and a relatively large stroke.

Potential attractive fields of application are:

- positioning of for example small mirrors, lenses, lasers and sensors in optical setups;
- positioning of samples in (electron-) microscopes for visualization and for material research (e.g. magnetic resonance force microscopy);
- actuators for use in space, (no lubrication, vacuum compatible);
- actuators with extreme demands regarding (low) electromagnetic fields.

## 6.1 Recommendations

Based on the research described in this thesis a number of recommendations can be formulated.

### Efficiency

Motor loss can cause a temperature rise and thereby a decrease of, for example, the positioning accuracy. The efficiency describes the motor loss. The efficiency of a SAW motor is small with respect to commercial traveling-wave motors. For example, the efficiency of the traveling-wave motor of Shinsei industry is 30% (Uchino 1998). The reported best performance SAW motor that uses coatings for improvement and no energy recycling (Nakamura et al. 2003) is approximately 1.3%. ( $F_x = 10$  N,  $\dot{x} = 0.8$  m/s,  $f = 10$  MHz,  $\hat{u}_z = 25$  nm,  $2a = 10$ mm  $\rightarrow P_{\text{motor}} \approx F_{x,\text{max}}\dot{x}_{s,\text{max}}/4 = 2$ W,  $P_{\text{in}} \approx 2P_{\text{wave}} \approx 4au_z^2\omega/(5 \cdot 10^{-12}) = 150$ W)

To improve the efficiency we recommend to apply unidirectional transducers (estimated gain of a factor 2). A second cause of efficiency decrease is that not all wave power is utilized for motion generation. In the example the slider width is 4mm and the IDT aperture width is 10mm. By reducing the IDT aperture width another factor 2.5 may be gained. So, the total efficiency could be 7%.

The wave power reaching the slider is partly used for motion generation, partly reflected and partly transmitted. Kurosawa et al. proposed energy circulation methods to reuse the transmitted energy. However, superposition of recycled energy and input energy appears

to be difficult due to a varying change of phase velocity along the slider-stator interface. As an alternative, we recommend to investigate the optimal slider length such that no wave energy is transmitted, but directly used for motion generation instead.

### **Wear**

Another important open aspect is the wear resistance of SAW motors, for example, in the context of lifespan and clean environments. The wear resistance has not yet been investigated for SAW-motors. Therefore, it is recommended to study the shape of the projections and the material/coating of slider and stator from a wear point of view.

### **Vacuum**

An analysis of the SAW motor operation in a vacuum environment is recommended to broaden the potential application field of SAW motors.

An experiment was performed to check if a SAW motor would still work under low-pressure conditions. To this end, a stator together with matching networks and a slider with an additional mass for preloading was placed in a vacuum chamber. The vacuum chamber was equipped with a cover made of glass such that the slider motion could be observed. The lowest pressure reached was 0.03 mbar. The motor seemed to operate well under these conditions. No quantitative measurements were performed, although it seemed that the low pressure did not influence the steady state velocity.

This result gives rise to recommend further study of the behavior in vacuum, e.g., the contact behavior.

### **Electromagnetic compatibility**

For the same reason, to broaden the potential application field, it is recommended to explore the electromagnetic compatibility. We do not expect problems with external electromagnetic fields. However, the IDT's and the matching networks radiated electromagnetic fields (when actuated). Shielding of those radiating elements is a possible way to obtain locally at the slider/stator contact a low electromagnetic field.

### **Squeeze film of air**

We concluded that motor force and motor velocity are improved by increasing the contact stiffness. One way to improve the contact stiffness is by optimizing the projection shape. However, this also influences the behavior of squeeze films of air between stator and slider. Therefore, it is recommended to find an optimal projection shape that has a high contact stiffness and still prevents the buildup of air films.

**Tracking error due to the stator roughness**

The observed tracking error in closed-loop control is related to the roughness periodicity of the stator surface. In order to reduce this tracking error we recommended to investigate stators with a *smaller roughness*. Alternatively, we recommend to *improve* the *sensitivity function* for the associated roughness frequency band, which implies an increase of the proportional gain and subsequently it requires an increase of the guiding vibration frequencies. Finally, since the error due to roughness is position dependent, it could be possible to compensate it by means of *feed forward control*.

# Appendix A

## Uniform plane wave solution

In this appendix, we illustrate the solution of uniform planes waves in a non-piezoelectric linear homogenous solid (Auld 1990). We start by introducing the in acoustics commonly used reduced notation of stress, strain and stiffness tensors.

### Reduced notation

The strain tensor  $\mathbf{S}$  is symmetric and is usually specified by one index (Auld 1990).

$$\mathbf{S} = \begin{bmatrix} S_{11} & S_{12} & S_{13} \\ S_{12} & S_{22} & S_{23} \\ S_{13} & S_{23} & S_{33} \end{bmatrix} = \begin{bmatrix} S_1 & \frac{1}{2}S_6 & \frac{1}{2}S_5 \\ \frac{1}{2}S_6 & S_2 & \frac{1}{2}S_4 \\ \frac{1}{2}S_5 & \frac{1}{2}S_4 & S_3 \end{bmatrix} \quad (\text{A.1})$$

Six instead of nine elements now describe the strain, often written as  $\mathbf{S} = [S_1, S_2, S_3, S_4, S_5, S_6]^T$ . The factor a half accounts for the reduction of elements. A similar reduced subscript notation exist for the stress tensor

$$\mathbf{T} = \begin{bmatrix} T_{11} & T_{12} & T_{13} \\ T_{12} & T_{22} & T_{23} \\ T_{13} & T_{23} & T_{33} \end{bmatrix} = \begin{bmatrix} T_1 & T_6 & T_5 \\ T_6 & T_2 & T_4 \\ T_5 & T_4 & T_3 \end{bmatrix} \quad (\text{A.2})$$

or  $\mathbf{T} = [T_1, T_2, T_3, T_4, T_5, T_6]^T$ . Moreover, an associated reduced stiffness matrix is derived from the stiffness tensor of equation 2.5. The components of the rank 4 stiffness tensor are dependent i.e.,  $c_{ijkl} = c_{jikl} = c_{ijlk} = c_{klij}$ , which restricts the number of elements to 21 rather than 81. Therefore, the reduced matrix notation can be used viz.  $c_{IJ}$  where  $I, J \in \{1, 2, 3, 4, 5, 6\}$ . The symmetry in the solid restricts the number of independent elements further. An isotropic solid, for example, has only two independent elements.

### Wave solution

Equation 2.6 can be described as a matrix multiplication

$$\rho \ddot{\mathbf{u}} - \mathbf{D}^T \mathbf{C} \mathbf{D} \mathbf{u} = 0 \quad (\text{A.3})$$

by using the matrix operator

$$\mathbf{D}^T = \begin{bmatrix} \frac{\partial}{\partial x_1} & 0 & 0 & 0 & \frac{\partial}{\partial x_3} & \frac{\partial}{\partial x_2} \\ 0 & \frac{\partial}{\partial x_2} & 0 & \frac{\partial}{\partial x_3} & 0 & \frac{\partial}{\partial x_1} \\ 0 & 0 & \frac{\partial}{\partial x_3} & \frac{\partial}{\partial x_2} & \frac{\partial}{\partial x_1} & 0 \end{bmatrix}$$

and the reduced  $6 \times 6$  stiffness matrix  $\mathbf{C}$ .

For time-harmonic fields the analysis is greatly simplified by the so-called phasor notation (Cheng 1989). For example, instead of using  $\hat{u} \cos(\omega t + \phi)$  in an analysis, we use  $\hat{u} e^{j(\omega t + \phi)}$ , where the real-part of the resulting exponential solution is calculated as the final step.

Consider an uniform plane wave that propagates along the  $\mathbf{l} = (l_1, l_2, l_3)^T$  direction. The general solution of a plane wave in a linear, homogenous solid is

$$\mathbf{u} = \hat{\mathbf{u}} e^{j(\omega t - k \mathbf{l} \cdot \mathbf{x})} \quad (\text{A.4})$$

To obtain the plane wave solution we need to find the amplitude vectors  $\hat{\mathbf{u}}$  and the wave vectors  $k$ . Substitution of equation A.4 in equation A.3 leads to

$$\begin{aligned} -\omega^2 \rho \hat{\mathbf{u}} + k_r^2 \mathbf{L}^T \mathbf{C} \mathbf{L} \hat{\mathbf{u}} &= 0 \\ \left( \frac{\omega^2}{k_r^2} \mathbf{I} - \mathbf{L}^T \mathbf{C} \mathbf{L} \frac{1}{\rho} \right) \hat{\mathbf{u}} &= 0 \end{aligned} \quad (\text{A.5})$$

where  $\mathbf{I}$  is a  $3 \times 3$  identity matrix and

$$\mathbf{L}^T = \begin{bmatrix} l_1 & 0 & 0 & 0 & l_3 & l_2 \\ 0 & l_2 & 0 & l_3 & 0 & l_1 \\ 0 & 0 & l_3 & l_2 & l_1 & 0 \end{bmatrix} \quad (\text{A.6})$$

The problem of the uniform plane wave solutions is reduced to an eigenvalue problem (e.g.  $(s\mathbf{I} - \mathbf{A})\mathbf{x} = 0$ ). The square roots of the eigenvalues  $\sqrt{\omega^2/k_r^2}$  correspond to the associate phase velocities  $c$  of the plane wave solution. The eigenvectors  $\hat{\mathbf{u}}$  determines the type of the plane wave.

**Example A.1.** Consider an uniform plane wave solution that propagates in a rotational symmetric solid (hexagonal crystal class, for example PZT in a plane normal to the poling axis) along the propagation vector  $\hat{\mathbf{l}} = (l_1, l_2, l_3)^T = (\cos(\phi), \sin(\phi), 0)^T$ . The reduced stiffness matrix is (Auld 1990)

$$\mathbf{C} = \begin{bmatrix} c_{11} & c_{12} & c_{13} & 0 & 0 & 0 \\ c_{12} & c_{11} & c_{13} & 0 & 0 & 0 \\ c_{13} & c_{13} & c_{33} & 0 & 0 & 0 \\ 0 & 0 & 0 & c_{44} & 0 & 0 \\ 0 & 0 & 0 & 0 & c_{44} & 0 \\ 0 & 0 & 0 & 0 & 0 & c_{66} \end{bmatrix}$$



where  $c_{66} = (c_{11} - c_{12})/2$ . The eigenvalues  $s = \frac{\omega^2}{k^2}$  are found by finding the roots of the characteristic polynomial:

$$\begin{aligned} & \left| s\mathbf{I} - \mathbf{L}^T\mathbf{C}\mathbf{L}\frac{1}{\rho} \right| = 0 \\ & \left| \begin{bmatrix} s - \frac{\cos(\phi)^2 c_{11} + \sin(\phi)^2 c_{66}}{\rho} & -\frac{\cos(\phi)c_{12}\sin(\phi) + \sin(\phi)c_{66}\cos(\phi)}{\rho} & 0 \\ -\frac{\cos(\phi)c_{12}\sin(\phi) + \sin(\phi)c_{66}\cos(\phi)}{\rho} & s - \frac{\cos(\phi)^2 c_{66} + \sin(\phi)^2 c_{11}}{\rho} & 0 \\ 0 & 0 & s - \frac{c_{44}}{\rho} \end{bmatrix} \right| = 0 \end{aligned}$$

The positive square roots of the eigenvalues are the phase velocities of the three plane waves modes.

$$c_l = \sqrt{\frac{c_{11}}{\rho}}, \quad c_{sv} = \sqrt{\frac{c_{44}}{\rho}}, \quad c_{sh} = \sqrt{\frac{c_{66}}{\rho}} \quad (\text{A.7})$$

( $c_{sv} = c_{sh}$  for an isotropic solid). From the eigenvectors, which are derived next, we can see that they relate respectively to a pure longitudinal, a pure shear wave polarized parallel to  $x_3$  axis (sv) and a pure shear wave polarized normal to the  $x_3$  direction (sh) (figure 2.4). Note that the values do not depend on the direction in the considered plane, i.e. the phase velocity is not a function of the angle  $\phi$ . The eigenvectors are determined by substitution of the eigenvalues in equation A.5 and solving for  $\hat{\mathbf{u}}$ .

$$\hat{\mathbf{u}}_l = \begin{bmatrix} \cos \phi \\ \sin \phi \\ 0 \end{bmatrix}, \quad \hat{\mathbf{u}}_{s,sv} = \begin{bmatrix} 0 \\ 0 \\ 1 \end{bmatrix}, \quad \hat{\mathbf{u}}_{s,sh} = \begin{bmatrix} -\sin \phi \\ \cos \phi \\ 0 \end{bmatrix}$$



# Appendix B

## Rayleigh wave solution in an isotropic half-space

In this appendix we derive the Rayleigh wave solution for an isotropic solid by means of the potential theory (figure 2.5). The reduced stiffness matrix of an isotropic material has two independent states.

$$\mathbf{C} = \begin{bmatrix} c_{11} & c_{12} & c_{12} & 0 & 0 & 0 \\ c_{12} & c_{11} & c_{12} & 0 & 0 & 0 \\ c_{12} & c_{12} & c_{11} & 0 & 0 & 0 \\ 0 & 0 & 0 & c_{44} & 0 & 0 \\ 0 & 0 & 0 & 0 & c_{44} & 0 \\ 0 & 0 & 0 & 0 & 0 & c_{44} \end{bmatrix} \quad (\text{B.1})$$
$$c_{11} = c_{12} + 2c_{44}$$

In the literature often the two Lamé constants,  $\lambda$  and  $\mu$ , are used to describe the wave equation of an isotropic solid.

$$\mathbf{C} = \begin{bmatrix} \lambda + 2\mu & \lambda & \lambda & 0 & 0 & 0 \\ \lambda & \lambda + 2\mu & \lambda & 0 & 0 & 0 \\ \lambda & \lambda & \lambda + 2\mu & 0 & 0 & 0 \\ 0 & 0 & 0 & \mu & 0 & 0 \\ 0 & 0 & 0 & 0 & \mu & 0 \\ 0 & 0 & 0 & 0 & 0 & \mu \end{bmatrix} \quad (\text{B.2})$$

Table B.1 shows the relations between the stiffness tensor elements, the Lamé constants and the Young's modulus  $E$ , the shear modulus  $G$  and Poisson's ratio  $\sigma$  (Gooberman 1968).

tensor elements	Lamé constants	Young's modulus and Poisson's ratio
$c_{11}$	$\lambda + 2\mu$	$\frac{E(1-\sigma)}{(1+\sigma)(1-2\sigma)}$
$c_{12}$	$\lambda$	$\frac{-E\sigma}{2\sigma^2 + \sigma - 1}$
$c_{44}$	$\mu$	$\frac{E}{2(1+\sigma)} = (G)$

Table B.1: Relation between variables.

Substitution of equation B.2 in equation A.3 yields

$$\rho \begin{pmatrix} \frac{\partial^2 u_x}{\partial t^2} \\ \frac{\partial^2 u_y}{\partial t^2} \\ \frac{\partial^2 u_z}{\partial t^2} \end{pmatrix} = \mu \begin{pmatrix} \frac{\partial^2 u_x}{\partial x^2} + \frac{\partial^2 u_x}{\partial y^2} + \frac{\partial^2 u_x}{\partial z^2} \\ \frac{\partial^2 u_y}{\partial x^2} + \frac{\partial^2 u_y}{\partial y^2} + \frac{\partial^2 u_y}{\partial z^2} \\ \frac{\partial^2 u_z}{\partial x^2} + \frac{\partial^2 u_z}{\partial y^2} + \frac{\partial^2 u_z}{\partial z^2} \end{pmatrix} + (\lambda + \mu) \begin{pmatrix} \frac{\partial^2 u_x}{\partial x^2} + \frac{\partial^2 u_y}{\partial x \partial y} + \frac{\partial^2 u_z}{\partial x \partial z} \\ \frac{\partial^2 u_x}{\partial y \partial x} + \frac{\partial^2 u_y}{\partial y^2} + \frac{\partial^2 u_z}{\partial y \partial z} \\ \frac{\partial^2 u_x}{\partial z \partial x} + \frac{\partial^2 u_y}{\partial z \partial y} + \frac{\partial^2 u_z}{\partial z^2} \end{pmatrix} \quad (\text{B.3})$$

or in compact form

$$\rho \frac{\partial^2 \mathbf{u}}{\partial t^2} = \mu \nabla^2 \mathbf{u} + (\lambda + \mu) \nabla (\nabla \cdot \mathbf{u}) \quad (\text{B.4})$$

where  $\mathbf{u}$  is the displacement vector  $(u_x, u_y, u_z)^T$ . By using Helmholtz theorem/decomposition (Cheng 1989)[p.64] we can write the displacement into the sum of gradient and curl:

$$\mathbf{u} = \nabla \phi + \nabla \times \psi \quad (\text{B.5})$$

$$= \begin{pmatrix} \frac{\partial \phi}{\partial x} + \frac{\partial \psi_z}{\partial y} - \frac{\partial \psi_y}{\partial z} \\ \frac{\partial \phi}{\partial y} + \frac{\partial \psi_x}{\partial z} - \frac{\partial \psi_z}{\partial x} \\ \frac{\partial \phi}{\partial z} + \frac{\partial \psi_y}{\partial x} - \frac{\partial \psi_x}{\partial y} \end{pmatrix} \quad (\text{B.6})$$

where  $\phi$  is a scalar  $\psi$  is a vector. Substitution in B.4 gives.

$$\rho \frac{\partial^2 (\nabla \phi + \nabla \times \psi)}{\partial t^2} = \mu \nabla^2 (\nabla \phi + \nabla \times \psi) + (\lambda + \mu) \nabla (\nabla \cdot (\nabla \phi + \nabla \times \psi)) \quad (\text{B.7})$$

By using some vector identities (Cheng 1989) where  $\mathbf{A}$  is a vector and  $V$  a scalar,

$$\nabla \times \nabla \times \mathbf{A} = \nabla (\nabla \cdot \mathbf{A}) - \nabla^2 \mathbf{A} \quad (\text{B.8})$$

$$\nabla \times \nabla V = 0 \quad (\text{B.9})$$

$$\nabla \cdot (\nabla \times \mathbf{A}) = 0 \quad (\text{B.10})$$

$$\nabla \cdot \nabla V = \nabla^2 V \quad (\text{B.11})$$

equation B.7 can be written as

$$\underbrace{\nabla \left( \rho \frac{\partial^2 \phi}{\partial t^2} - (\lambda + 2\mu) \nabla^2 \phi \right)}_{\text{gradient}} + \underbrace{\nabla \times \left( \rho \frac{\partial^2 \psi}{\partial t^2} - \mu \nabla^2 \psi \right)}_{\text{curl}} = 0 \quad (\text{B.12})$$

This equation is satisfied if

$$\rho \frac{\partial^2 \phi}{\partial t^2} - (\lambda + 2\mu) \nabla^2 \phi = 0 \Rightarrow \frac{1}{c_1^2} \frac{\partial^2 \phi}{\partial t^2} - \nabla^2 \phi = 0 \quad (\text{B.13})$$

$$\rho \frac{\partial^2 \psi}{\partial t^2} - \mu \nabla^2 \psi = 0 \Rightarrow \frac{1}{c_s^2} \frac{\partial^2 \psi}{\partial t^2} - \nabla^2 \psi = 0 \quad (\text{B.14})$$

where we used the relation  $c_1 = \sqrt{\frac{c_{11}}{\rho}} = \sqrt{\frac{\lambda+2\mu}{\rho}}$  and the shear phase velocity  $c_s = \sqrt{\frac{c_{44}}{\rho}} = \sqrt{\frac{\mu}{\rho}}$  (equation 2.9, table B.1).

### Finding $\phi$ and $\psi$

Assume that the scalar  $\phi$  and the vector  $\psi$  have the following form when searching for surface waves

$$\phi = f(z) e^{i(k_r x - \omega t)} \quad (\text{B.15})$$

$$\psi = \mathbf{g}(z) e^{i(k_r x - \omega t)} \quad (\text{B.16})$$

By substitution of  $\phi$  and  $\psi$  in equation B.13 and equation B.14 we find

$$\frac{d^2 f(z)}{dz^2} + (k_l^2 - k_r^2) f(z) = 0 \quad (\text{B.17})$$

$$\frac{d^2 \mathbf{g}(z)}{dz^2} + (k_s^2 - k_r^2) \mathbf{g}(z) = 0 \quad (\text{B.18})$$

The solutions of  $f(z)$  and  $\mathbf{g}(z)$  are

$$f(z) = F_1 e^{-z \sqrt{k_r^2 - k_l^2}} + F_2 e^{z \sqrt{k_r^2 - k_l^2}} \quad (\text{B.19})$$

$$\mathbf{g}(z) = \mathbf{G}_1 e^{-z \sqrt{k_r^2 - k_s^2}} + \mathbf{G}_2 e^{z \sqrt{k_r^2 - k_s^2}} \quad (\text{B.20})$$

where  $F_1$  and  $F_2$  are arbitrary scalar constants and  $\mathbf{G}_1$  and  $\mathbf{G}_2$  are arbitrary vector constants. Solutions with positive roots correspond to along surface motion (the motion decays for  $z \rightarrow -\infty$ ,  $k_r^2 > k_s^2 > k_l^2$ ). Therefore,  $\phi$  and  $\psi$  are

$$\phi = F_2 e^{z \sqrt{k_r^2 - k_l^2}} e^{i(k_r x - \omega t)} \quad (\text{B.21})$$

$$\psi = \mathbf{G}_2 e^{z \sqrt{k_r^2 - k_s^2}} e^{i(k_r x - \omega t)} \quad (\text{B.22})$$

### Boundary conditions

Consider again figure 2.5 where we assume an uniform wave field in  $y$ -direction and a stress free boundary ( $T_{zz} = T_3$  and  $T_{xz} = T_5$ ).

$$\begin{aligned}
 0 &= T_3 \\
 &= c_{12}S_1 + c_{11}S_3 \\
 &= \lambda \frac{\partial u_x}{\partial x} + (\lambda + 2\mu) \frac{\partial u_z}{\partial z} \\
 &= \lambda \left( \frac{\partial^2 \phi}{\partial x^2} - \frac{\partial^2 \psi_y}{\partial x \partial z} \right) + (\lambda + 2\mu) \left( \frac{\partial^2 \phi}{\partial z^2} + \frac{\partial^2 \psi_y}{\partial x \partial z} \right)
 \end{aligned} \tag{B.23}$$

$$\begin{aligned}
 0 &= T_5 \\
 &= c_{44}S_5 \\
 &= \mu \left( \frac{\partial u_x}{\partial z} + \frac{\partial u_z}{\partial x} \right) \\
 &= \mu \left( 2 \frac{\partial^2 \phi}{\partial x \partial z} - \frac{\partial^2 \psi_y}{\partial z^2} + \frac{\partial^2 \psi_y}{\partial x^2} \right)
 \end{aligned} \tag{B.24}$$

where we used the reduced notation (appendix A) and equation 2.4. We define  $\sqrt{k_r^2 - k_l^2} = q$  and  $\sqrt{k_r^2 - k_s^2} = s$ . By substitution of equations B.21 and B.22 in equations B.23 and B.24 we find

$$\begin{pmatrix} 2iqk & k_r^2 + s^2 \\ k_r^2 \frac{\lambda}{2\mu} - q^2(1 + \frac{\lambda}{2\mu}) & isk \end{pmatrix} \begin{pmatrix} F_2 \\ G_{2,y} \end{pmatrix} = 0 \tag{B.25}$$

By using the relation between the longitudinal and shear wave vector we find (equation A.7, table B.1 and  $k = \frac{\omega}{c}$ )

$$k_l^2 = \frac{\mu}{\lambda + 2\mu} k_s^2 \tag{B.26}$$

$$k_r^2 + s^2 = -k_r^2 \frac{\lambda}{\mu} + q^2(2 + \frac{\lambda}{\mu}) \tag{B.27}$$

Such that equation B.25 can be written as

$$\begin{pmatrix} 2iqk_r & k_r^2 + s^2 \\ k_r^2 + s^2 & -2isk_r \end{pmatrix} \begin{pmatrix} F_2 \\ G_{2,y} \end{pmatrix} = 0 \tag{B.28}$$

The characteristic polynomial of the matrix of equation B.28 is called the Rayleigh equation and is used to find the wave vector  $k_r$ . To find a non-zero solution, the characteristic polynomial of the previous matrix has to satisfy

$$4k_r^2 qs - (k_r^2 + s^2)^2 = 0 \tag{B.29}$$

In Auld (1990) an approximation of the solution is given

$$\frac{k_s}{k_r} \approx \frac{0.87 - 1.12\sigma}{1 + \sigma} \tag{B.30}$$

Next,  $F_2$  is derived as a function of  $G_{2,y}$  is (equation B.28)

$$\begin{aligned} F_2 &= i \frac{1}{2} \frac{(k_r^2 + s^2) G_{2,y}}{qk} \\ &= i 2 \frac{sk G_{2,y}}{k_r^2 + s^2} \end{aligned} \quad (\text{B.31})$$

Finally, by using

$$\begin{aligned} u_x &= \frac{\partial \phi}{\partial x} - \frac{\partial \psi_y}{\partial z} \\ u_z &= \frac{\partial \phi}{\partial z} + \frac{\partial \psi_y}{\partial x} \end{aligned} \quad (\text{B.32})$$

and substitution of equations B.21 and B.22 we can derive a relation for  $u_x$  and  $u_z$ .

$$\begin{aligned} u_x &= \frac{C}{2q} (2s q e^{zs} - (k_r^2 + s^2) e^{zq}) e^{i\omega t - i k_r x} \\ u_z &= i \frac{C}{2k_r} (2k_r^2 e^{zs} - (k_r^2 + s^2) e^{zq}) e^{i\omega t - i k_r x} \end{aligned} \quad (\text{B.33})$$

Hence, the real Rayleigh wave distribution is

$$\begin{aligned} Re(u_x) &= \frac{C}{2q} (2s q e^{zs} - (k_r^2 + s^2) e^{zq}) \cos(\omega t - k_r x) \\ Re(u_z) &= \frac{C}{2k_r} (2k_r^2 e^{zs} - (k_r^2 + s^2) e^{zq}) \sin(\omega t - k_r x) \end{aligned} \quad (\text{B.34})$$





# Appendix C

## Lamb dispersion curve

Figure 2.10 shows a dispersion curve of Lamb waves in an isotropic plate. This curve is obtained by a Matlab routine, which is based on a bisectional search algorithm. This routine solves the so-called Rayleigh-Lamb frequency equations given by Auld (1990).

The symmetric Rayleigh Lamb frequency equation is

$$\frac{\tan\left(1/2\sqrt{(\omega b/c_s)^2 - (\beta b)^2}\right)}{\tan\left(1/2\sqrt{(\omega b/c_1)^2 - (\beta b)^2}\right)} = -\frac{4(\beta b)^2\sqrt{(\omega b/c_1)^2 - (\beta b)^2}\sqrt{(\omega b/c_s)^2 - (\beta b)^2}}{((\omega b)/c_1)^2 - 2(\beta b)^2}$$

$$\frac{\tan\left(1/2\sqrt{(\pi y)^2 - x^2}\right)}{\tan\left(1/2\sqrt{a(\pi y)^2 - x^2}\right)} = -\frac{4x^2\sqrt{a(\pi y)^2 - x^2}\sqrt{(\pi y)^2 - x^2}}{(a(\pi y)^2 - 2(x)^2)^2} \quad (\text{C.1})$$

where  $\beta = \omega/c_{\text{Lamb}}$  is the wave vector and  $c_{\text{Lamb}}$  is the phase velocity. The plate thickness is  $b$  and  $c_s$  and  $c_1$  are the shear and longitudinal plane wave phase velocity respectively. Furthermore, we have used  $x = \beta b$ ,  $y = 2fb/c_s$  and  $a = (c_s/c_1)^2$ . Similarly, the asymmetric Rayleigh Lamb frequency equation is

$$\frac{\tan\left(1/2\sqrt{(\omega b/c_s)^2 - (\beta b)^2}\right)}{\tan\left(1/2\sqrt{(\omega b/c_1)^2 - (\beta b)^2}\right)} = -\frac{((\omega b)/c_1)^2 - 2(\beta b)^2}{4(\beta b)^2\sqrt{(\omega b/c_1)^2 - (\beta b)^2}\sqrt{(\omega b/c_s)^2 - (\beta b)^2}}$$

$$\frac{\tan\left(1/2\sqrt{(\pi y)^2 - x^2}\right)}{\tan\left(1/2\sqrt{a(\pi y)^2 - x^2}\right)} = -\frac{(a(\pi y)^2 - 2(x)^2)^2}{4x^2\sqrt{a(\pi y)^2 - x^2}\sqrt{(\pi y)^2 - x^2}} \quad (\text{C.2})$$

We have solved these equations by performing the following steps:

1. determine the intervals of the two tan-functions (begin and end point of the intervals) and make an ascending list of these points;
2. set an  $x$  value. Search for a  $y$ -solution of equation C.1 and C.2 within every two adjacent points of the list. Approach the solution by utilizing a bisectional algorithm.
3. Assign each found  $y$  to the proper mode.



# Appendix D

## IDT admittance matrix

In an equivalent circuit model each IDT finger is represented by a three-port network. One port is the electrical port and the other two ports are electrical equivalents of the acoustic ports. The total IDT model consists out of the cascade of three-port networks and can be represented by an admittance matrix  $Y$  (Campbell 1998). Figure D.1 shows a representation of the total model.

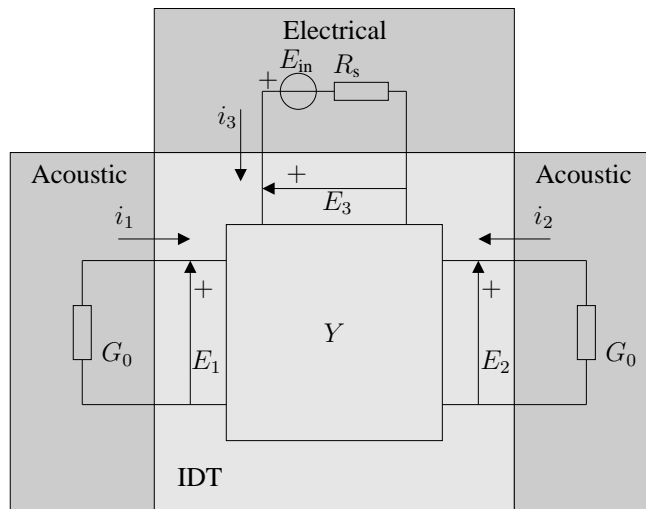


Figure D.1: Three port equivalent admittance network representation for an IDT.

The acoustic ports are one-dimensional, i.e., it is assumed that there is no diffraction such that a wave at each point can be represented by a scalar, e.g., the normal surface particle velocity. The equivalent current  $i$  and voltage  $E$  are related to the velocity  $v$  and force  $F$  by

$$E = \frac{F}{r} \tag{D.1}$$

$$i = \dot{u}_3 r \tag{D.2}$$

where  $r$  is the electric acoustic transformation ratio. When the electrode width equals the width of the gaps the value of  $r$  is

$$r = \sqrt{f_0 C_s K^2 Z_0} \quad (\text{D.3})$$

where  $K^2$  is the electromechanical coupling constant,  $C_s$  the static capacitance of one periodic section and  $f_0$  the IDT center frequency. An acoustic impedance  $Z_0$  can be found by the power flow and the normal particle velocity.

$$Z_0 = \frac{\mathcal{P}4a}{\hat{u}_3^2} \quad (\text{D.4})$$

where  $2a$  is the aperture width,  $\mathcal{P}$  the acoustic power flow per unit width and  $\hat{u}_3$  the amplitude of the normal particle velocity. The power flow per unit width is discussed in section 2.2.1. The equivalent acoustic admittance is

$$G_0 = \frac{r^2}{Z_0} \quad (\text{D.5})$$

$$= K^2 C_s f_0 \quad (\text{D.6})$$

We assume that reflections from IDT finger discontinuities can be disregarded. This assumption is valid if the ratio between film-thickness and the wavelength ( $h/\lambda_0$ ) is  $\ll 1\%$  (Campbell 1998). In that case the current-voltage relation is

$$\begin{pmatrix} i_1 \\ i_2 \\ i_3 \end{pmatrix} = \begin{pmatrix} Y_{11} & Y_{12} & Y_{13} \\ Y_{12} & Y_{11} & -Y_{13} \\ Y_{13} & -Y_{13} & Y_{33} \end{pmatrix} \begin{pmatrix} E_1 \\ E_2 \\ E_3 \end{pmatrix} \quad (\text{D.7})$$

The admittance matrix elements are

$$Y_{11} = -iG_0 \cot(N\theta) \quad (\text{D.8})$$

$$Y_{12} = iG_0 \csc(N\theta) \quad (\text{D.9})$$

$$Y_{13} = -iG_0 \tan(\theta/4) \quad (\text{D.10})$$

$$Y_{33} = i\omega C_T + i4NG_0 \tan(\theta/4) \quad (\text{D.11})$$

where  $N$  is the number of electrode pairs,  $\theta = 2\pi f/f_0$  the electrical transit angle and  $C_T = NC_s$  the total IDT capacitance. By terminating both acoustic ports with the characteristic admittance  $G_0$ , as shown in figure D.1, we can determine the relation between the input voltage  $E_3$  and the normal wave particle velocity.

$$\frac{\hat{u}_3}{E_3} = \frac{Y_{13}}{Y_{11} - Y_{12} + G_0} \frac{G_0}{r} \quad (\text{D.12})$$

$$= -\tan\left(\frac{1}{2}\frac{\pi f}{f_0}\right) \sin\left(\frac{N\pi f}{f_0}\right) e^{-\frac{iN\pi f}{f_0}} \frac{G_0}{r} \quad (\text{D.13})$$

$$(\text{D.14})$$

At the center frequency, the ratio is  $2NG_0/r$ . With the same termination, we can determine the electrical input admittance as well.

$$Y_{\text{el}} = -\frac{2Y_{13}^2}{Y_{11} - Y_{12} + G_0} + Y_{33} \quad (\text{D.15})$$

$$\approx \underbrace{8N^2G_0 \frac{\sin^2(x)}{x^2}}_{G_a} + i \underbrace{8N^2G_0 \frac{\sin(2x) - 2x}{2x^2}}_{B_a} + i\omega C_T \quad (\text{D.16})$$

where  $x = N\pi(f - f_0)/f_0$ ,  $G_a$  the unperturbed radiation conductance and  $B_a$  the unperturbed radiation susceptance. The given approximation is valid in the neighborhood of  $f_0$ .



# Appendix E

## Tangential stiffness

In section 3.2.3 we use the tangential stiffness of a sphere-plane contact. In this appendix, we give the non-linear tangential relation, which is used to find the linear approximation.

When a tangential force is applied to two bodies pressed into contact, which is less than the limiting force, no sliding motion will occur. Nevertheless, there will be a relative motion referred to as presliding displacement  $\delta_x$ . See figure E.1(a). The radius  $a$  is the contact radius as given by Hertz's theory ( $a = \sqrt{\delta_z R}$ ). The following example explains the physical behavior. If the normal force  $F_n$  is kept constant and the tangential (presliding) displacement is increased steadily from zero, micro-slip will occur at the edges of the contact area. See figure E.1(b). As the tangential displacement  $\delta_x$  approaches the maximum displacement  $\delta_{x,\max}$ , the stick radius  $c$  approaches zero and the stick region shrinks to a point at  $(x, y) = 0$ . Any attempt to increase  $\delta_x > \delta_{x,\max}$  causes the contact to slide.

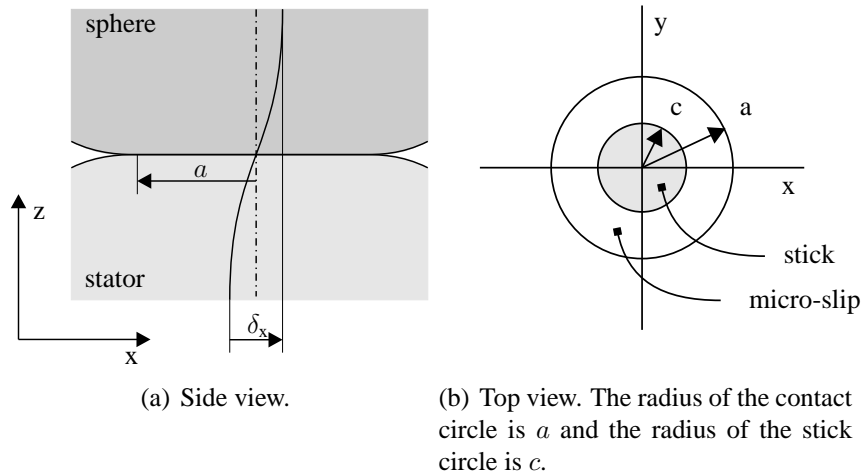


Figure E.1: The contact interface.

According to Johnson (1994), Cattaneo (1938) proposed a solution to the problem of tangential loading for a constant normal force  $F_n$ . Figure E.2 shows the corresponding constitutive nonlinear relation between the tangential force  $F_t$  and the presliding displacement

$\delta_x$ . The relation is described by

$$F_t = \mu_d F_n \left( 1 - \left( 1 - \frac{16G\delta_x\sqrt{\delta_z R}}{3\mu_d F_n} \right)^{3/2} \right) \Big|_{F_n=\text{const}}$$

where

$$G = \left( \frac{2 - \sigma_1}{G_1} + \frac{2 - \sigma_2}{G_2} \right)^{-1} \left[ \frac{N}{m^2} \right]$$

and  $G_1$  and  $G_2$  are respectively the shear modulus of slider and stator. For an isotropic material  $G_1 = \frac{E_1}{2+2\sigma_1}$ . The dynamic coefficient of friction is denoted by  $\mu_d$ .

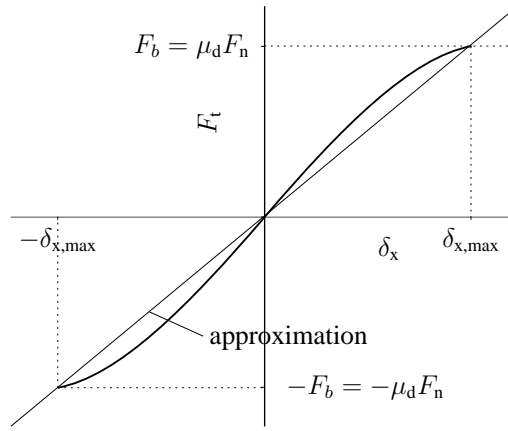


Figure E.2: Relation between tangential displacement  $\delta_x$  and tangential force  $F_t$  at a constant normal force  $F_n$ .

When the normal force is changing, the behavior may be quite complex, because normal force, normal stiffness and tangential stiffness are nonlinear, interacting functions of the normal displacement. In general, the state of contact between two bodies subjected to variations in normal and tangential load depends on the history. To a first approximation it is actually the breakaway displacement  $\delta_{x,\text{max}}$  that is constant (Armstrong-Hélouvy et al. 1994). The stiffness function is than

$$\begin{aligned} F_t &= \frac{F_b}{\delta_{x,\text{max}}} \delta_x \\ &= \frac{16G\sqrt{\delta_z R}}{3} \delta_x \\ &= k_t(\delta_z) \delta_x \end{aligned}$$

where  $F_b = \mu_d F_n$  is the breakaway force. The approximation is shown in figure E.2.



# Bibliography

- 20-sim (2003), 'Controllab products b.v.', www.20sim.com. version 3.4–3.6.
- Armstrong-Hélouvry, B., Dupont, P. & Candudas de Wit, C. (1994), 'A survey of models, analysis tools and compensation methods for the control of machines with friction', *Automatica* **30**(7), 1083–1138.
- Asai, K. & Kurosawa, M. K. (2004), 'Simulation model of surface acoustic wave motor considering tangential rigidity', *Electronics and Communications in Japan* **87**(2), 54–66.
- Asai, K., Kurosawa, M. K. & Higuchi, T. (2000), Evaluation of the driving performance of a surface acoustic wave linear motor, in 'Proc. of IEEE Ultrasonic Symp.', Vol. 3C.
- Asai, K., Kurosawa, M. K. & Toshiro, H. (1999), Novel power circulation methods for a surface acoustic wave motor, in 'IEEE Ultrasonics Symposium', Lake Tahoe, Nevada, U.S.A., pp. 667–670.
- Auld, B. A. (1990), *Acoustic Fields and Waves in Solids*, 2nd edn, Krieger publishing company, inc.
- Barth, H. V. (1973), 'Ultrasonic driven motor', *IBM technical disclosure bulletin* **16**, 2263–2271.
- Bergsma, D. J. & de Jong, N. R. E. (1999), Transport via solid waves, a direct driven ultrasonic motor using surface acoustic waves, Master's thesis, University of Twente. Committee: M. P. Koster, P. C. Breedveld, J. van Dijk.
- Breedveld, P. C. (1984), Physical Systems Theory in Terms of Bond Graphs, PhD thesis, University of Twente.
- Breedveld, P. C. (2000), An alternative model for static and dynamic friction in dynamic system simulation, in '1st IFAC conference on Mechatronic Systems, Darmstadt, Germany', pp. 717–722.
- Campbell, C. K. (1998), *Surface Acoustic Wave Devices for Mobile and Wireless Communications*, Academic Press, inc.
- Cattaneo, C. (1938), 'Sul contatto di due corpi elastici: distribuzione locale degli sforzi', *Rendiconti dell' Accademia nazionale die Lincei* **27**(6).

- Cheng, K. C. (1989), *Field and Wave Electromagnetics*, Addison-Wesley Publishing Company.
- Cheng, L. P., Zhang, G. M., Zhang, S. Y., Yu, J. & Shui, X. J. (2002), 'Miniaturization of surface acoustic waves rotary motor', *Ultrasonics* **39**, 591–594.
- Chiba, M., Takahashi, M., Kurosawa, M. & Higuchi, T. (1997), Evaluation of a surface acoustic wave motor output force, in 'Proc. IEEE Workshop on Micro Electro Mechanical Systems, MEMS', Nagoya, Japan, pp. 250–255.
- Coelingh, H. J. (2000), Design Support for Motion Control Systems - a mechatronic approach, PhD thesis, University of Twente.
- Davis, F. (1993), 'Matching network designs with computer solutions', Motorola Semiconductor Application Note, AN267/D. [www.freescale.com](http://www.freescale.com).
- De Benedictis, G. A. (2003), Position measurement of a surface acoustic wave motor, Research report 014CE2003, University of Twente.
- De Kruif, B. J. (2004), Function Approximation for Learning Control - a key sample based approach, PhD thesis, University of Twente, Enschede, Netherlands. ISBN 90-365-2050-9.
- Dijk, P. (2000), Development of a surface acoustic wave linear motor, Master's thesis, University of Twente. Committee: M.P. Koster, P. C. Breedveld, M. M. P. A. Vermeulen (Philips CFT), E. Gerritsen.
- dSPACE (2001), '[www.dspace.de](http://www.dspace.de)'.
- Dubrovin, B. A., Fomenko, A. T. & Novikov, S. P. (1984), *Modern Geometry-Methods and Applications, Part I. The Geometry of Surface, Transformation Groups, and Fields*, 2nd edn, Springer-Verlag New York.
- Faik, S. & Witteman, H. (2000), Modeling of impact dynamics: A literature survey, in 'International ADAMS User Conference'.
- Feenstra, P. J. & Breedveld, P. C. (2003), Analysis of a surface acoustic wave motor, in D. E. Yuhas & S. C. Schneider, eds, '2003 IEEE International Ultrasonics Symposium Proceedings', Hawaii, USA, pp. 1133–1136. ISSN: 1051-0117 ISBN: 0-7803-7923-3.
- Feenstra, P. J. & Breedveld, P. C. (2004), Parameter variation of a surface acoustic wave motor, in 'The 18th International Congress on Acoustics', Science Council of Japan, Acoustical Society of Japan, and Institute of Noise Control Engineering of Japan, Kyoto, Japan, pp. 189–192.
- Feenstra, P. J., Breedveld, P. C. & Van Amerongen, J. (2005), Actuation methods for a surface acoustic wave motor, in '2nd International Workshop on Piezoelectric Materials and Applications in Actuators', Heinz Nixdorf Institute, University of Paderborn, Paderborn, Germany,.

- Gooberman, G. (1968), *Ultrasonics Theory and Application*, The English Universities press ltd, St. Paul's House Warwick lane.
- Härdtl, K. H. (1982), 'Electrical and mechanical losses in ferroelectric ceramics', *Ceramics International* **8**(4), 121–127.
- Hélin, P. (1997), Theoretical and Experimental Studies of Ultrasonic Motors Using Lamb or Rayleigh Waves, PhD thesis, University of Valenciennes and Hainaut Cambrésis.
- Ikeda, T. (1990), *Fundamentals of Piezoelectricity*, Oxford University Press.
- Inagawa, K. & Koshiba, M. (1994), 'Equivalent networks for saw interdigital transducers', *IEEE Transactions on Ultrasonics, Ferroelectrics, and Frequency Control* **41**(3), 402–411.
- Ji, Y. & Zhao, C. (2005), A new non-contact ultrasonic motor with higher revolution speed, in 'International Workshop on Piezoelectric Materials and Actuators'.
- Johnson, K. L. (1994), *Contact Mechanics*, Cambridge University Press. ISBN 0-521-34796-3.
- Kamphuis, J. J. (2003), Rotating surface acoustic wave motor, Ioo-report 008ce2003, Control Laboratory, University of Twente.
- Karnopp, D. (1985), 'Computer simulation of stick-slip friction in mechanical dynamic systems', *Transactions of the ASME* **107**, 100–103.
- Karnopp, D. C., Margolis, D. L. & Rosenberg, R. C. (2000), *System Dynamics, Modeling and Simulation of Mechatronic Systems*, 3rd edn, John Wiley and Sons, Inc.
- Kino, G. S. (1987), *Acoustic waves: Devices, Imaging and Analog Signal Processing*, Prentice-Hall, Inc. corrected edition 2000.
- Kleesattel, C., Hills, F., Balamuth, L. & Kuris, A. (1962), 'Methods and means for driving small diameter shafts at high rotational speeds', Patent. Applicant: Cavitron ultrasonics inc, Patent number: US3058218.
- Koç, B., Başaran, D., Akin, T. & Erden, A. (2002), Design of a piezoelectric ultrasonic motor for micro-robotic application, in 'Int. Conf. Mechatronic Design and Modeling, Turkey', pp. 205–219.
- Koster, M. P. (2000), *Constructieprincipes voor het Nauwkeurig Bewegen en Positioneren*, Twente University Press, Enschede, Netherlands. In Dutch.
- Kurosawa, M., co-researchers & students (2004), 'Surface acoustic wave motor; papers of research project'. 1992.11 – 2004.9.
- Kurosawa, M. K., Itoh, H. & Asai, K. (2001), Optimization of slider contact face geometry for surface acoustic wave motor, in 'Proceedings of Micro Electro Mechanical Systems', pp. 252–255.

- Kurosawa, M., Takahashi, M. & Higuchi, T. (1994), An ultrasonic x-y stage using 10 MHz surface acoustic wave, in 'Proc. of IEEE Int. Ultrasonics Symp', Cannes, France, pp. 535–538.
- Kurosawa, M., Takahashi, M. & Higuchi, T. (1996), Optimum pre-load of surface acoustic wave motor, in 'IEEE International Ultrasonics Symposium, San Antonio, Texas'.
- Madou, M. J. (2002), *Fundamentals of microfabrication, the science of miniaturization*, 2nd edn, CRC Press.
- Mathworks, Inc. (2003), 'www.mathworks.com'. version 6.5.1.
- Morita, T., Kurosawa, M. K. & Higuchi, T. (1999), 'Simulation of surface acoustic wave motor with spherical slider', *IEEE Transactions on Ultrasonics, Ferroelectrics, and Frequency Control* **46**(4), 929–934.
- Munasinghe, M. & Farnell, G. W. (1972), Surface wave scattering at vertical discontinuities, in 'IEEE Ultrasonics Symposium Proceedings, New York', pp. 267–270.
- Nakamura, K. & Adachi, Y. (1998), 'Piezoelectric transformers using LiNbO<sub>3</sub> single crystals', *Electronics and Communications in Japan, Part 3* **81**(7). Translation.
- Nakamura, Y., Kurosawa, M. K. & Shigematsu, T. (2003), Effects of ceramic thin film coating on friction surfaces for surface acoustic wave linear motor, in 'Proc. of IEEE International Ultrasonics Symposium', Honolulu, Hawaii, U.S.A., pp. 1766–1769.
- Oliner, A. A., Farnell, G. W., Gerard, H. M., Ash, E. A., Slobodnik, A. J. & Smith, H. I. (1978), *Topics in Applied Physics - Acoustic Surface Waves*, Vol. 20, Springer-Verlag Berlin Heidelberg New York.
- Osakabe, N., Kurosawa, N., Higuchi, T. & O., S. (1998), Surface acoustic wave linear motor using silicon slider, in 'Proc. of IEEE Workshop on Micro Electro Mechanical Systems, MEMS', Heidelberg, Germany, pp. 390–395.
- Peeters, F. G. P. & Vermeulen, M. M. P. A. (2004), Development of controlled surface acoustic wave planar actuators, in 'The 18th International Congress on Acoustics', Science Council of Japan, Acoustical Society of Japan, and Institute of Noise Control Engineering of Japan, Kyoto, Japan, pp. 197–199.
- Philips (1997), *Data Handbook MA03, Piezoelectric Ceramics Specialty Ferrites*, Philips Components.
- Polderman, J. W. & Willems, J. C. (1998), *Introduction to Mathematical Systems Theory: A Behavioral Approach*, Springer-Verslag.
- Sashida, T. (1985), 'Motor device utilizing ultrasonic oscillation', Patent. Applicant: Sashida tushiiku (JP), Patent number: US4562374.
- Senturia, D. S. (2001), *Microsystem Design*, Kluwer Academic Publisher.
- Shigematsu, T. & Kurosawa, M. K. (2004), Nanometer resolution 2-d in-plane saw motor, in 'Actuator 2004, 9th International Conference on New Actuators', Bremen, Germany.

- Shigematsu, T., Kurosawa, M. K. & Asai, K. (2003), 'Nanometer stepping drives of surface acoustic waves motor', *IEEE Transactions on Ultrasonics, Ferroelectrics, and Frequency control* **50**(4), 376–385.
- Solidworks corporation (2004), 'www.solidworks.com'.
- Storck, H. (2004), Optimierung der Kontaktvorgänge bei Wanderwellenmotoren, PhD thesis, Universität Paderborn, Heinz Nixdorf Institut, Mechatronik und Dynamik. ISBN 3-935433-47-6.
- Takasaki, M., Osakabe, N., Kurosawa, M. K. & Higuchi, T. (1998), Miniaturization of surface acoustic wave linear motor, in 'Proc. of IEEE int. Ultrasonics Symposium', Sendai, Japan, pp. 679–682.
- Uchino, K. (1997), *Piezoelectric actuators and ultrasonic motors*, Kluwer Academic Publishers.
- Uchino, K. (1998), 'Piezoelectric ultrasonic motors: overview', *Smart Material Structures* **7**, 273–285.
- Uchino, K. (2000), *Ferroelectric Devices*, Marcel Dekker, Inc.
- Uchino, K. & Hirose, S. (2001), 'Loss mechanisms in piezoelectrics: How to measure different losses separately', *IEEE Transactions on Ultrasonics, Ferroelectrics, and Frequency Control* **48**(1), 307–321.
- Ueha, S. & Tomikawa, Y. (1993), *Ultrasonic Motors: Theory and Applications*, Oxford University Press Inc., New York. with contributions from M. Kurosawa and K. Nakamura.
- Van Amerongen, J. (1992), *Regeltechniek*, Vol. 1, 2nd edn, Open univeristeit, Heerlen. In Dutch.
- Van Amerongen, J. & Breedveld, P. C. (2003), 'Modelling of physical systems for the design and control of mechatronic systems (ifac professional brief)', *Annual Reviews in Control* **27**, Elsevier Ltd. **27**, 87–117.
- Van der Schaft, A. & Schumacher, J. M. (2000), *An Introduction to Hybrid Dynamical Systems*, Springer, London.
- Velthuis, W. J. R. (2000), Learning feed-forward control - theory, design and applications, PhD thesis, University of Twente, Enschede, The Netherlands. ISBN 90-36514126.
- Vermeulen, M. M. P. A., Peeters, F. G. P., Soemers, H. M. J., Feenstra, P. J. & Breedveld, P. C. (2002), Development of a surface acoustic wave planar motor under closed loop control, in '3rd Euspen International Conference', Eindhoven University of Technology, The Netherlands, pp. 107–110.
- White, R. M. (1970), Surface elastic waves, in 'Proceedings of the IEEE', Vol. 58, IEEE.
- Williams, A. L. W. & Brown, W. J. (1948), 'Piezoelectric motor', Patent. Applicant: Brush Dev Co, Patent number: US2439499.

- Yang, H., Chao, C.-K. & Wei, M.-K. (2004), 'High fill-factor microlens array mold insert fabrication using a thermal reflow process', *J. Micromech. Microeng* **14**, 1197–1204.
- Yoseph, B.-C., Xiaoqi, B., Hull, A. & Wright, J. (2003), 'Improved multiple-dof saw piezoelectric motors', <http://www.nasatech.com/Briefs/Feb03/NPO20859.html>. Caltech for NASA's Jet Propulsion Laboratory.
- Zhao, C. (2005), Development and applications of ultrasonic motors in china, in '2nd International Workshop on Piezoelectric Materials and Applications in Actuators', Heinz Nixdorf Institute, University of Paderborn, Paderborn, Germany,.

# Nomenclature

## Abbreviations and acronyms

AM	amplitude modulation
cog	center of gravity
CSSA	compensated single-sided actuation
dof	degrees of freedom
DSA	dual-sided actuation
EM	electromagnetic
$F_1$	lowest asymmetric Lamb wave mode
IDT	interdigital transducer
$L_1$	lowest symmetric Lamb wave
l	longitudinal wave
LP	low pass
LTI	linear time invariant
m-poc	multiple points of contact
MEMS	micro electro mechanical systems
PWM	pulse width modulation
r	Rayleigh wave
s	shear wave in an isotropic solid
s-poc	single point of contact
SAW	surface acoustic wave
sh	horizontally polarized shear wave
ss	steady state
SSA	single-sided actuation
sv	vertically polarized shear wave

## Calligraphic symbols

$\mathcal{P}$	time-average power flow
$\mathcal{X}$	Fresnel parameter [-] , page 31

## Greek symbols

$\delta$	indentation [m]
$\eta$	efficiency
$\epsilon$	error
$\lambda$	Lamé constant [N/m <sup>2</sup> ]; wavelength [m]

$\mu$	Lamé constant [N/m <sup>2</sup> ]; mean value
$\mu_d$	dynamic coefficient of friction [-]
$\mu_{st}$	static coefficient of friction [-]
$\omega$	radial frequency [rad/s]
$\psi$	angle where wave vibration velocity equals slider velocity [rad]
$\rho$	mass density [kg/m <sup>3</sup> ]
$\sigma$	Poisson's ratio [-]; standard deviation
$\theta$	angle where slider and stator make contact [rad]

## Operators

$\bullet^*$	complex conjugated of $\bullet$
$\cdot$	dot product
$\bar{\bullet}$	average of $\bullet$ per period of time
$\nabla \times \bullet$	curl of $\bullet$
$\dot{\bullet}$	time derivative of $\bullet$
$\nabla \cdot \bullet$	divergence of $\bullet$
$\nabla \bullet$	gradient of $\bullet$
$\hat{\bullet}$	amplitude of $\bullet$
$\propto$	proportional to

## Roman symbols

$2a$	aperture width [m]
$a_e$	distance between encoder and cog [m]
$a_m$	distance between slider and cog [m]
$A_n$	IDT weighting factor for fingeroverlap
$b$	stator thickness [m]
$B_a$	IDT radiation susceptance [1/ $\Omega$ ]
$c_\bullet$	phase velocity of $\bullet$ wave [m/s]; power constants in $\bullet$ direction, page 29
$c_{ijkl}$	element of stiffness tensor [N/m <sup>2</sup> ]
$C_{IJ}$	element of reduced stiffness tensor [N/m <sup>2</sup> ], page 135
$C_s$	IDT static capacitance of one periodic section [F]
$C_T$	IDT total static capacitance [F]
$dc$	duty cycle
$DV$	infinitesimal neighborhood, page 73
$E$	Young modulus [N/m <sup>2</sup> ]
$f$	frequency [Hz]
$F_n$	normal force [N]
$F_p$	preload force [N]
$F_{p,r}$	release preload force [N], page 84
$F_t$	tangential force [N]
$g$	gravitational acceleration [m/s <sup>2</sup> ]; air gap [m]
$G$	shear modulus [N/m <sup>2</sup> ]
$G_0$	equivalent acoustic admittance [1/ $\Omega$ ]
$G_a$	IDT radiation conductance [1/ $\Omega$ ]
$h$	IDT finger thickness [m]; impulse response
$j$	imaginary unit



$J$	inertia [kg m <sup>2</sup> ]
$k$	stiffness [N/m]
$k_{\bullet}$	wave vector of $\bullet$ wave [1/m]
$k_n$	normal ‘stiffness’ [N/m <sup>2/3</sup> ]
$k_t$	tangential stiffness [N/m]
$K^2$	Rayleigh wave electromechanical coupling factor [-]
$K_D$	derivative gain
$K_I$	integral gain
$K_P$	proportional gain
$K_v$	velocity constant
$\mathbf{l}$	wave propagation direction vector [m]
$m$	mass [kg]
$n$	speed-up factor , page 71
$n_{\text{length}}$	stator length in wavelengths [-]
$n_{\text{thickness}}$	stator thickness in wavelengths [-]
$N$	number of finger pairs [-]
$p$	number of projections
$p_Y$	maximal contact pressure [Pa]
$P$	power [W]
$r$	electric acoustic transformation ratio [V/N]; reference signal, page 148
$r_F$	force ratio [-], page 117
$r_v$	velocity ratio [-], page 117
$R$	radius [m]
$R_c$	dry (Coulomb) friction
$R_d$	tangential compliant damping [Ns/m]
$R_t$	equivalent non-linear damping [Ns/m]
$R_v$	flux reluctance [A/Wb]
$R_z$	normal air damping [Ns/m]
<i>slope</i>	steepness of dry friction implementation [-]
$S_{ij}$	element of strain tensor [-]
$S_I$	element of reduced strain tensor [-], page 135
$t$	time [s]
$T_r$	rise time [s]
$T_{ij}$	element of stress tensor [N/m <sup>2</sup> ]
$T_I$	element of reduced stress tensor [N/m <sup>2</sup> ], page 135
$\dot{u}_{\bullet}$	particle vibration velocity in $\bullet$ direction [m/s]
$\hat{u}_{z,r}$	‘release’ amplitude [m], page 51
$u$	plant input
$u_{\bullet}$	particle displacement in $\bullet$ direction [m]
$u_{\text{min}}$	actuation signal min, page 95
$u_{\text{plus}}$	actuation signal plus, page 95
$v_r$	sliding velocity [m/s]
$\ddot{x}$	tangential slider acceleration [m/s <sup>2</sup> ]
$\dot{x}$	tangential slider velocity [m/s]
$\dot{x}_{\text{max}}$	maximal slider velocity [m/s]
$\dot{x}_r$	normalized slider velocity [-]

---

$\dot{x}_s$	steady state slider velocity [m/s]
$x$	tangential slider displacement [m]
$x_c$	displacement center of gravity [m]
$x_e$	measured (encoder) displacement [m]
$x_{\text{length}}$	stator length [m]
$x_m$	slider displacement [m]
$Y$	yield stress [Pa]; electrical admittance [1/ $\Omega$ ]
$\dot{z}$	normal slider velocity [m/s]
$z$	normal slider displacement [m]
$Z$	electrical impedance [ $\Omega$ ]

# Index

- acoustics, 3
- actuation, 94
  - compensated single-sided, 96
  - dual-sided, 96
  - pulse-width modulation, 97
  - single-sided, 95
- air film, 3, 133
- AM, 14, 95, 127
- aperture width, 12, 30, 35, 120
- apodized IDT, 35
- attenuation, 32, 69, 92
  
- Barth, 2
- beating, 24
- breakaway displacement, 57
- Brown, 2
- bulk wave, *see* plane wave
  
- causality, 56
- ceramics, 41
- closed-loop control, 101
- computation time, 71
- contact model, 45, 58
- coupling factor, 36, 41, 42, 112
  
- dead zone, *see* threshold amplitude
- delta-function model, 36
- dielectric loss, 42
- diffraction, 30, 92, 120
- dispersion curve, 24, 145
- domain wall motion, 42
- dot product, 20
  
- edge transducer, 34
- efficiency
  - IDT, 40, 43
  - piezoelectric ultrasonic motor, 1, 132
  - SAW motor, 65, 132
- Einstein's summation convention, 18
  
- electromagnetic feedthrough, 40
- EM-fields, 41, 127, 133
- equivalent non-linear damper, 63
  
- far-field region, *see* Fraunhofer region
- force-ratio, 117
- Fraunhofer region, 31
- Fresnel region, 31, 120
  
- guiding dynamics, 87
  
- Hélin, 4
- Hertz theory, 47
- horizontally polarized shear wave, 20
- hybrid model, 71
  
- IDT, 12, 34, 116
  - admittance, 35, 149
  - insertion loss, 40, 43
- interdigital transducer, *see* IDT
- isotropic material, 20, 139
  
- Kurosawa, 3
  
- Lamé constants, 139
- Lamb waves, 23, 145
- leaky wave, 33
- longitudinal wave, 20
  
- m-poc, *see* multiple points of contact
- mass loading, 33, 41, 69
- matching network, 14, 39, 128
- mechanical loss, 42
- motor characteristic, 61
  - measured, 78
- multiple points of contact, 65, 75, 77
- mutual interference, 70
  
- near-field region, *see* Fresnel region
- non-leaky SAW, 28

- open-loop control, 100
- phase velocity, 20, 23, 46, 133
- plane wave solution, 19, 135
- power flow, 28, 122
- preload force
  - distribution, 69, 123
  - mechanism, 14, 126
  - variation, 83, 93
- projections, 3, 12, 114, 133
- propagation velocity, *see* phase velocity
- PWM, 97
- PZT, 11, 41, 112
- quality factor, 42, 112
- Rayleigh equation, 22, 142
- Rayleigh wave
  - at a thin layer, 23
  - in an isotropic half space, 21, 139
- reflection, 69
- release amplitude, 51, 62
- release preload force, 84, 116
- rise time, 51, 54, 61, 69
- s-poc, *see* single point of contact
- Sashida, 2
- SAW, 3, 44
- SAW motor
  - circular motion, 6
  - features, 8
  - planar motion, 6, 8
  - power, 64, 122
  - rotation, 7
- scattering, 34
- single crystal, 41, 42
- single point of contact, 46, 74
- slider, 12, 114
- squeeze film of air, *see* air film
- stator, 11, 112
  - roughness, 92, 134
- stepping motion, 101
- strain, 19, 135
- stress, 18, 135
- surface acoustic wave, *see* SAW
- thin-films, 41
- threshold amplitude, 62, 94, 95
- traveling wave motor, *see* Sashida
- triple transit interference, 40
- ultrasonic motor, 2
- velocity-ratio, 119
- vertically polarized shear wave, 20
- vibrometer, 15
- wave equation, 17
- wave scattering, 33
- wave vector, 20, 22
- wedge transducer, 34
- weighted IDT, *see* apodized IDT
- Williams, 2

# Summary

A Surface Acoustic Wave (SAW) Motor utilizes Rayleigh waves that propagate at the surface of a stator. Due to these waves, material particles at the stator surface describe a microscopic elliptical motion. Subsequently, the elliptical particle motion can generate a macroscopic motion of a slider that is pressed against the stator surface. The elliptical particle motion drives the slider by means of friction. The wave amplitude is small (nm) and the wave frequency is large (MHz).

This thesis introduces Rayleigh waves and describes the generation of Rayleigh waves. Furthermore, the principle of operation of a SAW motor is analyzed. The analysis is based on a contact model, which describes the behavior between slider and stator. Due to the contact model, the microscopic and the macroscopic behavior can be studied simultaneously. This model explains typical SAW motor features and determines the influence of parameters. The influence of the model parameters on the SAW motor behavior is studied in order to find the requirements for an optimal contact between slider and stator. The models are validated. To control the SAW motor a linear time invariant system model of the SAW motor is derived and the disturbance sources of the SAW motor are determined and discussed. For closed-loop control, it is useful to eliminate the existing varying dead-band between input and slider velocity. To this end, different actuation methods are investigated. Furthermore, controllers are designed, implemented and tested. Finally, the motor design is studied to obtain an indication for the applied materials, the geometry, the construction, the actuation and the practical limitations. Moreover, a design trajectory, to find initial design parameters, is proposed.



# Samenvatting

Een Surface Acoustic Wave (SAW) Motor maakt gebruik van Raleigh golven die propageren aan het oppervlak van een stator. Door deze golven beschrijven materiaaldeelteje aan het statoroppervlak een microscopische elliptische beweging. Deze beweging kan een macroscopische beweging van een slider, die tegen het stator oppervlak aangedrukt is, genereren. De aandrijving is gebaseerd op wrijving. De golfamplitude is klein (nm) is en de golffrequentie is hoog (MHz).

Dit proefschrift introduceert Rayleigh golven en beschrijft het opwekken van Rayleigh golven. Bovendien wordt het werkingsprincipe van de SAW motor geanalyseerd. De analyse is gebaseerd op een contactmodel dat het gedrag tussen slider en stator beschrijft. Doormiddel van het contactmodel kunnen beide; het microscopisch en het macroscopisch gedrag worden bestudeerd. Hiermee worden typische SAW motor kenmerken verklaard en wordt de invloed van de modelparameters gevonden. De invloed van de modelparameters op het SAW motor gedrag wordt bestudeerd voor het vinden van de eisen voor een optimaal slider-stator contact. De modellen worden gevalideerd. Voor het regelen van de SAW motor wordt een lineair tijdinvariant model van de SAW motor afgeleid en worden de storingsbronnen van de SAW motor bepaald en bediscussieerd. Voor gesloten lus regeling is het zinvol om de variërende dode-band tussen het ingangssignaal en de slidersnelheid te elimineren. Hiertoe worden een aantal mogelijke methodes bestudeerd en vergeleken op basis van effectiviteit en efficiency. Verder worden regelaars ontworpen, geïmplementeerd en getest. Tot slot wordt het SAW motorontwerp bestudeerd voor het verkrijgen van een indicatie van de toepasbare materialen, de geometrie, de constructie de actuatie en de praktische begrenzingen. Bovendien wordt een ontwerptraject, waarmee initiële ontwerpparameters gevonden kunnen worden, geïntroduceerd.





# Dankwoord

In de afsluiting van dit proefschrift wil ik graag een aantal mensen bedanken die op een directe dan wel indirecte manier een bijdrage hebben geleverd aan dit werk.

Natuurlijk mijn begeleiders; Peter Breedveld voor de kritische houding en de filosofische uitingen, die mijn kijk op de wetenschap én de maatschappij verbreed hebben; Job van Amerongen voor de inzet op organiserend en inhoudelijk vlak; Herman Soemers voor de mechatronische kennis en de pragmatische aanpak. Het was een voorrecht jullie als begeleiders te hebben, bedankt!

IOP voor de financiële steun; en de begeleidingscommissie, met leden uit industrie en universiteit, voor de feedback.

Philips Applied Technologies (Eindhoven), waar ik tijdens mijn promotieonderzoek regelmatig te gast was dank ik voor hun gastvrijheid. In het bijzonder dank ik Marc Vermeulen en Felix Peeters voor de vele waardevolle discussies.

De leerstoel Oppervlaktetechnologie en Tribologie (Dik Schipper c.s.) voor de faciliteiten.

In the final year, I had the pleasant opportunity to visit the Tokyo Institute of Technology, Japan. Thanks to both Dr. Kurosawa and Takashi Shigematsu for the wonderful, friendly and inspiring time during this visit.

Ook ben ik dank verschuldigd aan de collega's, studenten en buitenlandse gasten van de vakgroep regeltechniek voor de gezellige sfeer en de technische en inhoudelijke ondersteuning. Mark Verwoerd, met wie ik vier jaar het kantoor heb gedeeld, is een goede vriend geworden. Zijn brede interessegebied, belezenheid en zijn weldoordachte manier van spreken waren een voorbeeld voor mij. Met goede vriend Vincent Duindam verliet ik bijna dagelijks, *ge-triggered* (en opgeschrokken) door de omroepinstallatie, het EL/TN gebouw voor het fietstochtje richting Enschede centrum. Daarnaast heb ik veel goede herinneringen aan de stap-, schaats- en filmuitjes. Norbert Ligterink bedank ik voor de discussies over het werk, politiek en alle andere dingen en Jan Holterman voor zijn pragmatische werkgerelateerde vragen. I like to thank Job Kamphuis and Giuseppe de Benedictis for their contribution to the project. Verder dank voor de mannen van Control Lab Products (20sim) voor de gezelligheid en hun welwillende technische hulp bij simulatieproblemen. Also thanks to the colleagues of the Systems and Control group of the mathematics department for the good time.

Graag bedank ik Sjoerd Kramer en Pieter Kurpershoek voor de muzikale afleiding maar vooral vanwege de gesprekken tijdens de vele en lange koffiepauzes op onze oefenzaterdagen; Rein-Peter de Boer en Jaap Beetstra voor de vakanties en de gezelligheid tijdens de kleine uurtjes; Paul van Dijk voor de Engelse correcties.

Tenslotte dank ik mijn vader en moeder en de rest van mijn familie: Anneke & Wieberen, Jan, Jitte & Janneke en Pieter, voor de steun, interesse, nuchterheid en nog veel-veel meer.



# Curriculum vitae

Philippus Feenstra is geboren op 31 maart 1975 te Workum, Nederland. Hij doorliep de opleiding motorvoertuigtechniek aan de technische school Bolsward en de opleiding elektronica aan het MBO college te Sneek. Na het behalen van zijn propedeuse elektrotechniek aan de Noordelijke Hogeschool Leeuwarden, startte hij in 1995 met de studie elektrotechniek aan de Universiteit Twente. In 1999 liep hij stage bij de Vanderbilt University in Nashville Tennessee, VS en in 2000 studeerde hij af bij de leerstoel regeltechniek op het afstudeerproject: 'A library of Port-based Thermo-Fluid Submodels'. In januari 2001 startte hij met zijn promotieonderzoek 'Positioneren met akoestische oppervlakte golven' bij dezelfde leerstoel regeltechniek van de Universiteit Twente. Dit onderzoek vond plaats in samenwerking met Philips Applied Technologies. Binnen het kader van het onderzoek liep hij in maart 2004 stage in het laboratorium van de onderzoeksinitiator van de SAW motor aan de Tokyo Institute of Technology, Japan.

